VOL. 695 NO. 2 31 MARCH 1995
THIS ISSUE COMPLETES VOL. 695

JOURNAL OF CHROMATOGRAPHY A
INCLUDING ELECTROPHORESIS AND OTHER SEPARATION METHODS

ELSEVIER

JOURNAL OF CHROMATOGRAPHY A

INCLUDING ELECTROPHORESIS AND OTHER SEPARATION METHODS

Scope. The *Journal of Chromatography A* publishes papers on all aspects of **chromatography, electrophoresis** and related methods. Contributions consist mainly of research papers dealing with chromatographic theory, instrumental developments and their applications. In the *Symposium volumes*, which are under separate editorship, proceedings of symposia on chromatography, electrophoresis and related methods are published. *Journal of Chromatography B: Biomedical Applications* —This journal, which is under separate editorship, deals with the following aspects: developments in and applications of chromatographic and electrophoretic techniques related to clinical diagnosis or alterations during medical treatment; screening and profiling of body fluids or tissues related to the analysis of active substances and to metabolic disorders; drug level monitoring and pharmacokinetic studies; clinical toxicology; forensic medicine; veterinary medicine; occupational medicine; results from basic medical research with direct consequences in clinical practice.

Submission of Papers. The preferred medium of submission is on disk with accompanying manuscript (see *Electronic manuscripts* in the Instructions to Authors, which can be obtained from the publisher, Elsevier Science B.V., P.O. Box 330, 1000 AH Amsterdam, Netherlands). Manuscripts (in English; *four* copies are required) should be submitted to: Editorial Office of *Journal of Chromatography A*, P.O. Box 681, 1000 AR Amsterdam, Netherlands, Telefax (+31-20) 485 2304, or to: The Editor of *Journal of Chromatography B: Biomedical Applications*, P.O. Box 681, 1000 AR Amsterdam, Netherlands. Review articles are invited or proposed in writing to the Editors who welcome suggestions for subjects. An outline of the proposed review should first be forwarded to the Editors for preliminary discussion prior to preparation. Submission of an article is understood to imply that the article is original and unpublished and is not being considered for publication elsewhere. For copyright regulations, see below.

Publication information. *Journal of Chromatography A* (ISSN 0021-9673): for 1995 Vols. 683–714 are scheduled for publication. *Journal of Chromatography B: Biomedical Applications* (ISSN 0378-4347): for 1995 Vols. 663–674 are scheduled for publication. Subscription prices for *Journal of Chromatography A*, *Journal of Chromatography B: Biomedical Applications* or a combined subscription are available upon request from the publisher. Subscriptions are accepted on a prepaid basis only and are entered on a calendar year basis. Issues are sent by surface mail except to the following countries where air delivery via SAL is ensured: Argentina, Australia, Brazil, Canada, China, Hong Kong, India, Israel, Japan, Malaysia, Mexico, New Zealand, Pakistan, Singapore, South Africa, South Korea, Taiwan, Thailand, USA. For all other countries airmail rates are available upon request. Claims for missing issues must be made within six months of our publication (mailing) date. Please address all your requests regarding orders and subscription queries to: Elsevier Science B.V., Journal Department, P.O. Box 211, 1000 AE Amsterdam, Netherlands. Tel.: (+31-20) 485 3642; Fax: (+31-20) 485 3598. Customers in the USA and Canada wishing information on this and other Elsevier journals, please contact Journal Information Center, Elsevier Science Inc., 655 Avenue of the Americas, New York, NY 10010, USA, Tel. (+1-212) 633 3750, Telefax (+1-212) 633 3764.

Abstracts/Contents Lists published in Analytical Abstracts, Biochemical Abstracts, Biological Abstracts, Chemical Abstracts, Chemical Titles, Chromatography Abstracts, Current Awareness in Biological Sciences (CABS), Current Contents/Life Sciences, Current Contents/Physical, Chemical & Earth Sciences, Deep-Sea Research/Part B: Oceanographic Literature Review, Excerpta Medica, Index Medicus, Mass Spectrometry Bulletin, PASCAL-CNRS, Referativnyi Zhurnal, Research Alert and Science Citation Index.

US Mailing Notice. *Journal of Chromatography A* (ISSN 0021-9673) is published weekly (total 52 issues) by Elsevier Science B.V., (Sara Burgerhartstraat 25, P.O. Box 211, 1000 AE Amsterdam, Netherlands). Annual subscription price in the USA US$ 5389.00 (US$ price valid in North, Central and South America only) including air speed delivery. Second class postage paid at Jamaica, NY 11431. **USA POSTMASTERS**: Send address changes to *Journal of Chromatography A*, Publications Expediting, Inc., 200 Meacham Avenue, Elmont, NY 11003. Airfreight and mailing in the USA by Publications Expediting.

See inside back cover for Publication Schedule, Information for Authors and information on Advertisements.

0021-9673/95/$09.50

Printed in the Netherlands

CONTENTS

(Abstracts/Contents Lists published in Analytical Abstracts, Biochemical Abstracts, Biological Abstracts, Chemical Abstracts, Chemical Titles, Chromatography Abstracts, Current Awareness in Biological Sciences (CABS), Current Contents/Life Sciences, Current Contents/Physical, Chemical & Earth Sciences, Deep-Sea Research/Part B: Oceanographic Literature Review, Excerpta Medica, Index Medicus, Mass Spectrometry Bulletin, PASCAL-CNRS, Referativnyi Zhurnal, Research Alert and Science Citation Index)

REGULAR PAPERS

Column Liquid Chromatography

Gas Chromatography

Planar Chromatography

Electrophoresis

(Continued overleaf)

Contents (continued)

SHORT COMMUNICATION

Column Liquid Chromatography

Gas Chromatography

ELSEVIER

Journal of Chromatography A, 695 (1995) 165–174

JOURNAL OF CHROMATOGRAPHY A

Near-infrared laser-induced fluorescence detection in column liquid chromatography. A comparison of various lasers and detection systems
I☆. Continuous wave lasers

A.J.G. Mank*, N.H. Velthorst, U.A.Th. Brinkman, C. Gooijer

Department of General and Analytical Chemistry, Free University, De Boelelaan 1083, 1081 HV Amsterdam, Netherlands

First received 21 June 1994; revised manuscript received 2 December 1994

Abstract

Several lasers, i.e. HeNe lasers, diode lasers and an argon-ion–dye laser combination, are compared as excitation sources for near-infrared laser-induced fluorescence detection in column liquid chromatography. Using a model gradient liquid chromatography system, detection limits for disulphonated aluminum phthalocyanine (AlPcS2) were compared after optimization of the signal processing scheme for each laser. The best detection limit ($1.5 \cdot 10^{-13}$ M) was obtained for the argon-ion–dye laser combination, applying ratioing of emission and excitation light to reduce flicker noise. Utilizing diode laser excitation there is no need for ratioing so that emission collection can be improved and a detection limit similar to that obtained with the argon-ion laser can be achieved. As this device is very cheap, the diode laser is the best choice for most applications. If tunability over a large wavelength region is essential, the argon-ion–dye laser combination is a good but expensive alternative.

1. Introduction

Recently, much attention has been paid to the development of laser-induced near-infrared fluorescence methods for detection purposes in, for instance, conventional-size column liquid chromatography (LC). Compared with conventional helium–cadmium or argon-ion laser-induced fluorescence (LIF) [1], detection in the near-infrared (NIR) has some obvious advantages. First of all, cheap and stable helium–neon (HeNe) lasers and diode lasers can be used for excitation. Furthermore, background fluorescence intensity is low, Raman scatter is weak (proportional to λ^{-4}) and photochemical decomposition is negligible. On the other hand, the number of analytes that can be detected without chemical derivatization is limited; this explains the recent attention directed to the development of covalent-labelling procedures with NIR-absorbing fluorophores [2]. Still, photosensitizers (like phthalocyanines) used in photodynamic therapy form a very interesting and relevant group of compounds that can be excited directly [3].

In the present study the performance of the various lasers as excitation sources in NIR LIF detection after LC is examined. Part I is devoted

* Corresponding author.

☆ For Part II see Ref. [16].

0021-9673/95/$09.50
SSDI 0021-9673(94)01195-8

Table 1
Spectroscopic characteristics of several near-infrared lasers

Laser type	Wavelength (nm)	Pulsed/CW	Power (mW)[a]	Fluctuation (%)[b]
HeNe	633	CW	2–15	0.1–0.5
Diode	630–690	CW	3–30	0.1–0.5 (0.0025)
Argon-ion	Several lines[c]	CW	100[d]	0.5–3 (0.05)
Nd:YAG	1064/532/355[c]	Pulsed	20 000/6/10[d]	10–30 pulse-to-pulse
XeCl-excimer	308[c]	Pulsed	10 000/15/100[d]	2–3 pulse-to-pulse

[a] Peak power/pulse duration (ns)/repetition rate (Hz).
[b] Value between parentheses can be achieved with feedback stabilization.
[c] Indicates the need of a dye laser to obtain red or NIR laserlight.
[d] Laser dyes used: Rhodamine 101 (22% efficiency for argon-ion laser excitation), Oxazine 170 (20% efficiency for Nd:YAG laser excitation) and DCM (12% efficiency for XeCl-excimer laser excitation).

to continuous wave (CW) lasers, i.e. various diode and HeNe lasers as well as a tunable argon-ion–dye laser combination. Part II deals with the performance of readily tunable pulsed lasers (which are not often applied for LC–LIF detection), i.e. a frequency-doubled Nd:YAG laser and an excimer laser, both combined with dye lasers. Some general characteristics and spectroscopic features are presented in Table 1 [4].

Gradient LC of a mixture of disulphonated aluminum phthalocyanine (AlPcS2) isomers, containing 85% of one isomer, is used as a model LC system [5]. This mixture is considered one of the most relevant photosensitizers available for photodynamic therapy and was introduced only recently. Chromatographic separation of the various AlPcS2 isomers is necessary, because their spectroscopic properties are very similar and they are expected to show both different effectivity as photosensitizers and different retention mechanisms in the body [5].

2. Experimental

2.1 Chemicals

HPLC-grade methanol was purchased from J.T. Baker Chemicals (Deventer, The Netherlands). Purified disulphonated aluminum phthalocyanine (AlPcS2), synthesized by direct sulphonation of non-substituted AlPcCl and fractionated by reversed-phase (RP) LC, was obtained from Porphyrin Products (Logan, UT, USA). All laser dyes were obtained from Radiant Dyes (Wermelskirchen, Germany).

2.2 Chromatography

The degassed eluent was delivered by two Applied Biosystems (Foster Hill, CA, USA) Series 400 pumps, controlled by the computer of a 1000 S diode array detector. A Valco injection valve equipped with a 25-μl loop was used for sample injection on a 250×3.1 mm I.D. C_{18} (5-μm particles) Vydac (Hersperia, CA, USA) analytical column. A 10×3.0 mm I.D. C_{18} (20-μm particles) home-made precolumn was used to protect the analytical column. Linear gradient elution was performed from methanol–5 m*M* phosphate buffer (pH 4.0) (25:75, v/v) to methanol–5 m*M* phosphate buffer (pH 4.0) (90:10, v/v) in 15 min, at a flow rate of 1.0 ml min^{-1}, followed by a further 10 min isocratic elution.

2.3 Detection

Information about detection and signal processing instrumentation used and, if relevant, its optimization is given below.

General

The absorption spectrum of AlPcS2 was recorded on a DU-64 spectrophotometer (Beckman, Anaheim, CA, USA). The fluorescence spectra were recorded on a LS-50 spectrofluori-

meter (Perkin Elmer, Gouda, The Netherlands) equipped with a R928 photomultiplier (PMT) (Hamamatsu Photonics, Hamamatsu City, Japan).

The absorption maxima of AlPcS2 (ϵ = 180 000 l mol^{-1} cm^{-1}) in methanol and water are at 670.4 nm and 671.6 nm, respectively. The emission maxima are found at 678.0 nm and 680.0 nm, with corresponding fluorescence quantum efficiencies of 0.50 and 0.37, and fluorescence lifetimes of 6.2 ns and 5.1 ns, respectively [6]. Triplet state yields of 0.3–0.4 in water and methanol have been reported for several sulphonated phthalocyanines, with triplet state lifetimes of 250–500 μs [7–9]. In this paper a fluorescence quantum yield of 0.43, a fluorescence lifetime of 6.0 ns, a triplet state quantum yield of 0.33 and a triplet state lifetime of 300 μs are assumed for AlPcS2 in the LC eluent [9].

Detector cell

On-line fluorescence detection is performed with a two-fiber detector cell (Fig. 1), based on a home-made quartz flow cell (Suprasil I) with external dimensions of 4.0 × 4.0 × 10 mm and an internal bore of 1.1 mm. Collection of the fluorescence light takes place via a 60 cm long quartz fiber (1.2 mm outer diameter; 1.0 mm core diameter) with a 0.22 numerical aperture (Quartz and Silice, Uithoorn, The Netherlands). The cladding is stripped over a length of 7 mm, starting from the distal end of the fiber, to allow insertion of the fiber into the bore of the flow cell. A similar fiber is inserted from the other side of the flow cell for the collection of a small amount of light, elastically scattered by the eluent, to create a reference signal that is linearly dependent on the laser intensity.

A collimated laser beam is directed through the flow cell perpendicular to the flow direction. The fluorescence light is guided through the fiber to an adjustable lens holder, focused onto a PMT through a 2.5 cm $f/\# = 1$ lens and a set of emission filters that will change with the light source. Focusing is necessary because of the relatively small active area of the PMT (7.6 × 23 mm, rectangular). After intensity reduction with neutral-density filters to avoid overloading, the reference signal is guided through the other fiber to a similar PMT.

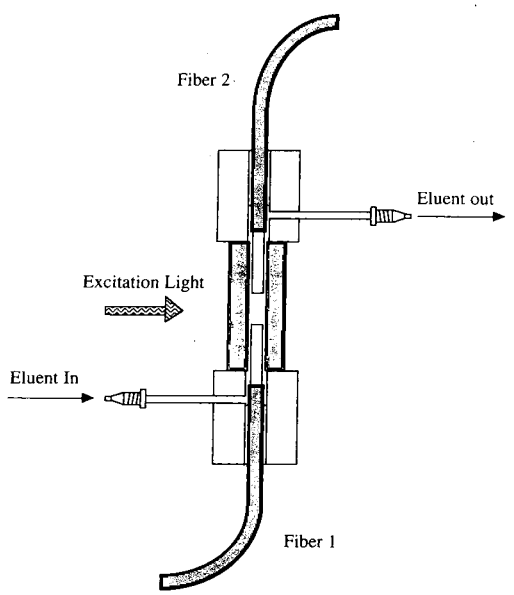

Fig. 1. Side view of the detector cell with two fibers put in from the top and the bottom, secured with fingertights; 1/16-in. LC connections are positioned perpendicular to the eluent stream through the flow cell.

Illuminated volume

The laser beam is collimated and adjusted to a beam diameter of 500 μm on entering the flow cell, using a number of lenses with different focal lengths. Apart from the diode lasers, the beam diameter was (500 ± 50) μm and gaussian in profile for all lasers tested. This corresponds to an illuminated volume of about 0.2 μl, which is small for conventional-size LC applications [10]. The beam emitted by diode lasers is elliptical, with a maximum "beam width" of (500 ± 50) μm and a maximum "beam height" of (190 ± 20) μm. The major axis is taken parallel to the fiber surface. Divergence of the excitation beam within the flow cell is limited to about 10 μm due to the small difference in refractive index between the LC eluent and the fused silica of the flow cell. A spatial filter (500 × 500 μm) is applied to remove any light emitted outside this region. Both fiber tips are positioned at 250 μm distance from the beam edge with home-made fingertights (Fig. 1).

Emission collection

Direct scatter from the flow cell and the fibers is negligible because of the spatial filter. The high reflections from the outer (air–fused silica) surface of the flow cell (4%) lie beyond the field of view of the fibers. Reflections on the inner (fused silica–eluent) surface are much lower in intensity (<0.4%) as a result of the smaller difference in the refractive index. Long-pass emission filters are used to remove the remaining elastic scatter.

Fluorescence background from the flow cell and eluent impurities is of little influence in the NIR region. Raman scatter forms the most significant source of background, though it has a low intensity and stretches over a large wavelength region; for example, the strong Raman band of water lies beyond 840 nm for excitation at 670 nm. A LS-740 0.5″ short-pass filter (Corion, Holliston, MA, USA) is therefore used in all detection setups to remove much of the unwanted Raman scatter. The use of polarization filters to remove scattered excitation light did not reduce the background enough to compensate for the loss of transmitted fluorescence signal.

The emission collection filter set was optimized for each tested laser by adding combinations of 2–4 mm RG5, RG665, RG695 long-pass filters (Schott Nederland, Tiel, The Netherlands). In all cases the filters were sufficient to remove the elastically scattered laser light. The transmission of emission light through bandpass filters was found to be very low and therefore such filters were not used in the present study.

NIR detection

Several detectors are available for NIR detection, i.e. various types of photodiodes and PMTs. Simple (p–i–n) silicon photodiodes with an acceptable noise equivalent power (NEP) can be used ($15 \cdot 10^{-14}$ W $\sqrt{\text{Hz}^{-1}}$ at 700 nm for a 25 mm^2 sensitive area) in combination with integrated preamplifiers [11]. Silicon avalanche photodiodes show a 10-fold lower NEP and a quantum efficiency (QE) of 0.7–0.8 between 600 and 800 nm.

In this study C31034A02 GaAs PMTs (Burle, Lancaster, PA, USA) (QE = 0.25 at 700 nm) are used for all detection set-ups, because signal-to-noise (S/N) ratios were at least 20-fold higher for the PMT, compared to the photodiode–preamplifier combinations. The PMTs are operated at 1750 V with an EG & G Ortec (Oak Ridge, TN, USA) Model 456H high-voltage power supply and cooled to −23°C with a PMT housing from Products for Research (Danvers, MA, USA), regulated with a home-made controller. Fast electronics supplied by Products for Research provided a 2.5 ns rise time and 33 ns transit time for the PMT.

2.4 Signal processing

Three types of processing of the PMT signal were used, i.e. direct amplification, analog ratioing and photon counting.

Direct amplification

The PMT output is passed through a current-to-voltage converter, based on a AD515ALH operational amplifier (Analog Devices, Norwood, MA, USA) in combination with different feedback resistors and capacitors to scale the conversion factor (Fig. 2, dashed lines). After conversion, a 1 Hz second-order low-pass R × C filter is applied and the signal is either displayed directly on a Kipp and Zonen (Delft, The Netherlands) BD111 recorder or digitized using an Apple Macintosh SE computer.

Analog ratioing

Compared to digital ratioing after data collection, analog ratioing has the advantage that the rate at which the fluorescence and the reference signal are compared can be much higher. An analog ratioing system was built and optimized as described in ref. 1 (Fig. 2, solid lines). The heart of the system is an Analog Devices AD538 analog multiplier, configured in a single quadrant analog division mode.

The reference signal applied is much more intense than the fluorescence signal to reduce the influence of shot noise; by utilizing a smaller amplification factor, the resulting signals are

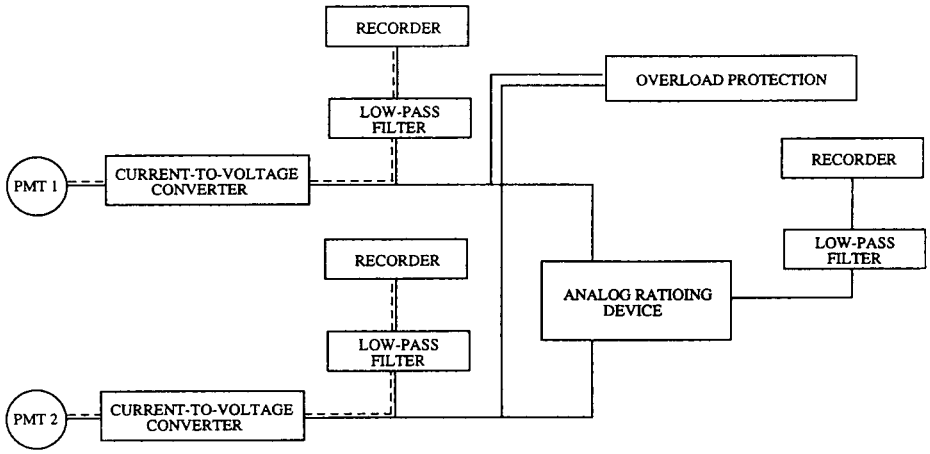

Fig. 2. Signal processing scheme. Dashed line = direct amplification; solid line = analog ratioing.

brought to the same intensity before ratioing is performed. Thus, under optimum conditions, ratioing allows detection limits to be determined by shot noise on the fluorescence signal.

Photon counting

Data from a SR400 photon counter (Stanford Research Systems, Palo Alto, CA, USA) are sent to an Apple Macintosh SE and handled in real time with a home-made programme that transforms the raw SR400 data into ASCII. Measurements can be performed using two detection channels at the same time, which allows ratioing after data collection.

The detection system was evaluated in terms of its "classic" photon counting performance [12]. For a PMT voltage of 1850 V, the dark current count rates were below 10 counts s^{-1} when using a photon counter threshold of −10 mV. At this PMT voltage nearly all photoelectron events induce a signal above the threshold, which is a prerequisite for photon counting since under shot noise-limited conditions photon counting is more sensitive than analog signal processing only if the discriminator coefficient is unity [13]. As the background rarely reached values below 1000 counts s^{-1}, dark current noise is negligible.

2.5 Laser systems

Two HeNe lasers, various types of diode lasers and an argon-ion–dye laser combination were tested.

HeNe lasers

The two lasers are HeNe(1): Spectra-Physics Model 117A (Mountain View, CA, USA), emitting 2 mW (TEM_{oo}); fluctuations in the output power are 0.1% for 1 min and 0.3% for 1 h, and HeNe(2): NEC (Tokyo, Japan) GLG5700/GLG5702 power supply, emitting 15 mW (TEM_{oo}); laser intensity instability, 0.2% for 1 min and 0.5% for 1 h.

Diode lasers

The operating characteristics of the diode lasers involved are given in Table 2. All diode lasers are biased by a LD2310 diode laser driver in combination with a AC9400 power supply (Seastar Optics, Seattle, WA, USA). Optical feedback is used to stabilize the diode lasers, which results in a maximum flicker noise of $8 \cdot 10^{-3}$% over 1 min and $1 \cdot 10^{-2}$% over 30 min. Applying a cheap LDD-200 driver unit (Meredith, Glendale, AZ, USA), which also uses an optical feedback loop, resulted in a short-term laser flicker noise of $5 \cdot 10^{-2}$%. Power

Table 2
Operating characteristics of the diode lasers used in this study

Diode laser (type)	Wavelength (nm)[a]	Maximum power (mW)	Operating current (mA)	Detection limit[b] (p*M*)
Philips CQL84/D	635	3	100	2 (1.5)
Toshiba TOLD 9410	650	3	80	0.7 (0.7)
Toshiba TOLD 9220	660	3	65	0.7 (0.7)
Toshiba TOLD 9211	670	5	55	0.3 (0.4)
Toshiba TOLD 9215	670	10	45	0.2 (0.3)

[a] Nominal values; characteristics never differed more than 1 nm from these values.
[b] Taken as $S/N = 3$ at maximum output power, 3 times determined; values obtained for the diode lasers in combination with the laser-line selector are given in parentheses.

stabilization is also useful because the power/current characteristics and thus the output intensity of diode lasers vary significantly with temperature.

A light-efficient Meredith AR coated multi-element LDC-10 lens (> 85% transmission) was applied to collimate the diode laser beam in all cases. If required, excitation wavelength selection was performed with a laser line selector (Applied Photophysics, London, England).

Argon-ion laser

A Coherent (Palo Alto, CA, USA) Innova 200-10 argon-ion laser is used for the excitation of a Coherent CR-590 Rhodamine 101 dye laser. Laser light of the fundamental frequency and non-lasing plasma lines are rejected by quartz prisms and glass cut-off filters. The selected excitation frequency is 635 nm; a power of 100 mW is available at the flow cell.

3. Results and discussion

3.1 HeNe lasers

To examine the importance of Raman scatter in NIR LIF detection during methanol–water gradient elution, Raman spectra were recorded applying 633 nm excitation (see Fig. 3). It is clear that both the total intensity of the Raman scatter and the fraction detected within the filter bandpass is much larger for methanol than for water (3.5:1). The short-pass filter reduces the background at least four times, while diminishing the transmitted intensity of the emission from the model compound with only some 25%. A chromatogram recorded for $1 \cdot 10^{-11}$ *M* (10 p*M*) AlPcS2 using the 15 mW HeNe laser and applying the direct detection scheme, is depicted in Fig. 4. The gradual increase of the background with time can be fully attributed to Raman scatter, which increases 2-fold during the gradient run which starts at 25% and ends at 90% methanol.

The detection limits obtained with the HeNe lasers are 1 p*M* (2 mW laser) and 0.4 p*M* (15 mW laser) ($S/N = 3$, peak-to-peak noise). The 2.5-fold improvement realized when using the more powerful HeNe laser indicates that shot noise dominates. With photon counting instead of direct detection, essentially the same detection limits were obtained. The linear dynamic range extends to about $1 \cdot 10^{-8}$ *M* and can be further increased to $1 \cdot 10^{-6}$ *M* by utilizing neutral density filters to avoid PMT overloading.

3.2 Diode lasers

The detection limits obtained with the five diode lasers (Table 2) range from 0.2 to 2 p*M* and, as for the HeNe lasers, ratioing does not improve these values; the linear dynamic range extends from the detection limit to about $1 \cdot 10^{-8}$ *M*, similar to the HeNe lasers. The flicker noise contribution of the diode lasers is negligible, even with the LDD-200 driver.

Analogous to gas lasers, diode lasers provide

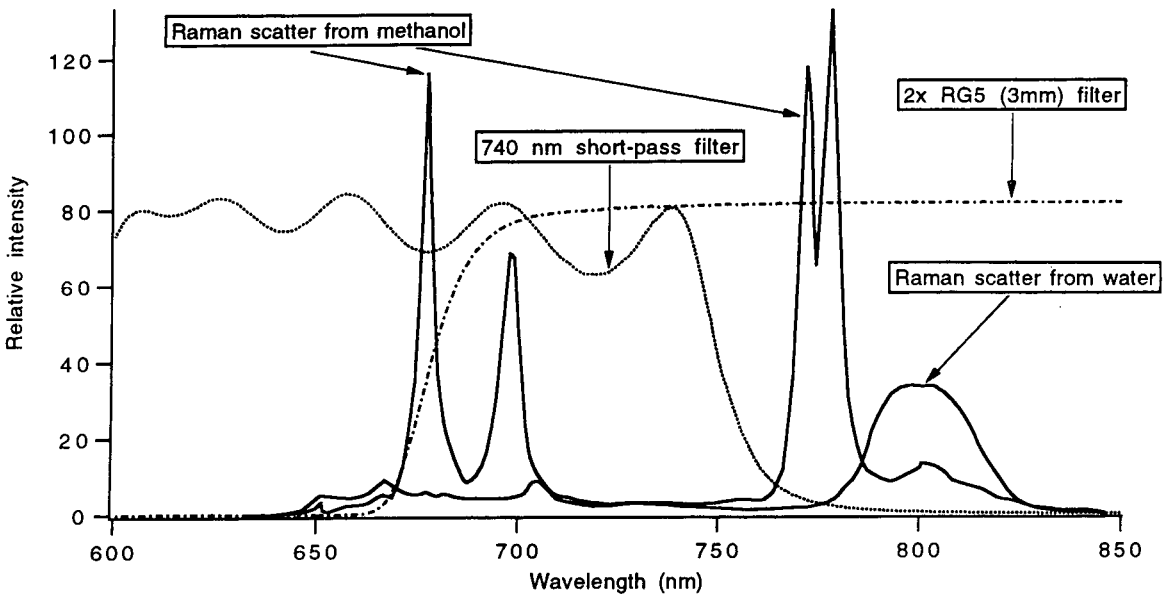

Fig. 3. Raman spectra of methanol and water (solid lines) and the relative transmittance of the applied filters for 633 nm excitation (dashed lines).

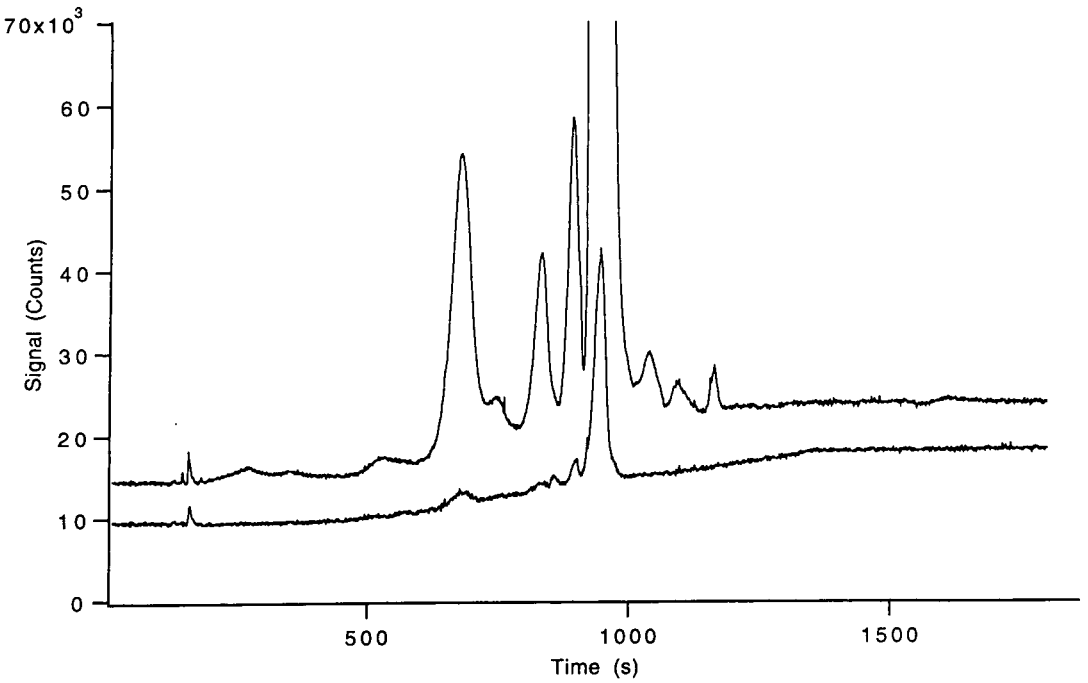

Fig. 4. Gradient LC chromatograms of 10 p*M* (lower trace) and 250 p*M* (upper trace) AlPcS2, recorded with the direct detection system using a 15 mW HeNe laser. For chromatographic conditions see Experimental.

spontaneous unpolarized emission in addition to laser light, which consists of a broad band, sometimes more than 100 nm wide (cf. ref. 14), and is often a major source of background. The higher the threshold current of the laser, the higher the fraction of non-lasing emission [14]. From Table 2 it is clear that especially the diode lasers emitting short-wavelength radiation have a high threshold current. Therefore, for these devices a laser line selector, which functions as a 2 nm bandpass filter (50% transmission; reducing the signal intensity 2-fold) around the lasing wavelength, was inserted in the excitation beam to remove spontaneous emission. Thus, the background is reduced up to 15-fold for the Philips CQL84/D at maximum operating current (see Fig. 5A). It is clear that except for the low-threshold TOLD 9215 in absence of the laser line selector, a large part of the background observed results from non-lasing emission (Fig. 5C). Nevertheless, in practice the improvement achieved by utilizing the laser line selector is only significant for the CQL84/D; see Table 2. Furthermore, the shot noise difference due to the 20 percent difference in Raman scatter at 635 nm and 670 nm is hardly detectable.

The repeatability of the alignment was checked by fivefold injection of $5 \cdot 10^{-11}$ *M* AlPcS2 on the same detection system. After each measurement the laser and the flow cell were taken from the optical bench and the fibers were removed from the flow cell. No more than 15% difference in *S/N* was found between any two of these measurements. Ten consecutive measurements without removing the fibers resulted in a R.S.D. of only 2.8%.

3.3 Argon-ion laser

When using direct current-to-voltage conversion of the PMT signal, the detection limit of AlPcS2 is 0.25 p*M* at 635 nm (100 mW), less than 2-fold better as obtained with the 15 mW HeNe laser.

Since for the argon-ion laser flicker noise contributions are significant, noise on the background increases faster during gradient elution than observed in Fig. 4. Using photon counting, the background at the start of the gradient was $(7.7 \pm 0.1) \cdot 10^4$ with a noise of $(1.9 \pm 0.1) \cdot 10^3$ counts and at the end of the run $(1.50 \pm 0.05) \cdot 10^5$ with a noise of $(3.1 \pm 0.15) \cdot 10^3$ counts. Ratioing enabled a reduction of the noise to $(1.20 \pm 0.06) \cdot 10^3$ and $(1.70 \pm 0.10) \cdot 10^3$ counts, respectively, and an improvement of the detection limit of AlPcS2 from 0.3 p*M* to 0.2 p*M*.

The flicker noise on the output power of the laser can be estimated using the above information and the fact that for the ratioing procedure a reference signal of $2.3 \cdot 10^6$ counts (30 × the background signal at the start of the gradient) was used. After correction for the introduction of additional shot noise by the reference signal (0.25%), the flicker noise in the output intensity of the argon-ion laser can be calculated to be about 1%. Thus, at the beginning of the gradient the relative importances of shot and flicker noise is 0.8 to 1.1; at the end their contributions are equal, i.e. $1.5 \cdot 10^3$ counts.

Analog ratioing gives a 0.15 p*M* detection limit for AlPcS2, a marginal improvement compared to photon counting. For all argon-ion laser based detection systems described, the linear dynamic range extends from the detection limit to about $1 \cdot 10^{-8}$ *M*.

3.4 Comparison

Comparison of the detection limits obtained for the various CW lasers (0.4 p*M* for the 15 mW HeNe laser; 0.2 p*M* for the 10 mW diode laser and 0.15 p*M* for the 100 mW argon-ion laser) shows that, as expected under shot noise-limited conditions, the analyte detectability improves with the square root of the laser power. To show this dependence, corrections have to be made for the excitation efficiency of the model compound and the fluorescence collection efficiency through the emission filters used to remove scattered excitation light. To quote one example, when comparing the performances of the 100 mW 635 nm argon-ion laser and the 10 mW 670 nm diode laser, the improvement is $\sqrt{10}$-fold, since at 635 nm excitation is 4.5-fold less efficient, while the emission collection efficiency is 2.3 times higher. As a result, the detection limit at 635 nm should

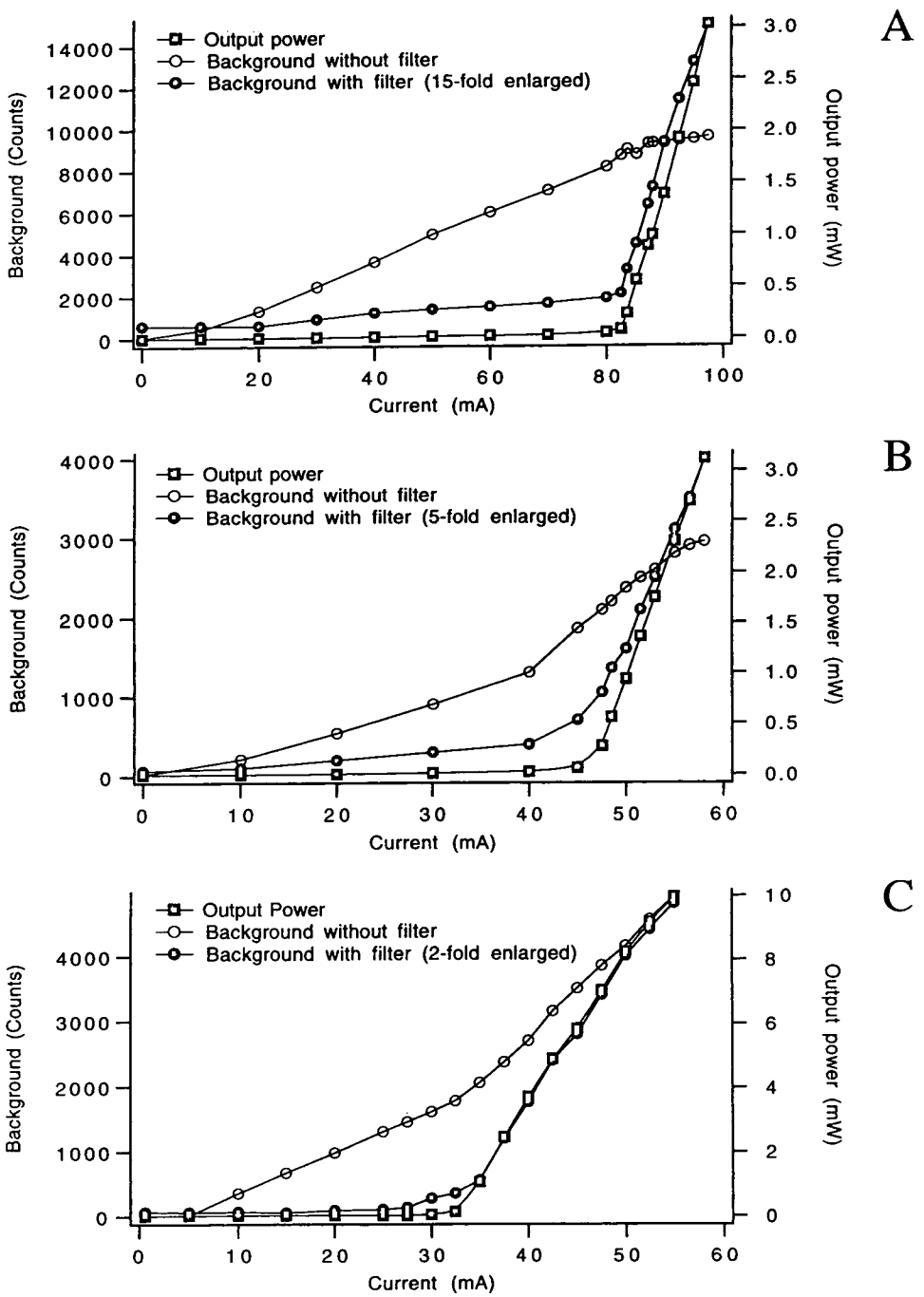

Fig. 5. Background (with and without laser line selector) and output power as a function of the current applied to the laser.

be about 1.5 times lower, provided the background remains the same, indeed very close to the observed ratio of 1.3.

After similar correction, the detection limits for the other CW lasers, including the different diode lasers, can also be explained by the differences in Raman scatter and excitation power if shot noise-limited conditions are assumed.

Since for both the HeNe and the diode lasers ratioing is not necessary, the second fiber in the flow cell can be used to detect the fluorescence signal, which effectively increases the emission collection efficiency 2-fold. Thus, similar detection limits were observed using the 10 mW diode laser and the argon-ion laser.

4. Conclusions

The present study shows that HeNe and diode lasers are appropriate excitation sources for NIR LIF detection in LC. They are by far the cheapest lasers available and due to their stability ratioing is not required; detection limits are better than 1 p*M* for AlPcS2 in standard solutions. Their lack of tunability is not a major disadvantage in LC detection. In view of the broad-band excitation spectra of analytes, in practice efficient excitation will be possible for a wide range of NIR-absorbing compounds by utilizing a number of diode lasers emitting at different wavelengths. More importantly, in everyday practice it will not often be possible to apply direct fluorescence detection in the NIR region; consequently, fluorescent tagging will be necessary in many cases [15] and the absorption wavelength of the label can be tailored to a wavelength available from a NIR emitting laser. A critical note should be made here. Although the detection of labelled compounds obviously can also be performed in the p*M* concentration range, derivatization of analytes at this concentration level is often not possible. Today it is increasingly being recognized that for analyte concentrations below 10^{-9} *M* problems are encountered either because reaction rates are not high enough or because side products and/or excess labelling reagent are present in the derivatization mixture. This implies that for detection after pre-column derivatization LIF detection in LC, the use of conventional lasers such as the argon-ion laser, can be considered an overkill. However, the use of cheap HeNe- and diode laser-based detection systems in combination with NIR-absorbing labels should prove to be a suitable alternative to existing labelling methods applicable at shorter wavelengths.

References

[1] J.M. Bostick, J.V. Strojek, T. Metcalf and T. Kuwana, *Appl. Spectrosc.*, 46 (1992) 1532.
[2] A.J.G. Mank, H. Lingeman and C. Gooijer, *Trends Anal. Chem.*, 11 (1992) 210.
[3] A.J.G. Mank, C. Gooijer, H. Lingeman, N.H. Velthorst and U.A.Th. Brinkman, *Proc. SPIE*, 2084 (1993) 255.
[4] J.W. Hofstraat, C. Gooijer and N.H. Velthorst, in G. Schulman (Editor), *Molecular Luminescence Spectroscopy Part 3*, (*Chemical Analysis Series*, Vol. 77), Wiley, NY, 1993, Ch. 9.
[5] A.J.G. Mank, C. Gooijer, H. Lingeman, U.A.Th. Brinkman and N.H. Velthorst, *Anal. Chim. Acta*, 290 (1994) 103.
[6] M. Ambroz, A. Beebey, A.J. MacRobert, M.S.C. Simpson, R.K. Svensen and D. Philips, *J. Photochem. Photobiol. B: Biol.*, 9 (1991) 87.
[7] R.K. Svensen, S. Fery-Forgues, A.J. MacRobert and D. Philips, in G. Moreno (Editor), *NATO ASI Series Vol. 15, Photosensitisation*, Springer, Berlin, 1988, p. 445.
[8] K. Lang, D.M. Wagnerová, P. Engst and P. Kubát, *J. Chem. Soc. Faraday Trans.*, 88 (1992) 677.
[9] A. Beeby, A.W. Parker, M.S.C. Simpson and D. Phillips, *J. Photochem. Photobiol. B.: Biol.*, 16 (1992) 73.
[10] V.R. Meyer, *J. Chromatogr.*, 334 (1985) 197.
[11] R.J. Fonck, R. Ashley, R. Durst, S.F. Paul and G. Renda, *Rev. Sci. Instrum.*, 63 (1992) 4924.
[12] H.V. Malmstadt, M.L. Franklin and G. Horlick, *Anal. Chem.*, 44 (1972) 63A.
[13] J.D. Ingle, Jr. and S.R. Crouch, *Spectrochemical Analysis*, Prentice Hall, Englewood Cliffs, NJ, 1988, p. 155.
[14] A.P. Larson, H. Ahlberg and S. Folestad, *Appl. Opt.*, 32 (1993) 794.
[15] A.J.G. Mank, E.J. Molenaar, H. Lingeman, C. Gooijer, U.A.Th. Brinkman and N.H. Velthorst, *Anal. Chem.*, 65 (1993) 2197.
[16] A.J.G. Mank, N.H. Velthorst, U.A.Th. Brinkman and C. Gooijer, *J. Chromatogr. A*, 695 (1995) 175.

ELSEVIER

Journal of Chromatography A, 695 (1995) 175–183

JOURNAL OF CHROMATOGRAPHY A

Near-infrared laser-induced fluorescence detection in column liquid chromatography. A comparison of various lasers and detection systems
II☆. Pulsed lasers

A.J.G. Mank*, N.H. Velthorst, U.A. Th. Brinkman, C. Gooijer

Department of General and Analytical Chemistry, Free University, De Boelelaan 1083, 1081 HV Amsterdam, Netherlands

First received 21 June 1994; revised manuscript received 2 December 1994

Abstract

The applicability of two pulsed lasers, a XeCl-excimer/dye laser and a Nd:YAG/dye laser combination, as excitation sources for near-infrared (NIR) laser-induced fluorescence (LIF) detection in column liquid chromatography (LC) is studied. Using gradient LC, the best detection limit for the model compound, disulphonated aluminum phthalocyanine (AlPcS2), is $4 \cdot 10^{-12}$ *M* obtained using the excimer/dye laser combination. This value is about 10-fold lower than obtained with the Nd:YAG laser, but 20-fold higher than for CW diode laser excitation, as reported in Part I of this study [*J. Chromatogr. A*, 695 (1995) 175]. Because of excitation saturation the optimum results were obtained using only a fraction of the available power. A detailed theoretical discussion is presented which underlines the experimental results and provides insight into the factors that determine the detection limits.

1. Introduction

In Part I of this study [1] the performance of continuous wave (CW) laser systems in near-infrared laser-induced fluorescence (NIR LIF) detection applied to conventional-size column liquid chromatography (LC) was studied, using gradient LC of disulphonated aluminum phthalocyanine (AlPcS2) as a model system. The present paper is devoted to pulsed lasers, i.e. the frequency-doubled Nd:YAG laser and the XeCl-excimer laser, both combined with dye lasers. Such lasers have rarely been used for detection in LC. In principle, they might be interesting because they are readily tunable not only in the visible but also (by utilizing frequency doubling techniques) in the UV part of the spectrum. Selectivity enhancement by the introduction of time-resolution has little potential because fluorescence lifetimes of most analytes in liquid solutions are close to or even shorter than the pulse duration; the fluorescence lifetime of AlPcS2 is 5 to 6 ns [2].

Compared with CW lasers, pulsed lasers exhibit some special features in fluorescence detection. Because of their extremely high peak powers, both excitation saturation and photo-

* Corresponding author.

☆ For Part I see Ref. [1].

0021-9673/95/$09.50
SSDI 0021-9673(94)01196-6

chemical decomposition of analytes are expected to play a role. The influence of pulse duration, repetition rate and average power has to be quantified together with the role of pulse-to-pulse fluctuations.

2. Experimental

2.1 Chemicals, chromatography, detection

Chemicals, LC instrumentation, general aspects of detection (cell construction, emission collection and NIR light detection) have been described in Part I [1]. For signal processing boxcar integration was used.

Boxcar integration

Two Stanford Research (Palo Alto, CA, USA) SR250 boxcar integrators were used to monitor the fluorescence and the reference signals. A Stanford Research SR235 analog processor unit transforms the voltage readout to a signal that is handled by a Stanford Research SR245 Computer Interface. Data are sent to a Macintosh SE computer and transformed to ASCII with a home-made program. Both channels can be used at the same time, allowing ratioing of the data in Igor (WaveMetrics, Lake Oswego, OR, USA).

To supply the boxcar channels with a trigger pulse, about 5% of the excitation light is directed towards a BPW 28 picosecond photodiode. For time-resolved detection a DB463 delay box (EG and G Ortec, Oak Ridge, TN, USA) is applied to optimize the delay. A gatewidth of 60 ns is used for fluorescence detection, starting 5 ns before the laser pulse reaches the flow cell because of the short fluorescence lifetime of the model compound.

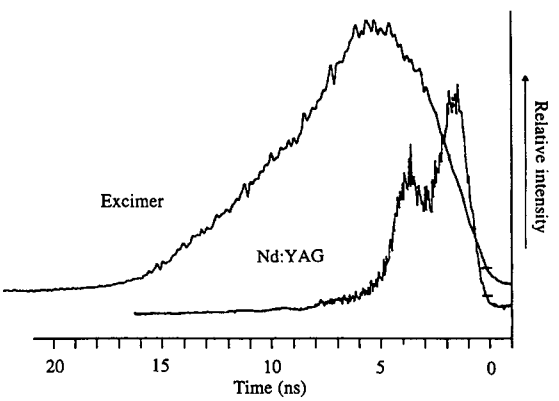

Fig. 1. Pulse shape for the Nd:YAG/dye laser combination and the excimer/dye laser combination, measured with a Siemens (München, Germany) BPW28 fast photodiode and a Tektronix (Beaverton, OR, USA) TDS50 two-channel digitizing oscilloscope.

2.2 Laser systems

The excimer/dye laser and the Nd:YAG/dye laser combination will be denoted without specifying the dye laser. Their pulse shapes are depicted in Fig. 1.

Nd:YAG laser

A YG580 Quantel frequency-doubled Nd:YAG laser is used in combination with an Oxazine 170-dye laser (TDL50), which delivers 16 mW at 670 nm with a repetition frequency of 10 Hz. With an average pulse length of 6 ns (Fig. 1), a peak power of about $2.7 \cdot 10^5$ W is available. Pulse-to-pulse fluctuations are 20% on average. Signals were averaged over 1 s (10 pulses) before further processing.

Excimer laser

A Lambda Physic Model LPX101i XeCl-excimer laser is used in combination with a Model LPD3000 DCM-dye laser, which delivers 250 mW at 670 nm with a repetition rate of 100 Hz. With an average pulse length of 15 ns (Fig. 1), this corresponds with a peak power of $1.7 \cdot 10^5$ W. Pulse-to-pulse fluctuations are 3% on average.

If required, the excitation power was reduced with standard neutral density filters. Signals were averaged over 1 s (100 pulses) before further processing.

3. Results and discussion

Pulsed lasers provide extremely high irradiances because the radiation energy is delivered during very short periods of time. As a result, apart from possible detector damage occurring at irradiances higher than $1 \cdot 10^8$ W cm^{-2}, saturation effects and photodestruction have to be taken into account. Two aspects will be discussed here, i.e. the degree of saturation during the laser pulses and the experimental optimization of NIR LIF detection.

At the excitation wavelength used (670 nm), the molar absorptivity, ϵ, of AlPcS2 is as large as 180 000 l mol^{-1} cm^{-1}. The absorption rate constant, k_a, can be calculated [3] from Eqn. 1:

$$k_a = 3.8 \cdot 10^{-21} \epsilon I, \quad (1)$$

where I is the incident light intensity (photons cm^{-2} s^{-1}). I is related to the average power of the laser (P in J s^{-1}), the laser beam cross section (D in cm^2), the emitted wavelength (λ in m), the Planck constant (h in J s) and the light velocity (c in m s^{-1}) according to:

$$I = (P\lambda)/(Dhc) \quad (2)$$

For simplicity, a uniform distribution of the laser light intensity over a circular cross section of the laser beam is assumed. Confining our attention to the Nd:YAG/dye laser combination operated at 670 nm, during a laser pulse (1.6 mJ, 6 ns) $5.3 \cdot 10^{15}$ photons pass through the flow cell. Using a circular beam with a diameter of 500 μm, this corresponds with an incident light intensity of $4.5 \cdot 0^{26}$ photons cm^{-2} s^{-1} and a k_a of $3 \cdot 10^{11}$ s^{-1}.

It is readily seen that under such efficient excitation conditions ground-state depletion (excitation saturation) will be complete after a time interval which is much shorter than the pulse length, since return to the ground state within this time is negligible. Assuming first-order kinetics, the relative number of molecules left in the ground state, $[A]/[A_0]$, after a certain excitation time, t, can be written as:

$$[A]/[A_0] = e^{-k_a t} \quad (3)$$

This implies that for $k_a = 3 \cdot 10^{11}$ s^{-1}, 99% of the molecules is excited within 0.1 ns. Of course, at lower irradiances the depletion process will be less rapid. Nevertheless, even if only 0.1% of the available laser power is used so that k_a is 1,000-fold lower, the role of saturation is obvious: less than 15% of the molecules will be left in the ground state at the end of the pulse. In other words, not even the use of only 0.1% of the available power will result in a noticeable loss of signal intensity. In fact, at lower irradiances, detectability will be improved, since scatter background is strongly reduced. Using the same approach it can be shown that the same is true for the excimer/dye laser combination that is examined in this study.

Of course, for laser pulses longer than the fluorescence lifetime of the analyte, the number of analyte molecules that is actually in the excited state during the laser pulse is strongly influenced by the simultaneous return of the molecules to the ground state. Therefore, Eqn. 3 can not be used for quantitative calculations. A more thorough treatment is required to obtain a reliable estimate of the number of photons that is emitted by a single molecule passing through the laser beam. This topic is discussed in the Appendix and applied to the excitation conditions at which the maximum signal-to-noise ratio (S/N ratio) is obtained for the two pulsed lasers examined. In section 3.4 the experimental detection limits obtained will be compared with those calculated in the Appendix.

For the Nd:YAG and the excimer laser the experimental optimization of NIR LIF detection was performed as follows.

3.1. Nd:YAG laser

The Nd:YAG/dye laser combination emits 1.6 mJ per pulse of 6 ns, so that the irradiance is $1.2 \cdot 10^8$ W cm^{-2} if the laser beam is collimated to a diameter of 500 μm. Because of the low pulse repetition rate (10 Hz) a substantial fraction of the sample passing through the detector flow cell will not be irradiated at all. Between two consecutive pulses (time interval, 0.1 s) at a

flow rate of 1 ml min^{-1}, 1.7 μl of eluent passes through the cell. Consequently, with an irradiated volume of only 0.2 μl (flow cell diameter, 1.1 mm; beam diameter, 500 μm), less than 12% of all molecules will be excited. The importance of saturation is obvious: multiple excitation of a particular analyte molecule within one laser pulse will hardly occur, since the fluorescence lifetime of AlPcS2 is 5–6 ns (similar to the laser pulse duration); by far the larger fraction of the molecules will only be excited once (cf. Appendix). It should be noted that excitation of molecules residing in the excited state is a real possibility and might result in enhanced photodestruction compared to steady-state conditions under which a normal population distribution is maintained.

Experiments with neutral density filters inserted in the excitation beam were performed to find the actual dependence of signal and background noise on laser power (see Fig. 2A). Excitation saturation is already observed at 1% transmission of the laser light, whereas the background noise (before ratioing) increases more or less linearly over the whole power range studied. Ratioing reduced the noise significantly, especially if higher excitation power is used and shot noise is less important. Fig. 2B shows the S/N ratio over the same power range. Maximum S/N is obtained at only 0.5% of the available laser power, which corresponds with 0.08 mW average power. Ratioing (after data collection) with a 30-fold higher reference signal (Fig. 3A) enhances the S/N ratio about 2.5-fold: the detection limit of AlPcS2, calculated from the LC chromatograms of Fig. 3, improves from $1 \cdot 10^{-10}$ M (Fig. 3B) to $4 \cdot 10^{-11}$ M (Fig. 3C).

The above result is not unexpected since pulse-to-pulse fluctuations of the Nd:YAG laser are significant while its repetition frequency is low. The resulting flicker noise is about 20% of the background signal (see Fig. 3A). This background signal is 2-fold higher than expected if only Raman scatter were present (see ref. 1). Apparently elastically scattered light is not completely removed, a supposition that is supported by the relatively small increase in background

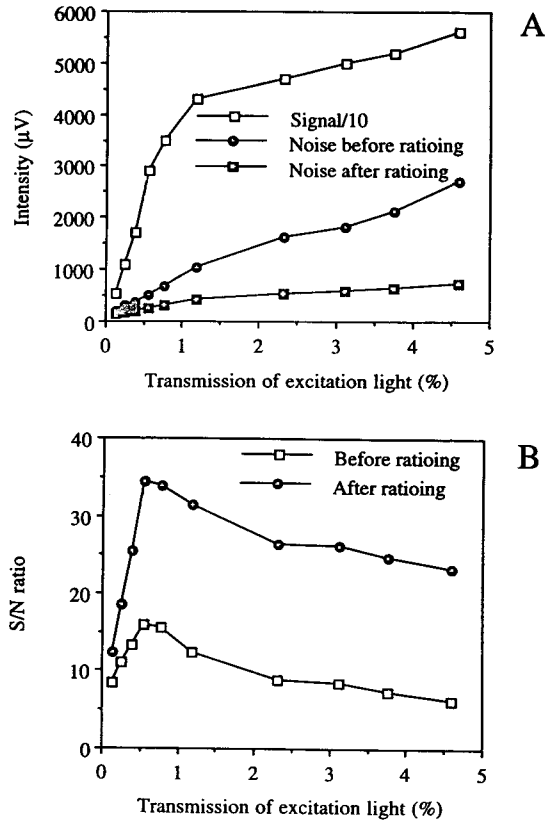

Fig. 2. Signal and background noise (A) and S/N ratio (B) as a function of the excitation power for the Nd:YAG laser.

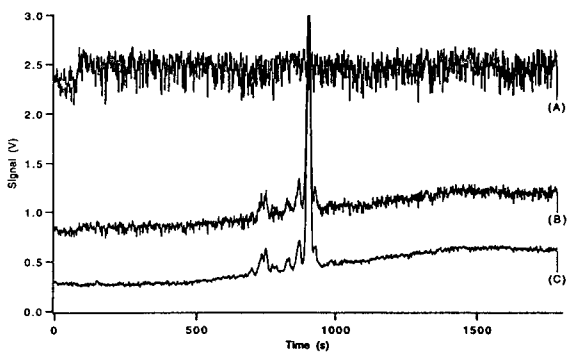

Fig. 3. LC chromatogram of $5 \cdot 10^{-10}$ M AlPcS2, recorded with the detection system using a Nd:YAG laser: (A) reference signal, divided by 10 to fit the scale; (B) fluorescence signal and (C) ratioed fluorescence signal, obtained by taking [(B)/(A)·2.5 V] − 0.5 V.

during LC gradient elution. Ratioing with the 30-fold higher reference signal efficiently removes the flicker noise from the chromatogram.

3.2. Excimer laser

Compared with the Nd:YAG laser, the excimer laser has a higher repetition rate, a longer pulse duration and less pulse-to-pulse fluctuations. At a repetition rate of 100 Hz, only 0.17 μl of sample passes the detector flow cell in the time interval between two consecutive pulses. In other words, all analyte molecules passing through the cell will be irradiated, but only very few will be excited by two consecutive laser pulses. Since the pulse is about 3 times longer (Fig. 1), multiple (2–3 times) excitation of a single analyte molecule is possible. The influence of pulse-to-pulse fluctuations (3%) is reduced to 0.3% if averaging is performed over 1 s or 100 pulses. This low value explains why in Fig. 4A the noise intensity increases with the square root of the laser power, indicating the predominance of shot noise. Thus, ratioing has no beneficial effect (Fig. 4B).

In view of the results obtained with the Nd:YAG laser, the excitation power was reduced to 20 mW with neutral density filters. Maximum S/N ratios are obtained at 5–7.5% of the available 20 mW (i.e. about 1.5 mW average) power (Fig. 4B). The detection limit for AlPcS2 is $4 \cdot 10^{-12}$ M.

Defocusing of the laser beam might result in better detection limits. However, increasing the beam diameter to 750 μm resulted in more scatter from the internal surface of the flow cell (1.1 mm bore). More importantly, the relative amount of flicker noise increased significantly, because spatial fluctuations in the beam resulted in variations in the amount of scatter from the eluent/silica interface inside of the flow cell. As a result, no gain in sensitivity is observed upon increasing the beam diameter.

Photochemical decomposition

The degree of decomposition depends on the chemical structure of the particular analyte, the

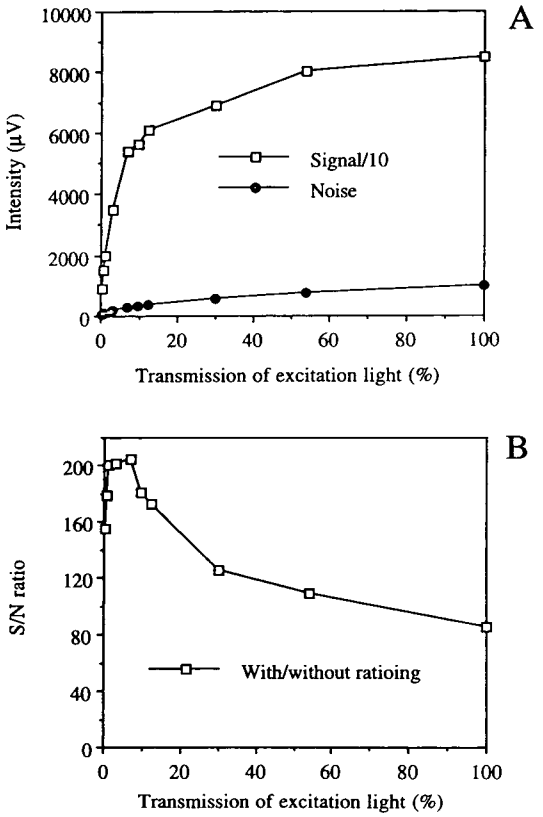

Fig. 4. Signal and background noise (A) and S/N ratio (B) as a function of the excitation power for the XeCl-excimer laser.

LC eluent flow rate and its composition [4]. Using flow injection of 1 ml of a $1 \cdot 10^{-10}$ M solution of AlPcS2 (excited at 1 mW average power), the signal height was independent of the flow rate over the range of 0.01–1 ml min^{-1}. At a flow rate of 0.01 ml min^{-1} any molecule can be excited at least 20 times by consecutive pulses of the excimer laser. This indicates that photodestruction of the present model compound is of minor importance, which is in line with the fact that phthalocyanines generally show high photostability [5]. One might argue that under steady-state conditions 20 excitations is rather limited [6], but here further excitation of excited molecules is a real possibility, which may result in

molecules that are more reactive than ground state molecules.

3.3. Experimental comparison

Obviously, the excimer laser is to be preferred over the Nd:YAG laser. Because of its higher repetition rate (100 Hz), the XeCl-excimer laser can excite all molecules in the present LC system. Furthermore, because of its longer pulse duration, the number of excitations per molecule within one pulse is in favour of the excimer laser. As a result, the optimum average excitation power for the XeCl-excimer laser is 15-fold higher than for the Nd:YAG laser: 1.4 mW and 0.08 mW, respectively.

3.4. Comparison with theory

The experimental differences in detection limits for the two pulsed lasers can be discussed theoretically. In the Appendix, the number of photons emitted per molecule in a flowing sample, n_f, after excitation with these lasers is calculated using an increment method. Under optimum experimental excitation conditions, n_f equals 0.4 for the Nd:YAG laser and 0.6 for the excimer laser, if the triplet state quantum yield (Q_T) of 0.33 is taken into account. Since excitation of a molecule by consecutive pulses can be neglected, the relative number of emitted photons s^{-1} is obtained by simply multiplying n_f with the repetition rate of the laser, giving 4.0 and 61, respectively (Table 1); theoretically 7740 photons s^{-1} are produced upon excitation with a 10 mW 670 nm CW diode laser (cf. Ref. [1]).

Obviously, the differences in background have to be considered as well. A major part of the background signal, n_b, is caused by Raman scatter, which does not show saturation and is proportional to the average laser power. The backgrounds observed for the diode laser and the excimer laser were 40 000 and 5600 photons s^{-1}, respectively. For the Nd:YAG laser, the background of 1400 photons s^{-1} probably contains some elastically scattered light in addition to Raman scatter. The remaining peak-to-peak noise on these backgrounds, completely determined by shot noise, is given in Table 1. Ratioing was performed if necessary to remove flicker noise. Dividing the relative signal (photons s^{-1}) by the peak-to-peak noise yields the relative S/N ratio (Table 1). Experimentally, the detection limits for the three laser systems stand as 1:20:200 (Table 2). For $Q_T = 0.33$, the corresponding calculated proportionality is 1:50:360, while for $Q_T = 0$ the proportionality is 1:30:250. Clearly, the high triplet yield for the model analyte favours the use of CW lasers.

In view of the simplifications introduced during the calculations, the results are satisfying: the theoretical and the experimental values show the

Table 1
Theoretical values for the relative NIR fluorescence signal height and noise amplitude upon excitation of AlPcS2 with different sources of laser light

Parameter	Diode laser	Excimer laser	Nd:YAG laser
Average power (mW)	10	1.4	0.08
Cross section beam (cm^2)	$1.0 \cdot 10^{-3}$	$2.5 \cdot 10^{-3}$	$2.5 \cdot 10^{-3}$
Repetition rate (Hz)	–	100	10
Relative signal (photons s^{-1})	7740 (7740)[a]	107 (61)[a]	6.0 (4.0)[a]
Peak-to-peak noise (photons s^{-1})[b]	800	300	150
Relative S/N ratio	9.7	0.36 (0.20)	0.040 (0.027)

[a] In parentheses: value found with a triplet state quantum yield of 0.33.
[b] Equivalent to $4 \cdot \sqrt{\text{background}}$.

Table 2
Experimental concentration detection limits for AlPcS2 in LC using NIR-LIF detection

Laser	Power (mW)[a]	Repetition rate (Hz)[b]	Ratioing[c]	Detection limit[d] (pM)
Nd:YAG/dye	0.08 ($1.3 \cdot 10^6$)	10 (6)	+	40
Excimer/dye	1.4 ($9.3 \cdot 10^5$)	100 (15)	−	4
Diode	10	CW	−	0.2

[a] In parentheses: peak power in mW.
[b] Between brackets: pulse width in ns.
[c] −: ratioing reveals no or limited improvement; +: significant improvement.
[d] Taken as $S/N = 3$ at maximum output power.

same trend. Hence the theoretical approach provides some insight into the factors that determine the attainable detection limits.

4. Conclusions

Pulsed lasers are less suitable than CW lasers for the trace-level detection of analytes in LC systems, even in the NIR region, where fluorescence background is negligible and Raman scatter is low. The high irradiance provided by pulsed lasers is of limited use. The detection limits for the model compound, AlPcS2, obtained with a CW diode laser, an XeCl-excimer laser and a Nd:YAG laser stand as 1:20:200, in good accordance with theory. Maximum S/N ratios occur at powers far below the available maximum (as low as 0.08 mW or 0.5% of the available power for the Nd:YAG laser). This is not due to flicker noise in the output of the lasers, but to excitation saturation. Time-resolved detection has little practical value, because it is not the background that limits the detection sensitivity.

Appendix

Calculation of the number of photons emitted per analyte molecule in a flowing sample upon excitation with either a pulsed or a CW laser

According to Ref. [3] the number of photons emitted per molecule passing through a flow cell, n_f, is given by:

$$n_f = (Q_f/Q_d)[1 - \exp\{-k_a k_d \tau_{Trans}/(k_a + k_f + k_a k_I/k_T)\}], \quad (4)$$

where Q_f is the fluorescence quantum yield and Q_d the photodestruction quantum yield for the analyte concerned; k_I is the rate constant of intersystem crossing, k_T the rate constant for the decay from the T_1 (triplet excited) to the S_0 (singlet ground) state and k_a the absorption rate constant ($S_0 \rightarrow S_1$), which can be calculated from Eqns. 1 and 2. The rate constant for photodestruction from the first excited singlet state (S_1) is indicated by k_d; τ_{Trans} is the transit time of a molecule through the laser beam, defined as the linear velocity of the eluent divided by the beam diameter. The S_1 population decays to S_0 with a rate constant $k_f = 1/\tau_f$, where τ_f is the fluorescence radiative lifetime.

For the pulsed lasers considered here, the term $k_a k_I/k_T$ can be deleted from Eqn. 4, because a molecule that enters the T_1 state can be considered photodestroyed: the large difference in the duration of the laser pulses and the T_1 state lifetime (< 20 ns and 300 μs, respectively) [2] makes it virtually impossible to return to S_0 before the end of the pulse. Thus, although actual photodestruction is negligible, intersystem

crossing has the same irreversible depleting effect on the S_0 state during a laser pulse.

Because the repetition rate is low (≤ 100 Hz), all molecules will have returned to the ground state before the next pulse. However, excitation of an individual molecule by a second laser pulse does not occur, because of the high flow rate used in the gradient LC separation. As a result Q_d can be replaced by Q_T, the quantum yield of triplet state formation, while k_d can be set equal to k_I or $(Q_T/1-Q_T)k_f$. Hence Eqn. 4 can be rewritten as:

$$n_f = (Q_f/Q_T)[1 - \exp\{-k_a(Q_T/1-Q_T)k_f\tau_{Trans}/(k_a+k_f)\}] \quad (5)$$

Eqn. 5 only applies to a system under steady-state conditions, which are not met since the pulse duration is on the same time scale as the processes concerned. For simple pulse shapes the pertinent kinetic equations may be solved analytically; they are, however, rather complicated [7]. As an alternative, computer programs can be used that allow numerical treatment of the problem. In this approach the laser pulse is divided in small time intervals, Δt, and the occupancies of the different molecular states at a particular time, t, are calculated by taking the values at $(t-\Delta t)$ as the starting set. In our case the situation can be simplified by considering any transfer to the triplet state as photodestruction (indicated by state D instead of T_1). This means that the relative number of molecules in the different states at time t (denoted as $[S_0]_t$, $[S_1]_t$ and $[D]_t$) can be calculated from Eqns. 6–8, given below:

$$[S_1]_t = [S_1]_{t-\Delta t} + k_a[S_0]_t\Delta t - k_f[S_1]_t\Delta t - k_d[S_1]_t\Delta t \quad (6)$$

$$[D]_t = [D]_{t-\Delta t} + k_d[S_1]_t\Delta t \quad (7)$$

$$[S_0]_t + [S_1]_t + [D]_t = 1 \quad (8)$$

Eqn. 6 deals with the occupancy of the first excited singlet state as a result of excitation, return to the ground state and transfer to D, Eqn. 7 gives the amount of analyte that is not available for excitation because of either actual photodestruction or transfer from S_1 to a state other than S_0 (in this case T_1) for a period of time that is much longer than the duration of the laser pulse, while Eqn. 8 is obvious. Combining Eqns. 6–8 results in:

$$[S_1]_t = [S_1]_{t-\Delta t} + k_a\Delta t - k_a[S_1]_t\Delta t - k_a[D]_t\Delta t - k_f[S_1]_t\Delta t - k_d[S_1]_t\Delta t \quad (9)$$

which can be rewritten as:

$$[S_1]_t = ([S_1]_{t-\Delta t} + k_a\Delta t - k_a[D]_{t-\Delta t}\Delta t)/(1 + k_a\Delta t + k_f\Delta t + k_d\Delta t + k_ak_d\Delta t^2) \quad (10)$$

To obtain the value of $[S_1]_t$ for a non-square laser pulse shape, the dependence of k_a on time has to be known. To simplify the calculations, we assumed a Gaussian decrease in light intensity during the laser pulse (Figs. 5 and 6). In these intensity distributions, which correspond reasonably well with the actual laser pulse profile (cf. Fig. 1), k_a is defined at different times during the pulse (using a 0.5 ns increment interval). With this information, a computer program loop can evaluate the value of $[S_1]_t$ at any time after the start of the pulse. Integration over the transit time gives n_f:

$$n_f = \int_0^t Q_f k_f [S_1]_t \Delta t \quad (11)$$

The results are visualized in Figs. 5 and 6. On the time scale of 50 ns, utilized in Figs. 5 and 6,

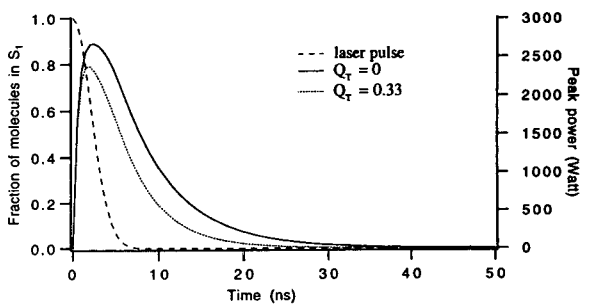

Fig. 5. Computational description of the laser pulse profile for the Nd:YAG laser and the relative number of molecules in the excited state as a result of this pulse, both with (dotted line) and without (solid line) considering transfer to the triplet state ($Q_T = 0.33$ and $Q_T = 0$, respectively). See text for further details.

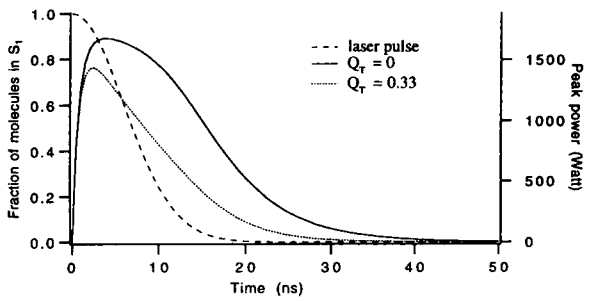

Fig. 6. Computational description of the laser pulse profile for the XeCl-excimer laser and the relative number of molecules in the excited state as a result of this pulse, both with (dotted line) and without (solid line) considering transfer to the triplet state ($Q_T = 0.33$ and $Q_T = 0$, respectively). See text for further details.

the decay of the triplet state is negligible. To show that the influence of a high triplet yield on the number of analyte molecules in S_1 during the laser pulse is rather strong, the curves obtained for $Q_T = 0$ or 0.33 are both given. Their difference will be quantified below.

It should be emphasized that for a CW laser with an average power equal to that of the Nd:YAG or the excimer laser, photodestruction and ground state depletion can be neglected: only a very small and constant fraction of analyte molecules will be in the excited state at any time, for example only 0.01% for the 10 mW 670 nm diode laser. As a result n_f is given by:

$$n_f = Q_f k_f [S_1] \tau_{Trans} \quad (12)$$

where $[S_1]$ represents the steady-state fraction of molecules in the S_1 state:

$$[S_1] = k_a/(k_a + k_f + k_a k_I/k_T)$$
$$= k_a/(k_a + k_f + k_a(Q_T/1 - Q_T)k_f/k_T) \quad (13)$$

The above approach permits a quantitative comparison of the performance of LIF detection set-ups using pulsed and CW lasers as excitation sources. Eqns. 11 (pulsed lasers) and 12 (CW lasers) were used to determine the relative signal (photons s^{-1}) for the 10 mW 670 nm diode laser, the excimer laser and the Nd:YAG laser, utilizing the following parameters: $\epsilon = 180\,000$ l mol^{-1} cm^{-1} at $\lambda = 670$ nm; $Q_f = 0.43$ and $\tau_f = 6$ ns; $Q_T = 0.33$ and $\tau_T = 300$ μs; the beam area is $2.5 \cdot 10^{-3}$ cm^2 for the pulsed lasers and $1.25 \cdot 10^{-3}$ cm^2 for the diode laser. The linear flow rate of the eluent was 1.7 cm s^{-1} (1.0 ml min^{-1}). All lasers were considered under optimal S/N conditions. Using the increment method n_f can be calculated; its value equals 0.6 for the Nd:YAG laser and 1.1 for the excimer laser without photodestruction or transfer to the triplet state ($Q_T = 0$), and 0.4 and 0.6, respectively, for $Q_T = 0.33$. The relative signals in photons s^{-1} (n_f multiplied by the repetition rate of the laser; cf. above) are given in Table 1. Optimum excitation is not achieved at maximum power, since no complete saturation is observed in either Fig. 5 or Fig. 6. At full power for the pulsed lasers, n_f can be calculated to be 3.5 and 8.2, respectively, for $Q_T = 0$, and 1.7 and 2.2 for $Q_T = 0.33$. Clearly, reducing the power more than 100-fold decreases n_f merely 4-fold, if transfer to the triplet state is taken into account. In reality this factor will be even smaller, because of increased photodestruction and ionisation.

The use of a laser that delivers longer pulses will not significantly enhance analyte detectability because of the high triplet state quantum yield. In fact, for an excimer laser delivering 10-fold longer pulses with the same average power, or a similar device delivering a 10-fold higher power within a pulse of normal duration, the signal would be enhanced only 60 and 20%, respectively, for $Q_T = 0.33$. Because the background noise is expected to increase by at least a factor $\sqrt{10}$, detectability will actually deteriorate.

References

[1] A.J.G. Mank, N.H. Velthorst, U.A. Th. Brinkman and C. Gooijer, *J. Chromatogr.* 695 (1995) 165.
[2] A. Beeby, A.W. Parker, M.S.C. Simpson and D. Phillips, *J. Photochem. Photobiol. B. : Biol.*, 16 (1992) 73.
[3] R.A. Mathies, K. Peck and L. Stryer, *Anal. Chem.*, 62 (1990) 1786.
[4] C.M.B. van den Belt, *Ph.D. Thesis*, Leiden University, The Netherlands, 1991.
[5] I. McCubbin, *J. Photochem.*, 34 (1986) 187.
[6] T. Hirschfeld, *Appl. Opt.* 15 (1976) 3135.
[7] I. Carmichael and G.L. Hug, *J. Phys. Chem.*, 89 (1985) 4036.

ELSEVIER

Journal of Chromatography A, 695 (1995) 185–193

JOURNAL OF CHROMATOGRAPHY A

Comparison of 1-(1-naphthyl)ethylcarbamate derivatives of a carbohydrate bonded chiral stationary phase☆

Apryll M. Stalcup*, Karen L. Williams

Department of Chemistry, 2545 The Mall, University of Hawaii-Manoa, Honolulu, HI 96822, USA

First received 13 June 1994; revised manuscript received 23 November 1994; accepted 23 November 1994

Abstract

New chiral stationary bonded phases (CSPs) based on derivatized malto-oligosaccharides are reported. Chiral separations are reported for 3,5-dinitrobenzoyl-derivatized amines and amino acids as well as some 3,5-dinitrophenylcarbamoylated alcohols. These new CSPs incorporate a 1-(1-naphthyl)ethylcarbamate (NEC) moiety which introduces additional stereogenicity and provides a useful probe for investigating chiral recognition. The elution order, when known, was dependent upon the configuration of the NEC substituent; that is, the *S* enantiomers were retained longest on the *S* column and the *R* enantiomers were retained longest on the *R* column. Elution order from the *RS* column, when known, was the same as that observed for the *S* column. In most cases, retention correlated with bonded ligand concentration on the silica substrate. In general, the best enantioselectivities and resolution were obtained on the *S* column.

1. Introduction

Many different types of chiral stationary phases (CSPs) including cyclodextrin [1,2], Pirkle [3,4], protein [5–9], and chiral crown ether phases [10,11] are currently available. Although each of these CSPs is very successful at separating large numbers of enantiomers which, in many cases, are unresolvable using any other CSP, there remains a large number of unresolvable enantiomeric compounds. In addition, incomplete understanding of the chiral recognition mechanisms of many of these CSPs limits the realization of the full potential of existing CSPs and hampers development of new CSPs.

Cellulosic and amylosic phases, in which the hydroxyl functionalities are usually extensively derivatized [12], have also been used successfully for enantioseparations [13,14]. The enantioresolution of these CSPs is reported to be very dependent upon the substituents appended onto the native carbohydrate [15]. These phases are comprised of mixtures of derivatized carbohydrate polymers which are coated onto large pore silica. Even though these phases exhibit admirable enantioselectivities, they have some serious disadvantages. The large polymer size requires the use of fragile, large pore silica. In addition, the secondary structure of the polymer, which seems to be important in chiral recognition, may be altered irreversibly by storing the columns in polar solvents and thus restricts the types of

* Corresponding author.

☆ Presented in part at the *18th International Symposium on Column Liquid Chromatography, Minneapolis, MN, May 8–13, 1994.*

0021-9673/95/$09.50
SSDI 0021-9673(94)01164-8

mobile phases that can be used. The complex polymeric nature of these chiral selectors and the importance of the secondary structure also hamper the development of adequate models for the chiral recognition mechanism on these phases [16].

Carbohydrate-based phases employing small sugar moieties have been investigated for their utility for biological samples containing proteins [17–19]. Although these types of phases have demonstrated some utility for the chromatographic analysis of proteins, little is known about their potential for enantiomeric separations. Given the well documented enantioselectivities of the cellulosic, amylosic and cyclodextrin phases, it is reasonable to expect considerable enantioselectivity from other carbohydrate-derived bonded phases as well. Indeed, Aburatani et al. [20], reported on the enantioselectivity of exhaustively carbamoylated oligosaccharides of varying lengths coated onto a silica substrate. In addition, the use of small sugar moieties as chiral bonded ligands may offer several advantages over cyclodextrin, cellulosic and amylosic moieties including enhanced stability and high bonded ligand density [21]. Further, the carbohydrates may be attached through a variety of linkages and there are a wide variety of carbohydrates commercially available. In addition, the use of small, well-defined carbohydrate moieties may provide some valuable insight into the chiral recognition mechanisms of the derivatized amylosic and cellulosic phases.

The purpose of this work was to investigate the potential of bonded carbohydrate-based high-performance liquid chromatographic (HPLC) stationary phases for chiral separations. A bonded phase derived from a maltooligosaccharide mixture was used as the focus of initial investigations because maltooligosaccharides are comprised of D-glucose, bonded through the same α-1,4 linkages as in cyclodextrin. It was thought that this structural similarity with cyclodextrins might provide some guidance with regard to chiral solute selection as well as chromatographic conditions for chiral separations. It was also anticipated that the native sugar CSPs might not exhibit tremendous enantioselectivity despite the potentially high surface concentration of bonded ligand. In contrast to the native cyclodextrin phases as well as the derivatized cellulosic and amylosic phases, inclusion complexation may not play a major role in the enantioselectivity of these sugar-derived CSPs because of the greater flexibility of the maltooligosaccharides relative to cyclodextrin, cellulosic or amylosic chiral selectors. In addition, in the reversed-phase mode, the more abundant solvent molecules might compete more effectively with the solute for the secondary hydroxyls than is possible on the cyclodextrin phases because there is no well-defined hydrophobic cavity for the solute to occupy on the native sugar phases. Therefore, work focussed on derivatized carbohydrate phases under normal-phase conditions.

Stalcup et al. [22], previously reported naphthylethyl carbamoylated cyclodextrin phases which exhibited enantioselectivity in the normal-phase mode. In the normal-phase mode, these phases seemed to have selectivities comparable to that obtained on a Pirkle-type naphthylvaline column and were very successful at resolving a wide variety of 3,5-dinitrophenylderivatives of alcohols, amines, amino alcohols, amino acids, and carboxylic acids. In many cases, the configuration of the β-cyclodextrin substituent dominated the observed enantioselectivity, but in some cases, the enantioselectivity of the cyclodextrin also made a contribution. In addition, it was found that sometimes this contribution was nonequivalent for the two substituent configurations. Because comparison of the enantioselectivities obtained on the *R*-, *S*- and racemically derivatized cyclodextrin CSPs provided valuable insight into the separation mechanism, the derivatives chosen for this study were 1-(1-naphthyl)ethylcarbamates. Maltooligosaccharide bonded phases were prepared and further derivatized with pure *R*-, pure *S*- or *RS*-naphthylethyl isocyanate. It should be noted that the *R*-, *S*- and *RS*-designations refer only to the configuration of the substituent and not the underlying maltooligosaccharide. To enhance

solute–CSP interactions, solutes were derivatized with either 3,5-dinitrobenzoyl chloride or azide.

2. Experimental

2.1. Chemicals

The various solutes and the 3,5-dinitrobenzoyl chloride derivatizing reagent were obtained from Aldrich (Milwaukee, WI, USA). Absolute ethanol was obtained from Quantum (Tuscola, IL, USA). All other solvents were all obtained from Fischer Scientific (St.Louis, MO, USA). The maltooligosaccharides were obtained from Pfanstiehl Laboratories (Waukegan, IL, USA).

For the amines and amino acid esters, about 10 mg was reacted with an excess amount of 3,5-dinitrobenzoyl chloride in acetone or tetrahydrofuran. The mixture was heated to 60°C for 20 min. The acetone was then evaporated off and the product was dissolved in either methanol or ethanol. The alcohols were derivatized according to the procedure of Pirkle et al. [23].

2.2. Chromatographic bonded phase

The native carbohydrate-bonded sorbent (5 μm, spherical, Kromasil) was prepared according to Stalcup and Williams [24]. Briefly, the bonded phase consists of a mixture of maltooligosaccharides (3 to 10 glucose residues; average of 4), covalently attached to the silica through a spacer. The composition of the oligosaccharide mixture, as provided by the vendor, is detailed in Table 1.

The two-step process involves initial attachment of the spacer with subsequent addition of the carbohydrate moiety. Further derivatization, using a large excess of reagent, was accomplished according to Stalcup et al. [22]. Carbon analysis was performed by Galbraith Laboratories (Knoxville, TN, USA). The bonding results are presented in Table 2. The surface concentration of the bonded carbohydrate was calculated based on an average molecular mass, which was derived from the composition data provided by the vendor. The bonded sorbents were slurry packed into a 250 × 4.6 mm stainless-steel column.

Table 1
Composition of maltooligosaccharide mixture

Oligomer	No. C	MW	%Comp.	(%)·(MW)
Glucose	6	180	0.0	0.00
Maltose	12	342	1.5	5.13
Maltotriose	18	504	27.9	140.62
Maltotetraose	24	666	15.6	103.90
Maltopentaose	30	828	38.3	317.12
Maltohexaose	36	990	14.0	138.60
Maltoheptaose	42	1152	1.2	13.82
Maltooctaose	48	1314	0.5	6.57

2.3. Equipment

The HPLC system used for these experiments consisted of a Shimadzu LC-600 and SPD-6A UV detector interfaced to a Chromatopac CR-501 data station. The flow-rate was typically 1.0 or 2.0 ml/min. Supporting evidence for chiral separation was supplied by repeating the separation at different wavelengths. The mobile phase was chloroform–methanol–*n*-heptane (50:3:47, v/v/v). Chromatographic experiments were conducted at 18°C.

3. Results and discussion

3.1. Bonding results

According to the carbon analysis data presented in Table 2, the carbohydrate bonding procedure yielded a sorbent with a loading of approximately 14% C of which ca. 5% is due to the linkage. Considering that approximately half of the molecular mass of carbohydrates is oxygen, this loading would correspond to loading of about 20% C for a conventional C_{18} bonded phase. According to Stalcup and Williams [25], typical total %C for cyclodextrin bonded phases are ca. 4–5%. Thus, the use of small, flexible

Table 2
List of bonded sorbents

Columns	$\%C^{a}_{spac}$	$\%C^{b}_{sugar}$	$\%C^{c}_{tot}$	[spacer][d]	[sugars][d]	[der][d]
R	4.95	14.30	19.92	2.76	1.12	0.94
S	4.98	14.46	24.21	2.78	1.14	2.10
RS	4.98	14.46	30.52	2.78	1.14	3.80

[a] %C due to spacer.
[b] %C due to spacer plus carbohydrates.
[c] %C due to spacer plus carbohydrates plus naphthylethylcarbamate substituent.
[d] Surface concentration in μmol/m^2; [der] = carbamate.

carbohydrate moieties does allow for higher bonded ligand density than achievable with the more bulky and rigid cyclodextrins.

As mentioned previously, the surface concentration of the bonded carbohydrates was calculated based on an average molecular mass (approximately a tetrasaccharide), derived from the homologue distribution data provided by the vendor. Although the maltooligosaccharide material was a heterogeneous mixture of homologues, it is quite possible that the bonded phase is fairly homogeneous due to exclusion of the larger homologues from the pores as well as greater diffusion of the lower molecular mass homologues into the pores [26]. Current work on CSPs derived from pure homologues may provide some insight regarding this issue and will be the subject of another report.

Derivatization of the bonded sorbent further increased the amount of %C. The *R* phase had the lowest degree of substitution while the *RS* phase had the highest degree of substitution. Assuming that the bonded ligand is a tetrasaccharide, the *R* phase had approximately 1 substituent/ligand, the *S* had about 2 substituents/ligand and the *RS* had about 3 substituents/ligand. Because the same amount of derivatizing reagent was used in each case, the low loading of the *R*-CSP prompted preparation of a second batch. The results were virtually identical. Although more work needs to be done, it is possible that the bonded ligands have *R*- and *S*-selective sites and this may account for the high degree of substitution on the *RS*-CSP. Each glucose residue contributes 3 hydroxyls. Thus, as can be seen from Table 2, the calculated degree of substitution for each phase indicates the presence of residual hydroxyls. In contrast, as mentioned previously, the cellulosic and amylosic phases are exhaustively derivatized [12].

3.2. Chromatographic Results

The chromatographic results obtained for the various compounds used in this study on this new bonded phase are reported in Tables 3–5. A typical chromatogram is shown in Fig. 1. In general (10 out of 14 compounds), the longest retention for the first eluting enantiomer was obtained on the racemic column. However, the highest selectivities were usually obtained on the *S* column (12 out of 14). In addition, the *S* column also usually exhibited the largest resolution (12 out of 14).

Carbamoylation of the sugar bonded phase with the naphthylethyl-isocyanates used in this study incorporates π-base groups on the bonded ligand which provide a site for π-acid/π-basic interactions and presents opportunities for hydrogen bonding and dipole stacking with the carbamate linkage which are not present on the native sugar phase. As indicated by the larger retention of almost all of the analytes on the *RS*-NEC [1-(1-naphthyl)ethylcarbamate] column relative to the other two columns, solute retention may be largely attributed to these $\pi-\pi$ interactions. Comparison of the retention on the *R* column for the first eluting enantiomers of α-methylbenzylamine ($k' = 3.44$) vs. 1-(4-nitro-

Table 3
Chromatographic data for 3,5-dinitrobenzoyl-derivatized amines on the NEC Maltooligosaccharide chiral stationary phases[a]

Compound	CSP	$k'(1)^b$	$k'(2)$	α	R_s
1-Cyclohexylethylamine	*R*	1.84	–	1.00	0.00
	S	2.00	–	1.00	0.00
	RS	1.98	–	1.00	0.00
α-Methylbenzylamine	*R*	3.44^S	6.53	1.90	1.88
	S	3.45^R	7.34	2.13	2.05
	RS	4.16^R	8.98	2.16	1.42
1-(4-Nitrophenyl)-ethylamine	*R*	8.92^S	10.50	1.18	0.52
	S	10.36^R	12.63	1.22	0.50
	RS	13.16	–	1.00	0.00
1,2,3,4-Tetrahydro-1-naphthylethylamine	*R*	1.58	2.64	1.67	1.09
	S	1.73	3.06	1.77	1.40
	RS	2.25	3.92	1.74	0.93
1-(1-Naphthyl)ethylamine	*R*	2.39^S	6.98	2.92	3.14
	S	3.15^R	10.79	3.42	2.75
	RS	3.80^R	12.87	3.39	2.11

[a] Mobile phase: $CHCl_3$–MeOH–C_7H_{16} (50:3:47).
[b] Configuration indicated as a superscript, when known.

Table 4
Chromatographic data for 3,5-dinitrobenzoyl-derivatized amino acid esters on the NEC Maltooligosaccharide chiral stationary phases[a]

Compound	CSP	$k'(1)^b$	$k'(2)$	α	R_s
Alanine ethyl ester	*R*	2.11^L	3.04	1.44	1.01
	S	1.86^D	3.05	1.64	1.26
	RS	2.53^D	4.07	1.61	0.90
Norleucine methyl ester	*R*	1.42	2.03	1.43	0.67
	S	1.35	2.40	1.78	1.40
	RS	1.50	2.55	1.70	0.71
Valine methyl ester	*R*	1.39^L	2.29	1.65	1.14
	S	1.15^D	2.21	1.92	1.67
	RS	1.53^D	2.84	1.86	0.98
Aspartic acid dimethyl ester	*R*	2.82^L	3.59	1.27	0.48
	S	2.43^D	3.25	1.34	0.67
	RS	2.93^D	3.61	1.23	0.27
Phenylalanine methyl ester	*R*	2.35^L	2.64	1.12	0.26
	S	2.14^D	3.03	1.42	0.78
	RS	2.44^D	3.29	1.35	0.26
p-Chlorophenylalanine ethyl ester	*R*	2.13	2.74	1.29	0.39
	S	2.00	3.31	1.66	1.12
	RS	2.04	3.20	1.57	0.57
Tyrosine methyl ester	*R*	22.30	34.05	1.53	0.90
	S	15.04	29.48	1.96	1.30
	RS	22.42	42.91	1.91	0.90

[a] Mobile phase: $CHCl_3$–MeOH–C_7H_{16} (50:3:47).
[b] Configuration indicated as a superscript, when known.

Table 5
Chromatographic data for 3,5-dinitrophenyl-derivatized alcohols on the NEC maltooligosaccharide chiral stationary phases[a]

Compound	CSP	$k'(1)$[b]	$k'(2)$	α	R_s
2-Butanol	*R*	1.90	–	1.00	0.00
	S	1.68	–	1.00	0.00
	RS	1.96	–	1.00	0.00
2-Hexanol	*R*	1.32	–	1.00	0.00
	S	1.22	–	1.00	0.00
	RS	1.36	–	1.00	0.00
2-Octanol	*R*	1.17	–	1.00	0.00
	S	0.95	–	1.00	0.00
	RS	1.00	–	1.00	0.00
sec-Phenethyl alcohol	*R*	2.85^S	3.44	1.21	0.54
	S	2.29^R	3.11	1.36	0.76
	RS	2.53^R	3.24	1.28	0.42
1,2,3,4-Tetrahydro-1-naphthol	*R*	2.16^S	2.74	1.27	0.63
	S	1.89^R	2.21	1.17	0.32
	RS	2.18	–	1.00	0.00
Cyclopropyl benzyl alcohol	*R*	3.10	–	1.00	0.00
	S	2.30	2.88	1.25	0.49
	RS	3.00	–	1.00	0.00

[a] Mobile phase: $CHCl_3$–MeOH–C_7H_{16} (50:3:47).
[b] Configuration indicated as a superscript, when known.

phenyl)amine ($k' = 8.92$) or 1,2,3,4-tetrahydro-1-naphthylamine ($k' = 1.58$) vs. 1-(1-naphthyl)ethylamine ($k' = 2.39$) would also tend to support this interpretation (Table 3).

3.3. Amines

As can be seen from Table 3, for all of the amines studied, the longest retention of the first eluting enantiomer was obtained on the *RS* column and the shortest retention was obtained on the *R* column. As can be seen from Table 2, this correlates with the amount of stationary phase loading. It is also important to note, however, that the correlation between retention and carbamate loading is more apparent for the second eluting enantiomer and that the overall dispersion of capacity factors on the three phases is greater for the later eluting enantiomers than the first eluting enantiomers. This seems reasonable given that the second eluting enantiomer interacts more strongly with the stationary phase than the first eluting enantiomer.

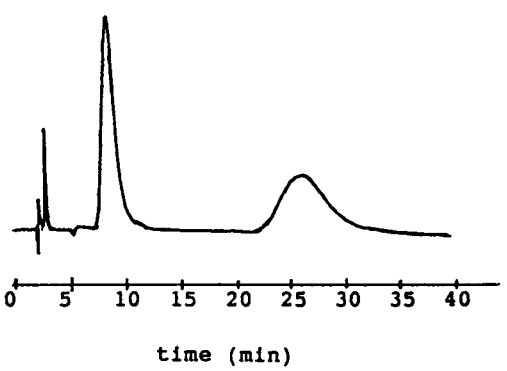

Fig. 1. Enantiomeric resolution of N-(3,5-dinitrobenzoyl)-1-(1-naphthyl)ethylamine on the *S*-NEC CSP. Mobile phase: $CHCl_3$–MeOH–heptane (50:3:47); 1 ml/min.

The importance of π-acid/π-basic interactions to retention may be indicated by the longer retention and stronger dependence of carbamate loading exhibited by 1-(4-nitrophenyl)ethylamine relative to the other amines studied.

When the elution order was known, the enantiomer which had the same configuration as the bonded ligand substituent was retained the longest while the *RS* column produced the same elution order as the *S* column. Superficially, this would seem to indicate that the substituent dominated the chiral interaction and that the

carbohydrate played little or no role in the overall chiral recognition. However, for α-methylbenzylamine, the highest selectivity was obtained on the *RS* column (α = 2.16 vs. 2.13 on *S* column; 1.90 on *R* column). In addition, the selectivities obtained for 1,2,3,4-tetrahydro-1-naphthylamine and 1-(1-naphthyl)ethylamine on the *RS* column (1.74 and 3.39) were only slightly less than those obtained on the *S* column (1.77 and 3.42). These results might suggest that the chiral recognition on the *RS* column may arise from chiral discrimination during the reaction with the isocyanate derivatizing agent. However, the lack of enantioselectivity for 1-(4-nitrophenyl)ethylamine on the *RS* column does not support this because comparable separations (1.18 vs. 1.22), with reversal of elution order, are obtained on the *R* and *S* columns. Thus, analogous to the derivatized cyclodextrin [22] and the derivatized cellulosic and amylosic CSPs [27], the underlying carbohydrate also seems to be contributing to the overall chiral recognition.

3.4. Amino acid esters

In the case of the aliphatic amino acid esters, the longest retention for the first eluting enantiomer was observed on the *RS* column (Table 4) as was seen for the amines. In contrast to the amines, however, the shortest retention was observed on the *S* column and not the *R*. As in the case of the amines, carbamate surface concentration seems to correlate better with retention for the second eluting enantiomer rather than the first. The highest selectivities for the aliphatic amino acid esters were obtained on the *S* column. In addition, the best resolution was obtained on the *S* column. Taken alone, the results obtained on the *RS* CSPs might suggest chiral discrimination in derivatization of the carbohydrate moieties. However, in the context of the results obtained for the amines, an alternative suggests itself. That is, as in the case of other derivatized carbohydrate-based phases [22,27], both the carbohydrate and the substituent contribute to chiral recognition but that the two configurations may contribute nonequivalently. For instance, although the *R* column had the lowest degree of substitution and this lesser substitution may be responsible for the generally smaller selectivities observed for this phase relative to the *S* and *RS* phases, this does not account for the intermediate retention observed on the *R* phase, relative to the *RS* (less than) or *S* (more than) columns. Recently, Kaida and Okamoto [27] reported that there was no evidence of chiral discrimination when racemic isocyanates were used to derivatize cellulose and amylose.

In the case of the aromatic amino acids, phenylalanine and tyrosine both had the longest retention on the *RS* column while *p*-chlorophenylalanine had the longest retention on the *R* column. The retention of the second eluting peak correlated with carbamate surface concentration only for phenylalanine. All three analytes exhibited the best separation and resolution on the *S* column. Although *p*-chlorophenylalanine had slightly reduced retention relative to phenylalanine, this may be due to the fact that the methyl ester of phenylalanine was used while the ethyl ester of*p*-chlorophenylalanine was used in this study. Stalcup et al. [22], reported reduced retention but enhanced enantioselectivity for tryptophan esters as the ester alkyl chain length increased. The same behavior may hold for these phases as well.

It is interesting to note the tremendous difference in retention for tyrosine methyl ester relative to the other two aromatic amino acid esters. Tyrosine has two functionalities available for derivatization. The incorporation of a second π-acidic functionality on the solute through derivatization, leading to enhanced associations with the bonded ligand substituents might account for this enhanced retention. However, NMR analysis of the tyrosine derivatization product confirmed the presence of the free hydroxyl. Hence, the enhanced retention of tyrosine may highlight the role of hydrogen bonding interactions to the overall retention mechanism.

3.5. Alcohols

Trends relating column loading or degree of substitution with retention or selectivity are even less readily apparent in the case of the alcohols

(Table 5) than in the case of the amines (Table 3) or amino acid esters (Table 4). For instance, *sec*-phenethyl alcohol and cyclopropyl benzyl alcohol both had the shortest retention but highest selectivities on the *S* column. In contrast, 1,2,3,4-tetrahydro-1-naphthol had the highest retention on the *RS* column but the highest selectivity on the *R* column. The lack of enantioselectivity for cyclopropyl benzyl alcohol or 1,2,3,4-tetrahydro-1-naphthol on the *RS* column may again dispute chiral discrimination during derivatization of the bonded ligand. The lack of chiral recognition on the *R* column for cyclopropyl benzyl alcohol was somewhat surprising considering that this CSP exhibited the longest retention for this compound. As in the case of the amines, the elution order, when known, was dictated by the configuration of the bonded phase carbamate substituent. It is interesting to note that the same elution orders were obtained for *sec*-phenethyl alcohol as for α-methylbenzylamine on all three columns. The role in elution order of the direction of the dipole moment of an amide adjacent to the chiral center has been the subject of some controversy [28,29]. In the present study, the carbamate linkage and the underlying carbohydrate further complicate the interactions. The overall reduced selectivities obtained for *sec*-phenethyl alcohol vs. α-methylbenzylamine and 1,2,3,4-tetrahydro-1-naphthol vs. 1,2,3,4-tetrahydro-1-naphthylamine may be reflective of the additional atom between the stereogenic center and the π-acidic 3,5-dinitrophenyl moiety. The importance of aromaticity in the solute in addition to the 3,5-dinitrobenzoyl moiety may be inferred from the lack of resolution obtained for the aliphatic alcohols and their generally low retention relative to the aromatic alcohols.

4. Conclusions

As can be seen from the results, maltooligosaccharide-based bonded phases have potential for chiral separations. Although this initial chromatographic study using the naphthylethyl carbamoylated maltooligosaccharide phases focussed on their normal-phase behavior using chloroform–heptane, the chiral recognition behavior of these phases under a variety of mobile phase conditions including the reversed-phase mode [30] is currently being investigated and will be reported elsewhere. In addition, the effect of carbohydrate chain length and the chiral recognition of other derivatized carbohydrate phases is being investigated.

Acknowledgements

The authors gratefully acknowledge the generous support of the National Institutes of Health, the National Science Foundation and the American Chemical Society Petroleum Research Fund.

References

[1] T.J. Ward and D.W. Armstrong, in M. Zief and L.J. Crane (Editors), *Chromatographic Chiral Separations*, Marcel Dekker, New York, NY, 1988, p. 131.
[2] D.W. Armstrong and W. DeMond, *J. Chromatogr. Sci.*, 22 (1984) 411.
[3] W.H. Pirkle, J.M. Finn, B.C. Hamper, J.L. Schreiner and J.R. Pribish, *Am. Chem. Soc. Symp. Ser.*, No. 185, 1982, Ch. 18.
[4] W.H. Pirkle and P.G. Murray, *J. Liq. Chromatogr.*, 13 (1990) 2123.
[5] J. Hermansson and M. Eriksson, *J. Liq. Chromatogr.*, 9 (1986) 621.
[6] G. Schill, I.W. Wainer and S.A. Barkin, *J. Liq. Chromatogr.*, 9 (1986) 641.
[7] S. Allenmark, *J. Liq. Chromatogr.*, 9 (1986) 425.
[8] M. Okamoto and H. Nakazawa, *J. Chromatogr.*, 508 (1990) 217.
[9] T. Miwa, H. Kuoda, S. Sakashita, N. Asakawa and Y. Miyake, *J. Chromatogr.*, 511 (1990) 89.
[10] T. Shinbo, T. Yamaguchi, K. Nishimura and M. Sugiura, *J. Chromatogr.*, 405 (1987) 145.
[11] M. Hilton and D.W. Armstrong, *J. Liq. Chromatogr.*, 14 (1991) 9.
[12] Y. Okamoto, T. Ohashi, Y. Kaida and E. Yashima, *Chirality*, 5 (1993) 616.
[13] H. Hopf, W. Grahn, D.G. Barrett, A. Gerdes, J. Hilmer, J. Hucker, Y. Okamoto and Y. Kaida., *Chem. Ber.*, 123 (1990) 841.
[14] Y. Okamoto, Y. Kaida, R. Aburatani and K. Hatada, *J. Chromatogr.*, 477 (1989) 367.
[15] Y. Okamoto, K. Hatano, R. Aburatani and K. Hatada, *Chem. Lett.* (1989) 715.

[16] T. Shibata, Y. Okamoto and K. Ishii, *J. Liq. Chromatogr.*, 9 (1986) 313.
[17] R.E. Huisden, T. Ooms, J.C. Kraak and H. Poppe, *Chromatographia*, 31 (1991) 263.
[18] R.E. Huisden, J.C. Kraak and H. Poppe, *J. Chromatogr.*, 508 (1990) 289.
[19] A.V. Kiselev, T.D. Khokhlova and Y.S. Nikitin, *Chromatographia*, 18 (1984) 69.
[20] R. Aburatani, Y. Okamoto and K. Hatada, *Bull. Chem. Soc. Jpn.*, 63 (1990) 3606.
[21] A.M. Stalcup, W. Wu and K.L. Williams, *Chirality*, submitted for publication.
[22] A.M. Stalcup, S.-C. Chang, and D.W. Armstrong, *J. Chromatogr.*, 540 (1991) 113.
[23] W.H. Pirkle, G. Mahler and M.H. Hyun, *J. Liq. Chromatogr.*, 9 (1986) 443.
[24] A.M. Stalcup and K.L. Williams, *Patent pending.*
[25] A.M. Stalcup and K.L. Williams, *J. Liq. Chromatogr.*, 15 (1992) 29.
[26] L.C. Sander and S.A. Wise, *J. Chromatogr.*, 316 (1984) 163.
[27] Y. Kaida and Y. Okamoto, *J. Chromatogr.*, 641(1993) 267.
[28] W.H. Pirkle and J.E. McCune, *J. Chromatogr.*, 469 (1989) 67.
[29] I.W. Wainer and M.C. Alembik, *J. Chromatogr.*, 367 (1986) 59.
[30] D.W. Armstrong, C.-D. Chang and S.H. Lee, *J. Chromatogr.*, 539 (1991) 83.

ELSEVIER

Journal of Chromatography A, 695 (1995) 195–204

JOURNAL OF CHROMATOGRAPHY A

Rapid ion-exchange displacement chromatography of proteins on perfusive chromatographic supports

Joseph A. Gerstner*, Joseph Morris, Tony Hunt, Richard Hamilton, Noubar B. Afeyan

PerSeptive Biosystems Inc., University Park at MIT, 38 Sidney Street, Cambridge, MA 02139, USA

First received 19 May 1994; revised manuscript received 12 December 1994; accepted 12 December 1994

Abstract

Displacement chromatography is an extremely powerful separation technique. However, it has not been widely accepted as a preparative technique due to the creeping flow-rates at which displacement separations have been demonstrated. In this work, the enhanced mass transport of perfusive chromatographic particles enabled displacement separations to be dramatically scaled-up with respect to flow-rate. At a flow-rate of 4 ml/min (1440 cm/h) on an analytical-scale column, crude β-lactoglobulin was displaced in only 90 s to yield ca. 18 mg each of pure β-lactoglobulin A and B. This represents an order of magnitude decrease in the time required for displacement separations. Thus, the operation of perfusive columns in the displacement mode offers an ultra-high throughput separation technique with outstanding resolving power even under heavily overloaded conditions.

1. Introduction

The last decade in liquid chromatography has seen the emergence of two potentially powerful advances in preparative chromatography: perfusive chromatographic supports and displacement chromatography. Perfusion chromatographic supports (POROS, PerSeptive Biosystems, Cambridge, MA, USA) attempt to minimize mass transfer resistances associated with conventional diffusive chromatographic supports by incorporating large diameter (6 000–8 000 Å) "through" pores into the sorbent particles [1,2]. These through pores provide for convective fluid flow into the particle that greatly enhances mass transfer to the sorbent phase enabling perfusion supports to operate at high flow-rates while retaining high efficiency [3]. Lloyd and Wagner [4] separated a six-protein mixture in approximately 1 min on a perfusion column at a flow-rate of 4.0 ml/min while the identical separation required 20 min at 1 ml/min on a conventional column. Using 20-μm reversed-phase particles, Fulton et al. [5] performed an analytical separation of a five-protein feed mixture in under 15 s. Fulton et al. [6] have also successfully employed perfusive supports for preparative separations by purifying 95 mg of a vasoactive intestinal polypeptide in a single 12-min run. The immobilization of antibodies onto perfusive chromatographic supports has enabled immunoassays to be performed in seconds which greatly facilities real-time monitoring of bioprocesses [7,8]. Gordon and Adams [9] have reported the

* Corresponding author.

0021-9673/95/$09.50
SSDI 0021-9673(94)01225-3

distinct advantages that preparative-scale perfusive particles possess over diffusive supports with regard to process development, scale-up and validation.

Displacement chromatography is an extremely powerful bioseparation tool due to the high throughput and product purity associated with the process [10–12]. This technique offers several advantages in preparative chromatography as compared to traditional preparative elution and gradient modes. The displacement process takes advantage of the non-linear adsorptive properties of biomolecules such that a larger feed can be separated on a given column with the purified components recovered at significantly higher concentrations. Furthermore, the tailing observed in preparative isocratic elution is greatly reduced in displacement chromatography due to the self-sharpening boundaries developed during the process. In contrast to preparative elution where the feed components are often diluted during the separation, the feed components can be significantly concentrated during the displacement procedure.

Preparative gradient separations also typically exhibit reduced peak tailing and significant concentration of feed components. However, if the feed components are readily separated employing step or linear gradients, then displacement may not offer significant advantages over these traditional techniques. Displacement chromatography should be considered primarily for separations possessing low separation factors. For these difficult separation problems, the desired level of purity is obtainable, if at all, only through shallow gradients (or isocratic conditions) where peak tailing typically becomes a concern. The ability of gradient separations to concentrate the product is not without its pitfalls. Since many proteins exhibit concentration-dependent aggregation affects, the high product concentrations reached in gradient separations can lead to aggregation and loss of bioactive product. Product concentration can be reduced in gradient separations by altering the "steepness" of the gradient, however, this changes the elution conditions and may lower product purity and recovery. Through appropriate manipulation of the displacer concentration in displacement separations, product concentration is readily controlled without affecting the overall separation. These advantages combine to make displacement chromatography an extremely attractive preparative technique for the isolation of biomolecules from the dilute solutions often encountered in biotechnology processes.

Displacement chromatography has been employed for the purification of a variety of protein mixtures using both anion- and cation-exchange supports. Peterson and co-workers [13–20] have extensively investigated the utility of carboxymethyldextrans (CM-D) to act as protein displacers in anion-exchange systems. Ghose and Mattiasson [21] have used carboxymethylstarch to displace lactate dehydrogenase from beef heart homogenate. Chondroitin sulfate, a constituent of connective tissue, has been used by Horvath and co-workers [22–24] for the displacement of protein mixtures. Cramer and co-workers [25,26] have explored the potential of cation-exchange displacement chromatography using Nalcolyte 7105, a water soluble coagulant, as a displacer. Gerstner and Cramer [27,28] have utilized protamine and heparin as displacers in cation- and anion-exchange systems, respectively. Jayaraman et al. [29] examined the effect of displacer molecular mass on separation efficiency by using dextran-based polyelectrolytes of various molecular masses as displacers in both cation- and anion-exchange systems. Jen and Pinto [30,31] have employed relatively low molecular mass displacers in anion-exchange systems.

These separations demonstrated the resolving power of displacement, but they were typically performed at volumetric flow-rates of less than 0.2 ml/min (ca. 60–75 cm/h) which in some instances lead to displacement run times exceeding 1 h. While linear flow-rates of 50–100 cm/h are typically employed for large diameter (>50 μm) preparative particles, these displacements were performed using analytical-scale particles (ca. 10 μm) where much higher linear velocities (300–700 cm/h) are the operating norm. At these higher linear velocities, displacement run times as short as 10 min should have been possible. Operating analytical columns in the

displacement mode at linear velocities well below those typically utilized for traditional techniques (i.e. gradient elution) has clouded the issue as to whether displacement is a more productive technique (in terms of mass of product/unit time) as compared to traditional modes. Subramanian and Cramer [32] explored the efficacy of displacement chromatography at a higher flow-rate (1 ml/min–360 cm/h) in 1989, however, displacements continue to be reported at reduced flow-rates.

In this work, we will couple the advantages of displacement chromatography with the high flow-rate efficiency of perfusive chromatographic supports to transform displacement chromatography into an extremely high throughput separation technique. The work also serves to demonstrate the dramatic effect that POROS perfusive supports can have on significantly reducing total chromatographic processing time for all modes of chromatography.

2. Experimental

2.1. Materials and apparatus

Analysis and perfusive displacement experiments and were performed using POROS 10 HQ (100 mm × 4.6 mm I.D., 10-μm particles) and POROS HQ/M (100 mm × 4.6 mm I.D., 20-μm particles) columns (PerSeptive Biosystems, Cambridge, MA, USA). A SynChropak Q300 column (100 mm × 4.6 mm I.D.) packed with 6.5-μm (300 Å pores) particles was employed for diffusive displacement experiments (SynChrom, Lafayette, IN, USA). Sodium chloride, sodium hydroxide, Tris–HCl, β-lactoglobulin A, β-lactoglobulin B, β-lactoglobulin (crude mixture of A and B) and heparin ammonium were purchased from Sigma (St. Louis, MO, USA). Polydiallyl dimethyl ammonium chloride (poly-DADMAC) and *o*-toluidine blue indicator were obtained from Nalco Chemical Company (Naperville, IL, USA). The HPLC system used in this study was a BioCAD 20 (PerSeptive Biosystems) which included an Advantec Model SF-2120 fraction collector (Advantec Toyo Kaisha, Japan).

2.2. Procedures

Displacement chromatography —perfusive

A POROS 10 HQ or a POROS HQ/M column was sequentially perfused with carrier, feed, displacer and regenerant solutions. The feed and displacer solutions were prepared in the carrier which was 100 m*M* Tris–HCl, pH 7.0. The feed consisted of 60 mg β-lactoglobulin (crude mixture of A and B) in 1.7 ml of carrier and the displacer was 7 ml of 12 mg heparin/ml. The fraction size was set at 200 μl. The regenerant was 1.0 *M* sodium chloride in 0.1 *M* sodium hydroxide. Flow-rates employed for the displacement experiments were varied from 1 to 4 ml/min (360–1440 cm/h). The feed was loaded at the same flow-rate employed for the displacement portion of the experiment.

Displacement chromatography —diffusive

A SynChropak Q300 column was employed for diffusive displacements. The feed and displacer solutions were prepared in the carrier which was 75 m*M* NaCl in 25 m*M* Tris–HCl, pH 6.5. The feed consisted of 50 mg β-lactoglobulin (crude mixture of A and B) in 2.0 ml of carrier and the displacer was 7 ml of 14.1 mg heparin/ml. The fraction size was set at 200 μl. The regenerant was 3.0 *M* sodium chloride. Flow-rates employed for the displacement experiments were varied from 0.2 to 1 ml/min (72–360 cm/h). The feed was loaded at the same flow-rate employed for the displacement portion of the experiment.

HPLC analysis

Fractions collected during displacement experiments were diluted 10 × with water and were analyzed by HPLC using linear gradient elution. Analysis for the β-lactoglobulins was performed using a POROS 10 HQ column with a linear gradient from 50 to 500 m*M* NaCl (constant buffer concentration of 10 m*M* Tris–HCl, pH 5.5) in 16.6 ml (10 column volumes) at a flow-rate of 2.0 ml/min (720 cm/h).

Titration assay for heparin analysis

Heparin concentration was measured using a colloidal titration assay provided by Nalco Chemical Company. For analysis of heparin, two drops of *o*-toluidine indicator were added to 100 ml of distilled water, the subsequent addition of heparin produced a colorimetric change. Titrating against polyDADMAC produced another colorimetric change. A linear calibration plot which was generated using known amounts of heparin, was used to quantify the unknown concentrations of heparin in the displacement fractions.

3. Results and discussion

The milk proteins β-lactoglobulin A and B form a good model system to demonstrate the resolving power of displacement chromatography since they differ in structure by only two amino acids [33]. Figs. 1–3 show the displacement separation of β-lactoglobulin A and B on a 10 HQ column (10-μm particles) at flow-rates from 1 to 4 ml/min (360–1440 cm/h). These separations demonstrate both the high flow-rate efficiency of POROS supports and the resolving power of displacement chromatography. The profiles at 1 (360 cm/h) and 2 ml/min (720 cm/h) (Figs. 1 and 2) are essentially identical as there are only two fractions of overlap between the zones of pure β-lactoglobulin B and β-lactoglobulin A. These displacement profiles also compare very favorably to those previously reported [15,22,23,28,29,31] which is remarkable since the current displacements were performed at flow-rates 10 to 20 times faster. As the flow-rate was increased to 4 ml/min (1440 cm/h) (Fig. 3), an additional fraction of overlap developed, but the overall profile still indicates an efficient displacement. As the flow-rate was increased from 1 to 4 ml/min, the protein displacement zones change from classic squares waves to roughly gaussian peaks. These changes in profile indicate that non-ideal effects (mass transfer and adsorption/desorption kinetics) are also increasing in magnitude. However, the result to focus attention on is the amount of overlap between the zones of pure β-lactoglobulin B and pure β-lactoglobulin A which does not substantially increase at the elevated flow-rates.

The histograms presented above do not always convey the true nature of the compositional changes that occur in the column effluent during a displacement. Fig. 4 presents the analytical chromatograms of the 200-μl fractions collected during the displacement from which the histogram presented in Fig. 2 was constructed. From

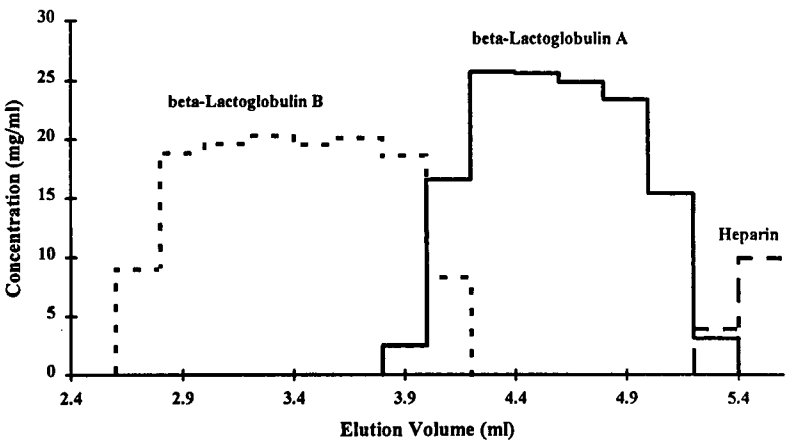

Fig. 1. Displacement chromatography of β-lactoglobulins at 1 ml/min. Column, 100 mm × 4.6 mm I.D. POROS 10 HQ (10-μm particles); carrier, 100 m*M* Tris–HCl, pH 7.0, displacer, 12 mg/ml ammonium heparin in carrier; feed, 60 mg β-lactoglobulin crude mixture in 1.7 ml carrier; fraction volume, 200 μl.

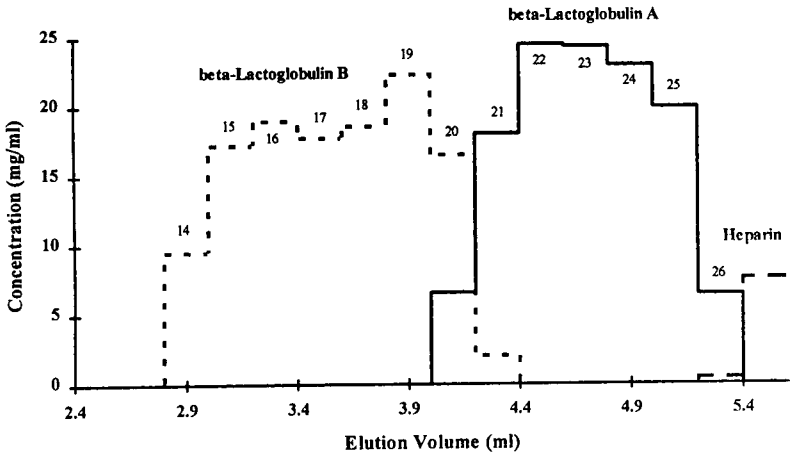

Fig. 2. Displacement chromatography of β-lactoglobulins at 2 ml/min. Chromatographic conditions as stated in Fig. 1 with the exception of flow-rate. Fraction numbers indicated on histogram.

fraction 13 to 14, the column effluent changed from no detectable protein to ca. 9 mg/ml β-lactoglobulin B. The next 5 fractions (15–19) contain the plateau region of the β-lactoglobulin B zone. Fractions 20 and 21 are the change-over region from pure β-lactoglobulin B to pure β-lactoglobulin A and the remaining fractions contain pure β-lactoglobulin A. The end of the displacement train is abrupt as the column outlet goes from ca. 5 mg/ml β-lactoglobulin A to no detectable protein in only one fraction (26 to 27). Closer examination of the cross-over fractions provides more evidence concerning the efficiency of the perfusion particles employed for this separation. From fractions 19–22, it can be seen that the effluent of the column during the displacement separation goes from pure β-lactoglobulin B (ca. 20 mg/ml) to pure β-lactoglobulin A (ca. 24 mg/ml) with only 400 μl of a mixed zone in-between. Clearly even at these elevated flow-rates, the experimental displacement profiles approach the square wave zones that are predicted by theory under ideal conditions.

While displacement of these proteins is impre-

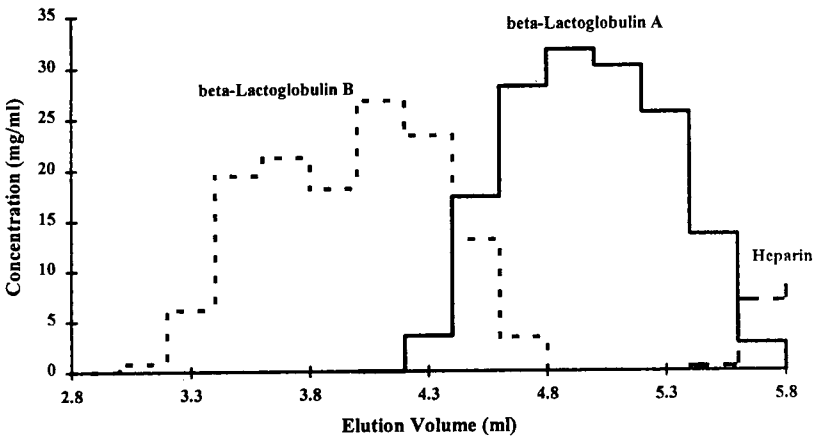

Fig. 3. Displacement chromatography of β-lactoglobulins at 4 ml/min. Chromatographic conditions as stated in Fig. 1 with the exception of flow-rate.

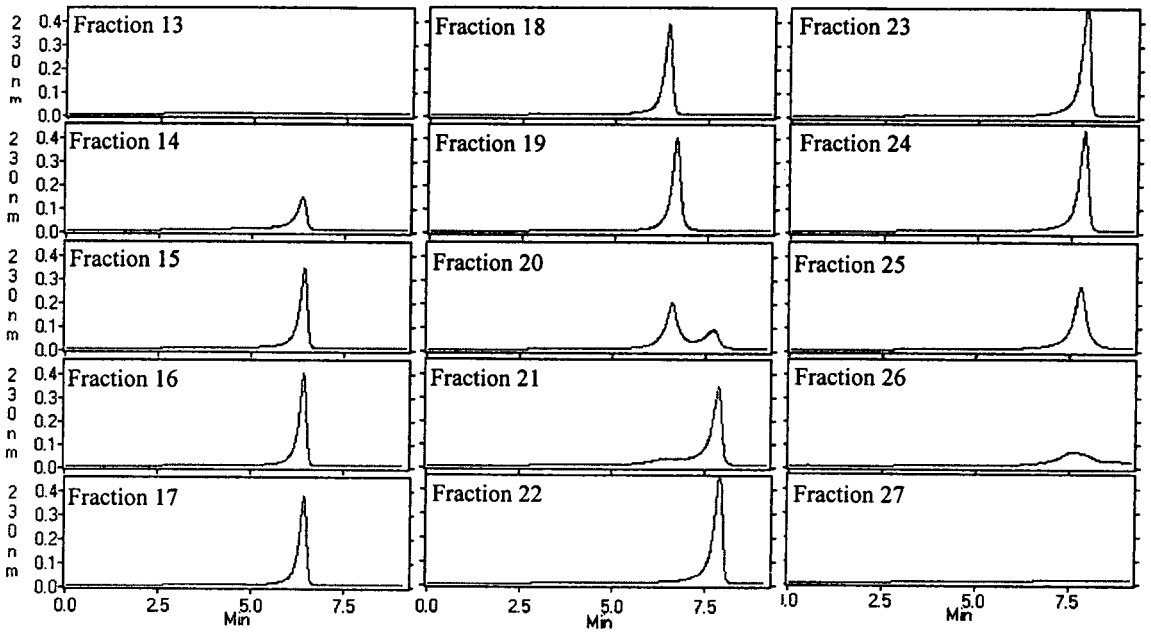

Fig. 4. Analytical chromatograms of fractions collected during the displacement separation performed at 2 ml/min on POROS 10 HQ column. *y*-Axes represent absorbance units.

ssive on the 10-μm system employed for these experiments, in order for displacement to be accepted as a preparative technique it must be performed on larger preparative-scale particles. Therefore, the displacement was scaled-up to a 20-μm particle system at a flow-rate of 2 ml/min (720 cm/h) with a minor loss in separation efficiency (Fig. 5). This elevated flow-rate should be compared to the 100 cm/h typically used on conventional soft gel chromatographic media.

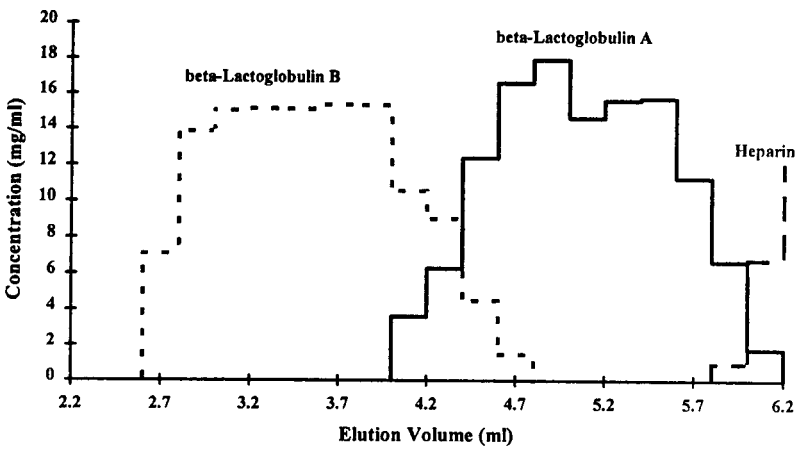

Fig. 5. Displacement chromatography of β-lactoglobulins at 2 ml/min using preparative POROS 20-μm particles. Chromatographic conditions as stated in Fig. 2 with the exception of the column: 100 mm × 4.6 mm I.D. HQ/M (20-μm particles).

Thus, the perfusive, high-efficiency nature of POROS particles enables high flow-rate displacements even on preparative-scale particles.

The high flow-rate efficiency of the POROS particles can be confirmed by comparing these perfusive displacements to displacements performed on a traditional diffusive particle. For this comparison, a particle of 6.5 μm diameter with 300-Å pores was chosen. The small pore diameter should assure that mass transport into the particle will primarily occur by diffusion. Displacements were performed at 0.2 ml/min (72 cm/h) and 1.0 ml/min (360 cm/h) to test the efficiency of a diffusive system at elevated linear flow-rates (Fig. 6). The initial displacement at a flow-rate of 0.2 ml/min is not as efficient as would be expected (Fig. 6A). There is a considerable amount of overlap between β-lactoglobulin A and the displacer. However, the small overlap (only 200 μl) between the protein zones is indicative of an efficient system. A plausible explanation is that the displacer experienced a higher degree of hindered diffusion as compared to the proteins. When the flow-rate was in-

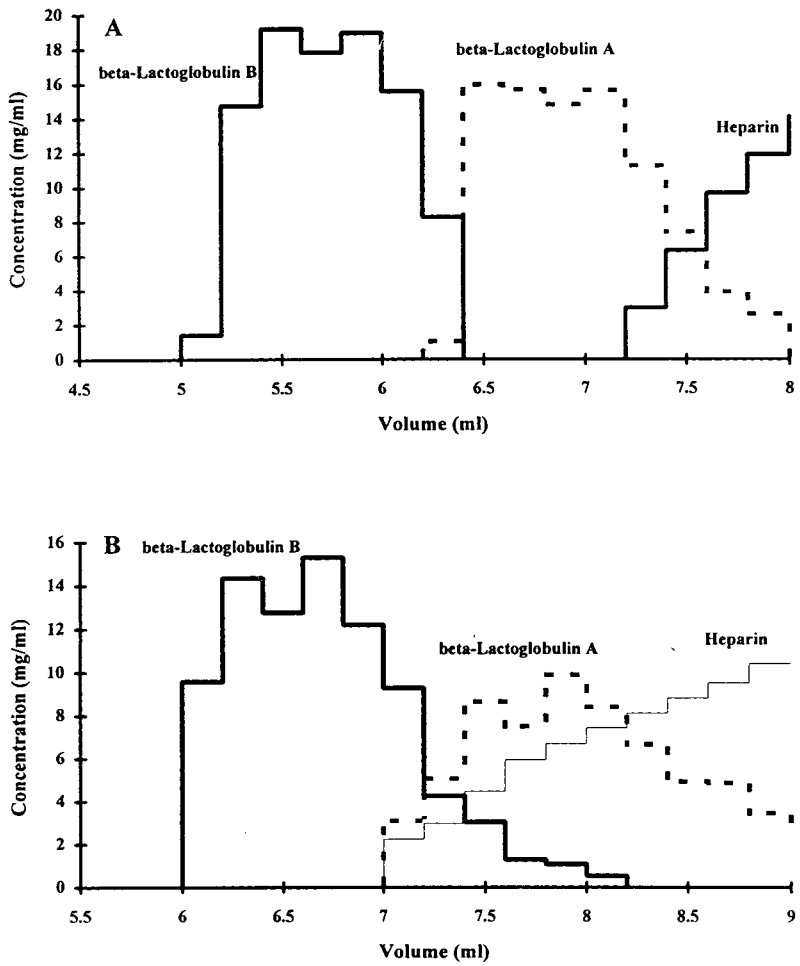

Fig. 6. Displacement chromatography of β-lactoglobulins on diffusive particles. Column, 100 mm × 4.6 mm I.D. Synchropak Q300 (6.5-μm particles); carrier, 75 m*M* NaCl in 25 m*M* Tris–HCl, pH 6.5, displacer, 14.1 mg/ml ammonium heparin in carrier; feed, 50 mg β-lactoglobulin crude mixture in 2.0 ml carrier; fraction volume, 200 μl; flow-rate, A (0.2 ml/min), B (1.0 ml/min).

creased to 1.0 ml/min, the displacement was a complete failure. The β-lactoglobulin A zone was completely engulfed by the displacer front which was now relatively diffuse. The zone of β-lactoglobulin A was also contaminated with a tail of β-lactoglobulin B. These results differ with those reported by Subramanian and Cramer [32] who showed efficient protein displacements at 1.0 ml/min (360 cm/h) on 5-μm, 300-Å pore particles.

The purity of β-lactoglobulin A and B recovered from displacement experiments is chromatographically compared to pure β-lactoglobulin A and B purchased from Sigma (Figs. 7 and 8). From these chromatograms, the β-lactoglobulins recovered from the displacement experiments appear as pure as the proteins obtained from Sigma. Figs. 7 and 8 show chromatograms from the middle of the respective displacement zone (either β-lactoglobulin A or B). These mid-

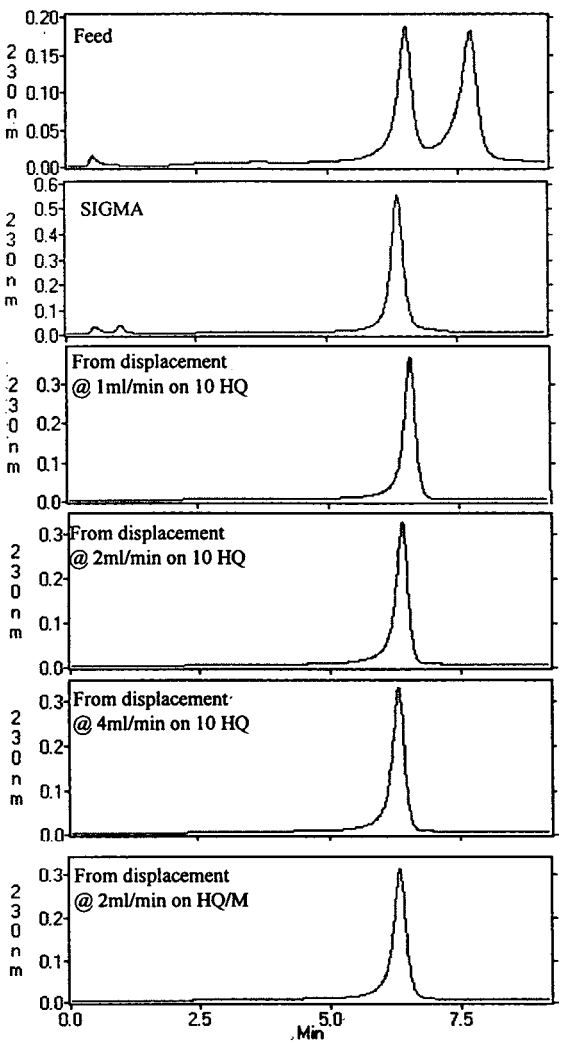

Fig. 7. Analytical chromatograms of representative fractions of β-lactoglobulin B recovered from displacement experiments compared to β-lactoglobulin B obtained from Sigma. y-Axes represent absorbance units.

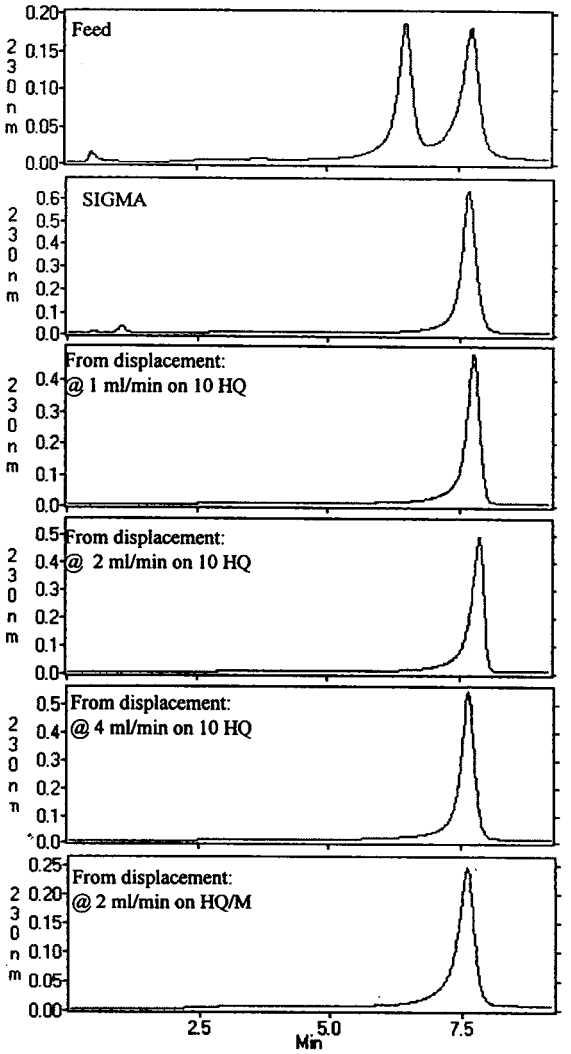

Fig. 8. Analytical chromatograms of representative fractions of β-lactoglobulin A recovered from displacement experiments compared to β-lactoglobulin A obtained from Sigma. y-Axes represent absorbance units.

zone fractions are representative of the pure β-lactoglobulin contained in that zone. (This observation is evident from Fig. 4 which shows analytical chromatograms of all fractions collected during a displacement.)

The productivity (defined as mg purified product/ml of column volume/h) of displacement chromatography performed on perfusive chromatographic supports is compared to that obtained using a traditional diffusive support (Table 1). The cycle time for a displacement run, which is composed of equilibration, feed, displacement and regeneration time, is an order of magnitude faster on the perfusive supports. The cycle time for the 4 ml/min displacement would be only 12 min as compared to approximately 2 h for a similar displacement performed on a diffusive support. The actual displacement portion of the 4 ml/min run was only 90 s in which time 18 mg of each β-lactoglobulin was recovered, pure. This order of magnitude increase in the productivity of this displacement chromatographic separation means that ca. 85 mg of pure β-lactoglobulin B *and* 85 mg of pure β-lactoglobulin A could be recovered every hour using only an analytical-scale column (100 mm × 4.6 mm I.D.). This is compared to only 5 mg each of β-lactoglobulin A and B that would be recovered using a diffusive matrix [28].

The purification of these closely related proteins is not a trivial task using traditional chromatographic techniques. Considerable effort was required to obtain the analytical gradient separation presented in the manuscript. The preparative separation of these proteins must be extremely difficult with the pure β-lactoglobulins recovered at low yields. The difficulty of this preparative separation is anecdotally confirmed by the pricing structure of β-lactoglobulins found in the Sigma catalog. The crude β-lactoglobulin mixture is valued at $25 (US) per gram whereas pure β-lactoglobulin B and β-lactoglobulin A are $496 (US) and $456 (US) per gram, respectively. Clearly, displacement chromatography offers several advantages for the preparative purification of these proteins as well as for more complex mixtures.

4. Conclusions

In this work we have demonstrated the ability of perfusion chromatographic supports to greatly enhance the throughput of displacement chromatography by enabling efficient displacements at elevated flow-rates. In only 90 s at 4 ml/min, we were able to purify by displacement chromatography 18 mg each of β-lactoglobulin A and B. We were also able to scale the displacement separation up to preparative scale (20-μm) particles and still obtain efficient displacements at 2 ml/min. In future work, we will explore displacement separations using even larger perfusive particles (50 μm) and will examine the resolving power of displacement using more complex mixtures.

Table 1

Displacement flow-rate (ml/min)	Recovery of β-lactoglobulin B (mg)[b]	Recovery of β-lactoglobulin A (mg)[b]	Cycle time[a] (min)	Productivity of β-lactoglobulin B ($mg/ml^{-1}h^{-1}$)	Productivity of β-lactoglobulin A ($mg/ml^{-1}h^{-1}$)
0.1[c]	13.2	11.6	133.9	3.0	2.7
1.0	21.5	23.0	17.7	44.0	47.1
2.0	20.9	18.4	13.8	54.6	48.1
4.0	18.5	17.4	11.9	56.2	53.1

[a] Cycle time = (feed volume + displacer breakthrough volume)/(displacement flow-rate) + (10 column volumes equilibration + 20 column volumes regeneration)/operating flow-rate. POROS 10 HQ operating flow-rate = 5 ml/min, for Ref. [28] operating flow-rate = 1 ml/min.

[b] Recovery of chromatographically pure protein.

[c] Data from Ref. [28], total β-lactoglobulin load = 40 mg.

References

[1] N.B. Afeyan, S.P. Fulton, N.F. Gordon, I. Mazsaroff, L. Varady and F.E. Regnier, *Biotechnology*, 8 (1990) 203.

[2] F.E. Regnier, *Nature*, 350 (1991) 634.

[3] N.B. Afeyan, N.F. Gordon, I. Mazsaroff, L. Varady, S.P. Fulton, Y.B. Yang and F.E. Regnier, *J. Chromatogr.*, 519 (1990) 1.

[4] L.L. Lloyd and F.P. Wagner, *J. Chromatogr.*, 512 (1990) 365.

[5] S.P. Fulton, N.B. Afeyan, N.F. Gordon and F.E. Regnier, *J. Chromatogr.*, 547 (1991) 452.

[6] S. Fulton, M. Meys, J. Protentis, N.B. Afeyan, J. Carlton and J. Haycock, *Biotechniques*, 12(5) (1992) 742.

[7] N.B. Afeyan, N.F. Gordon and F.E. Regnier, *Nature*, 358 (1992) 603.

[8] S.P. Fulton, M Meys, L Varady, R Jansen and N.B. Afeyan, *Biotechniques* 11(2) 1991 226.

[9] N. Gordon and M. Adams, *Gen. Eng. News*, August 1993.

[10] S.M. Cramer and G. Subramanian, *Sep. Purif. Methods*, 19(1) (1990) 31.

[11] J. Frenz and Cs. Horvath, in Cs. Horvath (Editor), *High Performance Liquid Chromatography, Advances and Perspectives*, Vol 5, Academic Press, New York, 1988, p. 211–314.

[12] Cs. Horvath, in F. Brunner (Editor), *The Science of Chromatography*, Elsevier, Amsterdam, 1985, p. 185.

[13] E.A. Peterson, *Anal. Biochem.* 90 (1978) 767.

[14] E.A. Peterson and A.R. Torres, *Anal. Biochem.*, 130 (1983) 271.

[15] A.R. Torres, B.E. Dunn, S.C. Edberg and E.A. Peterson, *J. Chromatogr.*, 316 (1984) 125.

[16] A.R. Torres, S.C. Edberg and E.A. Peterson, *J. Chromatogr.*, 389 (1987) 177.

[17] A.R. Torres and E.A. Peterson, *Anal. Biochem.*, 98 (1979) 353.

[18] A.R. Torres, G.G. Krueger and E.A. Peterson, *Anal. Biochem.*, 144 (1985) 469.

[19] B.E. Dunn, S.C. Edberg and A.R. Torres, *Anal. Biochem.*, 168 (1988) 25.

[20] A.R. Torres and E.A. Peterson, *J. Chromatogr.*, 604 (1992) 39.

[21] S. Ghose and B. Mattiasson, *J. Chromatogr.*, 547 (1991) 145.

[22] A.W. Liao, Z. El Rassi, D.M. Lemaster and Cs. Horvath, *Chromatographia*, 24 (1987) 881.

[23] A.L. Lee, A.W. Liao and Cs. Horvath, *J. Chromatogr.*, 443 (1988) 31.

[24] A. Liao and Cs. Horvath, in W.E. Goldstein, D. Dibiasia and H. Pedersen (Editors), *BioChemical Engineering VI*, Annals of the New York Academy of Sciences, Vol. 589, 1990, p. 182.

[25] G.Subramanian, M.W. Phillips and S.M. Cramer, *J. Chromatogr.*, 439 (1988) 341.

[26] G. Subramanian, M.W. Phillips, G. Jayaraman and S.M. Cramer, *J. Chromatogr.*, 484 (1989) 225.

[27] J.A. Gerstner and S.M. Cramer, *Biotechnol. Prog.*, 8 (1992) 540.

[28] J.A. Gerstner and S.M. Cramer, *BioPharm*, 5(9) (1992) 42.

[29] G. Jayaraman, S. Gadam and S.M. Cramer, *J. Chromatogr.*, 630 (1993) 53.

[30] S.C.D. Jen and N.G. Pinto, *J. Chromatogr.*, 519 (1990) 87.

[31] S.C.D. Jen and N.G. Pinto, *J. Chromatogr. Science*, 29 (1991) 478.

[32] G. Subramanian and S.M. Cramer, *Biotech. Progress*, 5(3) (1989) 92.

[33] H.A. McKenzie, in H.A. McKenzie (Editor), *Milk Proteins: Chemistry and Molecular Biology*, Academic Press, New York, 1971, pp. 257–330.

ELSEVIER

Journal of Chromatography A, 695 (1995) 205–221

JOURNAL OF CHROMATOGRAPHY A

Selectivity due to conformational differences between helical and non-helical peptides in reversed-phase chromatography

T.J. Sereda*, C.T. Mant, R.S. Hodges

Department of Biochemistry and the Medical Research Council of Canada Group in Protein Structure and Function, University of Alberta, Edmonton, Alberta T6G 2H7, Canada

First received 9 August 1994; revised manuscript received 17 November 1994; accepted 18 November 1994

Abstract

The reversed-phase retention behaviour of two series of peptides, one non-helical and the other α-helical, was studied under various linear AB gradients in order to determine the effect of peptide conformation on selectivity of the separation. The non-helical series, designated X1, with the sequence Ac-XLGAKGAGVG-amide, exhibited negligible α-helical content in a hydrophobic medium; whereas, the amphipathic α-helical series, designated AX9, with the sequence Ac-EAEKAAKEXEKAAKEAEK-amide, exhibited high α-helical content in a hydrophobic medium. We have shown that plots of $\log \bar{k}$ vs. $\bar{\phi}$ (where $\bar{k}$ is the median capacity factor and $\bar{\phi}$ is the median volume fraction of organic solvent) are very similar for any one peptide conformation, i.e., peptides from either the non-helical or amphipathic α-helical series exhibit similar S (solute parameter) values and the b (gradient steepness parameter) values are also similar for 17 different amino acid substitutions within each series of peptides. If mixtures of peptides from the two different series are separated using either increasing or decreasing gradient rates, large increases in resolution occur due to selectivity, which may be attributed to the difference in the $\log \bar{k}$ vs. $\bar{\phi}$ plots for each series of peptides. In addition, by using a polymer of an X1 peptide, which is 20 residues in length, it has been shown that the molecular mass difference between the X1 and the AX9 series of peptides is not sufficient to account for the selectivity difference. The S value of a non-amphipathic α-helical peptide further suggested that the difference in selectivity between the two series of peptides was due to differences in conformation. We believe that the peptide mixtures presented here provide a good model for studying selectivity effects due to conformational differences between peptides, an important concern when attempting to develop rational approaches to the prediction and optimization of peptide separation protocols from primary sequence information alone.

1. Introduction

The emergence over the past decade of reversed-phase chromatography (RPC) as the most widely used mode of high-performance liquid chromatography (HPLC) [1] has also seen a concomitant interest in method development protocols to maximise the excellent resolving power of this technique [2–6]. Indeed, this laboratory has been active for several years in developing empirical approaches to correlate the reversed-phase retention behaviour of peptides during linear gradient elution. This work has focused in two major areas: (1) prediction of peptide retention times during RPC from sequence information alone, based on the assignment of a specific hydrophobicity value to each amino acid side chain [7–9]; (2) prediction of the

* Corresponding author.

0021-9673/95/$09.50
SSDI 0021-9673(94)01147-8

effect of varying mobile phase components (e.g., ion-pairing reagent) [10] or run conditions (gradient-rate, flow-rate) [11] on peptide separations. From such studies, we are able to predict, with considerable accuracy, how manipulation of the mobile phase or run conditions will affect the selectivity (and, hence, resolution) of a particular peptide separation. These predictive approaches both rely on relating the predicted retention times of peptides of interest to that of the observed behaviour of a peptide standard [7–11]. This approach to the optimization of peptide resolution assumes that, when not subject to conformational restraints, the chromatographic behaviour of a peptide is mainly or solely dependent on amino acid composition. When one also takes into account the effect of peptide chain length, also independent of any conformational considerations, this assumption holds up well for most practical purposes, as evidenced by the successful use of a computer-based HPLC method development program, ProDigest-LC, derived from these principles [3,12].

It is well known that the general rule of thumb whereby it is assumed that the resolution between all peaks in a peptide mixture will increase with increased gradient time is not necessarily valid [5]. Indeed, variation of selectivity with gradient slope is commonly observed for peptides and proteins [13–18]. A very important, practical example is the occasional reversal of elution order of peptides when attempting to optimize the separation of peptide fragments from a protein digest [13], i.e., different peptides are affected to a different extent by changes in gradient slope. These selectivity variations arise from the way an individual peptide interacts with the hydrophobic stationary phase, a factor not taken into account in a purely empirical approach to prediction and optimization of peptide retention behaviour. Clearly, to enhance the value of such empirically derived predictive methods even further, it is necessary to take into account more stringently the way individual peptide solutes interact with a reversed-phase packing, i.e., a form of fine-tuning of predictions derived solely from the knowledge of peptide primary structure information. A prime resource for such fine-tuning is represented by the *linear solvent strength (LSS)* theory of gradient elution [19–23], which enables the researcher to assign parameters to peptidic solutes reflecting differences in both the magnitude and overall affinity of the hydrophobic contact area between the peptide and the hydrophobic stationary phase. The practical value of LSS theory has already been demonstrated by its application in the development of the DryLab HPLC optimization program [2,4,24].

Clearly, many and varied influences will impact on the way a particular peptide will interact with a reversed-phase packing. These will include characteristics of the peptide itself, e.g., amino acid composition [7,9], residue sequence [9,25,26], peptide length [8] and the presence of any secondary structure (α-helix or β-sheet) which will affect profoundly the way in which residues are orientated with respect to the stationary phase [9,27]; mobile phase (e.g., type of organic modifier, ion-pairing reagent, pH) [1,10,28,29] and run conditions (e.g., temperature) [28–30] make their own contribution to peptide chromatographic behaviour; finally, the effect of the stationary phase (e.g., type of ligand, ligand density, silica- versus non-silica-based) must also be considered [31,32]. In order to delineate the relative contribution of different peptide characteristics to its orientation with a reversed-phase packing, it is necessary to reduce as much as possible the number of variables which affect its retention behaviour.

The present study represents our initial investigation into how the presence of a defined structure (α-helix) affects the magnitude of the contact area of a peptide with a hydrophobic stationary phase, as expressed by LSS theory, and how this effect relates to selectivity differences between families of secondary structure (amphipathic versus non-amphipathic α-helices) as well as to differences between such structures and peptides with no ordered higher levels of structure (random coil). The importance of gauging the contribution of α-helical structure to the selectivity of peptide separations can be easily appreciated in such aforementioned applications as optimization of the separation of peptide

fragment mixtures from chemical or proteolytic digests of proteins; such mixtures typically contain peptides with α-helical potential. Thus, in the present study, RPC was applied, under defined mobile phase and run conditions, to linear gradient elution of series of synthetic model α-helical and non-helical peptides on an analytical reversed-phase column. We believed that observation of the retention behaviour of such peptide models would offer insight into the way such structures affect separation selectivity and, hence, how such information may be applied to the rational development of separation prediction and optimization protocols.

2. Experimental

2.1. Materials

HPLC-grade water and acetonitrile were obtained from BDH (Poole, UK). ACS-grade orthophosphoric acid was obtained from Anachemia (Toronto, Canada). Trifluoroethanol (TFE) was obtained from Sigma (St. Louis, MO, USA).

2.2. Instrumentation

Peptide synthesis was carried out on an Applied Biosystems peptide synthesizer Model 430 (Foster City, CA, USA). Crude peptides were purified by RPC using an Applied Biosystems 400 solvent delivery system connected to a 783A programmable absorbance detector.

The analytical HPLC system consisted of an HP1090 liquid chromatograph (Hewlett-Packard, Avondale, PA, USA), coupled to an HP 1040A detection system, HP9000 series 300 computer, HP9133 disc drive, HP2225A Thinkjet printer and HP7460A plotter.

Amino acid analyses of purified peptides were carried out on a Beckman Model 6300 amino acid analyser (Beckman Instruments, Fullerton, CA, USA).

The correct primary ion molecular masses of peptides were confirmed by time of flight mass spectroscopy on a BIOION-20 Nordic (Uppsala, Sweden).

2.3. Peptide synthesis

Peptides were synthesized by the solid-phase technique (SPPS) on co-poly(styrene–1% divinylbenzene) benzhydrylamine hydrochloride resin (0.92 mmol of amino groups/g resin) as described previously [33]. The cleaved peptide/resin mixtures were washed with diethylether (3×25 ml) and the peptides extracted with neat acetic acid (3×25 ml). The resulting peptide solutions were then lyophilized prior to purification.

2.4. Columns and HPLC conditions

Crude peptides were purified on a semi-preparative SynChropak RP-P C_{18} reversed-phase column (250×10 mm I.D., 6.5 μm particle size, 300 Å pore size) from SynChrom (Lafayette, IN, USA). The peptides were purified at pH 2 by linear AB gradient elution (0.5% B/min) at a flow-rate of 5 ml/min, where eluent A is 0.1% aqueous trifluoroacetic acid (TFA) and eluent B is 0.1% TFA in acetonitrile.

Analytical runs were carried out at pH 2 on an Aquapore RP-300 C_8 reversed-phase column (220×4.6 mm I.D., 7 μm particle size, 300 Å pore size) from Applied Biosystems, by employing linear AB gradient elution (0.5, 1, 2, 4% acetonitrile/min) at a flow-rate of 1 ml/min, where eluent A is 20 m*M* aqueous phosphoric acid and eluent B is 20 m*M* phosphoric acid in 50% aqueous acetonitrile.

2.5. Circular dichroism (CD) measurements

CD measurements were performed on a Jasco J-720 spectropolarimeter (Jasco, Easton, MD, USA). The cell was maintained at 25°C with a Lauda RMS circulating water bath (Lauda, Westbury, NY, USA). The instrument was routinely calibrated with *d*(+)-10-camphorsulphonic acid at 290.5 nm and with pantoyllactone at 219 nm by following the procedures outlined by the manufacturer. CD spectra were the average of

10 scans obtained by collecting data from 250 to 190 nm. The molar ellipticity is reported as mean residue molar ellipticity ($[\theta]$, with units of deg · cm^2/dmol) and calculated from the following equation: $[\theta] = [\theta]_{obs}\ (mrw)/10lc$, where $[\theta]_{obs}$ is the observed ellipticity in degrees, *mrw* is the mean residue weight (molecular mass of the peptide divided by the number of amino acid residues), *c* is the peptide concentration in g/ml and *l* is the optical path length in cm (0.0195 cm). Peptide concentrations were determined by amino acid analysis where the stock solution of the "native" model amphipathic α-helical peptide, designated AA9 (see Section 4.1.), was determined to be 5.62×10^{-4} *M* and that of a non-amphipathic α-helical peptide, designated naA, was determined as 1.99×10^{-4} *M*. CD spectra were measured of peptides dissolved in 40 m*M* aqueous phosphoric acid–TFE (1:1, v/v), where TFE is a solvent that induces helicity in single-chain potentially α-helical peptides [34,35].

3. Theoretical considerations

The LSS model describing mathematically the retention behaviour of solutes under gradient elution conditions has been reported in detail elsewhere [19–23] and only the appropriate equations used will be discussed here.

An important quantity in LSS theory is the gradient steepness parameter, *b*, which is a function of the separation conditions, e.g., the gradient time, flow-rate and mobile phase composition. The retention times of a peptide, t_{g1} and t_{g2}, obtained under two different gradient times, t_{G1} and t_{G2}, may be used to determine the gradient steepness parameter through the following expression:

$$b = t_0 \log \beta / \left[t_{g1} - (t_{g2}/\beta) + t_0'(t_{G1} - t_{G2})/t_{G2}\right] \quad (1)$$

where β is the ratio of gradient times, t_{G2}/t_{G1}, t_0 is the column dead time and t_0' is the column dead time plus the gradient elapse time (gradient elapse time = t_d, time it takes a change in mobile phase composition to move from the pump through the mixer and injector to the column inlet). The t_0 value, in min, was obtained by injecting a sample containing 1% TFA with the column in place [36]. The gradient elapse time was obtained by removing the column and measuring the time for the gradient to reach the detector when a switch from 0 to 50% B is made [36]. The t_0' value was calculated as the column dead time (t_0) plus the gradient elapse time (t_d). For our HPLC system, $t_0' = 3.73$ min and $t_0 = 2.83$ min.

Once a *b* value has been obtained, the median capacity factor, $\bar{k}$, (i.e., the capacity factor when the solute is at the midpoint of the column during a gradient run) and the median volume fraction of organic solvent, $\bar{\phi}$ (i.e., the volume fraction of organic solvent when the solute is at the midpoint of the column during a gradient run) associated with the elution of each peptide may be determined from the following relationships:

$$\bar{k} = 1/1.15b \quad (2)$$

$$\bar{\phi} = \phi_0 + \left[t_{g1} - t_0' - 0.3(t_0/b)\right](\Delta\phi/t_{G1}) \quad (3)$$

where $\Delta\phi = (\phi_f - \phi_0)$ and ϕ_0 is the initial value at time zero and ϕ_f is the final value, i.e., at the end of the gradient. It has been stated that, in order to optimize a particular separation, the $\log \bar{k}$ value should be within a narrow range of values, i.e., $0 \leq \log \bar{k} \leq 1$ [19,20]. It should be noted that the four different gradient rates used in this study for the separation of the synthetic peptides result in a $\log \bar{k}$ value that approximates this range of values. The $\bar{k}$ and $\bar{\phi}$ values obtained from Eqs. 2 and 3 may be related through the following expression:

$$\log \bar{k} = \log k_0 - S\bar{\phi} \quad (4)$$

Linear plots of $\log \bar{k}$ versus $\bar{\phi}$ were obtained in each case over the experimental range of conditions used and the reported *S* and $\log k_0$ values were obtained by analysing these data by linear regression. The parameters *S* and $\log k_0$ are related respectively to the hydrophobic contact area of the peptide and the affinity of this contact region for the hydrophobic stationary phase [18].

Although, strictly speaking, system-to-system consistency requires that solute resolution under gradient conditions requires a calculation that is different from isocratic conditions [19], for the sake of simplicity we have used the isocratic form of the equation to report resolution: $R_s = 1.176\Delta t/(w_{h1} + w_{h2})$, where Δt is the difference in retention time between the two peaks and w_{h1} and w_{h2} are the widths of the peaks at half height for the corresponding peaks [36].

4. Results and discussion

4.1. Design of model synthetic peptides

The suggestion that the solute parameter, S, is dependent on conformation, e.g., random coil versus ordered or native versus denatured has been considered previously [20]. For instance, in an attempt to determine the relationship between structure and the solute parameter, the S values of synthetic peptides of human growth hormone (hGH) were determined [37]; in another study [38], variations in S values of the peptides bombesin, β-endorphin and glucagon with increasing temperature were followed and related to temperature-induced conformational changes. Other studies produced observations that S values may vary considerably for series of peptides which differ markedly in length and sequence [22,39]; whilst only small S value variations were observed for minor changes in the sequence of peptide analogues of myosin light chain [40]. In these latter studies, the conformation of the peptides was not specifically defined or related to the resulting S values.

We believed the best initial approach to delineating the effect of α-helical structure on the solute parameter was to compare the retention behaviour of peptides with extremes of structure, i.e., either with as close to 100% α-helical conformation as possible or with the complete absence of α-helix. To this end, two series of peptides designed to exhibit markedly different conformational characteristics during RPC were synthesized, the sequences of which are shown in Fig. 1.

The peptide series designed to exhibit negligible α-helical structure (denoted X1 in Fig. 1), has the sequence Ac-Xxx-Leu-Gly-Ala-Lys-Gly-Ala-Gly-Val-Gly-amide, where Xxx represents the amino acid substituted at position 1; thus, G1 represents a 10-residue peptide with a glycine residue substituted at position 1. Based on the same sequence as peptide G1, the peptide designated $(G1)_2$, a 20-residue peptide (Fig. 1), was also synthesized in order to determine any molecular mass (or chain length) effect on the S value.

The second series of peptides, denoted AX9 (Fig. 1), has the sequence Ac-Glu-Ala-Glu-Lys-Ala-Ala-Lys-Glu-Xxx-Glu-Lys-Ala-Ala-Lys-Glu-Ala-Glu-Lys-amide, where Xxx represents the substituted position, a sequence known to have a high potential to form an α-helix, specifically an amphipathic α-helix [41,42]. In a similar manner to the designation of the X1 series of peptides, the analogues of this second series are identified by the substituted residue; thus, the designation AA9 refers to an alanine residue substitution at position 9 of the sequence, etc. An additional peptide, designated naA (Fig. 1), with the same composition as peptide AA9 but a different sequence was also synthesized. This peptide, also with high α-helical potential, represents a non-amphipathic α-helical control peptide to assess any effect of amphipathicity, as opposed to strictly α-helical conformational influences, on the S value of an α-helical peptide.

4.2. Conformation and helicity of model peptides

Conformation of the peptides was determined by CD in aqueous solution in the presence of 50% (v/v) TFE. As noted above, this solvent promotes helix formation only in regions of a polypeptide with some helical propensity [34,43–45]. This concentration of TFE is also a good mimic of the hydrophobic environment of RPC, known to induce and stabilize α-helical structure in potentially helical molecules [9].

It has been shown previously by Zhou et al. [9] that the sequence of the peptide series denoted X1 (Fig. 1) exhibits the desired negli-

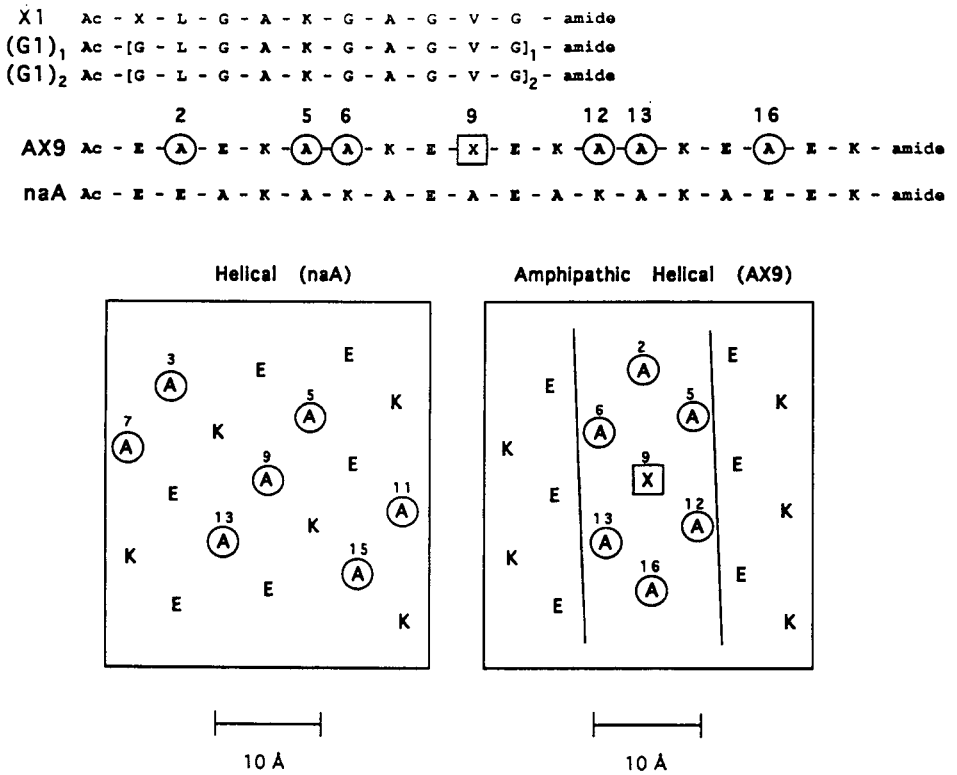

Fig. 1. Design of synthetic peptides. Top: sequence of the non-helical peptide analogues, denoted X1, the amphipathic α-helical peptides, denoted AX9, and the non-amphipathic α-helical peptide naA. In the X1 series, X refers to the amino acid substituted at position 1 of the 10 residue peptide. In the AX9 series, A represents the amino acid Ala which makes up the hydrophobic face (circled residues labelled 2, 5, 6, 12, 13, and 16) of the α-helical peptide and X refers to the amino acid substituted at position 9 (boxed residue labelled 9) in the α-helical peptide. The Lys (K) and the Glu (E) acid residues make up the hydrophilic face of the helix. The non-amphipathic α-helical peptide, naA, is of the same sequence as the AA9 peptide, except that the amino acid sequence is different such that the Ala residues are not all in the hydrophobic face as in peptide AA9. Bottom: Non-amphipathic α-helical and amphipathic α-helical peptides are represented as α-helical nets. The position of the α-carbon atom for each amino acid residue is denoted on the surface of a cylinder representing the α-helix having 3.6 residues per turn, with a 1.5 Å translation along the helix and a helix axis of 5 Å. This cylindrical surface area is depicted in two dimensions where the width of the α-helical net represents the circumference of the cylinder ($2\pi r = 31.4$ Å). The area between the solid lines of the amphipathic α-helical net represents the residues that are in the hydrophobic face of the peptide. In the naA peptide, it can be seen that the distribution of the Ala residues results in a non-amphipathic structure.

gible α-helical structure required for the present study.

Both peptides AA9 and naA exhibit CD spectra typical of α-helical proteins, with two minima at 222 and 207 nm [46] with α-helical contents exceeding 90% at 5°C using the molar ellipticity at 222 nm [41]. In addition, the $[\theta]_{220}/[\theta]_{207}$ ratio value is less than 1, suggesting that, in the presence of 50% TFE, peptides AA9 and naA are single-stranded α-helices [41,47,48]. It has been shown previously [49] that even 29- and 36-residue synthetic amphipathic α-helical peptides which form very stable coiled-coil structures are chromatographed as monomers during size exclusion HPLC in 0.1% aq. TFA containing 50% TFE. Taken together, these observations suggest that peptide AA9, as well as the non-amphipathic naA, will be chromatographed as a single-stranded α-helix during RPC.

4.3. RPC retention behaviour of amphipathic versus non-amphipathic α-helical peptides

Fig. 1 also shows the structures of the amphipathic α-helical series of peptides, AX9, and the non-amphipathic naA presented as α-helical nets. The amphipathic nature of the AX9 series is quite clear, with the circled alanine residues at positions 2, 5, 6, 12, 13 and 16 and the substituted residue at position 9 making up the hydrophobic face of the peptide. The orientation of hydrophobic residues along a helix in such a manner also gives rise to a preferred binding domain in RPC, whereby the observed peptide retention time is greater than would be expected from predictions based on sequence and chain length information alone [9,50]. In contrast, the helical net presentation of peptide naA, which has the same amino acid composition as peptide AA9, demonstrates a distribution of alanine residues throughout the helix, such that no preferred binding domain is formed; hence, naA would be expected to be eluted prior to AA9 from an RPC column [9,50].

4.4. Selectivity differences between non-helical and amphipathic α-helical peptides

Four analogues of the non-helical peptide series (peptides A1, L1, Y1 and F1) and four analogues of the amphipathic α-helical series (peptides AA9, AL9, AY9 and AF9) were run on a reversed-phase column at different linear gradient rates of 0.5%, 1%, 2% and 4% acetonitrile/min. From these data, the median capacity factor, $\bar{k}$, was calculated using Eqs. 1 and 2 and the median volume fraction, $\bar{\phi}$, was calculated using Eq. 3, as described in the Experimental section. Figs. 2, 3 and 4 show plots of $\log \bar{k}$ versus $\bar{\phi}$ for selected pairs of non-helical and amphipathic α-helical peptides; S and $\log k_0$ values subsequently obtained from these plots are reported in Table 1.

From Table 1, it can be seen that the S values

Table 1
Retention time, S and $\log k_0$ values of non-helical and amphipathic α-helical peptides

	t_g (min)[b]				S[c]	$\log k_0^c$
t_G (min)[a]	100	50	25	12.5		
Gradient rate (%)[a]	0.5	1	2	4		
Helical peptides[d]						
naA	30.10	17.79	11.19	7.70	33.2	4.34
AA9	39.65	22.72	13.77	9.04	27.2	4.93
AL9	48.15	27.06	16.06	10.20	24.1	5.44
AY9	40.25	23.04	14.02	9.18	24.9	4.62
AF9	47.25	26.60	15.90	10.12	23.4	5.20
Non-helical peptides[d]						
$(G1)_1$	21.85	14.73	10.34	7.66	13.2	1.53
$(G1)_2$	34.69	20.70	13.09	8.87	17.4	2.91
A1	23.47	15.61	10.80	7.90	13.0	1.63
L1	35.25	21.89	14.16	9.67	11.1	2.17
Y1	31.37	19.66	12.91	8.97	12.3	2.07
F1	38.13	23.35	14.93	10.12	10.5	2.24

[a] t_G represents the length of the linear AB gradient, in min, for a change from 0 to 100% B and the rate represents the equivalent % acetonitrile/min for the corresponding gradient time. For conditions, see Experimental.
[b] t_g represents the retention time of each peptide under linear AB gradient conditions.
[c] S and $\log k_0$ are determined by linear regression of the data from the $\log \bar{k}$ vs. $\bar{\phi}$ as described by Snyder and Stadalius [20]; see Experimental.
[d] For details of peptide designations, see Section 4.1. and Fig. 1.

obtained for the non-helical and amphipathic α-helical peptides represent a small range of values within each series of peptides (i.e., 10.5 to 13.0 and 23.4 to 27.2, respectively); in contrast, there is a significant difference in S values between the two series of peptides. According to Snyder [19], the separation of solutes of different S values may result in three different types of $\log \bar{k}$ vs. $\bar{\phi}$ plots; in addition, it is also suggested by Snyder and Stadalius [20] that any condition that affects the value of $\bar{k}$ (e.g., the gradient time, t_G) will result in a change in $\bar{\phi}$, this change in $\bar{\phi}$ subsequently resulting in a change in selectivity. Aguilar et al. [39] and Hearn et al. [15] also suggest that selectivity differences between polypeptides will be related to their respective S values.

The elution profiles shown in Figs. 2, 3 and 4, where selected pairs of peptides (each pair including one peptide from each peptide series) are separated under different gradient conditions, represent excellent practical examples of the three types of $\log \bar{k}$ vs. $\bar{\phi}$ plot discussed by Snyder [19]. Thus, very different effects of varying gradient rate on the selectivity of the separation of the peptide pairs are observed in Figs. 2–4.

From Fig. 2 (left), it can be seen that the non-helical peptide, L1, and the amphipathic α-helical peptide, AY9, have the same median capacity factor at a gradient rate of 1.8% acetonitrile/min, i.e., the point where the two plots intersect; thus, the two peptides are coeluted, as seen in Fig. 2 (right), panel B. Since the plots of the two peptides intersect at a point in the centre of the workable range of median capacity factor, i.e., where peptide retention times are neither too short nor too long for practical purposes, separation of the two peptides may be achieved either by decreasing the gradient rate (the more traditional approach) [Fig. 2 (right), panel A], or increasing the gradient rate (panel C) [19]. Thus, by decreasing the gradient rate from 1.8% acetonitrile/min (panel B) to 0.5%/min (panel A), peptides L1 and AY9 were separated by 5 min (from Table 1: AY9, $t_g = 40.25$ min; L1, $t_g = 35.25$ min). Alternatively, by increasing the gradient rate from 1.8%/min (panel B) to 4%/min (panel C), peptides L1 and AY9 are separated by 0.49 min (Table 1: L1, $t_g = 9.67$ min; AY9, $t_g = 9.18$ min). Note the reversal of peptide elution order between the two extremes of gradient rate, a consequence of the intersecting plots shown in Fig. 2 (left) and an excellent example of changes in separation selectivity due to significantly different peptide S values [13,17].

Fig. 3 represents a second type of $\log \bar{k}$ vs. $\bar{\phi}$ plot [19], where the lines for the two peptides intersect at the higher end of practically favourable median capacity factors. Thus, at a gradient rate of 0.77% acetonitrile/min, the median capacity factor for the non-helical/amphipathic α-helical peptide pair F1/AA9 is the same (Fig. 3, left); therefore, there is no separation selectivity and the peptides are coeluted [Fig. 3 (right), panel A]. Again in this case, the peptide S values are substantially different (Table 1: AA9, $S = 27.2$ and F1, $S = 10.5$) and a change in selectivity may be achieved by varying the gradient rate [19]. For this peptide pair, the best option clearly is to increase the gradient to separate the peptides within a reasonable run time. Thus, the separation improved progressively as the gradient rate was increased from 0.77% acetonitrile/min (panel A) to 1%/min (panel B) and, finally, to 4%/min (panel C). In addition, this separation was achieved within a short run time (< 10 min) and resulted in sharp solute peaks.

Fig. 4 shows the separation of the peptide pair L1/AL9, which also exhibit significantly different S values (Table 1: L1, $S = 11.1$ and AL9, $S = 24.1$). These peptides produce the third type of $\log \bar{k}$ vs. $\bar{\phi}$ plot [19], where the individual peptide plots intersect at the lower end of the practical working range of $\log \bar{k}$ values. Clearly, for this peptide pair, a decreasing gradient rate would be the appropriate method to improve the separation. Thus, decreasing the gradient rate from 4% acetonitrile/min [Fig. 4 (right), panel C] to 2%/min (panel B) and, finally to 0.5% acetonitrile/min (panel A) results in a progressive improvement in peptide separation; at a gradient rate of 0.5% acetonitrile/min, the peptides are separated by 12.90 min (Table 1: AL9, $t_g = 48.15$; L1, $t_g = 35.25$).

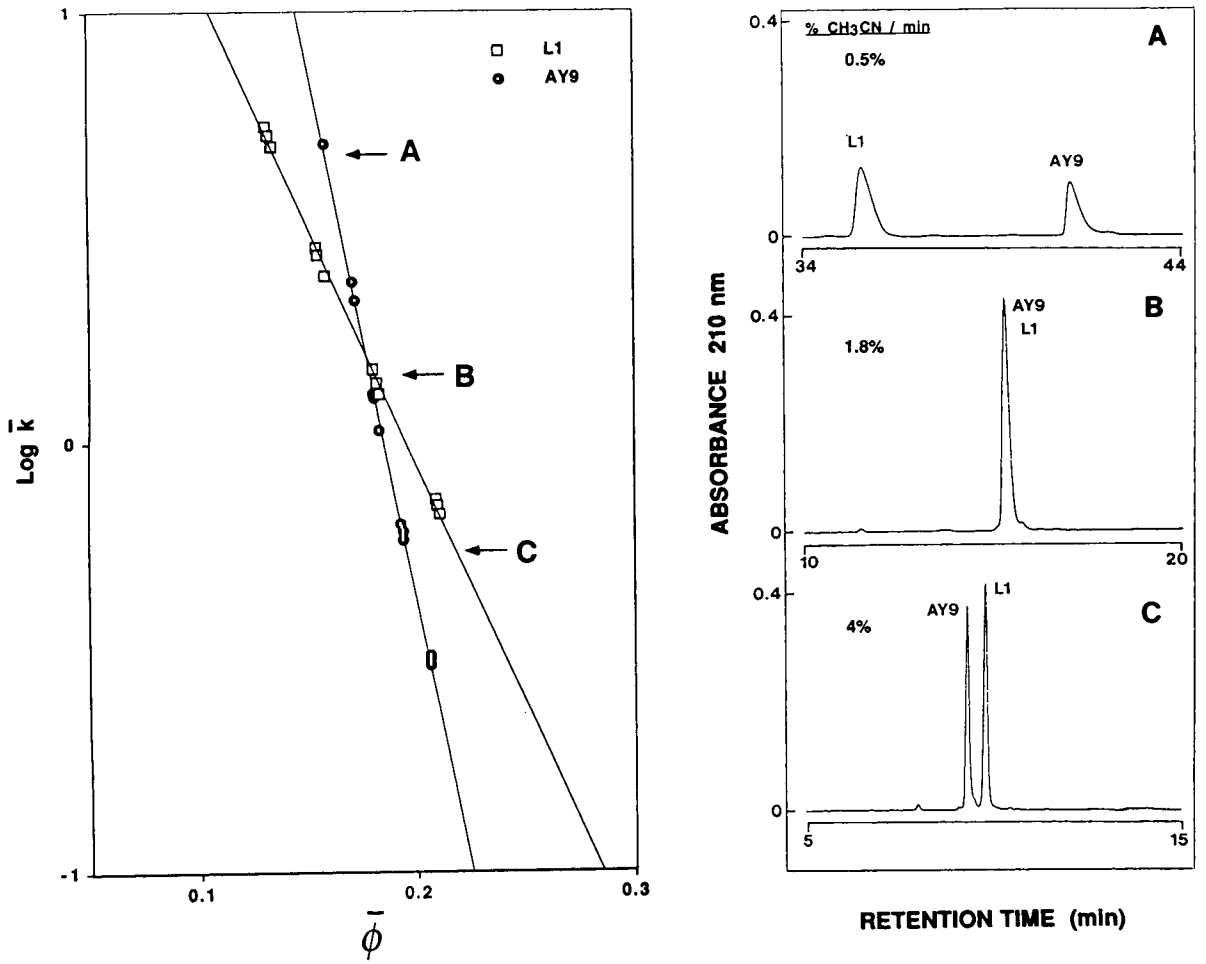

Fig. 2. Plot of log $\bar{k}$ vs. $\bar{\phi}$ and reversed-phase elution profiles of peptides L1 and AY9. Plot: values of log $\bar{k}$ and $\bar{\phi}$ were obtained by separating L1 and AY9 at four different gradient rates (see Table 1) and applying Eqs. 1, 2 and 3 to the retention time data as described in Experimental. Straight line plots were obtained by linear regression of the data. The labels A, B and C refer to the elution profiles shown in the right hand panels. RPC: peptides L1 and AY9 were separated at 0.5, 1.8 and 4% acetonitrile/min at a flow-rate of 1 ml/min where eluent A was 20 m*M* phosphoric acid and eluent B was 20 m*M* phosphoric acid in 50% aqueous acetonitrile.

4.5. Contribution of conformational differences to selectivity of peptide separations

We now set out to determine the role that conformation played in the selectivity differences apparent between the non-helical and amphipathic α-helical peptides demonstrated in Figs. 2–4 and Table 1. The peptide pairs of Figs. 2–4 not only differed in conformation (non-helical X1 series versus α-helical AX9 series), but also in molecular mass (or polypeptide chain length) (10-residue X1 series versus 18-residue AX9 series). Thus, it was now necessary to determine the contribution, if any, of hydrophobicity and molecular mass to the magnitude of the *S* values obtained for the two series of peptides in order to delineate the effect of α-helical conformation on separation selectivity.

Despite the significant range of hydrophobicities of the non-helical X1 series of peptides,

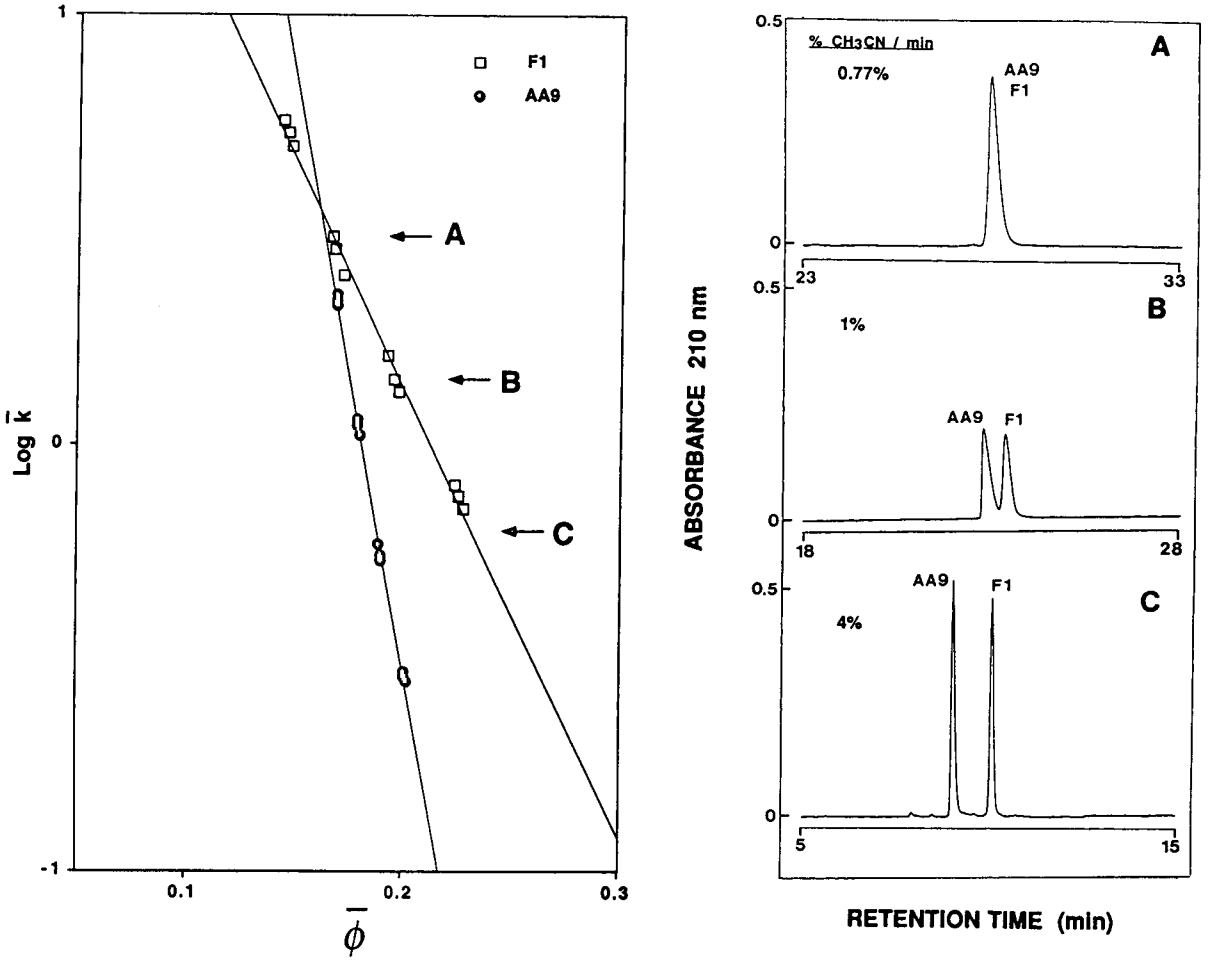

Fig. 3. Plot of $\log \bar{k}$ vs. $\bar{\phi}$ and reversed-phase elution profiles of peptides F1 and AA9. Plot: obtained as in Fig. 2. RPC: conditions as in Fig. 2, except that gradient rates of 0.77, 1.0 and 4% acetonitrile/min were used.

as expressed by their retention times (23.47 to 38.13 min at 0.5% acetonitrile/min; Table 1), the corresponding range of S values was relatively small (10.5 to 13.0; Table 1); similar observations were made for the amphipathic α-helical AX9 series of peptides where the retention times varied from 39.65 to 48.15 min with a small S value range of 23.4 to 27.2 (Table 1).

It has been observed that S is dependent on molecular mass; however, it has been found that this relationship is very much dependent on the peptides used in the determination [40]. It has therefore been suggested [22] that it is not the molecular mass per se that is important in determining S.

From Fig. 1, non-helical peptides $(G1)_1$ and $(G1)_2$ were now chromatographed at different gradient rates and their S values calculated from plots of $\log \bar{k}$ vs. $\bar{\phi}$. Peptide $(G1)_1$ is the glycine-substituted 10-residue analogue of the X1 peptide series; whereas, $(G1)_2$ is a 20-residue polymer of $(G1)_1$ and represents a non-helical control peptide similar in length to the 18-residue

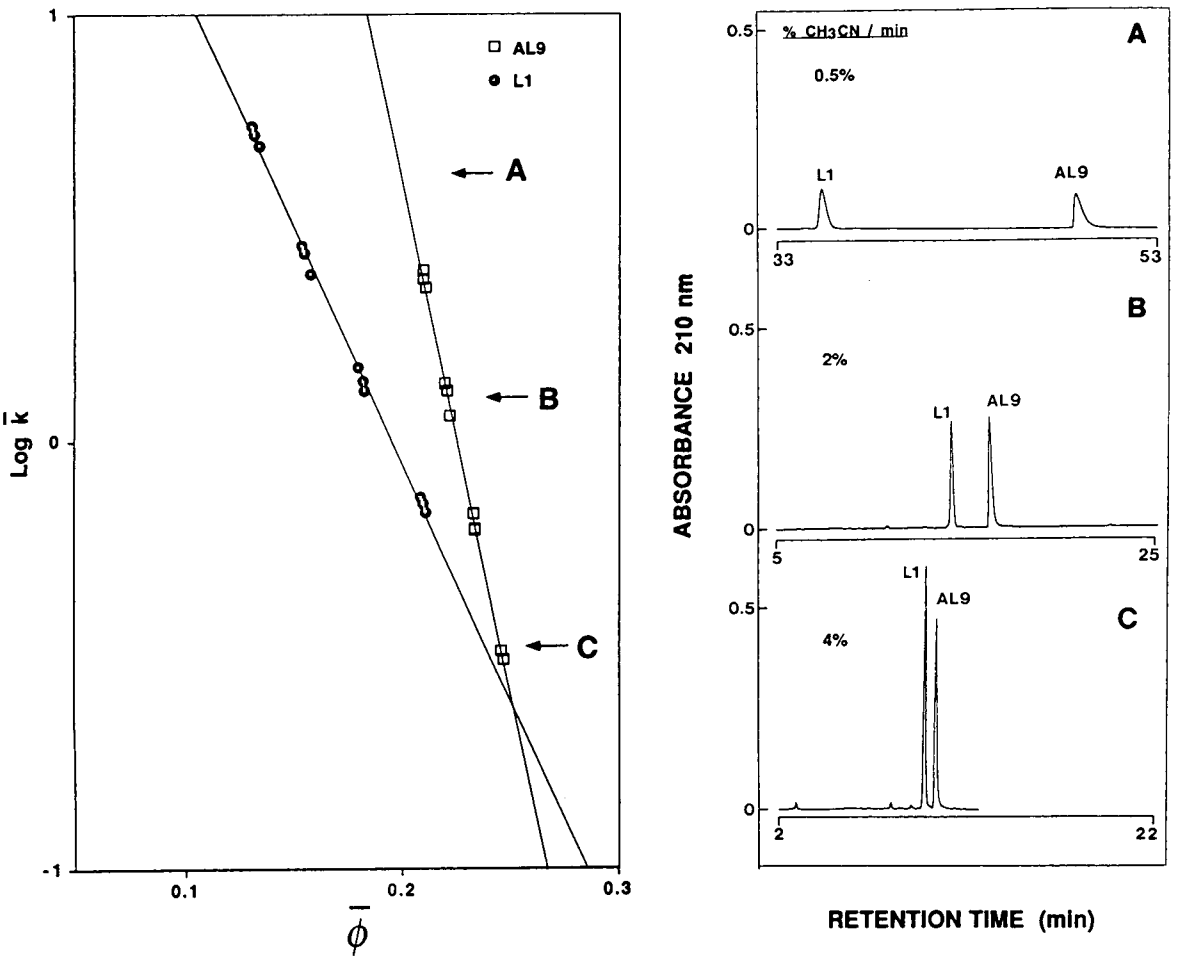

Fig. 4. Plot of $\log \bar{k}$ vs. $\bar{\phi}$ and reversed-phase elution profiles of peptides L1 and AL9. Plot: obtained as in Fig. 2. RPC: conditions as in Fig. 2, except that gradient rates of 0.5, 2.0 and 4% acetonitrile/min were used.

α-helical series of peptides (AX9). From Table 1, the $(G1)_1$ peptide has an S value (13.2) that is similar to the range of values determined for other non-helical 10-residue peptides, A1, L1, Y1 and F1 (10.5 to 13.0). In addition, it can also be seen that an increase in molecular mass (or chain length) from the 10-residue $(G1)_1$ to the 20-residue $(G1)_2$ ($S = 17.4$), resulted in an increase in S which is consistent with a previous suggestion that the S value may increase with molecular mass through simple peptide elongation [22], as in this example. Thus, although peptide chain length may contribute to some extent, the magnitude of the S value increase observed between the 10-residue and 20-residue peptides (13.2 to 17.4; Table 1) is not large enough to account for the significant differences in the range of S values (and, hence, selectivity differences) between the non-helical 10-residue X1 peptide series ($S = 10.5$ to 13.0; Table 1) and the 18-residue amphipathic α-helical AX9 peptide series ($S = 23.4$ to 27.2; Table 1). Despite the amino acid composition differences between the peptide series, we feel this is strong evidence

that the significantly different S values for the AX9 series of peptides in comparison to the non-helical X1 series is due mainly to the influence of the α-helical conformation of the former.

We now wished to determine whether the amphipathicity had any significant contribution to peptide S values separate from the conformational influence of the helix. The non-amphipathic α-helical peptide, naA (Fig. 1), and the amphipathic α-helical peptide AA9 have hydrophobic moments of 0.04 and 0.59, respectively, determined using the method and normalized consensus hydrophobicity scale of Eisenberg et al. [51]). The hydrophobic moment is a measure of amphipathicity, where the greater the value, the greater the amphipathicity [52]. Peptide naA exhibits a significantly different S value (33.2; Table 1) compared to the non-helical X1 peptides (a range of 10.5 to 13.0; Table 1). Instead, the value for peptide naA is of a magnitude similar to that of its amphipathic analogue, peptide AA9 (27.2; Table 1). Clearly, the amphipathicity of these α-helical peptides is not a major factor influencing peptide S values and, hence, separation selectivity, as compared

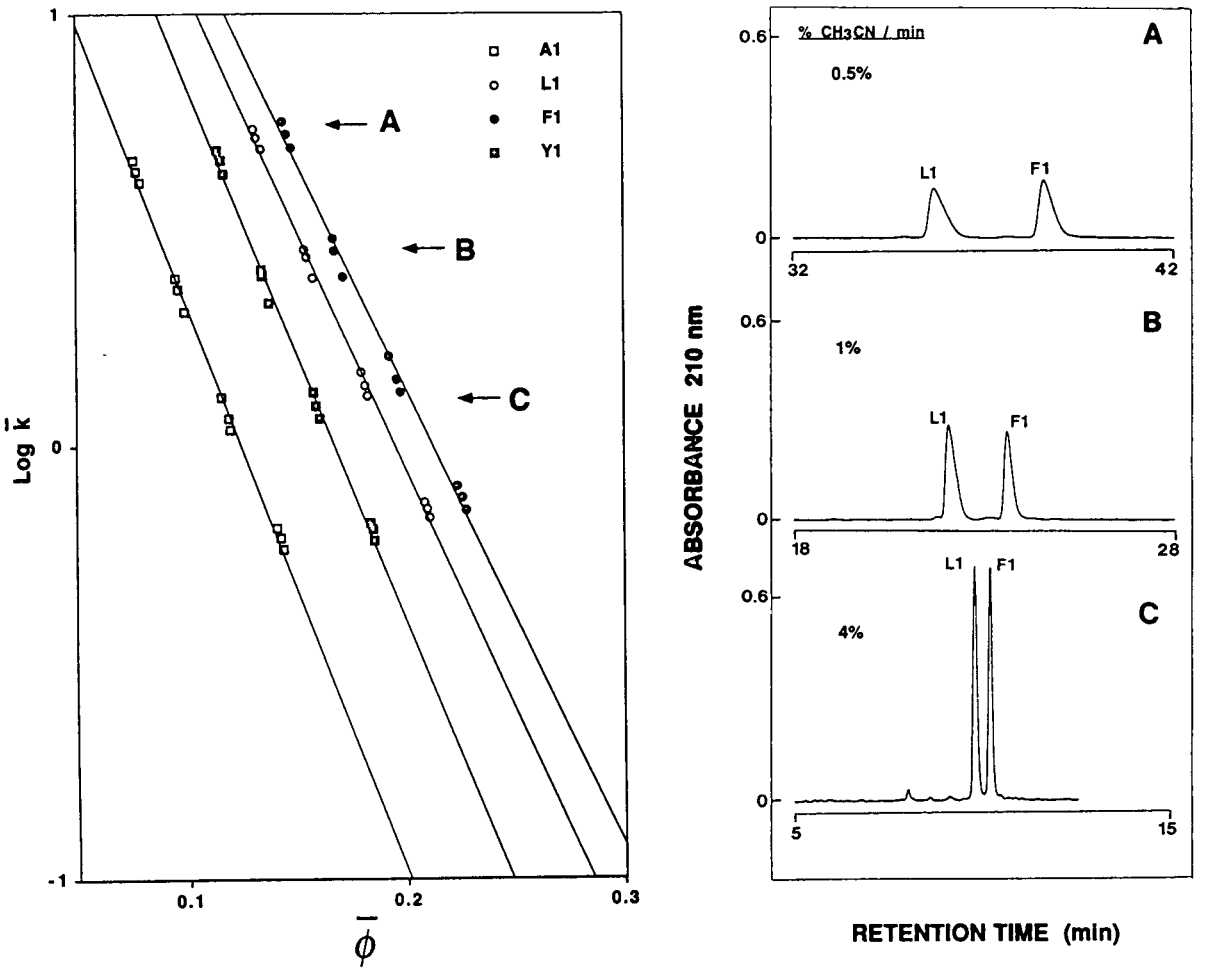

Fig. 5. Plot of $\log \bar{k}$ vs. $\bar{\phi}$ and reversed-phase elution profiles of the non-helical peptides A1, L1, Y1 and F1. Plot: obtained as in Fig. 2. RPC: conditions as in Fig. 2, except that gradient rates 0.5, 1.0 and 4% acetonitrile/min were used.

to the conformational differences between non-helical and helical peptides.

4.6. Resolution between mixtures of non-helical and amphipathic helical peptides

From Figs. 5 and 6, left panels, it can be seen that peptides of similar structure exhibit similar $\log \bar{k}$ vs. $\bar{\phi}$ plots and, therefore, a similar S value; this can also be seen from Table 1, where, as noted above, the non-helical and amphipathic α-helical peptides have a small intra-series range of S values (10.5 to 13.0 and 23.4 to 27.2, respectively). Since S for each series of peptides is represented by a small range of values, this suggests that improvement in resolution between peptides of the same series (and, thus the same conformation) may be obtained by a decreasing gradient rate. Fig. 5 illustrates this situation, where non-helical peptides L1 and F1, having similar values of S (L1 = 11.1 and F1 = 10.5, respectively; Table 1), exhibited a 1.2-fold change in resolution (3.5 to 4.2; Table 2) for a 2-fold (1% acetonitrile/min to 0.5%/min) decrease in gradient rate. Similar results can be seen in Fig. 6, where the two amphipathic α-

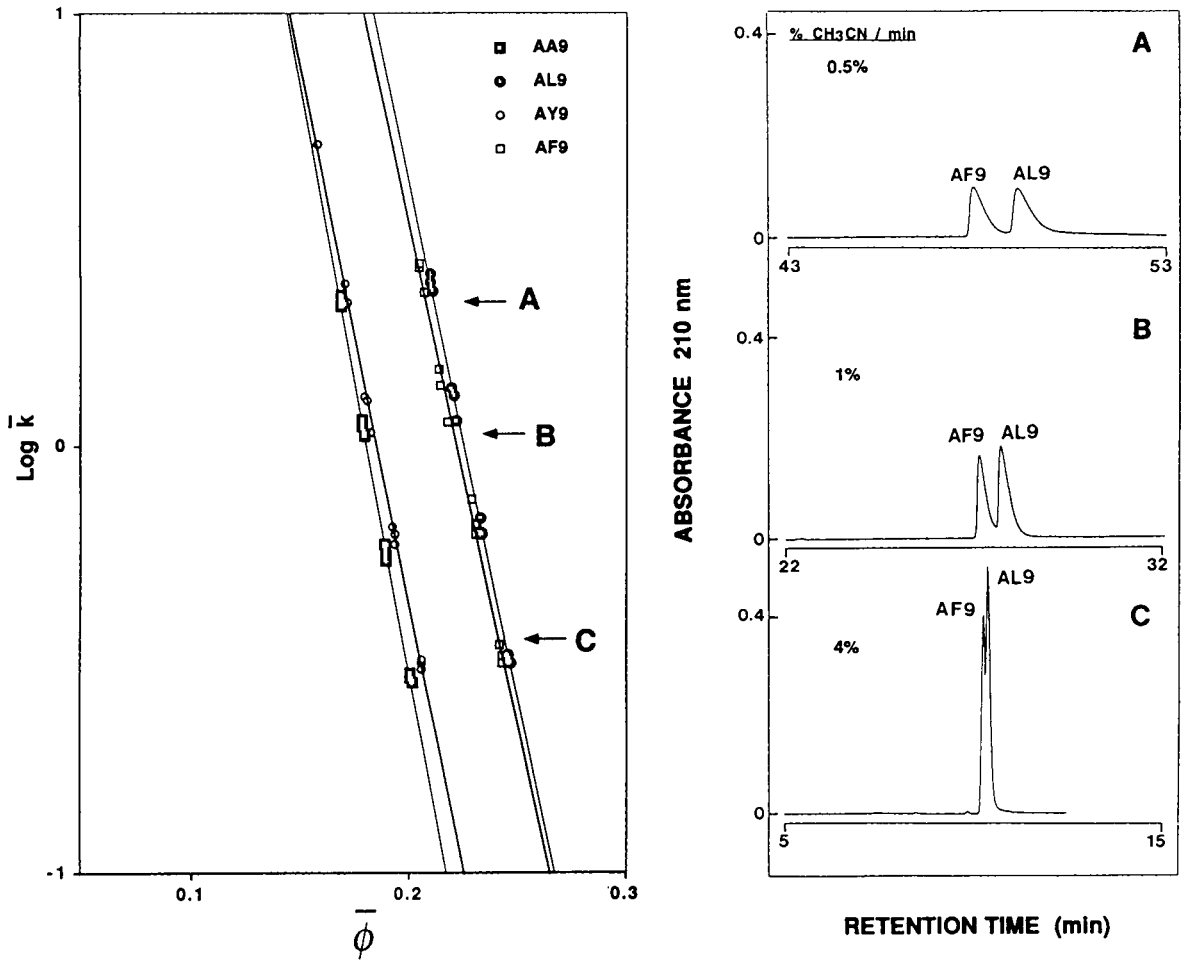

Fig. 6. Plot of $\log \bar{k}$ vs. $\bar{\phi}$ and reversed-phase elution profiles of the amphipathic α-helical peptides AA9, AL9, AY9 and AF9. Plot: obtained as in Fig. 2. RPC: conditions as in Fig. 2, except that gradient rates 0.5, 1.0 and 4% acetonitrile/min were used.

Table 2
Resolution for peptide pairs in Figs. 2–6

Figure[a]	Peptide pair[a]	% Acetonitrile/min[b]	Resolution (R_s)[c]
2	L1/AY9	0.5	7.6
		1.8	0
		4	2.7
3	F1/AA9	0.77	0
		1	1.5
		4	6.1
4	L1/AL9	0.5	17.5
		2	7.2
		4	2.1
5	L1/F1	0.5	4.2
		1	3.5
		4	2.2
6	AF9/AL9	0.5	1.5
		1	1.2
		4	-

[a] Refers to Figs. 2–6 and the corresponding peptide pair separated under the given linear AB gradient conditions (see Experimental for conditions).
[b] % Acetonitrile used for the separation of the reported peptide pair in panels A, B and C, respectively (lowest to highest gradient rate) of Figs. 2–6.
[c] $R_s = 1.176\Delta t/(w_{h1} + w_{h2})$, where Δt is the difference in retention times for the two peaks and w_{h1} and w_{h2} are the widths at half height for each corresponding peak.

helical peptides, AF9 and AL9, exhibited a 1.25-fold change in resolution (1.2 to 1.5; Table 2) for a 2-fold (1%/min to 0.5%/min) decrease in gradient rate.

This is in clear contrast to the situation where changes in selectivity, due to conformational differences between non-helical and amphipathic helical peptides, result in large changes in resolution. For example, in Fig. 2 (right), a decreasing gradient rate results in a large improvement in resolution for the peptide pair L1/AY9; thus, from Table 2, the resolution of this pair increases from 0 to 7.6 for a 3.6-fold decrease in gradient rate (1.8%/min to 0.5% acetonitrile/min). Similarly, in Fig. 4 (right), the resolution of the peptide pair L1/AL9 increases 2.4-fold (7.2 to 17.5; Table 2) for a 4-fold (2%/min to 0.5%/min) decrease in gradient rate. Increasing gradient rates are also shown to improve resolution in Figs. 2 and 3, where an increase in resolution of the peptide pair L1/AY9 (Fig. 2) from 0 to 2.7 (Table 2) is observed for a 2.2-fold (1.8%/min to 4% acetonitrile/min) increase in gradient rate and a 4.1-fold increase in resolution (1.5 to 6.1) of the peptide pair F1/AA9 (Fig. 3) is observed for a 4-fold (1%/min to 4%/min) increase in gradient rate. In these cases, the observed distinct improvements in peptide resolution are likely due solely to changes in selectivity.

Table 3 reports the gradient steepness parameter (b) and median capacity factor ($\bar{k}$) values obtained for 17 analogues of both the non-helical (X1) and α-helical (AX9) series of peptides. The b or $\bar{k}$ within each series of peptides are similar and would exhibit similar plots of $\log \bar{k}$ vs. $\bar{\phi}$ as those shown in Fig. 5 (non-helical peptides) and Fig. 6 (α-helical peptides). This further suggests that within each series of peptides there would only be small changes in selectivity with changes in gradient rate for any mixtures of these peptides. In contrast, there would be a much larger change in resolution of peptides between the two

Table 3
Retention time, gradient steepness parameter and median capacity factor of non-helical and amphipathic α-helical peptides

Amino acid substitution[a]	Helical peptides				Non-helical peptides			
	t_{g1} (min)[b] (2%)	t_{g2} (min)[b] (1%)	b[c]	$\bar{k}$[c]	t_{g1} (min)[b] (2%)	t_{g2} (min)[b] (1%)	b[c]	$\bar{k}$[c]
Ile (I)	16.14	27.13	1.20	0.72	13.72	21.44	0.75	1.16
Leu (L)	16.09	27.20	1.36	0.64	14.08	22.19	0.76	1.14
Phe (F)	15.92	26.78	1.28	0.68	14.83	23.66	0.75	1.16
Trp (W)	15.56	26.23	1.47	0.59	15.24	24.43	0.73	1.18
Val (V)	15.07	25.40	1.69	0.52	12.43	18.91	0.77	1.13
Met (M)	14.88	24.96	1.59	0.55	12.87	19.83	0.78	1.11
Cys (C)	13.97	23.03	1.44	0.60	11.46	16.90	0.74	1.17
Tyr (Y)	13.97	23.20	1.69	0.52	12.70	19.41	0.75	1.15
Ala (A)	13.76	22.81	1.74	0.50	10.66	15.69	0.90	0.97
Thr (T)	12.32	20.00	1.87	0.46	10.52	15.53	0.96	0.91
Glu (E)	12.13	19.77	2.24	0.39	10.73	15.62	0.81	1.08
Gly (G)	11.66	18.77	2.08	0.42	10.27	14.73	0.82	1.06
Ser (S)	11.51	18.36	1.83	0.47	10.12	14.66	0.92	0.94
Asp (D)	11.17	17.67	1.81	0.48	10.43	14.92	0.77	1.13
Gln (Q)	11.17	17.71	1.89	0.46	10.23	14.81	0.89	0.98
Asn (N)	10.14	15.66	1.91	0.45	10.06	14.49	0.90	0.97
Pro (P)	9.94	15.10	1.62	0.54	12.06	18.18	0.77	1.13

[a] Three letter and single letter code represents the amino acid substituted in position 9 of the helical peptide (AX9) or position 1 of the non-helical peptide (X1).
[b] Values between parentheses represent gradient rates. For run conditions, see Experimental.
[c] The gradient steepness parameter, b, and the median capacity factor, $\bar{k}$, are calculated as described by Snyder and Stadalius [20] (see Experimental). For a gradient rate of 2% acetonitrile/min, $t_G = 25$ min; for 1% acetonitrile/min, $t_G = 50$ min.

peptide groups with varying gradient rate due to the large inter-series selectivity differences.

5. Conclusions

In this report we have illustrated the use of two series of synthetic model peptides (non-helical or amphipathic α-helical) in order to demonstrate the selectivity that may be obtained in a reversed-phase separation based on conformational differences between the peptides. Peptides within a series, i.e., non-helical or amphipathic α-helical, exhibit very similar plots of $\log \bar{k}$ versus $\bar{\phi}$ (and, therefore, similar S values), with only small consequent changes in selectivity with changing gradient rate; whereas, peptide mixtures containing peptides from both series of peptides and, hence, containing peptides with large differences in S values, show a correspondingly greater change in separation selectivity with a gradient rate variation. These results are directly applicable to optimizing the separation of mixtures of peptides.

Acknowledgements

This work was supported by the Medical Research Council of Canada Group in Protein Structure and Function and by the Protein Engineering Network of Centres of Excellence program supported by the Government of Canada. We thank Paul Semchuck for synthes-

izing the peptides used in this study and Lorne Burke for technical assistance.

References

[1] C.T. Mant and R.S. Hodges (Editors), *High Performance Liquid Chromatography of Peptides and Proteins: Separation, Analysis and Conformation*, CRC Press, Boca Raton, FL, 1991.

[2] J.W. Dolan and L.R. Snyder, *LC·GC*, 5 (1987) 970.

[3] R.S. Hodges, J.M.R. Parker, C.T. Mant and R.R. Sharma, *J. Chromatogr.*, 458 (1988) 147.

[4] J.L. Glajch and L.R. Snyder (Editors), *Computer-Assisted Method Development for High-Performance Liquid Chromatography*, Elsevier, Amsterdam, 1990.

[5] N. Lundell, *J. Chromatogr.*, 639 (1993) 97.

[6] N. Lundell and K. Markides, *J. Chromatogr.*, 639 (1993) 117.

[7] D. Guo, C.T. Mant, A.K. Taneja, J.M.R. Parker and R.S. Hodges, *J. Chromatogr.*, 359 (1986) 499.

[8] C.T. Mant, T.W.L. Burke, J.A. Black and R.S. Hodges, *J. Chromatogr.*, 458 (1988) 193.

[9] N.E. Zhou, C.T. Mant and R.S. Hodges, *Pept. Res.*, 3 (1990) 8.

[10] D. Guo, C.T. Mant and R.S. Hodges, *J. Chromatogr.*, 386 (1987) 205.

[11] C.T. Mant, T.W.L. Burke, and R.S. Hodges, *LC·GC*, 12 (1994) 396.

[12] C.T. Mant, T.W.L. Burke, N.E. Zhou, J.M.R. Parker and R.S. Hodges, *J. Chromatogr.*, 485 (1989) 365.

[13] J.L. Meek and Z.L. Rossetti, *J. Chromatogr.*, 211 (1981) 15.

[14] J.L. Glajch, M.A. Quarry, J.F. Vasta and L.R. Snyder, *Anal. Chem.*, 58 (1986) 280.

[15] M.T.W. Hearn, M.I. Aguilar, C.T. Mant and R.S. Hodges, *J. Chromatogr.*, 438 (1988) 197.

[16] B.F.D. Ghrist and L.R. Snyder, *J. Chromatogr.*, 459 (1988) 25.

[17] T. Molnar, R. Boysen and P. Jekow, in J.L. Glajch and L.R. Snyder (Editors), *Computer-Assisted Method Development for High Performance Liquid Chromatography*, Elsevier, Amsterdam, 1990, p. 569.

[18] M.I. Aguilar, S. Mougos, J. Boublik, J. Rivier and M.T.W. Hearn, *J. Chromatogr.*, 646 (1993) 53.

[19] L.R. Snyder, in Cs. Horváth (Editor), *High Performance Liquid Chromatography: Advances and Perspectives*, Vol. 1, Academic Press, New York, NY, 1980, p. 207.

[20] L.R. Snyder and M.A. Stadalius, in Cs. Horváth (Editor), *High Performance Liquid Chromatography: Advances and Perspectives*, Vol. 4, Academic Press, New York, NY, 1986, p. 195.

[21] P. Jandera and J. Churácek, *Gradient Elution in Column Liquid Chromatography, Theory and Practice*, Elsevier, Amsterdam, 1985.

[22] M.T.W. Hearn and M.I. Aguilar, *J. Chromatogr.*, 359 (1986) 31.

[23] M.T.W. Hearn, in C.T. Mant and R.S. Hodges (Editors), *High Performance Liquid Chromatography of Peptides and Proteins: Separation, Analysis and Conformation*, CRC Press, Boca Raton, FL, 1991, p. 105.

[24] J.W. Dolan, D.C. Lommen and L.R. Snyder, *J. Chromatogr.*, 485 (1989) 91.

[25] Z. Iskandarini and D.J. Pietrzyk, *Anal. Chem.*, 53 (1981) 489.

[26] R.A. Houghten and S.T. DeGraw, *J. Chromatogr.*, 386 (1987) 489.

[27] M.L. Heinitz, E. Flanigan, R.C. Orlowski and F.E. Regnier, *J. Chromatogr.*, 443 (1988) 229.

[28] W.G. Burton, K.D. Nugent, T.K. Slattery, B.R. Summers and L.R. Snyder, *J. Chromatogr.*, 443 (1988) 363.

[29] K.D. Nugent, W.G. Burton, T.K. Slattery, B.F. Johnson and L.R. Snyder, *J. Chromatogr.*, 443 (1988) 381.

[30] D. Guo, C.T. Mant, A.K. Taneja and R.S. Hodges, *J. Chromatogr.*, 359 (1986) 519.

[31] N.E. Zhou, C.T. Mant, J.J. Kirkland and R.S. Hodges, *J. Chromatogr.*, 548 (1991) 179.

[32] C.T. Mant and R.S. Hodges, in B.L. Karger and W.S. Hancock (Editor), *High Resolution Separation of Biological Macromolecules, Methods in Enzymology*, Academic Press, FL, in press.

[33] T.J. Sereda, C.T. Mant, A.M. Quinn and R.S. Hodges, *J. Chromatogr.*, 646 (1993) 17.

[34] J.W. Nelson and N.R. Kallenbach, *Proteins: Structure, Function and Genetics*, 1 (1986) 211.

[35] J.W. Nelson and N.R. Kallenbach, *Biochemistry*, 28 (1989) 5256.

[36] C.T. Mant and R.S. Hodges, in C.T. Mant and R.S. Hodges (Editors), *HPLC of Peptides and Proteins: Separation, Analysis and Conformation*, CRC Press, Boca Raton, FL, 1991, p. 69.

[37] A.W. Purcell, M.I. Aguilar and M.T.W. Hearn, *J. Chromatogr.*, 476 (1989) 113.

[38] A.W. Purcell, M.I. Aguilar and M.T.W. Hearn, *J. Chromatogr.*, 592 (1992) 103.

[39] M.I. Aguilar, A.N. Hodder and M.T.W. Hearn, *J. Chromatogr.*, 327 (1985) 115.

[40] M.T.W. Hearn and M.I. Aguilar, *J. Chromatogr.*, 392 (1987) 33.

[41] N.E. Zhou, C.M. Kay, B.D. Sykes and R.S. Hodges, *Biochemistry*, 32 (1993) 6190.

[42] N.E. Zhou, O.D. Monera, C.M. Kay and R.S. Hodges, *Protein Peptide Lett.*, in press.

[43] S.R. Lehrman, J.L. Tuls and M. Lund, *Biochemistry*, 29 (1990) 5590.

[44] F. Sönnichsen, J.E. Van Eyk, R.S. Hodges and B.D. Sykes, *Biochemistry*, 31 (1992) 8790.

[45] M. Zhang, T. Yuan and H.J. Vogel, *Protein Science*, 2 (1993) 1931.

[46] Y.-H. Chen, J.T. Yang and H.M. Martinez, *Biochemistry*, 11 (1972) 4120.

[47] N.E. Zhou, C.M. Kay and R.S. Hodges, *J. Mol. Biol.*, 237 (1994) 500.

[48] T.M. Cooper and R.W. Woody, *Biopolymers*, 30 (1990) 657.
[49] S.Y.M. Lau, A.K. Taneja and R.S. Hodges, *J. Chromatogr.*, 317 (1984) 129.
[50] V. Steiner, M. Schär, K.O. Börnsen and M. Mutter, *J. Chromatogr.*, 586 (1991) 43.
[51] D. Eisenberg, E. Schwartz, M. Komaromy and R. Wall, *J. Mol. Biol.*, 179 (1984) 125.
[52] D. Eisenberg, R.M. Weiss and T.C. Terwilliger, *Nature*, 299 (1986) 371.

ELSEVIER

Journal of Chromatography A, 695 (1995) 223–228

JOURNAL OF CHROMATOGRAPHY A

Rapid assay of fatty acid composition using a portable high-performance liquid chromatograph for monitoring aquatic ecosystems☆

N.N. Sushchik*, M.I. Gladyshev, G.S. Kalachova, V.E. Guseynova

Institute of Biophysics/Siberian Branch of Russian Academy of Sciences, Akademgorodok, Krasnoyarsk 660036, Russian Federation

First received 10 May 1994; revised manuscript received 15 August 1994; accepted 9 November 1994

Abstract

The chromatographic conditions presented allowed the separation of the nitrophenacyl derivatives of standards of eleven free fatty acids (FFA) using a portable high-performance chromatograph, suitable for use aboard a research vessel. A statistically significant linear correlation between UV absorbance and amount of the analytes injected was obtained. The method was tested on FFA from algae cultural media. The method can be used for the ecological monitoring of natural waters.

1. Introduction

The composition of fatty acids in living organisms is known to be a very informative parameter. Recently, the extracellular free fatty acid (FFA) composition of natural waters was also demonstrated to be important for ecological surveys [1,2]. As shown, decoding the FFA composition provides an opportunity to determine the occurrence of limiting of phytoplankton growth and the phase of its seasonal dynamics, the potential kinetics of the ecosystem self-purification, etc. Moreover, the surface film of water (upper microlayer, ca. 50–100 μm) proved to be one of the most informative sampling sites, because the surface-active FFA exuded by organisms inhabiting the whole water column accumulate in this film owing to flotation and adsorption at the air–water interface. Thus, the surface film is a natural integrator of information on the whole aquatic ecosystem.

To obtain this information on the state of the ecosystem during ecological monitoring of extended natural water bodies, one needs to determine the FFA composition in water samples just after they have been taken, i.e., aboard a research vessel. Thus, two demands can be placed on a method for the determination of the FFA composition. First, it should be a micromethod, because the surface film samples are usually of small volume. Second, the chromatographic equipment should be suitable for operating under field conditions. Standard conventional methods of gas chromatography can hardly be

* Corresponding author.

☆ Presented at the *18th International Symposium on Column Liquid Chromatography, Minneapolis, 8–13 May 1994.*

0021-9673/95/$09.50
SSDI 0021-9673(94)01090-0

used in this environment, whereas a portable high-performance liquid chromatograph can be operated successfully, especially if it is suitable for narrow-bore columns. The determination of fatty acids by HPLC has recently been reported [3–6]. The aim of this work was to develop the method for the determination of FFA using a portable high-performance liquid chromatograph, suitable of use aboard a research vessel.

2. Experimental

2.1. Reagents and chemicals

Acids C10:0, C12:0, C14:0, C14:1 and C-iso-18:0 were purchased from Sigma (St. Louis, MO, USA) and C18:1, C18:2, C17:0, C16:0 and C18:0 from Merck (Darmstadt, Germany). *P*-Nitrophenacyl bromide and N,N-diisopropylethylamine were purchased from Aldrich (Milwaukee, WI, USA). Acetonitrile, ethanol and dimethylformamide (Reakhim, Angarsk, Russian Federation) were distilled before use. Water used for preparing eluents was doubly distilled. Mixtures of solvents used as the eluents were degassed under vacuum.

2.2. Preparation of fatty acid derivatives

Derivatization was carried out according Smith and Thompson [7] with some modifications. Briefly, a fresh solution containing 20 μmol of *p*-nitrophenacyl bromide and 40 μmol of diisopropylethylamine per 1 ml of dimethylformamide was added to dried FFA. The volume of the solution added depended on the approximate amount of FFA and ranged from 10 to 500 μl. FFA from the medium of a laboratory culture of the blue-green alga *Spirulina platensis* were extracted as described previously [2]. Briefly, lipids were extracted with chloroform and separated by TLC and FFA were eluted from silica gel with diethyl ether.

The reaction vial was closed and heated at 65°C for 15 min. After the reaction was completed, dimethylformamide was removed by rotary evaporation. This removal was applied because dimethylformamide had considerable absorbance at the wavelength used for FFA detection. Then the fatty acid derivatives were dissolved in a small volume of ethanol ranging from 50 to 1000 μl. Aliquots of the solution were injected directly into the chromatograph.

2.3. HPLC and GC analysis

Analyses were carried out using a Milikhrom-1 portable high-performance liquid chromatograph (Nauchpribor, Oriol, Russian Federation). The chromatograph was equipped with a 2600-μl syringe pump with flow-rate capabilities from 2 to 600 μl/min. The operating pressure was up to 5 MPa. The volumes injected ranged from 5 to 20 μl. The variable-wavelength UV detector monitored the absorbance from 190 to 360 nm. The absorbance range of the detector was from 0.05 to 12.8 AUFS. The detector was a single-beam instrument with a vibrating mirror that deflected the light beam passing through the sample and reference flow cells. The time constant was selectable in the range 0.15–20 s. The unique optical design of the detector allowed its successful operation under field conditions. Both flow cells (1.5 μl) had 1.5-mm light paths. The reference cell was filled with ethanol. The values measured were normalized by the electronics to the equivalent absorbance with a 10-mm light path and presented as an analogue output on the recorder. The accuracy of absorbance measurements was stated by the manufacturer to be 3%.

The derivatives were separated with a Separon C_{18} column (64 × 2 mm I.D., particle size 5 μm) (Nauchpribor) using step-gradient elution at a flow-rate of 50 μl/min. The gradient elution system consisted of following discrete steps: acetonitrile–water (70:30) and ethanol–water (82:18, 83:17, 84:16, 84.5:15.5 and 85:15, v/v). Each step was equal to 300 μl. The overall time of the chromatography did not exceed 45 min (including a reconditioning step). If necessary, the elution could be interrupted and a quasi-smooth spectrum could be registered with a wavelength increment of 2 nm.

The FFA composition of the oil of the berry of sea buckthorn (*Hippophae rhamnoides*) was studied by GC. For this purpose, methyl esters of FFA (FAME) were prepared. A detailed description of the preparation of FAME and GC was published previously [1]. Briefly, FAME were analysed using a Chrom-5 gas chromatograph (Laboratórní Přístroje, Prague, Czech Republic) with a glass column (3 m × 3 mm I.D.). Helium was used as the carrier gas and polyethylene glycol adipate on Celite 545 as the stationary phase. The column temperature was maintained at 170°C and a flame ionization detector was used.

2.4. Quantitative measurements

An ethanol solution containing 1 mg/ml each of myristic acid, oleic acid and of stearic acid was prepared. Then ten samples containing 50, 100, 150, 200, 250, 300, 350, 400, 450 and 500 μg of each acid were prepared and subjected to the derivatization procedure. After the reaction was completed and dimethylformamide had been removed, each sample was dissolved in 3 ml of ethanol and aliquots of 10 μl were chromatographed.

The areas of the peaks in the chromatograms were calculated by multiplying the heights of the peaks by the widths at half-height. The areas of the peaks was preferred to the heights because widths of the peaks of different fatty acids were not the same. The dependence of the peak area on the amount injected was fitted by linear least-squares for each fatty acid. The standard errors (SE) of the linear fits were calculated as follows:

$$SE_{yx} = s_y \sqrt{1 - r^2}$$

where s_y is the standard deviation of y (area) values and r is the correlation coefficient [8]. The precision of the method was estimated as the relative standard deviation (s_r):

$$S_r(\%) = SE_{yx}/M \cdot 100$$

where M is the mean of the y values.

3. Results and discussion

In order to determine the optimum wavelength of detection, the absorption spectra the derivatives of some fatty acids were recorded. The absorption spectrum of the derivative of palmitic acid is presented in Fig. 1; the spectra of the derivatives of the other fatty acids were similar. The length of the carbon chain and the number of double bonds for the different fatty acids did not affect the pattern of the spectrum. Therefore, the wavelength of maximum absorption (230 nm) was chosen for detection.

The fatty acids that were found to dominate in natural waters (saturated, monoenic, some dienic and branched acids) were taken as standards for the development of the separation procedure. Initially, for the separation of the FFA derivatives an isocratic mobile phase was used containing ethanol–acetonitrile–water (82:9:9, v/v/v) according to Smith and Thompson [7]. However, under these conditions most of the acids

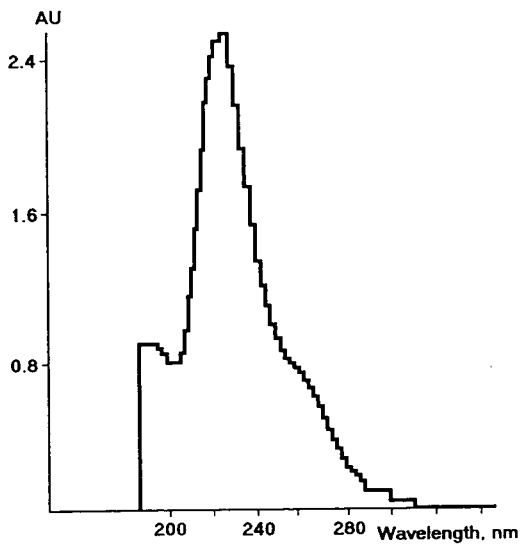

Fig. 1. Quasi-smooth spectrum of UV absorbance of nitrophenacyl derivative of palmitic acid obtained with the spectrophotometric detector of the portable HPLC equipment used in the stopped-flow mode. Amount injected, 1.48 nmol; volume injected, is 5 μl.

did not separate and the peaks emerged as wide and asymmetric bands. Much better resolution was obtained using gradient elution with ethanol–water mixtures, but palmitic and oleic acids were not resolved. The described six-step gradient (see Experimental) allowed a satisfactory resolution of this critical pair. Fig. 2 shows a chromatogram of the derivatives of eleven standard FFA separated with this elution system.

An essential factor in the separation was the acetonitrile–water step before the ethanol–water gradient. Acetonitrile and ethanol are known to have almost equal eluent strengths, but they show different selectivities because of the different types of molecular interactions between the solvents, stationary phase and analytes [9]. Hence it is possible that the successive effects of the solvents with two different selectivities played a key role in this critical separation.

For quantitative purposes the linearity of the method was investigated in the range 0.5–7.5 nmol each of myristic, oleic and stearic acids.

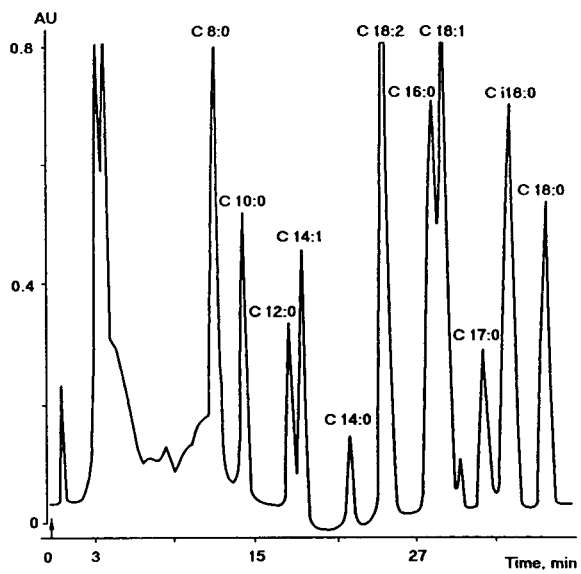

Fig. 2. Chromatogram of nitrophenacyl derivatives of standards of eleven fatty acids separated by gradient elution: acetonitrile–water (70:30, v/v) 6 min; ethanol–water (82:18, v/v) 6 min; (83:17, v/v) 6 min; (84:16, v/v) 6 min; (84.5:15.5, v/v) 6 min; (85:15 v/v) 6 min. Flow-rate, 50 μl/min; UV detection at 230 nm. The total amount of fatty acids injected, ca. 3 nmol; volume injected, 10 μl.

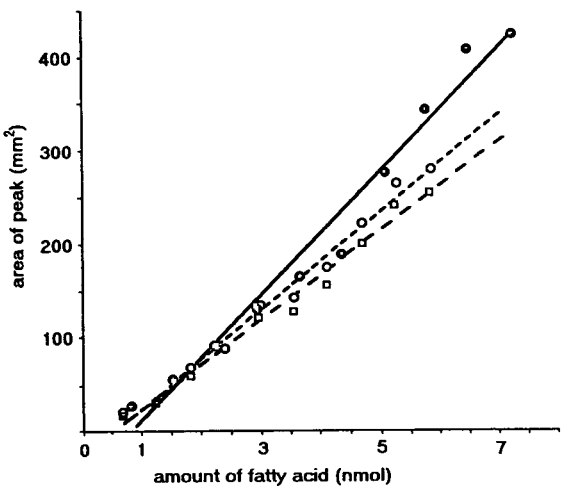

Fig. 3. Relationships between amounts of fatty acids injected and areas of the peaks in the chromatograms. Straight lines are linear least-squares fits. For coefficients of the fits, see Table 1. ● = C14:0; ○ = C18:1; □ = C18:0.

The relationships between amounts of fatty acids injected and the peaks areas in the chromatograms are shown in Fig. 3. As can be seen, the relationships between amount of fatty acid and peak area for the given ranges were satisfactorily linear, as was confirmed by the linear least-squares fits, which provided statistically significant coefficients (Table 1).

There were statistically significant differences between the values of the angle coefficients α for the pairs of acids C14:0–C18:1 (Student's test, $t = 3.17$) and C14:0–C18:0 ($t = 4.32$), whereas for the pair C18:1–C18:0 there was no significant difference ($t = 1.64$). Hence the length of the carbon chain of the acids may be of importance with regard to the absorption coefficients of the derivatives rather than the presence of double bonds. Differences in the slopes could result in inaccurate determination of the different acids if a single standard is used. However, as can be seen from Fig. 3, this inaccuracy would be negligible if the amount injected did not exceed 5 nmol of each fatty acid. Hence, for accurate determinations when a single standard is used, one should carry out measurements within this range of amounts. The relative standard deviations for the linear fits are given in Table 1.

Table 1
Calibration coefficients of linear equations $y = ax + b$, extracted by least-squares fit, where x is amount of FFA injected (nmol), y is area of peak of FFA in chromatograms (mm^2)

Acid	$a \pm SE$	t_a	$b \pm SE$	t_b	$M \pm SE_{yx}$	R.S.D. (%)
C14:0	63.7 ± 3.63	17.5	−47.9 ± 16.5	2.9	208.3 ± 22.7	10.9
C18:1	50.5 ± 2.03	24.9	−23.1 ± 7.4	3.1	141.0 ± 10.3	7.3
C18:0	46.0 ± 1.94	23.8	−19.7 ± 7.1	2.7	128.6 ± 9.8	7.6

SE = standard error; t = Student's t-value (degrees of freedom = 8); M = mean of y values; SE_{yx} = standard error for linear fits; R.S.D. = relative standard deviation ($n = 10$).

3.1. Application

The method was tested using the oil of the berry of sea buckthorn (*Hippophae rhamnoides*), which was chosen because its fatty acid composition is well known and fairly simple. The GC analysis of the FAME of the same sample was carried out simultaneously. Relative contents (percentage of the total FFA) of the acids obtained with HPLC and GC are presented in Table 2. These data were used for the identification of C18:3, C16:1 and C16:2 fatty acids. Although the relative contents of the fatty acids obtained with HPLC and GC were not identical (Table 2), the small number of acids (seven) in the sample and the regular sequence of their elution allowed their identification.

The compositions and concentrations of FFA in the medium for laboratory cultures of algae were demonstrated to be comparable to those of natural waters [2]. Thus, the medium of the laboratory culture of the blue-green alga *Spirulina platensis* was used for testing the method. Fig. 4 shows a typical chromatogram of FFA

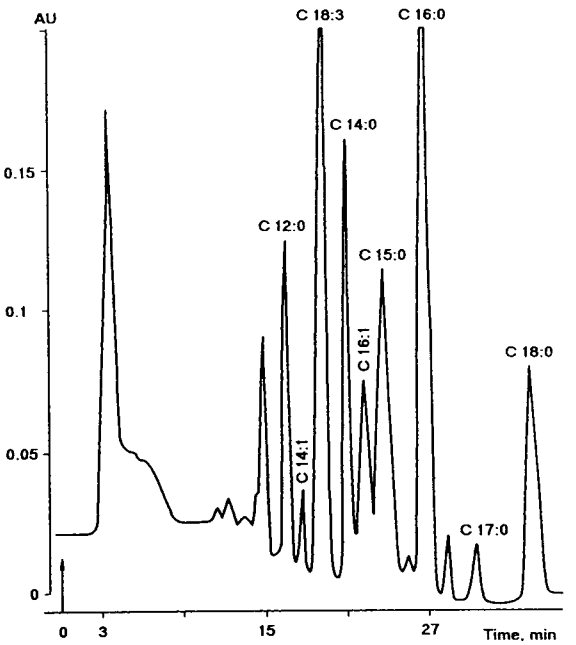

Fig. 4. Chromatogram of nitrophenacyl derivatives of FFA obtained from the medium of the laboratory culture of the blue-green alga *Spirulina platensis*. Chromatographic conditions as in Fig. 2.

Table 2
Relative contents of fatty acids (percentage of total) in the oil of the berry of sea buckthorn (*Hippophae rhamnoides*) obtained by HPLC and GC (data for a single measurement)

Method	Acid						
	16:0	16:1	16:2	18:0	18:1	18:2	18:3
HPLC	15.5	14.7	1.6	2.2	15.7	27.0	22.9
GC	13.8	9.8	0.5	2.1	14.5	32.2	27.0

obtained. The amount of FFA injected into the chromatograph was of the order of several picomoles.

4. Conclusions

A method for the determination of fatty acids was developed for a Milikhrom portable high-performance liquid chromatograph which is suitable for operating under field conditions. The gradient used allowed the separation of fourteen species of fatty acids including the critical pair C16:0–C18:1. Under the conditions adopted the retention time of the fatty acids derivatives decreased with decrease in the length of the carbon chain and with increase in the degree of unsaturation. Regularities in the elution obtained for the standards of fatty acids were successfully used for the identification of the fatty acids in natural samples. The method can be applied for both qualitative and quantitative measurements of FFA. For carrying out quantitative measurements the amount injected should not exceed 5 nmol for each fatty acid. Quantitative analyses need further thorough elaboration using diverse FFA species. The method can be used for ecological monitoring of natural waters.

Acknowledgement

This work was supported by grant No. 2F0073 of the Krasnoyarsk Regional Science Foundation (Siberia, Russian Federation).

References

[1] M.I. Gladyshev, G.S. Kalachova and N.N. Sushchik, *Int. Rev. Gesam. Hydrobiol.*, 78 (1993) 575.
[2] M.I. Gladyshev, N.N. Sushchik and G.S. Kalachova, *Dokl. Akad. Nauk* 329 (1993) 521.
[3] M. Tevini and D. Steinmuller, in A. Hensen, K.-P. Hupe, F. Lottspeich and W. Voelter (Editors), *High Performance Liquid Chromatography in Biochemistry*, VCH, Weinheim, 1985, Ch. 7, p. 383.
[4] J.D. Baty, R.G. Willis and R. Tavendale, *J. Chromatogr.*, 353 (1986) 319.
[5] H. Miwa and M. Yamamoto, *J. Chromatogr.*, 351 (1986) 275.
[6] W.W. Christie and K. Stefanov, *J. Chromatogr.*, 392 (1987) 259.
[7] L.A. Smith and J. Thompson, in H.F. Linskens and J.F. Jackson (Editors), *High-Performance Liquid Chromatography in Plant Science*, Springer, Berlin, 1987, p. 149.
[8] G.N. Zaytsev, *Statistics in Experimental Botany*, Nauka, Moscow, 1984 (in Russian).
[9] L.P. Snyder, *J. Chromatogr. Sci.*, 16 (1978) 223.

ELSEVIER

Journal of Chromatography A, 695 (1995) 229–235

JOURNAL OF CHROMATOGRAPHY A

Determination of phenolic acids in wine by high-performance liquid chromatography with a microbore column

Francesca Buiarelli, Giampaolo Cartoni*, Franco Coccioli, Zinovia Levetsovitou

Dipartimento di Chimica, Università "La Sapienza" di Roma, Piazzale Aldo Moro 5, 00185 Rome, Italy

First received 28 July 1994; revised manuscript received 25 October, 1994; accepted 25 October 1994

Abstract

A method for the extraction and separation of the non-volatile phenolic acids of wine is described. The extracts are analysed by HPLC with a microbore column and UV detection. The free phenolic acids and depsides in different wine samples were identified and determined.

1. Introduction

In a previous study [1], free phenolic acids in wine were separated and identified by HPLC after solid-phase extraction. Some compounds with retention times near those of phenolic acids were still present. In this work, an improved purification method was developed to obtain a better separation of the non-volatile phenolic compounds of wine. The fractions obtained were analysed by HPLC, using a microbore column (250 mm × 1.1 mm I.D.) and a rapid-scanning UV detector with a data system, for the identification of the characteristic peaks. The free phenolic acids were determined. The identities of the hydroxycinnamic acid–tartaric acid esters or depsides (esters of tartaric acid with cinnamic, caffeic, ferulic and *p*-coumaric acid) [2–4] were established through alkaline hydrolysis of the esters followed by HPLC of the free phenolic acids of the hydrolysate.

* Corresponding author.

2. Experimental

2.1. Apparatus

Two Phoenix 20 (Fisons) syringe pumps (master and slave) were interfaced to an external computer (IBM) for remote control operations. A rapid-scanning UV–Vis detector (Micro UVIS 20) was used. The injection valve was a Rheodyne Model 7520 with a 1.0-μl sample loop. The columns (250 mm × 1.1 mm I.D. and 500 mm × 1.1 mm I.D.) were slurry-packed in the laboratory with Spherisorb ODS_2 (5 μm) obtained from Phase Separations (Norwalk, CT, USA) [5].

2.2. Reagents

Distilled water was stored in glass, filtered and passed through a Norganic system cartridge (Millipore, Bedford, MA, USA).

The solvents methanol (HPLC grade), phosphoric acid and diethyl ether (RPE) (peroxides were eliminated by filtration through a CN

0021-9673/95/$09.50
SSDI 0021-9673(94)01046-3

disposable extraction column) were obtained from Carlo Erba (Milan, Italy). Polyethylene glycol 20 000 (PEG) and phenolic acids were purchased from Fluka (Buchs, Switzerland). All the cinnamic acids were in the *trans* form.

Phosphate buffer (pH 2.4) was prepared by adding 1.15 g of ammonium dihydrogenphosphate to 0.2 ml of phosphoric acid and diluting to 1 l with distilled water. The pH was monitored and more phosphoric acid was added if needed. This stock solution was filtered through a 0.45-μm Millipore filter and stored at 4°C. A 70.23-g amount of sodium perchlorate was added to this buffer solution. Phosphate buffer (pH 8.0) was prepared by mixing 47.5 ml of 0.1 *M* Na_2HPO_4 and 2.5 ml of 0.1 *M* KH_2PO_4. This stock solution was then filtered through a 0.45-μm Millipore filter and stored at 4°C.

A 3-ml Sep-Pak C_{18} cartridge was obtained from Waters (Milford, MA, USA) and a Bakerbond (quaternary amine) and a 3-ml CN cartridge from J.T. Baker (Phillipsburg, NJ, USA). The Sep-Pak C_{18} and CN cartridges were washed with methanol and stored in methanol and the Bakerbond cartridge with 1–2 column volumes of methanol, water, 0.1 *M* HCl and water.

2.3. Standards

A 2-mg amount of gallic acid (**1**) and 1 mg of 3,4-dihydroxybenzoic acid (**2**), vanillic acid (**3**), caffeic acid (**4**), syringic acid (**5**), *p*-coumaric acid (**6**) and ferulic acid (**7**) were each dissolved in 1 ml of methanol. The following amounts of the acids were transferred into a screw-capped vial and diluted to 900 μl with methanol: **1** 15, **2** 100, **3** 25, **4** 20, **5** 20, **6** 15 and **7** 25 μl. These solutions were stored at −20°C in the dark for no longer than 2 months.

2.4. Preparation of wine samples

After evaporation of the alcohol under vacuum below 30°C, to 1 ml of red or 2 ml of white wine was added a solution of phosphate buffer (pH 8) (1.0 ml for red and 1.5 ml for white wine). This solution was extracted with 3 × 1.5 ml of diethyl ether and the extracts were collected, dried over anhydrous sodium sulphate and evaporated under nitrogen (below 30°C in the dark). The residue was dissolved in 50 μl of methanol (alkaline extract). The remaining solution of wine was acidified with 6 *M* HCl to about pH 1.0. This solution was extracted with 3 × 1.5 ml of diethyl ether saturated with PEG [6]. The extract, dried over anhydrous sodium sulphate, was divided into two parts and evaporated under nitrogen. One residue sample was dissolved in 50 μl of methanol (acid extract); the second residue was dissolved in 2 ml of water and passed through the strong anion-exchange cartridge. The trapped compounds were washed with water and eluted with 14 ml of phosphate buffer (pH 2.4)–sodium perchlorate. This solution was passed through a Sep-Pak C_{18} cartridge. The acidic compounds were recovered by elution with 2 ml of methanol. The solution was dried and evaporated as above and the residue was dissolved in 50 μl of methanol (anionic extract). These extraction procedures are outlined in Fig. 1.

The solutions were stored in 1-ml screw-

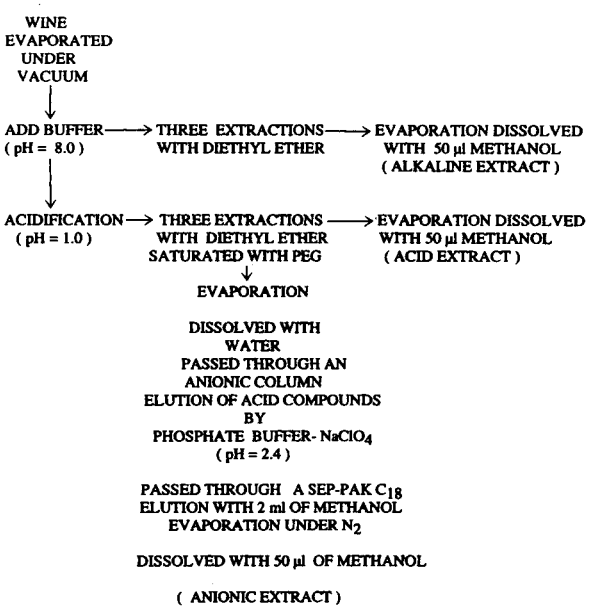

Fig. 1. Sample treatment for extraction of non-volatile compounds from wine.

Table 1
Recovery of standard acids added to 1 ml of red wine (mean of seven determinations)

No.	Acid	Recovery (%)	R.S.D. (%)
1	Gallic	75.6	3.5
2	3-4-Dihydroxy-benzoic	88.6	11.5
3	Vanillic	83.1	9.0
4	Syringic	85.3	10.2
5	Caffeic	85.1	8.9
7	*p*-Coumaric	84.1	9.6
8	Ferulic	80.4	8.5

capped vials (conical bottom) at −20°C in a freezer.

2.5. Hydrolysis of depsides

To 2-ml wine samples were added 2 ml of 2 *M* NaOH solution after evaporation of ethanol as described. The mixture was allowed to stand at room temperature, in the dark, for 48 h under nitrogen [2,7]. The alkaline solution was acidified to pH 1.0 and the free phenolic acids were extracted as described for the acid extract.

2.6. Recoveries

The recoveries were measured as outlined in Fig. 1 for acid extracts. Six samples of Corvo red wine and six of the same wine with 250 μl of the standard mixture added, were analysed (Table 1).

3. Results and discussion

Fig. 2 shows the chromatogram of cinnamic and benzoic acid standards. At 280 nm, all seven peaks are detected, whereas at 320 nm, only the peaks of caffeic, *p*-coumaric and ferulic acids are detected. In nature the cinnamic acids are present as *trans* isomers, but on exposure to UV radiation or daylight there is a gradual formation of *cis* isomers [8]. Figs. 3 and 4 show the chromatograms of the acids extracted from red and white wine, respectively, with detection at

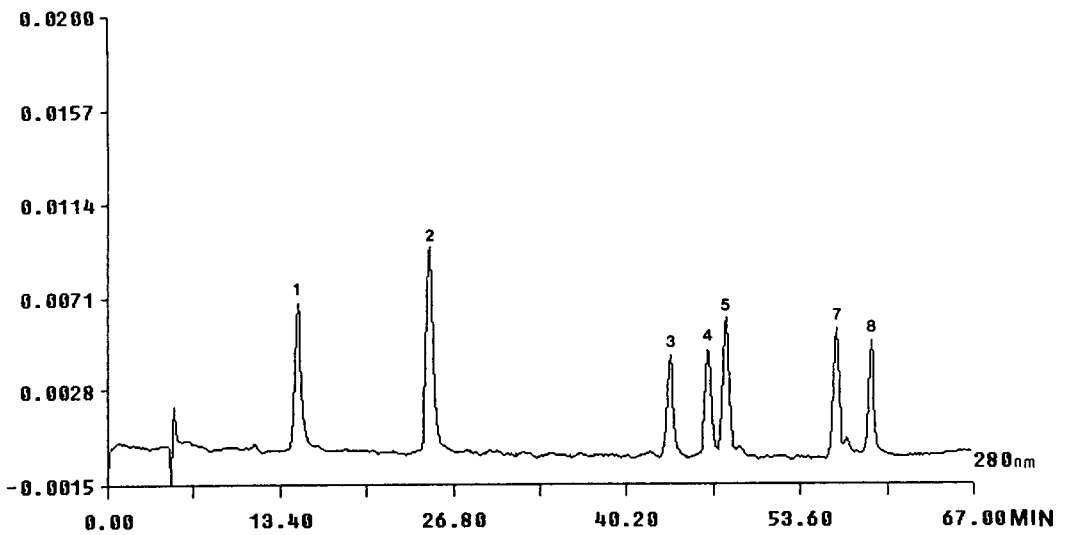

Fig. 2. Chromatogram of standard mixture (1 μl) detected at 280 nm. Peaks: 1 = gallic acid; 2 = 3,4-dihydroxybenzoic acid; 3 = vanillic acid; 4 = caffeic acid; 5 = syringic acid; 7 = *trans*-*p*-coumaric acid; 8 = ferulic acid. Column, ODS_2 (250 mm × 1.1 mm I.D.); flow-rate, 40 μl/min; mobile phase, A–methanol–phosphate buffer (pH 2.4) (95:5), B = phosphate buffer (pH 2.4)–distilled water (5:95), with the gradient 0 min, 100%B; 67 min, 56A%; 70 min, 100%A.

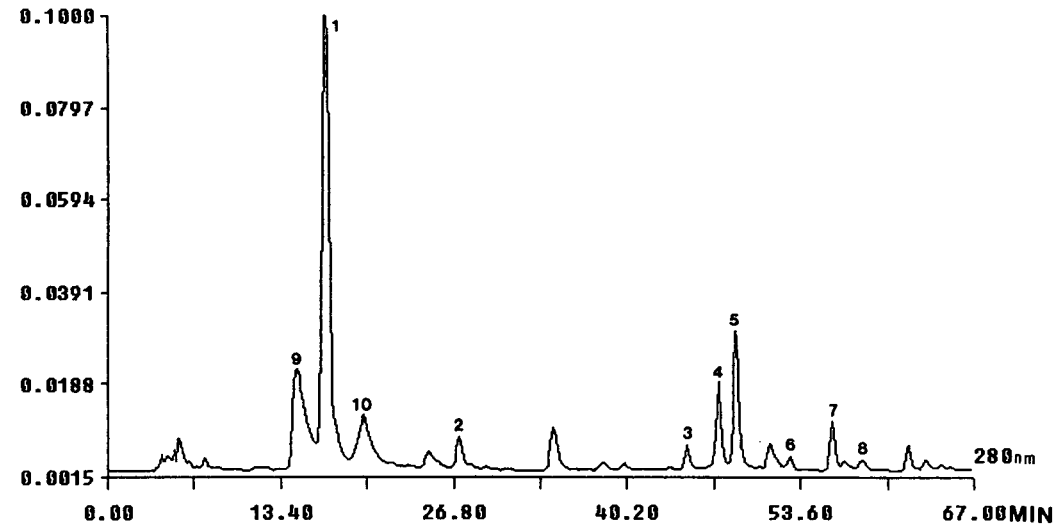

Fig. 3. Chromatogram of Corvo red wine (acid extract). Peaks as in Fig. 2; 6 = *cis*-*p*-coumaric acid; 9 = depside of caffeic acid; 10 = depside of *p*-coumaric or ferulic acid.

280 nm. Peak 9 (Fig. 3) is the depside of caffeic acid (**9**) whereas peak 10 is the *p*-coumaric or ferulic depside that also absorbs at 350 nm.

The second purification step (anionic extract) (Fig. 5) was carried out only as a confirmatory test. Here the acids are better separated from the impurities and the depsides are not present. Some different solvents were tested and the best recoveries were obtained with diethyl ether (peroxide free) saturated with PEG.

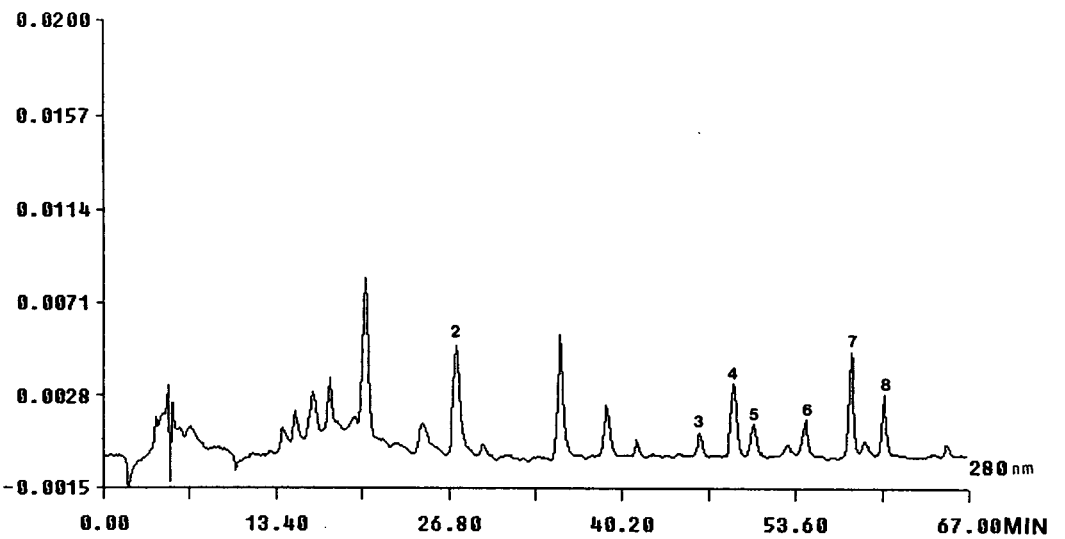

Fig. 4. Chromatogram of Corvo white wine (acid extract). Peaks as in Fig. 2.

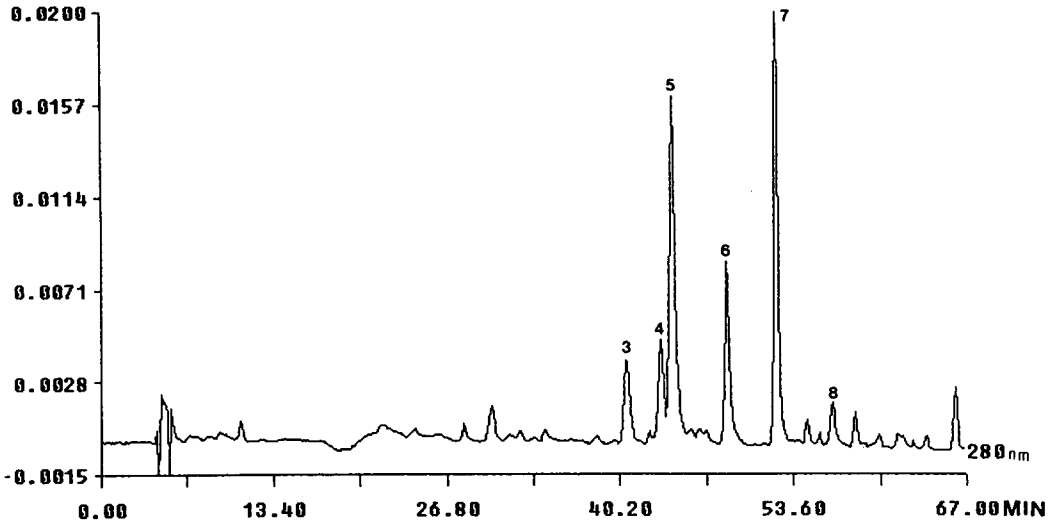

Fig. 5. Chromatograms of anionic extract of Corvo red wine detected at 280 nm. Peaks and conditions as in Fig. 1.

Recoveries at different pH (8–10) were also investigated by adding 2 ml of distilled water to 50 μl of phenolic acids solution and treating the samples as illustrated in Fig. 1 (acid extract). At pH 10, *trans*-caffeic acid is decomposed and *trans-p*-coumaric acid is partially converted into the *cis*-isomer.

To confirm the presence of cinnamic acid depsides, an alkaline hydrolysis of wine was carried out to obtain tartaric acid and free

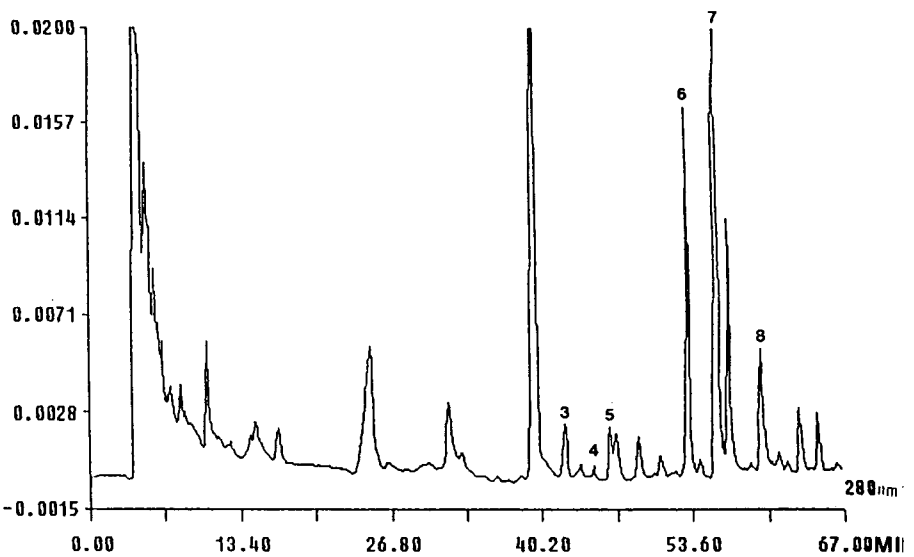

Fig. 6. Chromatogram of Corvo red wine after alkaline hydrolysis and acid extraction, with detection at 280 nm. Peaks and conditions as in Fig. 2.

phenolic acids. The caffeic acid is completely decomposed, because the wine samples were maintained in alkaline solution for a long time. Fig. 6 shows the chromatogram obtained after alkaline hydrolysis. Peaks 9 and 10, assigned to depsides in Fig. 3 are no longer present and there are large amounts of *cis*- and *trans*-*p*-coumaric and ferulic acid. The quantitative data are reported in Table 2 (average data from six determinations for each sample). In white wine, gallic acid is present in small amounts. For the determination of *p*-coumaric acid, the absorption coefficient at 280 nm was used, where the two forms (*trans* and *cis*) have the same absorption.

Fig. 7 shows the chromatogram of red Corvo wine obtained after direct acid extraction (pH

Table 2
Phenolic acid concentrations (μg/l) in wine, vermouth and beer

Acid[a]	Corvo (red)	Chianti (red)	Salice Salentino (red)	Cerveteri (red)	Porto (white)	Vermouth (red Martini)	Verdicchio (white)
1	455.1	409.1	217.7	290.5	182.8	–	–
2	72.8	120.7	79.2	52.5	81.2	45.2	15.0
3	33.7	24.6	17.0	22.4	42.4	29.5	7.3
4	83.7	47.3	91.7	86.7	27.7		14.4
5	70.4	24.8	40.0	23.1	81.5	52.6	3.8
6	2.3	5.1	5.0	2.9	5.4	3.3	3.8
7	26.3	10.3	15.6	19.8	14.1	5.1	13.2
8	11.4	9.8	7.2	12.5	7.4	4.6	7.2

	Vernaccia San Gimignano (white)	Frascati Superiore (white)	Robola (white)	Pinot Grigio (white)	Cerveteri (white)	Corvo (white)	Moretti beer
1	–	–	–	–	–	–	–
2	51.3	24.2	64.9	12.6	14.1	61.0	
3	7.9	5.4	4.6	4.2	4.5	5.1	16.1
4	41.0	23.4	38.8	27.6	49.6	15.1	4.2
5	9.9	3.2	–	4.3	3.6	4.4	2.2
6	5.4	4.3	12.1	3.4	4.1	3.4	–
7	13.3	14.3	60.8	11.6	4.4	7.1	17.1
8	10.8	13.3	21.6	11.7	3.2	9.3	40.4

	Ciro (white)	Fontana Candida (white)	R.S.D. (%)[b]
1	–	–	2.0
2	10.9	21.0	3.1
3	5.7	4.6	4.8
4	24.3	12.7	2.9
5	3.0	3.1	5.4
6	3.9	4.6	10.4
7	2.6	8.9	6.1
8	6.7	8.3	5.8

[a] See Table 1
[b] $n = 6$

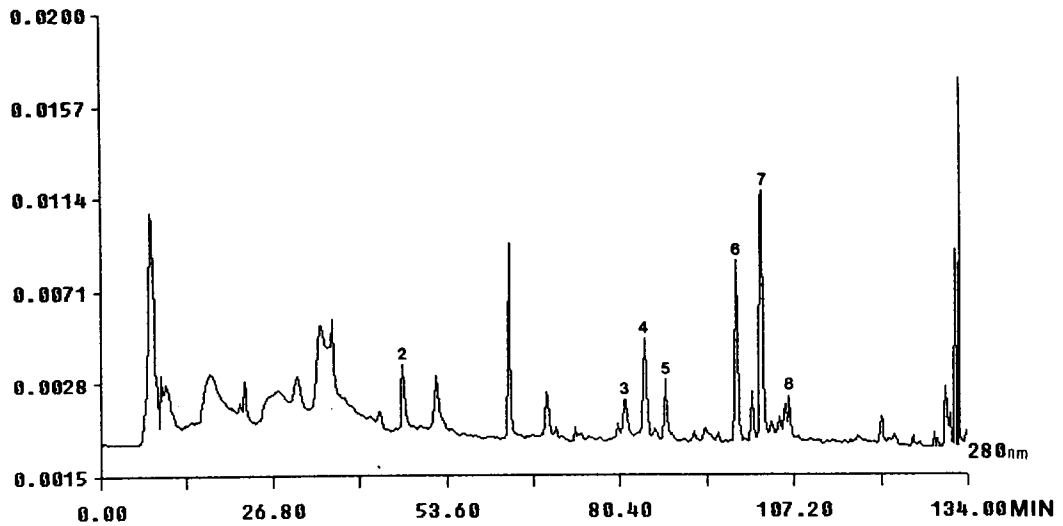

Fig. 7. Chromatogram of Corvo red wine after direct acid extraction (pH 1.0). Column 2 (500 mm × 1.1 mm I.D.). Conditions as in Fig. 2 except that the gradient was doubled in time.

1.0), utilizing a 500-mm microbore column. A good separation was obtained for all the compounds investigated.

References

[1] G.P. Cartoni, F. Coccioli, L. Pontelli and E. Quattrucci, *J. Chromatogr.*, 537 (1991) 93–99.
[2] B.Y. Ong and C.W. Nagel, *J. Chromatogr.*, 157 (1978) 345–355.
[3] C.S. Ough and M.A. Amerine, *Methods for Analysis of Must and Wines*, Wiley, New York, 2nd ed., 1988, p. 166.
[4] I. Correa-Gorospe, M.C. Polo and T. Hernandez, *Food Chem.*, 41 (1991) 135–146.
[5] M. Benincasa, G.P. Cartoni and F. Coccioli, *Ann. Chim. (Rome)*, 77 (1987) 801–811.
[6] P.M. Culbreth and E.J. Sampson, *J. Chromatogr.*, 212 (1981) 221–228.
[7] L. Paronetto, *Polifenoli e Tecnica Enologica*, Edagricole, Bologna, 1977, p. 84.
[8] G. Kahnt, *Phytochemistry*, 6 (1967) 755–758.
[9] M.L. Scarpati and G. Oriente, *Tetrahedron*, 4 (1958) 43–48.
[10] E.J. Conkerton and D.C. Chapital, *J. Chromatogr.*, 281 (1983) 326–329.

ELSEVIER

Journal of Chromatography A, 695 (1995) 237–242

JOURNAL OF CHROMATOGRAPHY A

Chemiluminescent detection of artemisinin Novel endoperoxide analysis using luminol without hydrogen peroxide

Michael D. Green[a,*], Dwight L. Mount[a], G. Daniel Todd[a], Anthony C. Capomacchia[b]

[a]*Entomology Branch, Division of Parasitic Diseases, National Center for Infectious Diseases, Centers for Disease Control and Prevention, Public Health Service, US Department of Health and Human Services, 1600 Clifton Road, Mailstop F-12, Atlanta, GA 30333, USA*

[b]*Department of Pharmaceutics, College of Pharmacy, University of Georgia, Athens, GA, USA*

First received 3 June 1994; revised manuscript received 13 December 1994; accepted 14 December 1994

Abstract

A novel method for artemisinin quantitation employing high-performance liquid chromatography (HPLC) with chemiluminescence (CL) detection in the absence of hydrogen peroxide (H_2O_2), is reported. After elution from the HPLC column, artemisinin is combined with an alkaline solution of hematin and luminol. The resulting CL signal is detected by use of a spectrofluorometer with the excitation lamp disabled, and is proportional to artemisinin concentration. The CL method was optimized and applied to the analysis of artemisinin in spiked human serum.

CL in the absence of H_2O_2 or other known oxidizing species is remarkable since such oxidizers are usually required to produce CL from luminol under alkaline conditions. Artemisinin, a naturally occurring sesquiterpene, is one of several natural products that contain an endoperoxide functional group. Since H_2O_2 is not needed in the analysis, the endoperoxide moiety on artemisinin is implicated as a contributing source of superoxide radicals required for the light-producing reaction with luminol.

1. Introduction

Artemisinin or qinghaosu is a naturally occurring sesquiterpene endoperoxide (Fig. 1) that is receiving considerable attention in the treatment of malaria because of growing resistance of *Plasmodium falciparum* strains to traditional quinoline-based antimalarial drugs [1,2].

Detection of artemisinin has proven to be a challenge as it does not possess any sensitive or

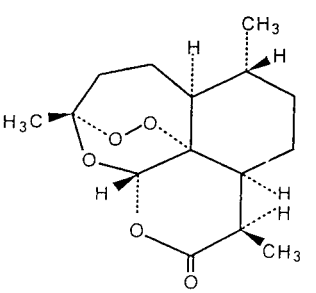

Fig. 1. Structure of artemisinin.

* Corresponding author.

0021-9673/95/$09.50
SSDI 0021-9673(94)01236-9

specific spectrophotometric characteristics. Although artemisinin does absorb ultraviolet radiation between 210 and 220 nm, the extinction coefficient is relatively small and detection at the lower wavelengths usually results in poor selectivity and increased baseline noise when high-performance liquid chromatographic (HPLC) methods are used. Precolumn and postcolumn derivatization methods have been developed to convert artemisinin into a compound that absorbs UV radiation at longer wavelengths [3–5]. These methods lack adequate sensitivity and specificity and can be very time-consuming. An HPLC method that uses reductive electrochemical methods has been reported for artemisinin detection [6]. A disadvantage to this method is that detection interferences due to oxygen in the mobile phase require rigorous deoxygenation prior to and during analysis.

We now report a novel detection method for the analysis of artemisinin involving a chemiluminescent (CL) reaction with luminol, utilizing hematin as a catalyst. Luminol, with either cytochrome *c* or a heme compound as catalysts, has been used for CL detection of lipid hydroperoxides [7–10]. The CL response produced by the oxidized luminol in alkaline solution catalyzed by iron(III) from hematin, cytochrome *c* and ferric ions normally requires H_2O_2 or some other oxidizing species [11]. The iron-catalyzed reduction of peroxides involves the formation of free radicals which react with luminol to produce the CL.

Meshnick et al. [12] have reported evidence of iron-dependent free radical formation from the endoperoxide moiety of artemisinin. Free radicals ($A^{\cdot}$) formed in this manner could react with both the luminol anion (LH^-) and O_2 to form the luminol radical anion ($L^{\cdot -}$) and superoxide (O_2^-), respectively. The latter two species, which are requisite for CL in this system, react to form the luminol hydroperoxide (LOO^-) anion. It forms a covalent bond with the paracarbon atom to give the transient luminol endoperoxide (LOOL). The latter decomposes to give an aminophthalate (AP) in the lowest excited singlet state (^1AP) and N_2. The excited aminophthalate then gives off CL as it returns to the ground state as shown in the scheme below [8,9,11]. If O_2^- is cleaved off as indicated by the results of Meshnick et al. [12], then step (a) in the following scheme would not be needed.

(a) $A^{\cdot} + O_2 \rightarrow O_2^- + A$

(b) $A^{\cdot} + LH^- \rightarrow L^{\cdot -} + A$

(c) $L^{\cdot -} + O_2^- \rightarrow LOO^-$

(d) $LOO^- \rightarrow LOOL$

(e) $LOOL \rightarrow {}^1AP + N_2$

(f) $^1AP \rightarrow h\nu + AP$

The CL detection method described in this paper is optimized with respect to sensitivity (optimum response for artemisinin) and the linearity and precision of the CL response evaluated using a flow-injection technique prior to its application in an HPLC system for the analysis of artemisinin in serum.

2. Experimental

2.1. Reagents[1] and standards

The CL reagent, consisting of a solution of 15 μg/ml luminol (Sigma, St. Louis, MO, USA) and 30 μg/ml hematin (Sigma) in 0.1 *M* sodium hydroxide, was allowed to stand for about 30 min before use. This reagent was prepared daily although weekly preparations may be used if stored away from light. Hemin (Sigma) and cytochrome *c* (Sigma) were also investigated for use as a catalyst for the CL reaction. Artemisinin was obtained from Sigma. The artemisinin derivatives: artemether, arteether and their main metabolite, dihydroartemisinin were provided as a generous gift from Dr. P. Olliaro, World Health Organization.

A stock solution of artemisinin was prepared

[1] Use of trade names is for identification only and does not imply endorsement by the Public Health Service or by the US Department of Health and Human Services.

by adding the compound to a 10-ml glass volumetric flask that had been previously tared on a Mettler AE163 balance. The weight of the compound was 0.0020 g. The flask was then filled to the mark with methanol and sonicated for about 5 min. The final stock concentration was 200 μg/ml. Concentrations of 100, 50, 10, 5, 2.5, 1, 0.5, and 0.25 μg/ml were then prepared from the stock. Standard samples were stored at 4°C to reduce evaporation and equilibrated to room temperature before analysis.

2.2. Apparatus and conditions

In the flow-injection technique, the CL reagent was combined with the sample carrier solvent in a PCRS 500 reaction module (Kratos, Ramsey, NJ, USA) by means of a μLC-500 Isco syringe pump (Isco, Lincoln, NE, USA). The PCRS 500 reaction module consists of a mixing device designed to induce a flowing vortex in the inlet fluid streams and a reaction coil where convoluted tubing is used to minimize band broadening. A Rheodyne sample injector valve Model £7125 (Rheodyne, Cotati, CA, USA) with a 10-μl sample loop was used to deliver the sample into the carrier stream. The carrier stream, consisting of methanol, was delivered to the reaction module by a SP8700XR LC reciprocating pump (Spectra-Physics Analytical, Fremont, CA, USA). The subsequent CL reaction produced by the combined sample and CL reagent was detected by a photomultiplier tube (PMT) from a Perkin-Elmer (Norwalk, CT, USA) 650-S fluorescence spectrophotometer fitted with a flow cell with a path length of 8 mm and volume of 20 μl. The emission wavelength and slit width were set at 425 nm and 20 nm, respectively. The flow-rate for the sample carrier solvent and CL reagent was 0.5 ml/min for both streams with a dead volume of about 1.1 ml from the point of mixing to the detector. The CL signal was recorded by using an HP 3390A integrator (Hewlett-Packard, Palo Alto, CA, USA).

Artemisinin was chromatographically separated from dihydroartemisinin and interfering endogenous components of extracted serum by the addition of a 15 × 0.2 cm Ultrasphere octadecylsilyl (ODS) bonded silica column with a particle size of 5 μm (Beckman, Fullerton, CA, USA) to the flow-injection system described above.

Further modifications of the detection system were made to maximize the signal response for the HPLC analysis of artemisinin in spiked serum. A section of PTFE tubing (0.51 mm I.D.) was placed directly over the opening of the PMT. The opening was covered with aluminum foil to prevent light leak and to reflect the light generated by the sample back to the PMT.

Artemisinin and dihydroartemisinin were eluted from the column at about 7 and 4 min, respectively, with an acetonitrile–water (50:50, v/v) mobile phase pumped at a flow-rate of 0.3 ml/min. The CL reagent flow-rate was 0.5 ml/min.

2.3. Extraction of artemisinin from serum

Human serum was spiked with artemisinin to yield a final concentration of 25, 50, 250 and 500 ng/ml. Dihydroartemisinin was added to each sample and used as an internal standard. The samples were allowed to equilibrate at room temperature for 7 h prior to storage at 0°C.

Artemisinin and dihydroartemisinin were extracted from spiked serum using a quick and simple solid-phase extraction technique. An Empore, 4 mm diameter C_{18} extraction membrane was prepared by passing 0.5 ml of methanol followed by 0.5 ml of water. The membrane was not allowed to dry before sample application. One ml of serum was centrifuged to eliminate particulates, passed directly through the membrane and subsequently washed by passing 0.3 ml of water. Elution of artemisinin and dihydroartemisin was accomplished by passing 0.1 ml of 65% acetonitrile through the membrane. Extraction recovery ranged from 65 to 91% at serum artemisinin concentrations between 25 and 500 ng/ml ($n = 3$ for each concentration). An aliquot of 50 μl of the eluate was injected directly into the HPLC system.

3. Results and discussion

3.1. Chemiluminescent method optimization and evaluation

Using the flow-injection technique, we optimized artemisinin detection by adjusting the hematin and luminol concentrations of the CL reagent (Fig. 2). The flow-rate ratio of the carrier stream to the CL reagent stream was also optimized while maintaining a total flow of 1 ml/min (Fig. 3).

Using hematin as the catalyst is desired because it is relatively inexpensive and it facilitates a quicker reaction, resulting in higher sensitivity. Less sensitivity was observed when cytochrome *c* was substituted for the hematin. The use of freshly prepared hemin in the CL reagent exhibited a very weak CL response from luminol and artemisinin. Exposure of hemin to 0.1 *M* NaOH for about 6 h resulted in increased CL response, comparable to that observed with hematin. Conversion of hemin to hematin occurs under alkaline conditions and accounts for this. Very alkaline conditions (0.1 *M* NaOH) afforded the greatest sensitivity.

The flow-injection technique was used in determining the linearity and variability of response for the CL detection method before the detection method was applied to an HPLC system. A log–log transformation of artemisinin mass versus CL response curve was linear over the range of 2.5 to 2000 ng ($y = 1.17x - 0.29$, $r = 0.999$, $n = 9$ data points). Within-day response variability was assessed by determining the coefficient of variation (standard deviation of the mean divided by the mean multiplied by 100) from the signal peak heights produced by five replicate injections of 10 μl from each artemisinin concentration. The coefficient of variation for day-to-day response variability was determined from the mean signal ($n = 5$) from each of five days. The coefficient of variation for within day and day-to-day variability was $\leq 5\%$ from 25 to 2000 ng of artemisinin and $< 20\%$ from 2.5 to 10 ng of artemisinin. The limit of detection for artemisinin under these conditions is 2.5 ng and is defined as the minimum mass that gave a peak height (signal response) of three times the baseline noise. The relatively high coefficient of variation at the lower amounts of artemisinin is a result of the small perturbation of the carrier stream caused by sample injection.

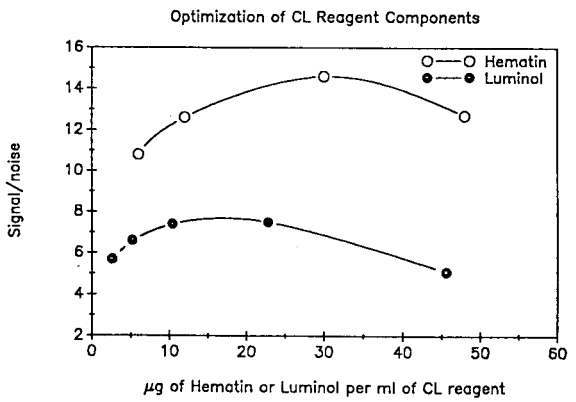

Fig. 2. Effects of hematin or luminol concentrations on the chemiluminescent response of artemisinin. Concentrations of luminol were varied while the concentration of hematin was kept constant at 27 μg/ml. Concentrations of hematin were varied while luminol concentration was constant at 15 μg/ml. The optimal concentration (maxima) of each component were used in subsequent analyses.

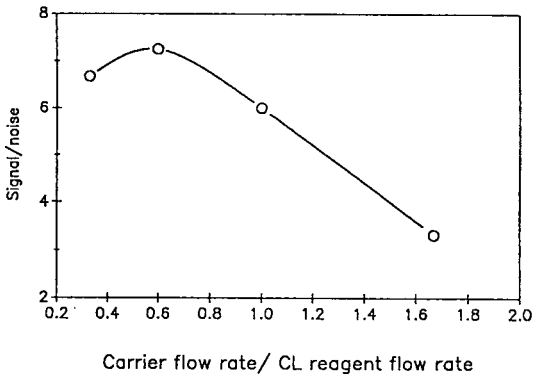

Fig. 3. Adjustment of the flow-rate ratio between the carrier stream and the chemiluminescence (CL) reagent. The total flow-rate was maintained at 1.0 ml/min.

Artemether, arteether and dihydroartemisinin are derivatives of artemisinin that also possess the endoperoxide moiety. Their ability to produce a chemiluminescent reaction under the above conditions was tested. Although the chemiluminescent response for dihydroar-

temisinin is comparable to artemisinin, the response produced by the other artemisinin derivatives, arteether and artemether were about 1000 fold less. This observation is likely to be related to the stability of these endoperoxides when exposed to an alkaline environment. For example, Idowu et al. [13] has reported that unlike artemisinin, arteether is stable in alkaline solution.

3.2. HPLC of spiked serum

The chromatogram shown in Fig. 4 demonstrates that artemisinin can be extracted from serum, separated from dihydroartemisinin and endogenous compounds by HPLC and detected by the CL reaction with luminol. From this chromatogram, a detection limit of 10 ng/ml of artemisinin in 1 ml of serum was determined, which corresponds to a peak height of three times the baseline noise. The sensitivity of this method is comparable to currently available methods and may be improved by further instrumental modifications.

The analysis of artemisinin in spiked serum was evaluated in terms of day-to-day variability (Table 1). Although a log–log conversion produced a linear relationship over the wide artemisinin mass range (2.5–2000 ng) in the flow-injection evaluation, a direct linear relationship between artemisinin concentration and signal response was observed over the on-column artemisinin mass range of 12.5 to 250 ng and used to determine the calculated serum artemisinin concentration. Even though dihydroartemisinin was used as an internal standard in the chromatographic analysis, another suitable internal standard must be used, as dihydroartemisinin is a metabolite of artemisinin and will be present in actual biological samples.

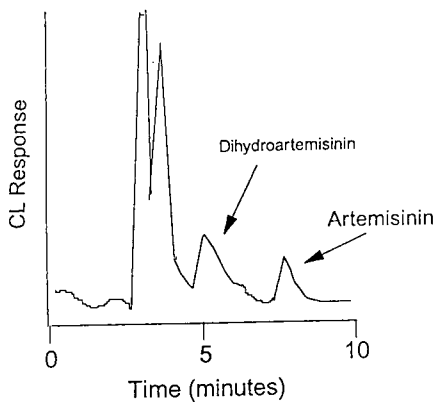

Fig. 4. HPLC chromatogram of artemisinin in spiked serum. An aliquot of 50 μl (50%) of total extract from spiked serum (25 ng/ml) was injected into the HPLC system described in the Experimental section. CL response is equivalent to 12.5 ng of artemisinin on-column.

Table 1
Day-to-day variability of artemisinin concentration in spiked serum samples

Amount added (ng/ml)	Calculated amount (mean ± S.D.) $n = 5$	R.S.D. (%)
25	24 ± 3	13
50	50 ± 6	12
250	254 ± 18	7
500	493 ± 12	3

Peak height ratio of artemisinin to dihydroartemisinin was used to quantitate in all samples. Standard curve ranged from 25 to 500 ng/ml and the correlation coefficient of concentration vs. response was 0.998 ± 0.002, $n = 5$ determinations.

4. Conclusions

The discovery that artemisinin and dihydroartemisinin can be detected by a light producing reaction with luminol provides a new and promising detection method for HPLC analysis of these compounds in body fluids. The many advantages of HPLC with CL detection include selectivity, high sensitivity, wide dynamic range and use of inexpensive and simple equipment [14].

The CL response is thought to be derived from the endoperoxide moiety of artemisinin and dihydroartemisinin yet the response is greatly diminished for the artemisinin derivatives, artemether and arteether. These compounds, which also contain an endoperoxide, have an ether group substituted for the keto group of

artemisinin. Therefore the diminished CL response is attributed to the greater stability of these compounds in alkaline solution due to the ether arrangements. Although hematin is thought to act as a catalyst under the described conditions, it may also be a source of oxygen free-radicals contributing to the chemiluminescent response.

The assay has good potential use for the analysis of dihydroartemisinin. Dihydroartemisinin, which is biologically active against malaria [2] has recently become very important due to reports of its suggested neurotoxicity [15]. Therefore, a sensitive and precise analysis method using chemiluminescent detection for dihydroartemisinin in biological fluids is currently being optimized and evaluated.

References

[1] R.H. Black, C.J. Canfield, D.F. Clyde, W. Peters and W.H. Wernsdorfer, in L.J. Bruce-Chwatt (Editor), *Chemotherapy of Malaria*, World Health Organization, Geneva, 1981, pp. 102–117.
[2] D.L. Klayman, *Science*, 228 (1985) 1049–1055.
[3] H.N. ElSohly, E.M. Croom and M.A. ElSohly, *Pharm. Res.*, 4 (1987) 258–260.
[4] S. Zhao, *Analyst*, 112 (1987) 661–664.
[5] C.G. Thomas, S.A. Ward and G. Edwards, *J. Chromatogr.*, 583 (1992) 131–136.
[6] V. Melendez, J.O. Peggins, T.G. Brewer and A.D. Theoharides, *J. Pharm. Sci.*, 80 (1991) 132–138.
[7] K. Belghmi, J. Nicolas and A. de Paulet, *J. Biolumin. Chemilumin.*, 2 (1988) 113–119.
[8] T. Miyazawa, K. Fujimoto and S. Oikawa, *Biomed. Chromatogr.*, 4 (1990) 131–134.
[9] A. Capomacchia, J. Cho, N. Do and O. Bunce, *Anal. Chim. Acta*, 266 (1992) 287–294.
[10] R. Saeki, H. Inaba, T. Suzuki and T. Miyazawa, *J. Chromatogr.*, 606 (1992) 187–193.
[11] E. Miller and I. Fridovich, *J. Free Rad. Biol. Med.*, 2 (1986) 107–110.
[12] S. Meshnick, Y. Yang, V. Lima, F. Kuypers, S. Kamchonwongpaisan and Y. Yuthavong, *Antimicrob. Agents Chemother.*, 37 (1993) 1108–1114.
[13] O.R. Idowu, J.L. Maggs, S.A. Ward and G. Edwards, *Tetrahedron*, 46 (1990) 1871–1884.
[14] K. Robards and P. Worsfold, *Anal. Chim. Acta*, 266 (1992) 147–173.
[15] T.G. Brewer, S.J. Grate, J.O. Peggins, P.J. Weina, J.M. Petras, B.S. Levin, M.H. Heiffer and B.G. Schuster, *Am. J. Trop. Med. Hyg.*, 51 (1994) 251–259.

ELSEVIER

Journal of Chromatography A, 695 (1995) 243–257

JOURNAL OF CHROMATOGRAPHY A

Ultraviolet–visible detection for capillary gas chromatography and combined ultraviolet–mass spectrometry using a remote flow cell

Murray Hackett[a,1], Houle Wang[a], Glenn C. Miller[a], Darryl J. Bornhop[a,b,*,2]

[a]*Department of Biochemistry, University of Nevada, Reno, NV 89557, USA*

[b]*Linear Instruments Corporation, 2325 Robb Drive, Reno, NV 89523, USA*

First received 22 August 1994; revised manuscript received 1 November 1994; accepted 9 November 1994

Abstract

A scanning UV–Vis detector, linked by fiber optics to a heated remote flow cell, was interfaced to a gas chromatograph and gas chromatograph–mass spectrometer equipped with conventional split/splitless injectors and a 30 m × 0.32 mm, 0.25 μm capillary column. Gas-phase UV spectra with a 3 nm effective bandpass are shown for benzene, biphenyl, anthracene, phenanthrene, benzo-α-pyrene, methylanisoles and polychlorinated biphenyls. Chromatograms at a single wavelength are presented for Aroclors 1254 and 1221. A dual mass–UV chromatogram is shown for unleaded gasoline. Calibration curves generated for aromatic hydrocarbons suggest linearity of detector response over a range of about 10^4. A total absorbance chromatogram is shown for four components of a test mixture. Detection limits for a moderate UV absorber, biphenyl, were 1.0 ng in summed scanning mode and 750 pg in single-wavelength mode, using a criterion of three standard deviations of the baseline noise. The single-wavelength detection limit for naphthalene, a stronger UV absorber, was 90 pg.

1. Introduction

Since the first paper by Kaye [1] published in 1962, there have been less than twenty papers published in the open literature dealing with UV detection schemes for gas chromatography, exclusive of photoionization detectors. Given the ubiquitous nature of UV–Vis spectrophotometers and UV HPLC detectors, it seems somewhat anomalous that UV detection for GC has not attracted more attention.

Previous work has included packed-column GC with combined absorbance and fluorescence detection [2,3], capillary GC with single-wavelength UV detection [4], and packed-column GC with modified commercial photodiode array LC detectors [5–7]. Russian- and Chinese-language papers have also described combined GC–UV [8,9]. More recently, GC–UV spectra of chlorobenzene isomers have been published [10]. The details of our initial hardware design, with emphasis on the cooling requirements, flow cell temperature stability, optics, and a review of previous work (up to 1991) have been presented

* Corresponding author.

[1] Present address: Departments of Chemistry and Pathology, University of Virginia, Charlottesville, VA 22901, USA.

[2] Present address: Department of Chemistry and Biochemistry, Texas Tech. University, Lubbock, TX 79409, USA.

0021-9673/95/$09.50
SSDI 0021-9673(94)01105-2

elsewhere [11] and will only be briefly summarized. Here we report improved flow cells and demonstrate their application with chromatograms, spectra, calibration data and detection limits. We also discuss the instrumentation in terms of its operating characteristics, analyte specificity and how the technique may be improved in the future.

This UV detection scheme collected "on the fly" full-scan (192–360 nm) spectra or single-wavelength chromatograms from capillary GC peaks. The non-destructive nature of GC–UV lends itself to hyphenated techniques, in which the heated exit line of the GC–UV flow cell can serve as the inlet for another detector, such as a flame ionization detector, mass spectrometer, electron-capture detector or Fourier transform (FT) infrared spectrometer. In this report we describe an instrument that consisted of a quadrupole mass spectrometer with a gas-phase UV detector built into the transfer line between the gas chromatograph and the ion source. This arrangement allowed collection of simultaneous gas-phase UV spectra and 70 eV positive ion electron impact mass spectra.

2. Description of instrumentation

2.1. GC–UV flow cells and remote detector

All data were collected using one or the other of two prototype GC–UV systems, which were based on somewhat different flow cells. However, the dimensions of the illuminated portions were the same. The earlier design, similar to that reported in [11], consisted of a heated, gold-plated, stainless-steel flow cell of "Z" type configuration [12] with an illuminated volume of approximately 85 μl and a pathlength of 12 mm. The body was surrounded by an aluminum heat sink which contained cooling passages, the sample and reference photodetectors (Hamamatsu S1226-8BQ, Bridgewater, NJ, USA), and associated current-to-voltage conversion electronics. Remote operation was accomplished by connecting the photodetectors to a commercial UV detector (Model 206HR; Linear Instruments, Reno, NV, USA) with a heat-stable, fiber optic beam splitter [11,13]. The 3 mm O.D. fiber optic bundle was assembled using polyimide-based high-temperature adhesives (High Light Fiber Optics, Caldwell, ID, USA). The scanning monochromator, forward optical bench design of the detector did not require the sample cell to be placed directly in a straight-line configuration between the monochromator and photodetectors, thus lending itself to use with a heated, remote flow cell. This, in turn, allowed physical separation of the high-heat and room temperature portions of the system. The remote flow cell approach would not have been feasible using any existing diode array-based detector. Diode array designs reported in the open literature [6,7] have been restricted to flow cell temperatures at or below 150°C, which limits applicability of the device to molecules with significant vapor pressures at this temperature.

The most significant barrier to the development of GC–UV has been control of thermal noise. At temperatures required for GC work, noise from black body radiation was a significant problem [11]. This difficulty was overcome by cooling the photodetectors and associated electronics while still keeping them in close proximity to the heated portion of the flow cell. This configuration also minimized the number of elements in the optical train, thus keeping light loss to a minimum. Using photoelements designed specifically to have low response in the IR region allowed us to generate noise and drift values comparable to those for similar equipment used for HPLC detection at room temperature, measured at 254 nm in the scanning mode: $2 \cdot 10^{-5}$ AU short-term noise and $1 \cdot 10^{-4}$ AU/h drift with a flow cell temperature of 350°C. The sample light levels were ratioed with the reference beam intensity to minimize drift associated with lamp instabilities and other factors independent of the actual sample absorbance. The system had an effective bandpass of about 3 nm.

The most recent flow cell design, utilized to construct the tandem GC–UV–MS instrument, used the "U-cell" configuration [4], shown in Fig. 1. This design allowed easier manipulation of the inlet and exit lines, and the dead volume was smaller by several μl. As with the Z-cell, all contact surfaces were gold plated to minimize

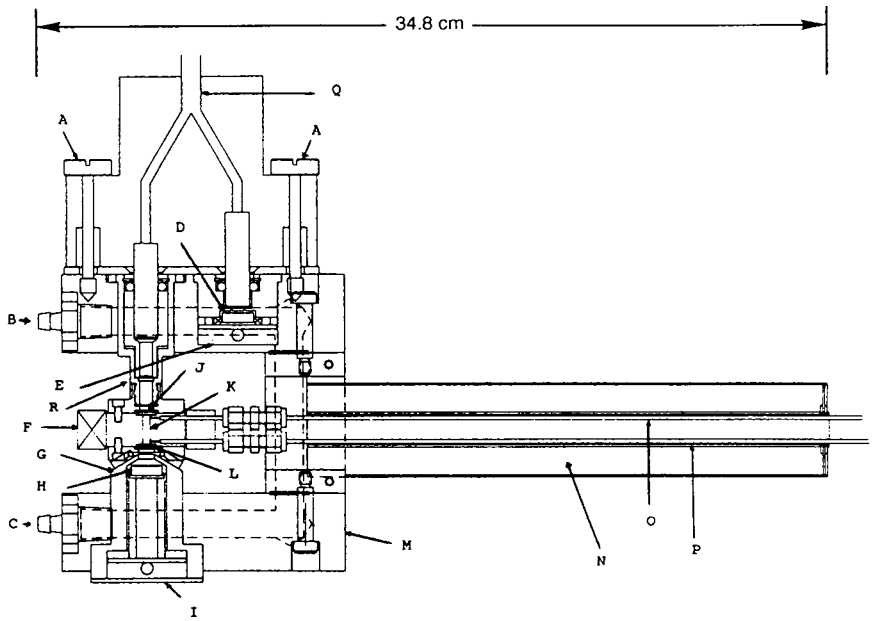

Fig. 1. Line drawing of the "U" flow cell. A = Thumb screws, beam splitter; B = coolant inlet; C = coolant outlet; D = reference photodiode; E = reference preamplifier; F = band heater; G = IR photon "hood"; H = sample photodiode; I = sample preamplifier; J = sapphire window with gaskets; K = flow cell, 12mm × 3 mm; L = sapphire window with gaskets; M = aluminum heat sink; N = transfer line heater; O = sample inlet line; P = sample exit line; Q = fiber optic beam splitter; R = lens.

analyte degradation (Hammon Metal Plating, Palo Alto, CA, USA). A cold shield, consisting of an aluminum cone-shaped hood (see Fig. 1) was introduced between the heated region of the cell and the sample photodetector to physically block IR photons from the cell's periphery from striking the photoelement. This was done without vignetting rays of interest.

The cooling system for both cells consisted of a standard recirculating chiller (Model 1165; VWR Scientific, San Francisco, CA, USA) using water–ethylene glycol (50:50) at 15°C.

The Z-cell was connected, through a heated transfer line, to a GC system (5830A; Hewlett-Packard, Avondale, PA, USA) modified for split/splitless capillary operation (J & W, Rancho Cordova, CA, USA). The separate transfer line [14] was constructed of 1 m of thin-wall 1.59 mm O.D. stainless-steel tubing, Swagelok end fittings, heat tape and glass wool. Heat was controlled by a simple Variac. The capillary column was inserted through the transfer line directly into the flow cell in a manner similar to a direct insertion GC–MS interface.

2.2. Flow cell optical design considerations

The critical parameters were the pathlength, refractive index perturbations, scattering, light throughput, and flow cell volume. It was important to maximize the absorbance pathlength for Beer's law considerations, while minimizing the effective flow cell volume for separation performance [12]. This was accomplished by using optical design software (Beam 4; Stellar Software, Berkeley, CA, USA) running on an MS-DOS computer. Using a fixed pathlength of 12 mm and a diameter of 3 mm, we first constructed an optical train based on constraints including: (1) the positions of the sapphire flow cell windows; (2) the minimum diameter of the cell; (3) the window and active surface area of the photodetector; and (4) the fiber optic used to launch the excitation light (Figs. 1 and 2). Once

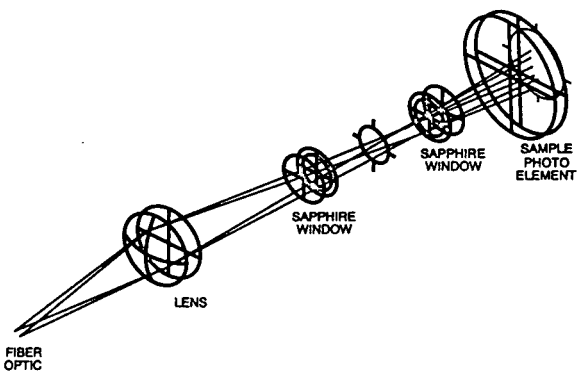

Fig. 2. Flow cell optics, showing the simulated paths of two rays of light at 210 nm.

the major components were chosen, a set of rays was defined by wavelength, position along the optical path, and divergence. Wavelengths were chosen based on typical UV–Vis absorbance applications, we used 210, 254 and 546 nm. The fiber optic employed a high density quartz bundle. Ignoring packing losses, we assumed the bundle would produce a diverging beam of uniform intensity and predictable diameter. A quantitative measure of beam diversion was obtained based on the numerical aperture of the fiber optic, 0.22, and defined the angle from normal that the rays traversed as they exited the bundle. Fig. 2 shows only two sets of rays for clarity. These two sets of rays originate from the edge of the fiber optic and the center, respectively. After evaluation of several optical elements, it was found that the beam could be effectively focused with a single plano-convex lens (JLM Optical, Rochester, NY, USA). This lens was chosen to be an achromatic singlet with an effective focal length, at 546 nm, of 11 mm. Through iterative calculations the position of the focusing lens was determined such that light throughput was maximized and scattering effects due to wall interactions were minimized. For the 210 nm light traced in Fig. 2, the focus is 3.9 mm from the end window of the cell. The paraaxial focus of light is wavelength dependent, therefore optical analyses at 254 and 546 nm were also performed. With proper placement of the lens (Figs. 1 and 2) it was found that the beam focus remained within the flow cell across the UV (180–400 nm) and into the visible (to 700 nm).

Design investigations were performed to evaluate the use of a second lens to capture and focus the rays that exit the flow cell. The normal losses expected due to the addition of an extra optical component outweighed the advantage of collecting marginal rays.

With all optical components defined, additional ray tracing analysis was performed. This was accomplished by running a number of random ray calculations at various wavelengths. These rays were launched from the fiber optic, traced through the optical train and quantified as a percentage of rays launched versus rays collected. It was found that under the worst-case scenario 80% of all rays launched traversed the flow cell and hit the photocell active surface. Further, it was observed that at 210 and 254 nm very few rays struck the wall of the flow cell or were scattered out of the optical path.

2.3. GC–UV–MS

For these experiments the U-cell prototype was used, which was constructed with an integrated heated transfer line (1.59 mm O.D. thin-wall stainless-steel tubing) that contained both entrance and exit lines (Fig. 1). This device was placed on a stand constructed of plywood and particle board at the back of the GC–MS system transfer line oven (Finnigan MAT Model 4023, San Jose, CA, USA). A hole in the GC–MS transfer line oven, originally designed for a jet separator used for packed columns, accommodated the flow cell transfer line in a 90° configuration relative to the MS transfer line oven. The hole had to be enlarged by 3 mm with a file and tin snips. The GC column entered the transfer line oven through a hole in the top of the GC oven (Finnigan MAT Model 9610), as for the normal capillary GC–MS arrangement. The end 20 cm or so was carefully bent to 90° and inserted into the flow cell/transfer line assembly until resistance was felt. A 60 cm length of 0.53 mm I.D. deactivated fused-silica tubing (Supelco, Bellefonte, PA, USA) was used for the

exit line of the U-cell, and was inserted directly into the ion source block of the mass spectrometer. Swagelok end fittings with Vespel ferrules (Supelco) for the inlet/exit lines and high-temperature polyimide gaskets for the two flow cell sapphire windows [11] provided gas-tight seals. The 206 detector, and the box containing the flow cell/transfer line heating controller and 24 V d.c. power supply, were placed on shelves constructed approximately 18 cm above and slightly to the left of the gas chromatograph. The heating controller (Watlow Series 408, St. Louis, MO, USA) was of design similar to that used in the Z-cell prototype, but used 24 V d.c. instead of 120 V a.c. to drive two matched heating elements instead of just the band heater (Watlow Model B1EOLA1) on the flow cell proper. The transfer line was eliminated as a separately controlled heated zone.

2.4. Data systems

The UV detector was controlled by a microcomputer (Model PS2 55 SX; IBM, San Jose, CA, USA) running Windows-based (Microsoft, Redmond, WA, USA) data acquisition software, originally designed for conventional analytical-scale HPLC (206 software, Linear Instruments). Although intended for use with peaks requiring somewhat slower time constants, this software worked well for all but the fastest peaks eluting from a 0.32 mm capillary GC column, with minimal peak distortion when the shortest rise time filter was used, 0.1 s. The rise time control was based on a second-order Bessel filter, encoded in firmware within the 206, that served the same purpose as the traditional resistance–capacitance (RC) filter [15] used in chromatography to avoid recording events, e.g. high-frequency noise, occurring with a faster time constant than those of interest. The rise time filter was set to a value of twice the desired RC time constant to achieve similar results [13], no more than one third the FWHH (full width at half height) peak width. Mass spectral data were collected with a standard Finnigan INCOS data system running on a Nova 4C computer.

3. Experimental

3.1. Reagents

Benzene (Burdick & Jackson, Muskegon, MI, USA), hexane, toluene and methanol (Fisher, Fair Lawn, NJ, USA) were HPLC grade and used as received. Anthracene, 2-methylanisole, 3-methylanisole, 4-methylanisole, nitrobenzene, 1,2,4,5-tetramethylbenzene, *o*-xylene, *m*-xylene, *p*-xylene (Aldrich, Milwaukee, WI, USA), phenanthrene (J.T. Baker, Phillipsburg, NJ, USA), coumarin (U.S. Biochemicals, Cleveland, OH, USA) and benzo-α-pyrene (Sigma, St. Louis, MO, USA) were used as received. Biphenyl was recrystallized in our laboratory from a technical-grade product. Aroclors 1221 and 1254 (Monsanto, St. Louis, MO, USA) were technical formulations used as received. 1,1-Dichloro-2,2-bis(*p*-methoxyphenyl)ethene (DMDE) was synthesized from the dehydrohalogenation of 1,1,1-trichloro-2,2-bis(*p*-methoxyphenyl)ethane (methoxychlor). Methyl parathion was recrystallized from a technical formulation (Pennwalt, Monrovia, CA, USA). All chemicals used in this study were checked for identity and purity using MS and condensed-phase UV–Vis spectrophotometry.

3.2. Conditions

Chromatographic conditions used with the GC–UV, GC–MS and GC–UV–MS instruments were the same: Grob-type splitless injection at 300°C, 1 min delay, 1 m × 0.32 mm retention gap; program, 30°C hold 2 min, 30–60°C at 20°C/min, 60–280°C at 5°C/min; helium carrier at 68.9 kPa head pressure, 30 cm/s linear velocity at 200°C for the Z-cell GC–UV system, as determined by methane injection with a flame ionization detector in place of the UV flow cell; linear velocity varied slightly ($< 10\%$) for the GC–MS and GC–UV–MS; temperatures were MS source 270°C, MS vacuum manifold 100°C, transfer lines 300°C, UV flow cells 300°C, unless otherwise indicated. The column used for all data reported in this paper was a 0.32 mm × 30

meter, 0.25 μm stationary phase thickness DB5 (J & W).

3.3. Chromatographic efficiency

Absolute retention times divided by peak widths at FWHH, t_R/w_H, were calculated for the Z-cell GC–UV system, GC–MS, and combined U-cell GC–UV–MS. We report the data shown in Table 1 in this manner so as to avoid the requirement for isothermal conditions implied by the various expressions used for theoretical plate calculations. Each component of the test mix shown in Table 1 was present at a concentration of 100 ng/μl in hexane, 1.0 μl was injected. Rather than try to match linear velocities exactly, each GC system was individually optimized in terms of carrier gas flow-rate to reach the highest efficiency consistent with the UV scanning speed limitation discussed below in Sections 3.5 and 4.3. Each instrument configuration was operated under the same temperature regimen. Calculations for the GC–MS and GC–UV–MS were made with RIC (reconstructed ion current) data.

3.4. Condensed-phase spectrophotometry

A DU-70 UV–Vis scanning spectrophotometer (Beckman Instruments, Fullerton, CA, USA), with an effective bandpass of 2 nm, was used as described above for checking the purity of reagents. It was also used to generate the condensed-phase spectra of biphenyl in hexane (see Fig. 5), and the molar absorptivities in Table 2. The instrument was scanned from 190 to 360 nm. For the molar absorptivity calculations, single-wavelength mode was used at λ_{max} for each compound, and the log ϵ values calculated from the Beer–Lambert Law [16].

3.5. Scanning parameters and signal processing for GC–UV

The detector was scanned in the UV mode from 192 to 360 nm with a 2-nm step over a period of approximately 1.0 s at a fixed sampling rate of 96 points/s, with the exception of anthracene, which was scanned from 200 to 380 nm. After the raw data were acquired, the files were transferred to another DOS personal computer running Sigmaplot software (Jandel Scientific, Sausalito, CA, USA), which was used to plot all optical spectra and chromatograms. All gas-phase spectra were smoothed using the binomial three-point method given by Bevington [17]. To facilitate off-line data transfers and to integrate chromatographic peaks for the biphenyl calibration data, it was necessary to write two short programs in the C computer language (Borland Turbo C, Scotts Valley, CA, USA). The peak

Table 1
t_R/w_H Values for test mix using GC–MS, GC–UV and GC–UV–MS

Compound[a]	RRT[b]	t_R/w_H		
		GC–MS	GC–UV	GC–UV–MS
Benzene	1.00	Solvent front	102	Solvent front
Toluene	1.49	106	91	Solvent front
Nitrobenzene	4.61	183	169	182
1,2,4,5-TMB	4.93	198	194	201
Naphthalene	5.58	232	218	173
Coumarin	7.90	272	272	253
MP	9.50	686	404	467
DMDE	11.31	666	513	533

Numbers given are means from three replicate determinations. All retention times had R.S.D. values of <2%.
[a] TMB = Tetramethylbenzene; MP = methyl parathion; DMDE = 1,1-dichloro-2,2-bis(*p*-methoxyphenyl)ethene.
[b] Relative retention on the GC–UV system.

Table 2
Condensed-phase log ϵ values and GC–UV single-wavelength detection limits at λ_{max}

Compound	λ_{max} (hexane) (nm)	log ϵ	λ_{max} (GC–UV) (nm)	MDL (pg)
Benzene	204	3.90	194	1300
Toluene	206	3.86	192[a]	5500
Naphthalene	221	5.06	211	90
Biphenyl	202	4.66	195	750
Anthracene	252	5.34	236	40

Analytes were injected in amounts expected to yield S/N of 5:1 and detection limits (minimum level of detection, MDL) were calculated as discussed in the text. Numbers given are means from three replicates, R.S.D. values were $<5\%$.
[a] Shoulder or end absorbance.

integration was based on a simple summation algorithm. Calibration statistics were generated with Mathcad software (MathSoft, Cambridge, MA, USA) running on an MS-DOS computer, using weighted versions of the regression equations given by Miller and Miller [18]. To create the TAC (total absorbance chromatogram) of the test mix (Table 1), shown in Fig. 9, a third C program was written. The TAC plot was analogous to an RIC plot in GC–MS or a Gram–Schmidt vector orthogonalization in GC–FT-IR; the program summed all wavelengths over each scan. The C source code is available from the authors, and has been published in a doctoral dissertation [19].

3.6. Preparation of environmental samples

Drums (55 gallons) of unknown liquids were sampled by hand with the aid of a small pump into glass jars sized to hold about 50 ml of sample. A few μl were removed in the laboratory, diluted 10 to 100 $\times$ with hexane, with 1 μl injected into the GC–UV–MS instrument.

4. Results and discussion

4.1. Spectral quality

The gas-phase UV spectra of four aromatic compounds, shown in Figs. 3 and 4, illustrate the analyte specificity inherent in the method. Note the fine structure characteristic of the B band, a forbidden transition [16], in the gas-phase spectrum of benzene in Fig. 4. Although broadened, as expected [20], fine structure for benzene absorbance was still seen at 275°C. The expected band broadening and decrease in molar absorptivity with increasing transfer line/flow cell temperature [20,21] have been observed to occur for benzene (Fig. 4) and toluene (data not shown) when analyzed over a range of temperatures from 50 to 350°C. All four compounds shown in Figs. 3 and 4 yielded spectra which were manually searched against data bases of condensed-phase spectra acquired using non-polar solvents. For instruments of similar resolution, GC–UV spectral features tend to be broadened and hypsochromically shifted when compared with those observed in the condensed phase. The band narrowing effects expected due to the absence of solvent seemed to be balanced by the thermal band broadening effects, such that the net result of these opposing forces were spectra which were similar to those acquired in non-polar liquids. Comparisons between condensed-phase and GC–UV gas-phase spectra are expected to become more complex when polar solvents, analytes capable of forming hydrogen bonds, etc. are used. The incorporation of a supersonic jet expansion, as has been accomplished for UV fluorescence detection combined with GC [22], would serve to narrow spectral bands in gas-phase absorption measurements. However, in its present state of development, this modification would add additional mechani-

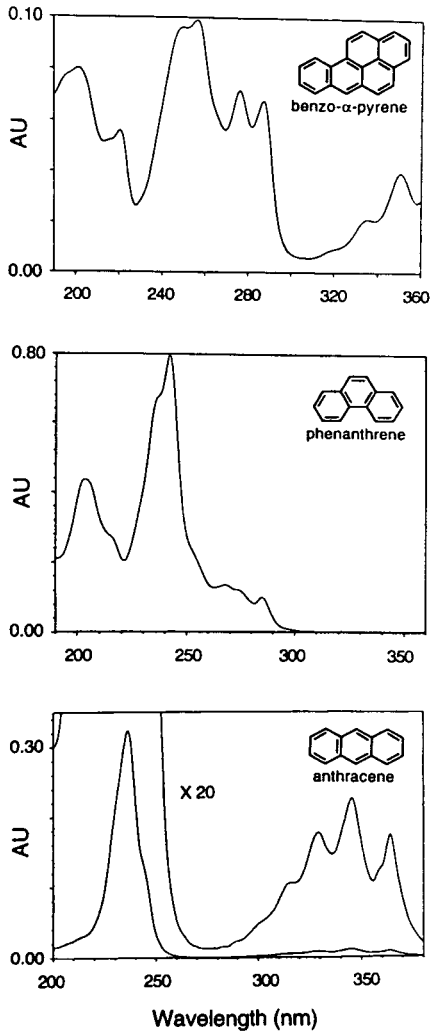

Fig. 3. Spectra of aromatic hydrocarbons acquired in the gas phase using the Z-cell GC–UV instrument. The flow cell was heated to 280°C.

cal complexity and potential sources of non-linear response.

In Fig. 5, a spectrum of biphenyl in hexane, at room temperature, is compared with a spectrum acquired from a GC peak at 300°C. They are similar, with the exception that the primary and secondary bands are slightly blue shifted in the gas phase relative to condensed-phase measurements.

UV spectra have long been known to show significant differences among closely related isomers [16]. This was illustrated by comparing the GC–UV spectra of 100 ng each of *ortho*-, *meta*- and *para*-substituted methylanisoles (Fig. 6). The mass spectra of methylanisoles acquired with the GC–UV–MS instrument (data not shown), M_r 122, differed slightly in the relative abundances of fragment ions at m/z 91 and 107; otherwise they were the same, and similar to library spectra. This difference was more pronounced between the *meta*- and the *ortho*-/*para*-substituted isomers, but it was not possible to distinguish the *ortho*/*para* isomers from one another. The *para*/*meta* isomers also coeluted under our GC conditions. The UV spectrum of each isomer was sufficiently different due to shifting in the *K* band region to allow unambiguous identification.

Polychlorinated biphenyls (PCBs) are complex mixtures of closely related isomers, which have been of environmental interest. Spectra for the four largest peaks in the GC–UV chromatogram of Aroclor 1221 (Fig. 7A), are superimposed and plotted in Fig. 7B. All four peaks were readily differentiated based on the *K* band region in their absorbance spectra [16], without recourse to taking first or second derivatives. Aroclor 1221 is a technical formulation of PCBs consisting primarily of isomers substituted with one and two chlorines [23]. Additional chlorination was expected to yield broader, more diffuse absorbance bands [24]. This was observed in spectra (not shown) taken from the GC–UV chromatogram of Aroclor 1254, shown in Fig. 8, a material which consists primarily of four, five and six chlorine-substituted isomers [23]. Positive identification would, in this case, still rely heavily on retention time. The single-wavelength chromatograms shown in Figs. 7A and 8 are analogous to an extracted ion profile in GC–MS, in that they were extracted from full-scan data.

Results to date suggest the spectra for compounds presented in this paper are reproducible, within the specifications published for the unmodified LC detector [13], over a broad range of flow cell temperatures, flow-rates, and GC temperature programs (accuracy ± 1 nm, precision better than 0.01 nm). As with ion relative abun-

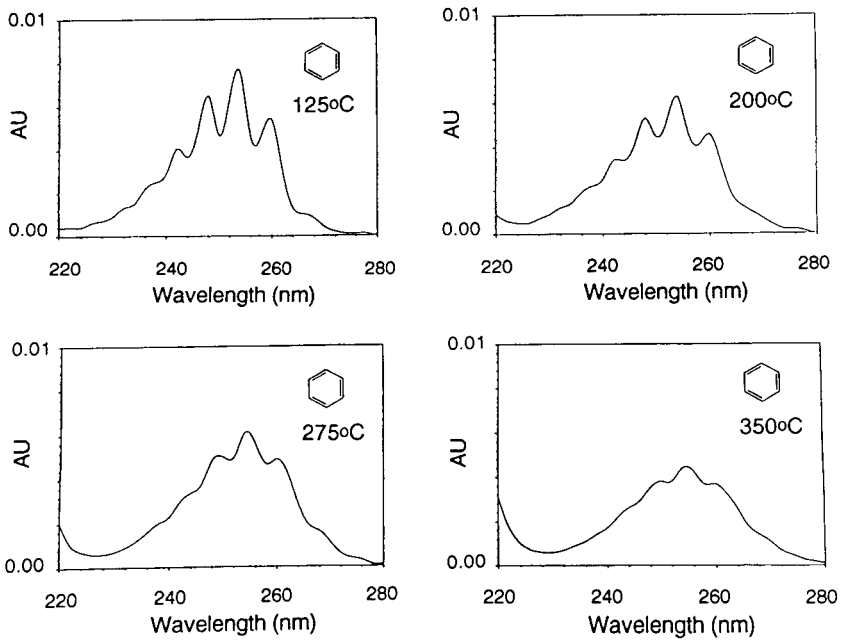

Fig. 4. Fine structure region of the GC–UV spectrum of benzene at four flow cell temperatures.

dance measurements in GC–MS, the least spectral distortion was observed with spectra taken from the center of the GC peaks.

4.2. Linearity of detector response and detection limits

A standard curve for biphenyl was linear over a range of about 10^4. These data were acquired using the Z-cell. The linear regression calculations were weighted by the inverse S.D. for the three replicates at each concentration such that the lowest concentrations would have the strongest influence on the coefficients: $R^2 = 0.994$, slope $= 5.62 \cdot 10^{-5}$ AU min μl/ng, intercept $= -1.8 \cdot 10^{-6}$ AU min, $n = 18$ observations at 6 concentrations, S.D. (of the y-residuals) $= 6.6 \cdot 10^{-6}$ AU min, $\text{S.D.}_{\text{slope}} = 5.9 \cdot 10^{-7}$ AU min μl/ng, $\text{S.D.}_{\text{int}} = 6.4 \cdot 10^{-7}$ AU min. Chromatographic band broadening became significant ($> 10\%$) above 500 ng/μl, but peak area remained linear up to 2.0 μg/μl. This calibration curve was based on absolute detector response, in the single-wavelength mode at 200 nm, without the use of an internal standard. Similar linear responses were observed with more polar materials, coumarin [11] and underivatized phenols, e.g. pentachlorophenol. We attribute these results to the absence of solvent effects in the gas phase. Calibration curves plotted for benzene and toluene were limited to a linear dynamic range of about 10^3 due to their low molar absorptivities. Good linearity was also observed when biphenyl calibration data, acquired using full-scan mode, were plotted both as abstracted single-wavelength chromatograms and as TACs. Using the TAC chromatogram improved biphenyl detection limits by a factor of 6, when compared to the single-wavelength chromatogram at 200 nm abstracted from full-scan data, giving a value of 1.0 ng at three times the standard deviation of the baseline noise, $3\ \text{S.D.}_n$ [25]. Fig. 9 shows the S/N improvement observed when a TAC of the relevant wavelengths was compared with a single-wavelength chromatogram for the test mix (Table 1). Improvement in S/N was compound dependent, and fell in the range of 4 to 8×. For sake of clarity, only the early eluters are shown in Fig. 9.

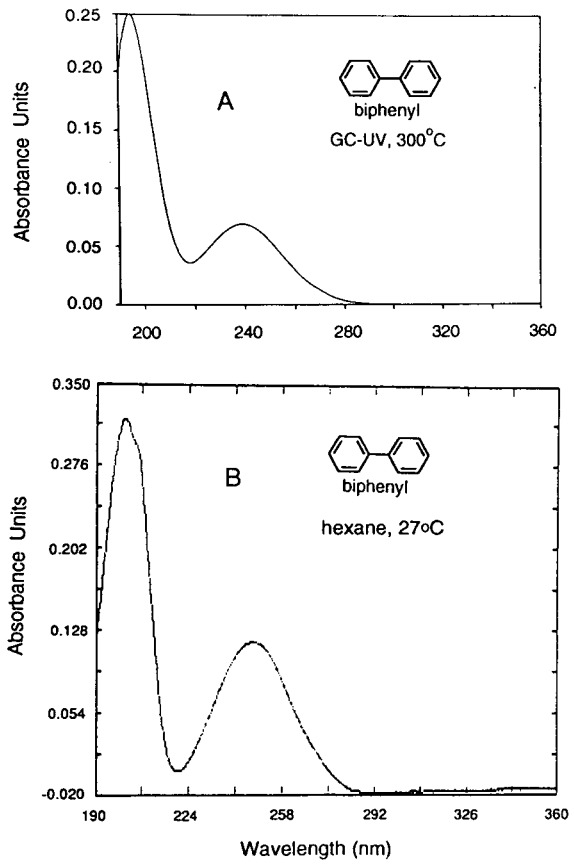

Fig. 5. Biphenyl spectra acquired in the vapor phase with 100 ng injected into the GC–UV system (A), and in the condensed phase at room temperature (B).

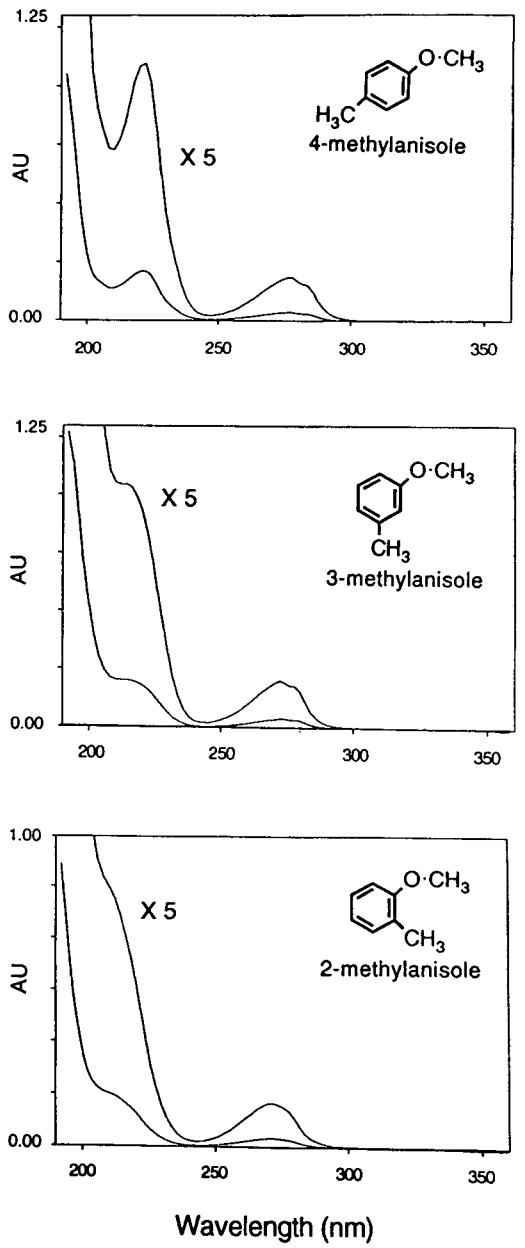

Fig. 6. GC–UV time-slice spectra collected for 100 ng each of methylanisole isomers. The flow cell temperature was 250°C.

TACs were not displayed in "real time" during data collection and had to be generated post-run.

Observed detection limits, based on a criteria of 3 $S.D._n$, were directly proportional to molar absorptivity. The condensed-phase log ϵ values, for five analytes and their single-wavelength GC–UV detection limits, are shown in Table 2. No attempt has been made to account for injector efficiency, temperature programming or other environmental influences which might arise under different conditions. Deviations from the Beer–Lambert law have not been observed to date, within the mass loading limits imposed by the DB5 capillary column employed for sample introduction. More work needs to be done to examine the roles of flow cell temperature, GC oven programming, and scanning parameters on

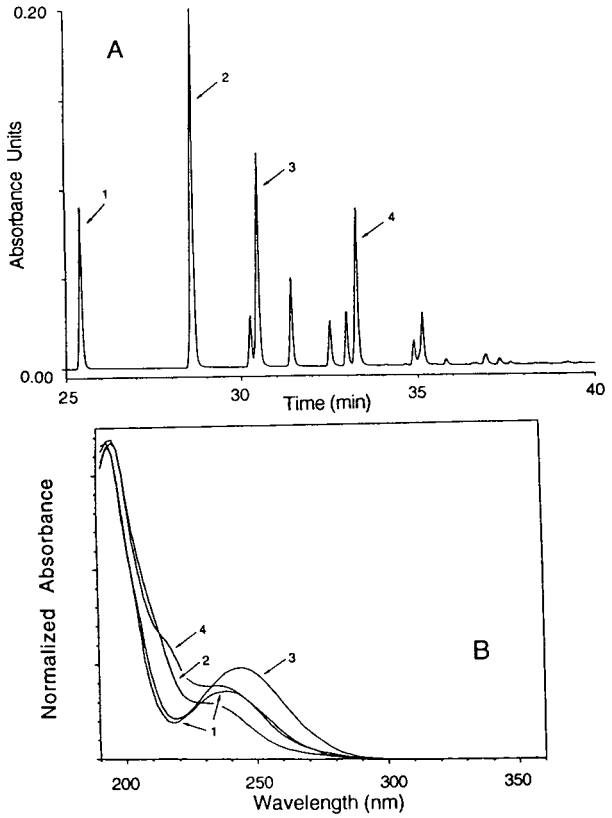

Fig. 7. Arochlor 1221, 1 μg/μl in hexane, 1-μl injection, single-wavelength (200 nm) chromatogram (A), and four time-slice spectra representing the peaks indicated are superimposed (B) after being normalized to the same relative intensity.

detector response before a definitive statement can be made as to its suitability for quantitative GC work.

4.3. Extracolumn band broadening and chromatographic performance

Because of the flow cell volume employed, it was anticipated that some peak broadening would be observed, relative to a chromatographic system optimized for use with the mass spectrometer alone. However, the loss in chromatographic efficiency introduced by the use of the U-cell in series with the mass spectrometer was small, about 10%. Table 1 shows a comparison

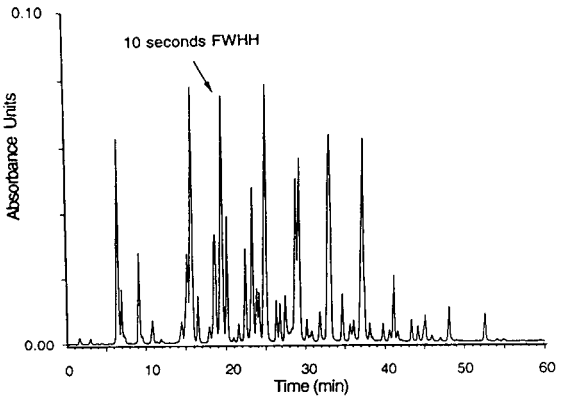

Fig. 8. Single wavelength (220 nm), Arochlor 1254, 1 μg/μl in hexane, 1-μl injection, acquired as described under *Conditions*, with the exception that a 1°C/min ramp was used in order to resolve as many peaks as possible.

of t_R/w_H values [26] measured with the Z-cell GC–UV system, GC–MS and GC–UV–MS. The results for the combined GC–UV–MS U-cell-based system differed only slightly from those for the Z-cell GC–UV. Both systems showed a significant loss in efficiency for the two highest boilers, methyl parathion and DMDE, when compared to the GC–MS without the UV flow cell. This same difference in performance for higher boilers was also observed when the GC, normally used with the Z-cell, was used with a capillary optimized flame ionization detector instead. Such differences were not unexpected when comparing results from systems, such as those described here, with split/splitless injectors of different design [27]. This efficiency comparison also ignored the influence of vacuum on the column exit of the GC–MS. The hexane solvent front was 30% wider with the GC–UV–MS when compared to the unmodified GC–MS, such that benzene and toluene peaks were obscured in the RIC trace. This was probably due to vacuum effects within the flow cell/exit line. This vacuum was observed to be significant, in that slight leaks in the polyimide flow cell gaskets led to higher pressures ($5 \cdot 10^{-5}$ Torr; 1 Torr = 133.322 Pa) in the mass analyzer. When the leaks were repaired, the vacuum returned to normal values ($8 \cdot 10^{-7}$ Torr). The data in Table 1 are

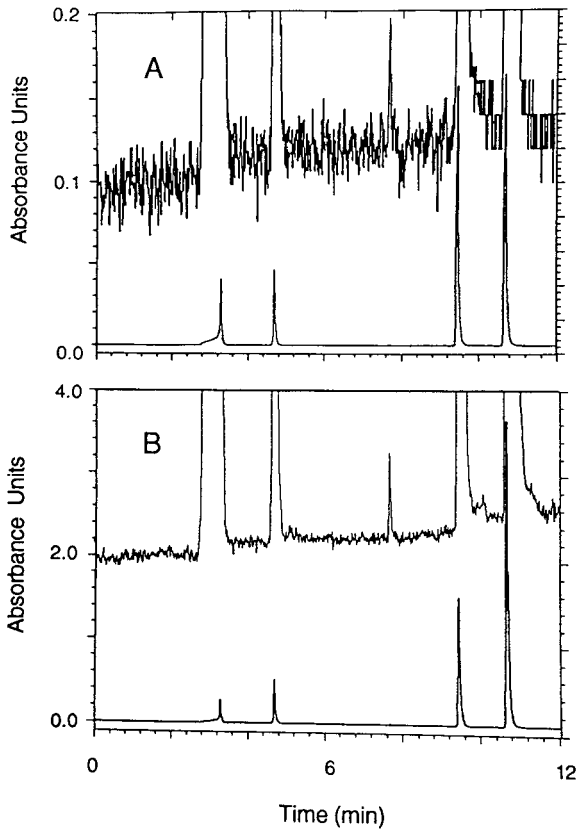

Fig. 9. Full-scan data collected for 1 μl of test mix, showing the elution of the first four components, benzene, toluene, nitrobenzene and 1,2,4,5-tetramethylbenzene. Single-wavelength (200 nm) chromatogram (A) and TAC (total absorbance chromatogram) summed over the relevant wavelengths (192–220 nm, B). Upper traces show 200× magnification of the baseline. The small peak was an impurity.

intended to demonstrate how the GC–UV instrument compared with an established technique, in terms of chromatographic efficiency, rather than to stress the absolute magnitude of the reported values. The best overall results with scanning UV detection, and apparent sensitivity, were achieved when the helium carrier gas flow-rate was slightly lower than that of an optimization based purely on minimizing the height equivalent to a theoretical plate (HETP) or similar metric. This was at least in part due to the requirements of the data system, which had a fixed data collection rate of 96 points/s. This collection rate is slow for capillary GC, particularly when scanning over the 85 intervals required for a 190–360 nm scan incremented every 2 nm. A capillary peak, e.g. the peak indicated in Fig. 8, which is 10 s wide FWHH, is sampled 11 times at a given wavelength. This sampling rate was adequate for generating spectra and TAC plots in most cases. Because of this limitation, the system was not reliable for peaks faster than about 4 s FWHH, using the scanning parameters and data collection electronics employed in this study. One could, however, increase the number of samples/peak by choosing a larger scanning increment, e.g. 4 or 6 nm. In practice, the sampling rate became an issue when 0.32 mm columns were used at carrier flow-rates higher than those used for data reported here. To adequately determine to what extent the 85-μl flow cell volume contributes to band broadening with 0.32 mm columns, more work needs to be done with the flow cell exit line at atmospheric pressure, and the scanning speed limitation removed. Single-wavelength detection would be one option.

The introduction of a make-up flow of 2–5 ml/min of helium through a coaxial tee fitting, at the point where the transfer line joins the flow cell, resulted in a 10% gain in chromatographic efficiency. However, this increased flow-rate resulted in an approximately 50% loss in apparent sensitivity for early eluters, benzene and toluene, contained in the test mix described in Table 1. Later-eluting peaks, i.e. those with higher capacity factors, were also affected, but not as severely. The sensitivity reduction was probably caused by a combination of two factors. This is a concentration-sensitive, as opposed to a mass-sensitive, detector. Increasing the gas flow at the detector reduced the concentration of analyte present during any one time slice of the peak volume. By increasing dC/dt (rate of change in concentration with respect to time) and thus narrowing the earliest peaks to a point approaching the maximum efficiency of the column, they became too "fast" for the data system. At 2 s FWHH a peak might be sampled only

three or four times in scanning mode, with a 2-nm increment, and thus artificially truncated. Further experimentation with make-up flows for columns of 0.32 mm I.D. or larger was abandoned. Experimentation with capillary columns of smaller I.D. than 0.32 mm has not been performed in our laboratory, but has been attempted by others [28]. Due to the relatively large volume of the flow cell, it was anticipated that it would not be applicable to GC columns with an I.D. of less than 0.30 mm, or to "fast" GC.

Six repeated 1.0-μl manual injections of the standard test mix (Table 1) using the Z-cell instrument yielded an R.S.D. of 5% for peak areas. The use of an autosampler would likely give better repeatability.

4.4. Application to environmental samples

About 100 samples of organic liquids from hazardous waste sites in the western USA have been analyzed qualitatively using the U-cell-based GC–UV–MS system, with emphasis on BTX (benzene, toluene, xylenes). Most of these unknowns came from unmarked drums of technical-grade products derived from petroleum. The gas-phase UV data were especially helpful with respect to identifying signals for aromatic compounds of regulatory interest that were "buried" under signals from much higher concentrations of aliphatic compounds, rendering the MS data useful primarily for the aliphatics. This point is illustrated by a representative GC–UV–MS chromatogram of unleaded gasoline, Fig. 10. The BTX peaks were confirmed by comparing their time-slice UV spectra and retention times with those from standards run under the same conditions. Benzene and toluene were readily identified in the unknowns based on UV spectra alone. However, the time-slice GC–UV spectra of the xylene isomers were identical and similar to condensed-phase spectra, below 230 nm. The xylenes lacked sufficient S/N in the weak B band region, at higher wavelength, to discern any isomer specific fine structure. Subtle differences among xylene isomers have been observed in condensed-phase spectra, acquired using isooctane solvent [29].

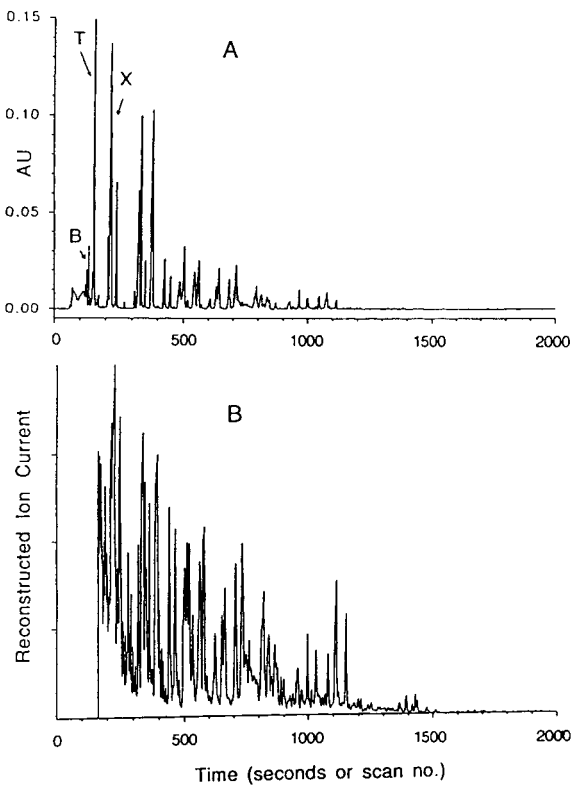

Fig. 10. GC–UV–MS dual chromatogram of unleaded gasoline diluted 1:20 with hexane, 1-μl injection. UV flow cell 250°C, order of elution for the BTX fraction (A, 200 nm) was benzene, toluene, *m*-xylene, *p*-xylene, *o*-xylene. MS data (B) were summed from m/z 50 to 550, 1 scan/s, ion source and transfer lines 250°C.

5. Conclusions

The Z-cell and U-cell GC–UV instruments were used successfully as specific detectors for aromatic compounds, which could also provide gas-phase spectral data for qualitative organic analysis. The detection hardware for the technique was relatively uncomplicated, both with respect to its construction and its application.

Molar absorptivities for transitions in the near UV are higher than those in the IR, making the UV method inherently capable of lower detection limits, for moderate to strong UV absorbers ($\epsilon > 10\,000$). The detection limits achievable for biphenyl, a representative analyte for full-scan and single-wavelength GC–UV, were reasonable for practical application (see Table 2 and discussion above) but would have to be improved, by at least two orders of magnitude, to compete with other sensitive detection methods, e.g. MS.

Calculating the TAC in the acquisition software, in real time, is an obvious improvement that would eliminate the need for much tedious off-line data processing. The TAC improved detection limits for full-scan data and would be a more informative way of observing the UV chromatograms in real time, as opposed to monitoring a single wavelength.

Our implementation of GC–UV was limited to compounds which absorb light above 190 nm. Kaye [1] demonstrated the possibility of extending a GC–UV instrument into the middle UV region, where $n \rightarrow \sigma^*$ and end absorbance from $\sigma \rightarrow \sigma^*$ transitions are observed, but common GC carrier gases are transparent. Extending the lower scanning limit of the GC–UV system from 190 to 160 nm would widen the applicability of the instrumentation to that of a non-destructive, universal detector for volatile organics.

Acknowledgements

We acknowledge engineering support provided by Louis Hlousek, Rick Mikulski and Ray Bryan. Scot Weinberger and John Wangsgaard are acknowledged for valuable discussions. Support for this work by Linear Instruments (now a part of Spectra-Physics Analytical, a division of Thermo Separation Products) and the University of Nevada is gratefully acknowledged. We thank Lin Guo for her assistance with the graphics. M.H. wishes to thank Don Hunt for giving him time off from his regular duties to write the manuscript.

References

[1] W. Kaye, *Anal. Chem.*, 34 (1962) 287.
[2] D.L. Van Engelen, A.K. Adams and L.C. Thomas, *J. Chromatogr.*, 331 (1985) 77.
[3] D.L. Van Engelen, L.C. Thomas and E.H. Piepmeier, *J. Chromatogr.*, 405 (1987) 191.
[4] M. Novotny, F.J. Schwende, M.J. Hartigan and J.E. Purcell, *Anal. Chem.*, 52 (1980) 736.
[5] M. Kube, M. Tierney and D.M. Lubman, *Anal. Chim. Acta*, 171 (1985), 375.
[6] V. Lagesson and J.M. Newman, *J. High Resolut. Chromatogr. Chromatogr. Commun.*, 11 (1988) 577.
[7] V. Lagesson and J.M. Newman, *Anal. Chem.*, 61 (1989) 1249.
[8] D.M. Lisitsyn and V.I. Gorshkov, *Vses. Nauchno-Issled. Geologorazved. Neft. Inst.*, 246 (1983) 28.
[9] T. Ding and Z. Yan, *Fenxi Huaxue*, 13 (1985) 310.
[10] D.J. Bornhop and J.G. Wangsgaard, *J. High Resolut. Chromatogr.*, 14 (1991) 344.
[11] D.J. Bornhop, L. Hlousek, M. Hackett, H. Wang and G.C. Miller, *Rev. Sci. Instrum.*, 63 (1992) 191.
[12] C.F. Poole and S.A. Schuette, *Contemporary Practice of Chromatography*, Elsevier, Amsterdam, 1986, Ch. 5.
[13] *Linear UVIS-206 Multiple Wavelength Detector*, Instruction Manual, Linear Instruments, Reno, NV, 1989, Ch. 7.
[14] T.G. Hartman, J. Lech, V.G. Saltamach and R.T. Rosen, *Mass Spec Source*, 13 (1990) 31.
[15] H.V. Malmstadt, C.G. Enke and S.R. Crouch, *Electronics and Instrumentation For Scientists*, Benjamin Cummings, Reading, 4th ed., 1981, Ch. 6.
[16] R.M. Silverstein, G.C. Bassler and T.C. Morrill, *Spectrometric Identification of Organic Compounds*, Wiley, New York, 4th ed., 1981, Ch. 6.
[17] P.R. Bevington, *Data Reduction and Error Analysis for the Physical Sciences*, McGraw-Hill, New York, 1969, p. 257.
[18] J.C. Miller and J.N. Miller, *Statistics for Analytical Chemistry*, Ellis Horwood, New York, 3rd ed., 1993, Ch. 5.
[19] M. Hackett, *Thesis*, University of Nevada, Reno, NV, 1991.
[20] E. Wieteska, in T. Nowicka-Jankowska, K. Gorczyńska, A. Michalik and E. Wieteska, *Analytical Visible and Ultraviolet Spectrometry (Wilson and Wilson's Comprehensive Analytical Chemistry*, edited by G. Svehla, Vol. 29), Elsevier, Amsterdam, 1986, Ch. 3.
[21] K. Gorczyńska, in T. Nowicka-Jankowska, K. Gorczyńska, A. Michalik and E. Wieteska, *Analytical Visible and Ultraviolet Spectrometry (Wilson and Wilson's Comprehensive Analytical Chemistry*, edited by G. Svehla, Vol. 29), Elsevier, Amsterdam, 1986, Ch. 9.
[22] S.J. Hein, E.H. Piepmeier and L.C. Thomas, *J. Chromatogr.*, 557 (1991) 39.

[23] M.D. Erickson, *Analytical Chemistry of PCBs*, Butterworth, Boston, MA, 1986, Ch. 2.
[24] E.S. Stern and C.J. Timmons, *Electronic Absorption Spectroscopy in Organic Chemistry*, Edward Arnold, London, 1970, Ch 6.
[25] C.J. Kirchmer, in L.A. Currie (Editor), *Detection in Analytical Chemistry (ACS Symposium Series*, No. 361), American Chemical Society, Washington, DC, 1988, Ch. 4.
[26] C.F. Poole and S.A. Schuette, *Contemporary Practice of Chromatography*, Elsevier, Amsterdam, 1986, Ch. 1.
[27] K. Grob, *Classical Split and Splitless Injection in Capillary GC*, Hüthig, Heidelberg, 2nd ed., 1988.
[28] R. Gale, USFWS, Columbia, MO, personal communication.
[29] M.J. Kamlet (Editor), *Organic Electronic Spectral Data, Vol. 1, 1946–1952*, Interscience, New York, 1960, p. 203.

ELSEVIER

Journal of Chromatography A, 695 (1995) 259–265

JOURNAL OF CHROMATOGRAPHY A

Determination of ethyl carbamate in alcoholic beverages by capillary multi-dimensional gas chromatography with thermionic specific detection

Ya-Ping Ma, Fu-Quan Deng, Dai-Zhou Chen, Shou-Wei Sun*

National Research Centre for Certified Reference Materials, No. 7, District 11, Heping Li, 100013 Beijing, China

First received 25 July 1994; revised manuscript received 31 October 1994; accepted 22 November 1994

Abstract

A specific, sensitive capillary multi-dimensional gas chromatographic method with thermionic specific detection (TSD) combined with internal standard methodology to identify ethyl carbamate (EC), a well known carcinogen, in various fermented alcoholic beverages is described. The basic procedures for sample preparation were similar to a modification of the LCBO (Liquor Control Board of Ontario) procedure, except that isopropyl carbamate (i-PC) was used as an internal standard. In the multi-dimensional gas chromatographic process, EC and i-PC were co-eluted on a polar capillary precolumn of BP-20, and then switched together to a non-polar OV-1 analytical column by the heart-cutting technique to resolve them and finally detected by TSD. The linear range of the calibration graph was from 10 to 550 ppb with a correlation coefficient of 0.9996. For a liquor containing 124.6 ppb of EC, the relative standard deviation was 2.0% and the detection limit was 1 ppb.

1. Introduction

Ethyl carbamate (EC) occurs in most fermented foods and alcoholic beverages [1,2]. However, it was recognized as a chemical carcinogen [3], and the Canadian Federal Government has introduced regulatory limits to control the incidence of EC in alcoholic beverages [4]. A number of methods for detecting and determining EC using different techniques have been reported. All of these methods involved some form of extraction and concentration treatment, followed by chromatographic separation with either flame ionization detection (FID), selective detection or some kind of mass spectrometric detection technique (MS). Dennis et al. [5] evaluated three different detection methods: with a thermal energy analyser (TEA), with a Hall electrolytic conductivity detector (HECD) in the nitrogen mode and MS. They found that the detection limits were similar and concluded that TEA was consistently more reliable than HECD in terms of detection limits. Two-dimensional capillary gas chromatography (GC) with dual flame ionization detectors using the external standard technique was introduced by Van Ingen et al. [6]. Sponholz [7] evaluated various methods, they believed that the two-dimensional capillary gas chromatography is the best method in terms of its relatively simple instrument requirements.

Recently, in cooperative trial studies on the

* Corresponding author.

0021-9673/95/$09.50
SSDI 0021-9673(94)01155-9

determination of EC in alcoholic beverages, thermionic specific detection (TSD) or alkali flame ionization detection (AFID) methods have been widely used [8]. Although the absolute response of TSD may vary from one manufacturer to another, the detection limits are affected mainly by different chemical procedures and chromatographic methods. About 20 years ago, Walker et al. [9] described an analysis by packed column GC using a variety of detection methods including TSD. They reported that this procedure was able to detect 100 μg/l of EC in wine. Drexler and Schmid [10] developed a rapid and simple procedure using TSD after solid–liquid extraction. The detection limit of their method was also 100 μg/l. Joe et al. [11] were able to improve on the original method by further concentrating the sample and adopting a more rigorous clean-up regime, and were able to detect 10 μg/l of EC. Baumann and Zimmerli [12] reported a method using capillary AFID after column extraction, with a detection limit of 20 μg/l. For distilled spirits, Aylott et al. [13] reported capillary chromatography with TSD and a sample preparation procedure similar to that of the LCBO (Liquor Control Board of Ontario). The detection limit of their method was 5 μg/l. It seems that all these TSD methods are not sensitive enough to ensure compliance with the Canadian guidelines. Further improvement is still needed, and one approach is to form ethyl dimethyl carbamate by methylation. Bailay et al. [14] reported that this procedure can enhance the AFID response at least tenfold to obtain a detection limit of 1 μg/l.

In this paper, we describe an improved multidimensional capillary GC method using TSD and a special internal standard, with which very reliable and accurate results were obtained.

2. Experimental

2.1. Reagents

Reagents were of analytical-reagent grade from Beijing Chemicals Factory, (Beijing, China). Methylene chloride was purified by distillation on a 2-m Vigreux column. Before using, the purity was checked by concentrating 200 ml of the distilled solvent to 0.5 ml with a rotary evaporator and measuring the gas chromatogram of the residue, which must be free of interfering peaks for determination of EC. Other reagents used were sodium sulfate (anhydrous granular), ethyl acetate, potassium chloride, benzene, absolute ethanol and sodium hydroxide. Pure water was obtained by passing tap water through an ion-exchange column and then distilling it twice with a quartz glass device.

2.2. Primary standards

EC (chemical pure; Beijing Chemicals Factory) was purified by recrystallization from benzene. The purity was checked by GC with a OV-1 capillary column (15 m × 0.53 μm I.D., 1.2 μm film thickness). No impurities were found in the chromatogram.

Isopropyl carbamate (i-PC) (Tokyo Kasei Industry, Tokyo, Japan) was tested by the same GC method as for EC and no impurities were detected.

2.3. Standard solution preparation

A stock standard solution of EC in ethanol (1 mg/ml) was prepared, then a working standard solution of 100 μg/ml was prepared by diluting this solution tenfold with ethanol.

A stock standard solution of i-PC in ethanol (1 mg/ml) was prepared, then a working solution of 100 μg/ml was prepared by diluting this solution tenfold with ethanol.

2.4. Apparatus

All glass ware was obtained from the Beijing Glass Ware Factory. Before use, it was scrupulously cleaned with chromic acid, thoroughly washed with distilled water and dried at 120°C. An RE-51 rotary evaporator and an AC-11 micropipette were obtained from Yamato. The accuracy of the micropipette were calibrated by weighing with a precision balance. The calibrated volumes were used later in quantitative

calculations. A Sichromat-2 multi-dimensional gas chromatograph (Seimens) equipped with an SP3700 thermionic specific detector (Varian) was used throughout. The base and the heater of the detector were reconstructed to fit the Sichromat-2. A BP-20 (polyethylene glycol) column (25 m × 0.33 mm I.D. × 0.5 μm film thickness) (SGE) was installed in the first oven as a precolumn. An OV-1 fused-silica capillary column (25 m × 0.33 mm I.D. × 0.5 μm film thickness) (Chromatographic Laboratory, Beijing University) was installed in the second oven as an analytical column. FID and a TSD were used for detection of the chromatograms from the precolumn and analytical column, respectively. Nitrogen was used as the carrier gas with linear velocities of 22 cm/s for the precolumn and 27 cm/s for the analytical column. The initial temperature of the first oven was held at 55°C for 4 min, then programmed to 155°C at 4°C/min, held at 155°C for 8 min, then again programmed to 220°C at 15°C/min. The second oven was operated isothermally at 70°C. A Type 3056 multi-pen recorder (Yokagawa Kokuskin Electron) was used to recorded the chromatograms, and a Model 3394 integrator (Hewlett-Packard) was also connected to the amplifier output cable of the TSD instrument for processing the chromatographic trace. Splitless injection was used, 2 μl of extract were injected. Inlet purge was activated after 1 min and the injector temperature was 230°C.

2.5. Procedure

Sample preparation

First, the liquor samples were adjusted to an alcoholic strength near 20% (v/v) (10% for wine) with pure water, then 50 μl of 100 μg/ml i-PC internal standard solution were added to 50 g of each of these samples. These sample solutions were adjusted to pH 10 with 6 *M* NaOH solution and then saturated with KCl and extracted with 3 × 70 ml of methylene chloride. The extracts were dried with anhydrous sodium sulfate and concentrated under reduced pressure at 29°C with a rotary evaporator to a volume of about 5 ml. The residue was transferred to a concentrator tube and 0.50 ml of ethyl acetate was added as a keeper solvent. Under a gentle stream of nitrogen, the volume of the extracts were reduced to 0.5 ml.

Quantification

To constructing a calibration graph, 50 g of a 20% (v/v) aqueous ethanol solution were added to each of six 200-ml separating funnels, then 5, 10, 20, 50, 100, 150, 200 and 250 μl of EC working solution were added to each of the six funnels. These correspond to standard concentrations of 10, 20, 40, 100, 200, 300, 400 and 500 μg/kg (ppb), respectively. Then 50 μl of the 100 μg/ml i-PC working standard solution were added to each separating funnel to obtain an internal standard concentration of 100 μg/kg. These standard solutions were extracted and concentrated in the same manner as in the sample preparation described above. Calibration graphs of peak-area ratio of EC to i-PC versus EC concentration were used to calculate unknown concentrations.

Gas chromatographic analysis

To determine the retention times of EC and i-PC, 0.2 μl of mixed standard solution (containing 10 ng each of EC and i-PC) was injected into the gas chromatograph. The retention times of EC and i-PC under the above conditions were 22 min 5 s. Then 2 μl of concentrated extract of standards or samples were injected into the gas chromatograph. With the heart-cutting technique, the fraction that eluted from the precolumn from 21 min 50 s to 22 min 20 s was switched to the analytical column, and was developed by a two-dimensional chromatographic process.

3. Results and discussion

3.1. Internal standard methodology in multi-dimensional gas chromatography

For quantitative analysis, choosing an appropriate internal standard to match the multi-dimensional gas chromatograph is always a troublesome problem. Obviously, with the heart-

cutting technique, the retention behaviour of the internal standard must be identical with that of the analyte on the pre-column, otherwise, the internal standard and the analyte will be detected by the monitoring detector and the main detector respectively. Hence there will be a standardization problem owing to the different responses of the two detectors. In addition, resolution on the pre-column will be difficult for complex samples. Therefore, the external standard method is always to be recommended in multi-dimensional GC.

Many compounds were screened and finally we found that i-PC fulfils the strict criteria for use as an internal standard. Fig. 1 shows the multi-dimensional gas chromatogram of a standard solution and indicates that EC and i-PC can be co-eluted on the BP-20 phase of the pre-column and with heart-cutting technique switched to the OV-1 phase of the analytical column and there be resolved. The co-elution of EC and i-PC on a Carbowax-20M phase was reported by Lau et al. [15] and they used a 30 m × 0.25 mm I.D. × 0.15 μm DB-Wax column to investigate the GC and MS properties of alkyl carbamates.

3.2. Detection limits

The chemical noise from the complex matrix was effectively minimized by the high resolving power of the multi-dimensional GC technique. Also, the instability of the thermionic specific detector that was always encountered with temperature programming was eliminated by operating the analytical column isothermally. Hence both the chemical and electrical noise were minimized. For these reasons, the detection limit was considerably improved, being as low as at least 1 ppb. Fig. 2 represents the multi-dimensional gas chromatograms of a wine sample that contained 22.1 ppb of EC.

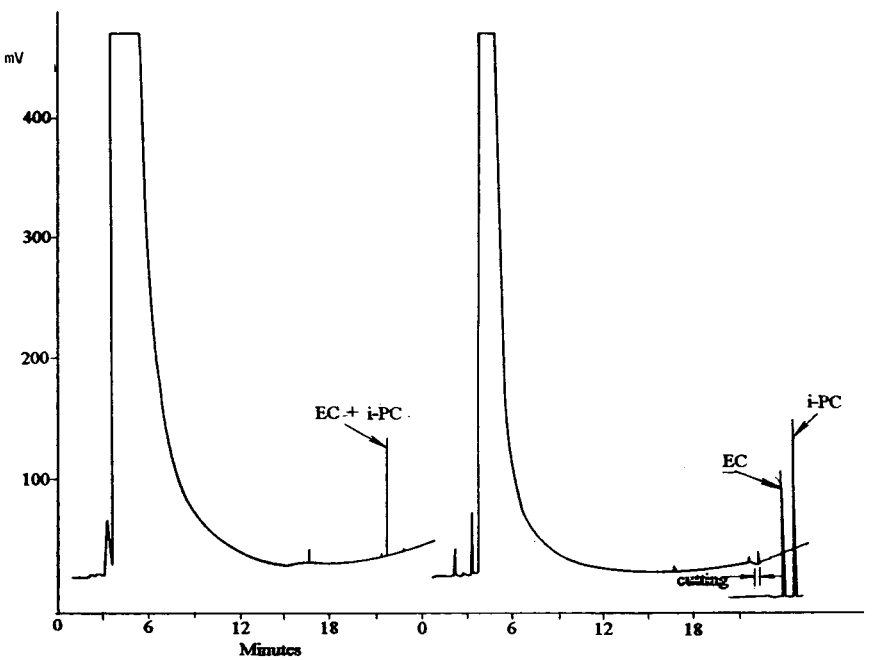

Fig. 1. Multi-dimensional gas chromatograms of a standard solution (containing 100 ng each of EC and i-PC). Left: precolumn chromatogram obtained on a BP-20 column (25 m × 0.33 mm I.D. × 0.25 μm) using FID without heart-cutting. Right: precolumn chromatogram (top) and an analytical column chromatogram (bottom) obtained on an OV-1 column (25 m × 0.33 mm I.D. × 0.25 μm) using FID with heart-cutting.

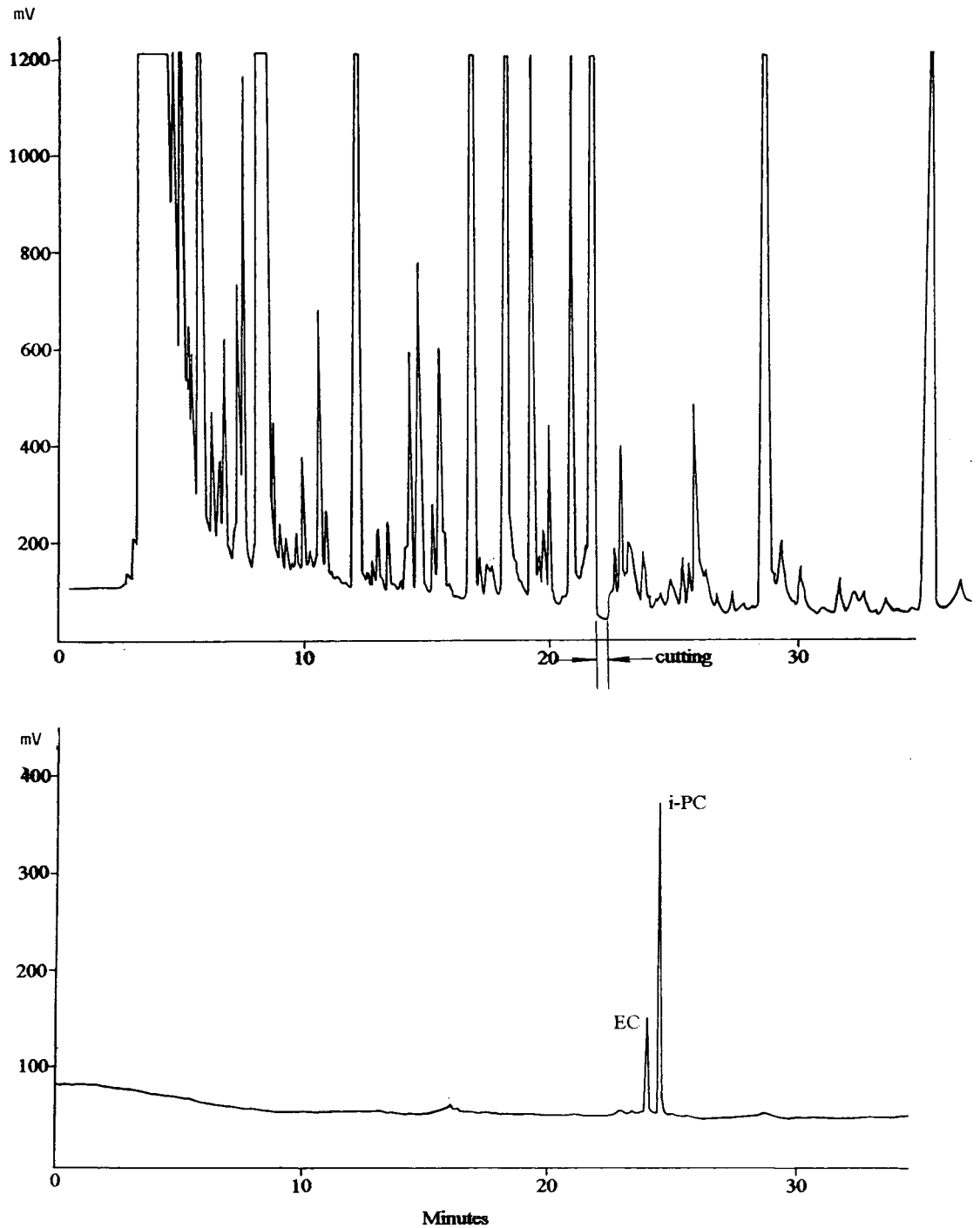

Fig. 2. Multi-dimensional gas chromatograms of a wine containing 22.1 ppb of EC. Left: capillary precolumn chromatogram obtained by FID without heart-cutting. Right: capillary precolumn chromatogram obtained by FID (top) and an analytical column chromatogram obtained by TSD (bottom) with heart-cutting.

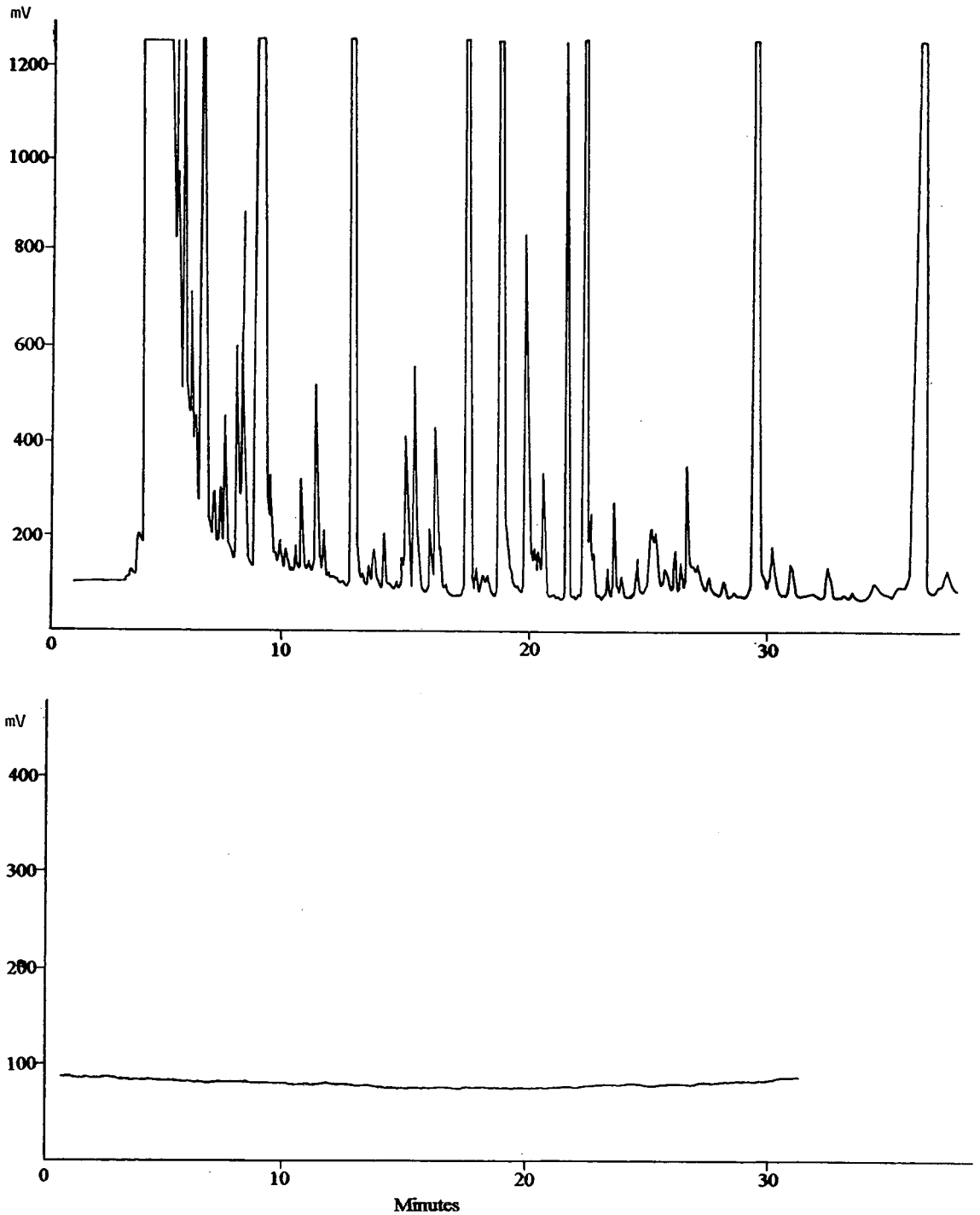

Fig. 2 (*continued*).

Table 1
Measurement precision

Sample	Concentration measured (ppb)	Mean value (ppb)	R.S.D. (%)
Liquor	123.3, 123.7, 124.3, 122.2, 130.8, 122.2, 125.7	124.6	2.0
Rice wine	72.6, 70.0, 68.2, 70.7, 67.3, 66.4, 67.0	68.9	3.0

3.3. Calibration and calculation

From 10 to 500 ppb of EC, the measured relationship between peak-intensity ratios (y) and concentration of EC (x) for the calibration mixtures can be expressed by the regression equation $y = 0.0007 + 0.0161x$, with a correlation coefficient of 0.9994. This shows that the linearity is very satisfactory, and the straight line almost passes through the origin.

3.4. Precision and accuracy

The precision of the method was calculated by analysing seven replicates each for two typical Chinese wines, one a distilled liquor and the other a rice wine. The results obtained are given in Table 1.

The assay accuracy of the method was determined by analysing a wine sample that contained 22.1 ppb of EC as the mean value of three determinations. To this wine sample, 50 ppb of EC were added prior to extraction and the mean recovery determined was 96%.

4. Conclusion

Using a nitrogen-specific detector and a special internal standard technique, a multi-dimensional gas chromatographic method was developed that offers a routine method for detecting ethyl carbamate in alcholic beverages.

References

[1] C.S. Ough, *J. Agric. Food Chem.*, 24 (1976) 323.
[2] C.S. Ough, *J. Agric. Food Chem.*, 24 (1976) 328.
[3] R.L. Tatken and R.L. Lewis, Sr. (Editors), *Registry of Toxic Effects of Chemical Substances*, Vol. 1, US Department of Health and Human Services, Cincinnati, OH, 1981–82, p. 829.
[4] *Canadian Food and Drug Regulations (with Amendments to December 1986)*, Department of National Health and Welfare, Ottawa, 1981, Division 16, Table 14.
[5] M.J. Dennis, N. Howarth, R.C. Massey, I. Parker, M. Scotter and J.R. Startin, *J. Chromatogr.*, 369 (1986) 193.
[6] R.H.M. Van Ingen, I.M. Nijssen, F. Van der Berg and H. Maarse, *J. High. Resolut. Chromatogr. Chromatogr. Commun.*, 10 (1987) 151.
[7] W.R. Sponholz, *Git Spez. Chromatogr.*, 11 (1991) 86–90 and 92–93.
[8] M.J. Dennis, R.C. Massey, M. Pointer and P. Willetts, *J. High Resolut. Chromatogr.*, 13 (1990) 247.
[9] G. Walker, W. Winterlin, H. Fonda and J. Seiber, *J. Agric. Food Chem.*, 22 (1974) 944.
[10] W. Drexler and E.R. Schmid, *Ernährung*, 13 (1989) 591.
[11] F.L. Joe, D.A. Kline, E.M. Miletta, J.A. Roach, E.L. Roseboro and T. Fazio, *J. Assoc. Off. Anal. Chem.*, 60 (1977) 509.
[12] U. Baumann and B. Zimmerli, *Mitt. Geb. Lebensmittelunters Hyg.*, 77 (1986) 327.
[13] R.I. Aylott, A.S. McNeish and D.A. Walker, *J. Inst. Brew.*, 93 (1987) 382.
[14] R. Bailey, D. North, D. Myatt and J.F. Lawrence, *J. Chromatogr.*, 369 (1986) 199.
[15] B.P.-Y. Lau, D. Page and D. Weber, *Can. J. Spectrosc.*, 34 (1989) 53.

ELSEVIER

Journal of Chromatography A, 695 (1995) 267–277

JOURNAL OF CHROMATOGRAPHY A

Sampling characteristics of octadecylsiloxane-bonded silica particle-embedded glass fiber discs for solid-phase extraction

Mary L. Mayer[a], Colin F. Poole[a,1,*], Michael P. Henry[b]

[a]*Department of Chemistry, Wayne State University, Detroit, MI 48202, USA*

[b]*ANSYS, Inc., 2 Goodyear, Irvine, CA 92718, USA*

First received 3 August 1994; revised manuscript received 13 December 1994; accepted 14 December 1994

Abstract

Forced flow planar chromatography was used to characterize the physical and retention properties of an octadecylsiloxane-bonded particle-embedded glass fiber medium used for solid-phase extraction. The carbon loading, intraparticle porosity, binding capacity, and hydrophobicity index indicate that the medium has a large volume of bonded phase essentially filling the pore volume. The interparticle porosity and specific permeability indicate favorable flow characteristics. The flow resistance parameter and the diameter of the largest pore by the bubble method are consistent with a macroscopic homogeneous medium structure free of holes and channels. The silanophilic index indicates a significant concentration of accessible silanol groups and/or other strong hydrogen-bond acid sites. A comparison of retention characteristics to a common cartridge sorbent using the solvation parameter model indicated that the cartridge sorbent had a more favorable cavity term for retention but the particle-embedded glass fiber medium was more competitive with the sample solvent, water–methanol (99:1), for the retention of polar compounds with significant dipole-type interactions and those behaving as hydrogen-bond bases. The physical and retention properties of the particle-embedded glass fiber medium confirm its suitability for use in solid-phase extraction.

1. Introduction

The conventional approach to solid-phase extraction takes advantage of the sampling characteristics of short chromatographic columns, generally referred to as cartridges [1]. New developments in solid-phase extraction for water analysis include the introduction of particle-loaded membranes [2–4], particle-embedded glass fiber discs [5,6], and solvent free microextractions using polymer coated fibers [7]. Rigid discs containing sorbent particles embedded in a glass fiber supporting matrix for solid-phase extraction were introduced in 1990. It is claimed that these low-bed-mass extraction discs offer a number of advantages over conventional solid-phase extraction cartridge devices, such as elimination of channeling, cleaner extracts, reduced sample and solvent requirements, and ease of in situ derivatization.

Inadequate control of the packing density of conventional solid-phase extraction cartridge devices results in channeling during sample applica-

* Corresponding author.

[1] Present address: Department of Chemistry, Imperial College of Science, Technology and Medicine, South Kensington, London SW7 2AY, UK.

0021-9673/95/$09.50
SSDI 0021-9673(94)01238-5

tion and is the principle cause of poor sampling performance and, under some circumstances, results in poor reproducibility [8]. A further consequence of channeling is that cartridge sorbent beds are larger than they need be to avoid premature breakthrough resulting in increased non-specific sorption of the sample matrix and recovered extracts that are more complex than is desirable for trace analysis. These problems are avoided in a rigid matrix of low bed mass. Use of the disc format increases the cross-sectional area available to the sample compared to cartridge columns, increasing sample processing rates.

Forced flow planar chromatography provides a unique approach to study the physical and retention characteristics of particle-loaded membranes under conditions similar to those used in solid-phase extraction [9,10]. A wide range of physical characteristics relevant to their function as sorbents are easily and quantitatively obtained providing a framework to establish the general range of optimum sampling conditions and to evaluate specific conditions that affect the recovery of individual analytes. An extension of these studies to particle-embedded glass fiber discs is the purpose of this paper.

2. Experimental

Organic solvents and water were Omnisolv grade from EM Science (Gibbstown, NJ, USA). Other chemicals were reagent grade or better and obtained from several sources. Glass fiber sheets containing embedded octadecylsiloxane-bonded silica particles of the same composition used to prepare SPEC®-47-C18AR (cat. nos. 747-19), a 47-mm extraction disc used for environmental applications, were provided by ANSYS (Irvine, CA, USA).

The glass fiber sheets were cut to 20×10 cm pieces and supported by an identical sized sheet of aluminum of a similar thickness to that used in the preparation of aluminium backed TLC plates. All four edges of the glass fiber sheets were sealed with paraffin wax and two narrow channels cut through the medium with a scalpel at positions corresponding to the inlet and outlet troughs in the cushion insert used to direct the eluent flow. The glass fiber medium was installed in the overpressured development chamber without using a mask around the medium and its support.

2.1. Forced flow chromatography

The apparatus used to determine the physical and retention properties of the particle-embedded glass fiber medium is described in detail elsewhere [9,11]. It consists of a Chrompres 25 overpressured development chamber (Factory of Laboratory Instruments, Budapest, Hungary) operated at a cushion pressure of 20 bar, a Model 2350 reciprocating-piston pump (ISCO, Lincoln, NE, USA), a Supco DPG-500 high-pressure transducer (Cole-Parmer, Chicago, IL, USA), a Rheodyne 7125 valve injector with a 20-μl sample loop (Anspec, Ann Arbor, MI, USA), and a UV-50 variable-wavelength detector (Varian Instruments, Walnut Creek, CA, USA) operated at $\lambda = 270$ nm and 0.1 AU full scale. A Nelson Analytical 9000 series A/D interface (PE Nelson, Cupertino, CA, USA) and an Epson Apex 200 computer running under PE Nelson 2100 PC integrator software (revision 5.1) were used for data acquisition. A microburette was used to accurately calibrate the flow-rate.

The theoretical basis and experimental protocol for the methods used to calculate the porosity, permeability, apparent particle diameter, and flow resistance of the particle-loaded membranes by forced flow planar chromatography are outlined elsewhere [8,9,12]. The same procedures were used in these studies for the particle-embedded glass fiber medium. The hydrophobicity index, based on the ratio of the capacity factors of *n*-pentylbenzene and *n*-butylbenzene in methanol–water (4:1), and the silanophilic index, from the ratio of the capacity factors of caffeine and phenol in methanol–water (3:7), were determined according to the scales described by Kimata et al. [13]. A second estimate of the hydrophobicity index, based on the ratio of the capacity factors for anthracene and benzene in acetonitrile–water (65:35), and the

silanophilic index, from the ratio of the capacity factors for N,N-diethyl-*m*-toluamide and anthracene in acetonitrile, were determined as described by Walters [14].

2.2. Flow-through porosity and binding capacity

Measurement of flow-through porosity by the bubble point method was made by retaining an 8-mm disc of the C18AR medium in an ANSYS solid-phase extraction device. Isopropanol was the wetting solvent and nitrogen was applied to the bottom of the disk until the gas just broke through to form a bubble. Eq. 1 was used to calculate the diameter of the largest pore.

$$d = C(\gamma/P) \tag{1}$$

where d is the pore diameter (μm), γ the surface tension (dynes/cm), P pressure in p.s.i. and C is a constant equal to 0.415 when the above units are used.

Binding capacities of the C18AR medium were determined by pumping solutions of a well-retained compound through a disc of known mass, until breakthrough occurred. The quantity bound under these conditions is expressed as a percentage by weight of the total disc mass.

2.3. Calculation of medium properties from the breakthrough model

In previous studies it was demonstrated that a breakthrough model proposed by Lovkvist and Jonson [15] provides a reasonable description of the sampling characteristics of particle-loaded membrane and cartridge sampling devices, Eq. 2 [8,9,16]

$$V_B = (a_o + a_1/n + a_2/n^2)^{-1/2}(1 + k_s)V_m \tag{2}$$

where a_o, a_1 and a_2 are constants determined for a particular breakthrough level, n the number of theoretical plates for the sampling device, k_s the solute capacity factor with the sample solvent as the mobile phase, and V_m the holdup volume of the sampling device. Under normal sampling conditions n is small (usually < 20) and does not vary strongly with flow-rates in the normal operating range. The quotient in Eq. 2 containing n varies over a narrow numerical range and V_m is fixed by the design of the device. Thus the most important factor for determining the breakthrough volume under normal sampling conditions is the solute capacity factor.

Poole and co-workers [8,10,16,17] have shown that the retention characteristics of a sorbent under solid-phase sampling conditions can be predicted for a wide range of solutes using a solvation parameter model set up as indicated below

$$\log SP = c + mV_X/100 + rR_2 + s\pi_2^H + a\alpha_2^H + b\beta_2^H \tag{3}$$

where SP is the correlated solute property, in this case either the capacity factor at a fixed mobile phase composition or the breakthrough volume determined for the sample solvent, V_X is the solute's characteristic volume, R_2 the solute's excess molar refraction, π_2^H is a measure of the solute's ability to stabilize a neighboring dipole by virtue of its capacity for orientation and induction interactions, and α_2^H and β_2^H are parameters characterizing the solute's hydrogen-bond acidity and hydrogen-bond basicity, respectively. The system constants m, r, s, a, b and c are solute independent and characteristic of the sampling system (sorbent and sample solvent). These parameters are evaluated by multiple linear regression analysis by determining the property SP for a series of solutes with known explanatory variables. Once established, the property SP can be estimated for any solute under the same conditions provided that the solute's explanatory variables are known or can be reasonably estimated from empirical combining rules [18].

The retention properties of the particle-embedded glass fiber medium were determined as the capacity factors for a series of varied solutes as a function of mobile phase composition over the range methanol to methanol–water (3:7). The data were fitted to a linear or second order polynomial equation of the type

$$\log k_s = z_o + z_1\Theta + z_2\Theta^2 \tag{4}$$

where Θ is the volume fraction of methanol in water (% v/v). The coefficients z_o, z_1, and z_2 and the statistics for the fit of the experimental data to Eq. 4 are summarized in Table 1. The values of k_s in water–methanol (99:1) were obtained by extrapolation using Eq. 4. The extrapolated capacity factors contain additional uncertainty over the experimental values. This was unavoidable because of the excessively long retention times and difficult to detect broad and distorted peaks observed at low methanol concentrations for the solutes which made direct measurements impossible to obtain. The experimental values of $\log k_s$ and the extrapolated values for $\log k_s$ in water–methanol (99:1) were used to determine the system constants in Eq. 3. The explanatory variables for the solutes used in Eq. 3 were taken from refs. [18–20]. For convenience they are assembled in Table 2. The characteristic molecular volumes were calculated from incremental constants using the method described by Abraham and McGowan [21]. Multiple linear regression analysis was performed using the program SPSS V4.0 (SPSS, Chicago, IL, USA) on an Epson Apex 200 personal computer.

3. Results and discussion

3.1. Physical characteristics of the glass fiber medium

Forced flow planar chromatography enabled the determination of a number of physical and chemical properties of the particle-embedded glass fiber medium to be made that would have been difficult by other means. These are summa-

Table 1
Coefficients for the variation of retention for the particle-embedded glass fiber medium with methanol–water composition, Eq. 4

Solute	z_o	z_1 ×10²	z_2 ×10⁴	r	Range (% v/v methanol)
Benzene	2.172	−2.70		1.00	100–50
Toluene	4.936	−9.10	4.029	1.00	100–50
n-Propylbenzene	4.459	−4.80		1.00	100–70
Naphthalene	3.179	−3.50		1.00	100–60
Anthracene	4.628	−4.80		1.00	100–70
Chlorobenzene	2.948	−3.40		1.00	100–60
1,2-Dichlorobenzene	3.441	−3.90		0.99	100–70
1,2,4-Trichlorobenzene	3.943	−4.20		1.00	100–70
Bromobenzene	2.806	−3.10		1.00	100–60
1,2-Dibromobenzene	3.531	−3.80		1.00	100–70
Pentan-2-one	1.531	−3.00	0.884	1.00	100–30
Hexan-2-one	1.621	−2.30		0.99	100–30
Nitrobenzene	2.098	−2.70		1.00	100–30
Anisole	2.399	−3.00		1.00	100–30
Benzaldehyde	1.749	−2.50		1.00	100–30
Benzonitrile	2.219	−4.20	1.461	1.00	100–30
Acetophenone	2.325	−4.20	1.280	1.00	100–40
Benzyl alcohol	1.659	−3.40	1.027	1.00	100–30
1-Phenylethanol	2.198	−4.50	1.601	1.00	100–30
Benzamide	1.492	−4.30	1.821	1.00	100–30
Acetanilide	2.029	−4.70	1.905	1.00	100–30
Phenol	1.251	−2.20		1.00	100–30
2-Chlorophenol	1.927	−2.80		1.00	100–30
2-Methylphenol	1.959	−2.90		1.00	100–30
4-Methylphenol	1.824	−2.70		1.00	100–30

Table 2
Explanatory variables for the solvation parameter model, Eq. 3

Solute	V_x/100	R_2	π_2^H	α_2^H	β_2^H
Naphthalene	1.085	1.340	0.92		0.20
Anthracene	1.454	1.340	0.92		0.20
Benzene	0.716	0.610	0.52		0.14
Toluene	0.857	0.601	0.52		0.14
n-Propylbenzene	1.139	0.604	0.50		0.15
Chlorobenzene	0.839	0.718	0.65		0.07
1,2-Dichlorobenzene	0.961	0.872	0.78		0.04
Bromobenzene	0.891	0.882	0.73		0.09
1,2-Dibromobenzene	1.066	1.190	0.96		0.04
1,2,4-Trichlorobenzene	1.083	0.980	0.81		
Pentan-2-one	0.828	0.143	0.68		0.51
Hexan-2-one	0.969	0.136	0.68		0.51
Nitrobenzene	0.891	0.871	1.11		0.28
Acetophenone	1.014	0.818	1.01		0.48
Anisole	0.916	0.708	0.75		0.29
Benzonitrile	0.871	0.742	1.11		0.33
Benzaldehyde	0.873	0.820	1.00		0.39
Benzyl alcohol	0.916	0.803	0.87	0.33	0.56
1-Phenylethanol	1.057	0.784	0.83	0.30	0.66
Acetanilide	1.113	0.870	1.40	0.50	0.67
Benzamide	0.973	0.990	1.50	0.49	0.67
Phenol	0.775	0.805	0.89	0.60	0.30
2-Chlorophenol	0.898	0.853	0.88	0.32	0.31
2-Hydroxytoluene	0.916	0.840	0.86	0.52	0.30
4-Hydroxytoluene	0.916	0.820	0.87	0.57	0.31

rized in Table 3 along with some representative values obtained for an octadecylsiloxane-bonded silica particle-loaded membrane. The total porosity of the particle-embedded medium is similar to that of the particle-loaded membrane (both of which are similar to typical values for slurry-packed HPLC columns). This is an indication of a good packing structure. The particle-embedded glass fiber medium, and to a lesser extent the particle-loaded membrane, posses very little intraparticle porosity. This results from the dense loading of octadecylsiloxane groups essentially filling the pore volume and is confirmed by the relative weight of bonded phase as a fraction of the disc weight, the high binding capacity of the discs, and the high values for the hydrophobicity indexes. Given the intended use of the particle-embedded medium for solid-phase extraction such large volumes of octadecylsiloxane groups are advantageous in promoting retention and favorable breakthrough volumes.

The silanophilic indexes are consistent with a significant concentration of accessible silanol groups and/or other strong hydrogen-bond acid sites. The high hydrophobicity index and silanophilic index, taken together, are typical of polymeric octadecylsiloxane-bonded phases formed from multifunctional silanes in the presence of water. Such phases show greater resistance to acid hydrolysis for sampling aqueous solutions at low pH because of their abundant surface and polymer cross-links.

The interparticle porosity and high specific permeability of the particle-embedded medium indicate favorable flow characteristics. The glass fiber medium is a heterogeneous mixture of glass fibers and embedded sorbent particles with flow properties that can be represented by an optimum particle bed with an average particle

Table 3
Characteristic properties of the SPEC-C18AR particle-embedded glass fiber medium and a J.T. Baker ODS particle-loaded membrane

Property	Value	
	Particle-embedded medium	Particle-loaded membrane [9]
Total porosity, ϵ_T	0.51	0.52
Interparticle porosity, ϵ_u	0.47	0.37
Intraparticle porosity, ϵ_i	0.04	0.15
Apparent average particle diameter, d_p (μm)	15.3	7.7
Specific permeability, B (10^{14} m^2)	8.38	2.5
Flow resistance parameter, ϕ	971	1000–1250
Diameter of largest pore (μm)	5	
Media density (g/ml)	0.49	
Weight of media that is carbon (% w/w)	9.1	
Media surface area (m^2/g)	250	
Average pore diameter of silica before bonding (nm)	8	6
Binding capacity of media (% w/w)	12	
Hydrophobicity index		
Kimata[1]	1.52	1.55
Walters[2]	4.81	5.38
Silanophilic index		
Kimata[3]	0.72	0.64
Walters[4]	1.74	1.34

[1] Normal range of values characterized as low to high 1.3 to 1.52 [13].
[2] Values >4.0 characterized as highly loaded [14].
[3] Values 0.42 to 0.66 characteristic of bonded phases formed with trifunctionalsilanes [13].
[4] Values >1.2 characterized as high [14].

diameter of 15.3 μm. The favorable flow resistance parameter and the diameter of the largest pore by the bubble method, 5 μm, are consistent with a macroscopic homogeneous structure free of holes and channels.

3.2. Retention characteristics of the glass fiber medium

The system constants for the solvation parameter model as a function of mobile phase composition are summarized in Table 4. The statistics of the fit for the measured values to Eq. 3 are within normal expectations and the estimated values for water–methanol (99:1) are acceptable for the estimation of safe sampling volumes. Clearly, the estimated system constants for water–methanol (99:1) are not as good as the experimental values for the middle range of solvent compositions where the capacity factors are most accurately determined. Some deviation from the extrapolated values for k_s in water–methanol (99:1) can be anticipated due to the irregular changes in k_s normally observed at low modifier concentrations.

For evaluation the system constants as a function of mobile phase composition are plotted in Fig. 1. Only the cavity term (m-constant) and interactions with n- and π-electron pairs (r-constant) have positive values and favor extraction by the solvated sorbent. The m-constant increases with decreasing methanol concentration indicating that collapsing the solute cavity in the mobile phase becomes increasingly more favorable as the water structure builds up in the mobile phase. By comparison the r-constant is much less significant and not a major contributing factor to retention. All polar interactions

Table 4
System constants and statistics for the fit to the solvation parameter model for the data obtained by forced flow planar chromatography

Mobile phase composition (% v/v methanol)	System coefficients[a]						Statistics[b]			
	m	*r*	*s*	*a*	*b*	*c*	*R*	*S.E.*	*F*	*n*
100	0.58			−0.63	−0.42	−0.91	0.954	0.08	68	25
	(0.11)			(0.08)	(0.09)	(0.11)				
90	0.89	0.11	−0.18	−0.62	−0.72	−0.78	0.991	0.05	204	25
	(0.09)	(0.07)	(0.07)	(0.06)	(0.06)	(0.07)				
80	1.27	0.12	−0.39	−0.48	−1.07	−0.61	0.990	0.06	186	25
	(0.12)	(0.09)	(0.10)	(0.07)	(0.12)	(0.10)				
70	1.63	0.11	−0.36	−0.52	−1.40	−0.61	0.992	0.07	210	24
	(0.14)	(0.10)	(0.11)	(0.08)	(0.13)	(0.11)				
60	1.75	0.27	−0.45	−0.63	−1.49	−0.44	0.992	0.06	163	20
	(0.21)	(0.09)	(0.09)	(0.07)	(0.15)	(0.15)				
50	1.93	0.19	−0.50	−0.53	−1.57	−0.21	0.988	0.05	84	17
	(0.23)	(0.09)	(0.09)	(0.07)	(0.16)	(0.16)				
40	2.13	0.30	−0.39	−0.56	−1.84	−0.22	0.983	0.07	52	15
	(0.31)	(0.12)	(0.12)	(0.09)	(0.20)	(0.23)				
30	2.75	0.37	−0.48	−0.71	−1.65	−0.48	0.996	0.03	180	14
	(0.16)	(0.07)	(0.06)	(0.05)	(0.06)	(0.12)				
1	4.27		−0.37	−0.58	−2.45	−0.49	0.968	0.26	71	20
	(0.38)		(0.29)	(0.28)	(0.32)	(0.38)				

[a] Values in parentheses represent standard deviations.
[b] R = multiple linear regression coefficient, $S.E.$ = standard error in the estimate, F = Fischer F-statistic, and n = number of solutes.

favor retention in the mobile phase. The hydrogen-bond acidity of water dominates the polar interactions indicating that the solvated sorbent is unable to compete effectively with water for the retention of hydrogen-bond bases. The mobile phase is a stronger hydrogen-bond base than the solvated sorbent but changes in the hydrogen-bond base character of the system (a-constant) are not a strong function of the mobile phase composition.

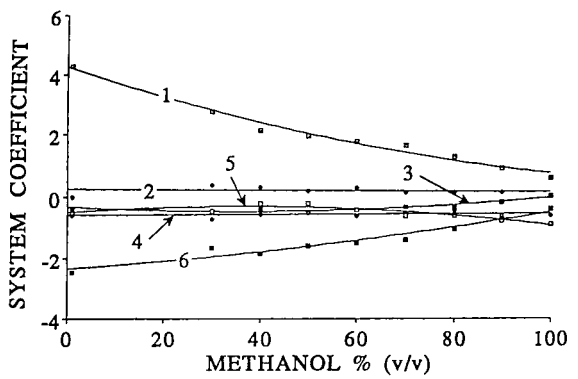

Fig. 1. Variation of the system coefficients as a function of the mobile phase composition for the octadecylsiloxane-bonded silica particle-embedded glass fiber medium. Identification: 1 = m; 2 = r; 3 = s; 4 = a; 5 = c; and 6 = b.

3.3. Comparison of retention characteristics of different extraction media

A comparison of the extraction properties of the octadecylsiloxane-bonded silica particle-embedded medium, particle-loaded membranes [10,16] and a typical cartridge sorbent [8] is summarized in Table 5. Differences in the system constants with the same bulk sample solvent composition are due to differences in the extraction properties of the solvated sorbent. The extraction properties of the Varian Sample Preparation Products particle-loaded membrane and the ANSYS particle-embedded medium, coincidentally, are virtually identical, with both being similar to the extraction properties of the

Table 5
Comparison of system constants for different octadecylsiloxane-bonded silica (ODS) sorbents used in solid-phase extraction

(i) Sample solvent 70% (v/v) methanol in water ($\log k_s$)

System constants	ANSYS ODS media	Varian ODS membrane	J.T. Baker ODS cartridge
m	1.63	1.63	2.12
r	0.11	0.11	0.16
s	−0.36	−0.37	−0.44
a	−0.52	−0.52	−0.32
b	−1.40	−1.40	−1.59
c	−0.61	−0.61	−0.71

(ii) Sample solvent 1% (v/v) methanol in water

	Extrapolation method ($\log k_s$)		Direct method ($\log V_B$)
	ANSYS ODS media	J.T. Baker ODS cartridge	J.T. Baker ODS membrane
m	4.27	5.65	5.14
r		0.70	
s	−0.37	−0.76	−0.92
a	−0.58	−0.40	−1.05
b	−2.45	−3.26	−2.24
c	−0.49	−1.18	−1.23

J.T. Baker cartridge sorbent with methanol–water (7:3, v/v) as the sample solvent. The choice of methanol–water (7:3) as the mobile phase for comparison was dictated by the high flow resistance of the Varian Sample Preparation Products membrane, which prevented useful measurements by forced flow planar chromatography from being made in predominantly aqueous mobile phases [10]. The results serve the purpose of indicating that the extraction properties of the particle-embedded medium are in no way atypical of expected sorption interactions for more familiar solid-phase extraction sorbents.

Also compiled in Table 5 are estimated system constants for the ANSYS particle-embedded fiber glass medium and the J.T. Baker cartridge sorbent [8] obtained by the extrapolation method as well as system constants determined by the direct method for a J.T. Baker particle-loaded membrane [16] for more typical solid-phase extraction conditions with water–methanol (99:1) as the sample solvent. The most noticeable difference between the three materials is the greater difficulty of cavity formation in the particle-embedded glass fiber medium (*m*-constant), which result in a decrease in general retention, accompanied by a more favorable capacity for dipole-type interactions (*s*-constant), which leads to a relative increase in the retention of dipolar and polarizable compounds. The particle-embedded medium and the particle-loaded membrane have a similar hydrogen-bond acidity (*b*-constant) and are more competitive with water for the retention of hydrogen-bond base solutes than is the cartridge sorbent. The cartridge and particle-embedded medium have similar hydrogen-bond basicity (*a*-constant) and are more competitive with water than the particle-loaded membrane sorbent for the retention of

hydrogen-bond acids. As a group the three sampling devices show similar trends in their retention characteristics with individual differences in the capacity for specific intermolecular interactions that are not unexpected for bonded phases of the octadecylsiloxane type.

3.4. Contribution of solute properties to retention

The difference in estimated retention properties of the particle-embedded glass fiber medium and the cartridge sorbent can be highlighted by considering the contribution of individual intermolecular interactions to the retention of a few solutes with varied properties, Table 6. These are broken out as the contribution of solute size and non-polar interactions represented by $(mV_x/100)$ with possibly a contribution from the c term in Eq. 3, and individual polar interactions represented by rR_2, $s\pi_2^H$, $a\alpha_2^H$, and $b\beta_2^H$. For non-polar and weakly polar solutes like n-propylbenzene the cartridge sorbent is more retentive because of its more favorable cavity term supplemented by a small contribution from the rR_2 term. For polar compounds the difference in retention properties is less marked due to the more favorable dipole–dipole, dipole–induced dipole and solute hydrogen-bond base interactions of the particle-embedded media compared to those of the cartridge sorbent. Most dipolar compounds are also hydrogen-bond bases and the difference in retention for compounds like benzonitrile, acetophenone, anisole, hexan-2-one, and heptanal is not as great as for solutes lacking significant polar interactions. The difference in the sum of the polar interactions does not completely offset the difference in ease of cavity formation so that the cartridge sorbent shows greater retention overall. When the $a\alpha_2^H$ term is considered it favors retention by the cartridge sorbent for compounds like phenol, 1-phenylethanol, and hexan-1-ol, but this advantage is offset by the more favorable dipole and solute hydrogen-bond base interactions with the particle-embedded media.

Table 6
Contribution of different intermolecular interactions to retention for octadecylsiloxane-bonded silica particle-embedded glass fiber media and a cartridge sorbent

Solute	Sorbent type	Intermolecular interactions						Estimated log k_s
		$mV_x/100$	rR_2	$s\pi_2^H$	$a\alpha_2^H$	$b\beta_2^H$	c	
n-Propylbenzene	Cartridge	6.44	0.42	−0.38		−0.49	−1.18	4.8
	Glass fiber	4.86		−0.19		−0.37	−0.49	3.8
Benzonitrile	Cartridge	4.92	0.52	−0.84		−1.08	−1.18	2.3
	Glass fiber	3.72		−0.41		−0.81	−0.49	2.0
Acetophenone	Cartridge	5.73	0.49	−0.77		−1.56	−1.18	2.8
	Glass fiber	4.33		−0.37		−1.18	−0.49	2.2
Phenol	Cartridge	4.38	0.56	−0.68	−0.24	−0.98	−1.18	1.9
	Glass fiber	3.31		−0.33	−0.35	−0.74	−0.49	1.4
1-Phenylethanol	Cartridge	5.97	0.55	−0.63	−0.12	−2.15	−1.18	2.4
	Glass fiber	4.51		−0.31	−0.17	−1.62	−0.49	1.9
Anisole	Cartridge	5.18	0.50	−0.57		−0.95	−1.18	3.0
	Glass fiber	3.91		−0.28		−0.71	−0.49	2.4
Hexan-2-one	Cartridge	5.47	0.10	−0.52		−1.66	−1.18	2.2
	Glass fiber	4.14		−0.25		−1.25	−0.49	2.2
Hexanal	Cartridge	5.48	0.10	−0.49		−1.47	−1.18	2.4
	Glass fiber	4.14		−0.24		−1.25	−0.49	2.2
Hexan-1-ol	Cartridge	5.72	0.15	−0.32	−0.15	−1.56	−1.18	2.7
	Glass fiber	4.32		−0.16	−0.21	−1.18	−0.49	2.3

4. Conclusions

Forced flow planar chromatography provides a versatile approach to study the characteristic physical and retention properties of glass fiber media and particle-loaded membranes intended for use in solid-phase extraction. In this way it is demonstrated that the octadecylsiloxane-bonded, particle-embedded, glass fiber media are macroscopically homogeneous with favorable flow characteristics for solid-phase extraction. The high loading of bonded phase results in retention characteristics for the particle-embedded glass fiber media which are similar to those of particle-loaded membranes and conventional cartridge sorbents.

The solvation parameter model provides insight into the composition of fundamental interactions that are responsible for the retention of individual solutes. The model provides a good description of the experimental data for those regions of the mobile phase composition where accurate capacity factor measurements can be made. For the case most relevant to practical applications of solid-phase extraction, a sample solvent of water–methanol (99:1), the fit is not as good because excessive retention times prevent direct measurement of the capacity factor values. Estimated values obtained by polynomial extrapolation are only approximate because of the length of the extrapolation employed (from water–methanol ratios of 7:3 to 99:1) and because of the likelihood that at very low methanol compositions deviation from the results obtained at higher methanol compositions probably occur. In the only case where it has proven possible to make direct capacity factor measurements for a cyanopropylsiloxane sorbent under solid-phase extraction conditions the deviations from values predicted by extrapolation and measured experimentally are small but significant [22]. For this reason the prediction of $\log k_s$ values by Eq. 3 cannot be made to better than 0.26 log units from the extrapolated experimental data, which is a significantly larger uncertainty than is typical of the equation fit to experimental data of about 0.05 to 0.08 log units. Not withstanding the uncertainty with which $\log k_s$ can be estimated the solvation parameter model provides a useful first round prediction of the breakthrough volume of a solute using Eq. 2 given that the value for the holdup volume, V_m, is easily calculated for any extraction disc (or could be estimated from the data given in Table 3) and the kinetic component, which has a narrow numerical range for any selected level of breakthrough [8], is taken as a psuedoconstant. The complementary explanatory variables to the system constants are known for in excess of 1000 compounds [18–20], and others can be estimated from simple combining rules, making the application of Eq. 3 to the estimation of breakthrough volumes using the particle-embedded glass fiber media widely accessible for many compounds of environmental interest.

References

[1] C.F. Poole and S.K. Poole, *Chromatography Today*, Elsevier, Amsterdam, 1991.
[2] D.R. Hagen, C.G. Markell, G. Schmitt and D.D. Blevins, *Anal. Chim. Acta*, 236 (1990) 157.
[3] M.L. Mayer and C.F. Poole, *Anal. Chim. Acta*, 294 (1994) 113.
[4] D. Barcelo, S. Chiron, S. Lacorte, E. Martinez, J.S. Salau and M.C. Hennion, *Trends Anal. Chem.*, 13 (1994) 352.
[5] D.D. Blevins and S.K. Schultheis, *LC–GC Mag.*, 12 (1994) 12.
[6] G.M. Hearne and D.O. Hall, *Am. Lab.*, 1993, 28H.
[7] Z. Zhang, M.J. Yang and J. Pawliszyn, *Anal. Chem.*, 66 (1994) 844A.
[8] K.G. Miller and C.F. Poole, *J. High Resolut. Chromatogr.*, 17 (1994) 125.
[9] W.P.N. Fernando, M.L. Larrivee and C.F. Poole, *Anal. Chem.*, 65 (1993) 588.
[10] M.L. Mayer, S.K. Poole and C.F. Poole, *J. Chromatogr. A*, (1995) in press.
[11] W.P.N. Fernando and C.F. Poole, *J. Planar Chromatogr.*, 4 (1991) 278.
[12] W.P.N. Fernando and C.F. Poole, *J. Planar Chromatogr.*, 3 (1990) 389.
[13] K. Kimata, K. Iwaguchi, S. Onishi, K. Jinno, R. Eksteen, K. Hosoyo, M. Araki, and N. Tanaka, *J. Chromatogr. Sci.*, 27 (1989) 721.
[14] M.J. Walters, *J. Assoc. Off. Anal. Chem.*, 70 (1987) 465.
[15] P. Lovkvist and J.A. Jonson, *Anal. Chem.*, 59 (1987) 818.

[16] M.L. Larrivee and C.F. Poole, *Anal. Chem.*, 66 (1994) 139.
[17] S.K. Poole and C.F. Poole, *Analyst*, submitted for publication.
[18] M.H. Abraham, *Chem. Soc. Rev.*, 22 (1993) 73.
[19] M.H. Abraham, J. Andonian-Haftvan, G.S. Whiting, A. Leo and R.S. Taft, *J. Chem. Soc. Perkin Trans.*, 2 (1994) 1777.
[20] M.H. Abraham, *J. Phys. Org. Chem.*, 6 (1993) 95.
[21] M.H. Abraham and J.C. McGowan, *Chromatographia*, 23 (1987) 243.
[22] D.S. Siebert and C.F. Poole, *J. High Resolut. Chromatogr.*, in press.

ELSEVIER

Journal of Chromatography A, 695 (1995) 279–285

JOURNAL OF CHROMATOGRAPHY A

On-line kinetic monitoring for biochemical reactions using multi-point detection in high-performance capillary electrophoresis

Peng Sun, Richard A. Hartwick*

Department of Chemistry, State University of New York at Binghamton, Binghamton, NY 13902, USA

First received 3 August 1994; revised manuscript received 7 October 1994; accepted 7 October 1994

Abstract

The potential utility of high-performance capillary electrophoresis for on-line kinetic monitoring of biochemical reactions is demonstrated using a multi-point detection method. The adenosine deaminase-catalyzed deamination of adenosine to inosine is studied. The deamination speed increases with the increase in enzyme concentration in the run buffer. Degradation of heme protein, myoglobin, has been investigated by this method. Under certain electrophoretic conditions, the degradation follows first-order kinetics. The degradation rate constant increases with an increase in temperature and the electric field applied to the capillary does not appreciably effect the degradation rate.

1. Introduction

High-performance capillary electrophoresis (HPCE), as a complementary method to high-performance liquid chromatography (HPLC), has become an important analytical technique [1–5]. It has been successfully used for the separation of small ions [6,7], peptides [8,9], carbohydrates [10], polymers such as proteins and nucleic acids [11–14] and chiral molecules [15–18]. The broad application range and the high performance demonstrated by HPCE have attracted much interest. More recent research efforts involve the application of HPCE to the study of biomolecular interactions such as determination of binding constants [19–21] and enzyme activities [22–24].

However, there has been little information in literature regarding the use of HPCE for monitoring reaction rates. Karger and co-workers [25,26] reported that degradation of myoglobin appeared to occur as temperature was elevated from 20 to 50°C because of the reduction of Fe^{3+} to Fe^{2+} in myoglobin. The conversion from Fe^{3+} to Fe^{2+} was found to follow first-order kinetics by adjusting the time that myoglobin spent in the capillary using electric field variations. To the best of our knowledge, no on-line kinetic study method has been published using HPCE. Recently, Srichaiyo and Hjertémn [27] developed a simple multi-point detection method for HPCE. They used this method to study the unexpected, discontinuous change of a DNA sample during an HPCE run. This method also has been used for the dispersive study of oligonucleotides in gel filled capillaries [28]. The simple multi-point

* Corresponding author.

SSDI 0021-9673(94)00967-8

detection method offers a very useful tool for the on-line monitoring of analytes for HPCE.

In this paper, the feasibility of using HPCE for on-line kinetic studies is demonstrated using a multi-point detection method. Enzyme catalyzed deamination of adenosine to inosine is studied by this method. The effect of enzyme concentration on the deamination speed is investigated. The degradation of myoglobin protein is also monitored by this method. The kinetics, influence of temperature and the electric field on the reaction are also presented.

2. Experimental

2.1. Reagents and materials

Adenosine (A), inosine (I), adenosine deaminase (ADA) from calf spleen and horse heart myoglobin [type III, iron present in the ferric(Fe^{3+})state] were obtained from Sigma (St. Louis, MO, USA). Tris(hydroxymethyl)aminomethane (Tris) was purchased from Bio-Rad Labs. (Richmond, CA, USA) and boric acid from Fisher Scientific (Fair Lawn, USA NJ). Reagent-grade 3-methylphenol was obtained from Aldrich (Milwaukee, WI, USA).

2.2. Apparatus

The experiments were performed on an HPCE apparatus which was designed and constructed in our laboratory. The instrument consisted of a laboratory-made Plexiglass box, a Spectra 100 UV detector (Thermo Separation Products, Freemont, CA, USA) a CZE 1000 PN 30 high-power supply (Spellman, Plainview, NY, USA) and a high-power supply local control (Chamonix Industries, Johnson City, NY, USA) for adjustment of the actual separation voltage. A special cell, which was fitted to the detector [28], was used for multi-point detection. The cell body was constructed by gluing two fabricated pieces of metal. There was a small hole in the center of the lower part of the cell and a ball lens was inserted. A fused-silica capillary with 150 cm total length (75 μm I.D. $\times$ 360 μm O.D.; Polymicro Technologies, Phoenix, AZ, USA) was used in this work. Four detection windows (with effective lengths of 35, 66.5, 97.5 and 129 cm) were opened on the capillary by burning off the external coating. The capillary was bent into loops with the four windows on top of each other in a slit located on the upper part of the cell. There was a securing arm crossing the slit on each side of the cell which kept the looped capillary in position and aligned in the slit. During an HPCE run, the solutes in the capillary could be detected four times as they passed through the light path at different times. The detection wavelength was 260 nm for adenosine and 214 nm for myoglobin. The detector rise time was 0.1 s. Neutral molecule, 3-methylphenol, was used as a reference standard in all the HPCE runs. The run buffer in the capillary was renewed after each run. 0.1 *M* Tris, 0.025 *M* boric acid buffer at pH 8.63 or 0.025 *M* borate buffer at pH 8.01 were used as run buffers. Temperature inside the Plexiglass box was increased by using a space heater and cooling was achieved with a fan. The electrophoregrams were processed on a SP-4400 integrator (Thermo Separation Products).

3. Results and Discussion

3.1. Enzyme-catalyzed adenosine deamination

ADA is a highly specific enzyme that catalyses the deamination of adenosine to inosine with liberation of NH_3 as follows [29]:

$$\text{adenosine} + H_2O \xrightarrow{\text{ADA}} \text{inosine} + NH_3$$

A genetic lack of adenosine activity causes an abnormality in purine nucleoside metabolism that selectively kills lymphocytes (a type of white blood cell) [30]. The consequent lack of lymphocytes mediates the immune response and can cause severe combined immunodeficiency disease. Without special protective measures, the disease is invariably fatal in infancy due to overwhelming infection. Enzyme catalyzed

deamination is an active area in biochemistry and clinical chemistry research.

Fig. 1 shows the electropherograms of an adenosine and inosine mixture sample before (a) and after (b) enzymatic reaction. It can be seen that within 10 min after the addition of ADA to the sample, all the adenosine is deaminated to inosine, since only one peak (inosine) is detected after the enzymatic reaction. To study the reaction rate and enzyme concentration influence on the reaction, different amounts of ADA have been added to run the buffer, and the looped capillary is then filled with this buffer. Fig. 2 represents the electropherograms obtained from the multi-point detection method. It can be seen that before the addition of ADA enzyme to the run buffer (Fig. 2a), no adenosine deamination happens. After ADA enzyme is added to the run buffer (Fig. 2b), adenosine starts to be deaminated to inosine.

In order to monitor the deamination of adenosine accurately, 3-methylphenol (P) has been used as a reference standard. According to

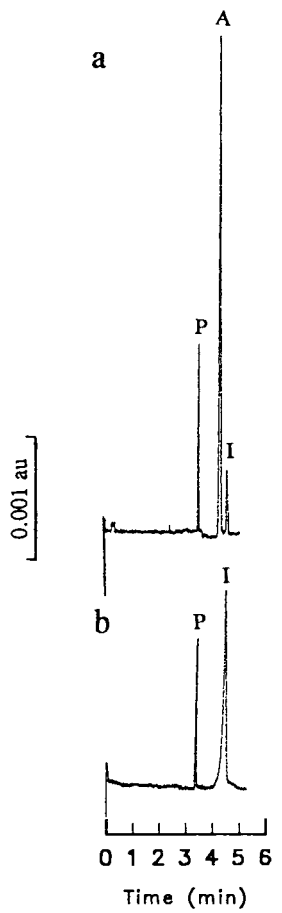

Fig. 1. Electropherograms of a mixture of adenosine (A), inosine (I) and 3-methylphenol (P). Sample was $2.76 \cdot 10^{-3}$ *M* adenosine and $4.86 \cdot 10^{-4}$ *M* inosine in water. Capillary: 75 μm I.D. × 360 μm O.D. bare capillary with 35 cm effective length. Electric field: 167 V/cm. Injection: 6 cm × 6 s. Run buffer: 0.025 *M* borate at pH 8.01. (a) Before adenosine deaminase treated; (b) after 10 min adenosine deaminase treated.

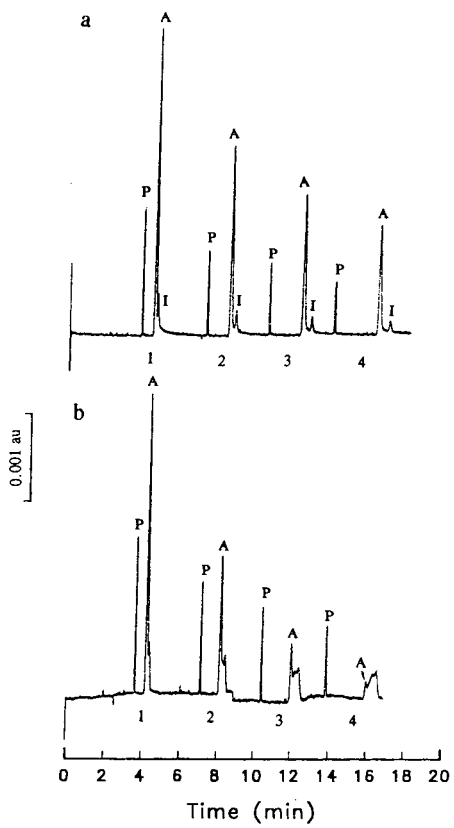

Fig. 2. Electropherograms of adenosine (A), inosine (I) and 3-methylphenol (P) mixture obtained from four consecutive detection. Capillary: 75 μm I.D. × 360 μm O.D. bare capillary with 150 cm total length. The four effective window lengths were 35, 66.5, 97.5 and 129 cm. Electric field: 167 V/cm. Injection: 6 cm × 10 s. Temperature: 25°C. Run buffer: (a) 0.025 *M* borate at pH 8.01; (b) 0.025 *M* borate with 0.04 units/ml adenosine deaminase at pH 8.01.

Beer's law, the absorbance of a specific sample solution can be expressed as:

$$A = \varepsilon bC \quad (1)$$

where A is the absorbance, ε is the molar extinction coefficient of sample, b is the light path length and C is the sample concentration. Since a ball lens is used to focus the light, the light path lengths may vary slightly at different detection windows. Consequently, the integrated absorbance areas obtained from different windows can change even if the amount of sample does not. However, this error can be corrected by using a reference standard, 3-methylphenol in this case. When samples pass through the first detection window, the absorbance of the reference standard is given by:

$$(A_P)_1 = \varepsilon_P b_1 (C_P)_1 \quad (2)$$

the absorbance of adenosine is:

$$(A_A)_1 = \varepsilon_A b_1 (C_A)_1 \quad (3)$$

So,

$$\frac{(A_A)_1}{(A_P)_1} = \frac{\varepsilon_A \cdot (C_A)_1}{\varepsilon_P \cdot (C_P)_1} \quad (4)$$

When the samples pass through the second window, the following relationship exists:

$$\frac{(A_A)_2}{(A_P)_2} = \frac{\varepsilon_A \cdot (C_A)_2}{\varepsilon_P \cdot (C_P)_2} \quad (5)$$

Since the reference standard 3-methylphenol (P) does not participate in the enzymatic reaction, the amount of 3-methylphenol stays constant as it migrates in the capillary. As a result, one can use the ratio of integrated absorbance area of adenosine (A) to that of the reference standard at different detection windows to monitor the change of adenosine reactant. Before enzyme ADA is added to the buffer, the deamination of adenosine does not occur. The amount of adenosine does not change as it migrates through the capillary. Theoretically, one should obtain the following results at four detection windows:

$$\frac{(A_A)_1}{(A_P)_1} = \frac{(A_A)_2}{(A_P)_2} = \frac{(A_A)_3}{(A_P)_3} = \frac{(A_A)_4}{(A_P)_4} = \text{constant} \quad (6)$$

Eq. 6 has been proven by the experimental data. In Fig. 3, it can be seen that before the addition of ADA enzyme to the run buffer (line 1), the ratio of integrated area of A to that of P does not change at different windows. A straight line parallel to the time axis is obtained. After the addition of ADA to the run buffer, the adenosine deamination occurs (Figs. 2 and 3).

It is known that under certain conditions, enzyme concentration can affect the rate of enzymatic reactions. The higher the enzyme concentration, the faster the rate [30]. Fig. 3 illustrates the influence of ADA concentration in the run buffer on the adenosine deamination. It can be seen that deamination of adenosine to inosine increases as the enzyme concentration in the buffer increases. When the enzyme concentration is lower than 0.04 units/ml, the amount of adenosine injected in the capillary is relatively

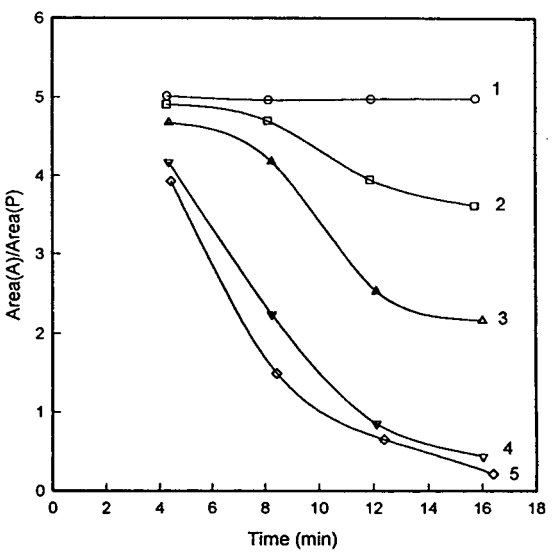

Fig. 3. Influence of adenosine deaminase (ADA) concentration in the run buffer on adenosine deamination. Electrophoretic conditions as in Fig. 2. The concentrations of ADA in the buffer were: (1) 0 units/ml; (2) 0.01 units/ml; (3) 0.02 units/ml; (4) 0.04 units/ml; (5) 0.06 units/ml.

high compared to ADA, and the reaction rate is slow at the beginning. As adenosine migrates in the capillary, the amount of adenosine decreases because of deamination, while the enzyme concentration does not change. Thus, more of the adenosine can be catalyzed by ADA, and reaction rate increases until it reaches a maximum value. After almost all of the adenosine has been deaminated, the rate decreases again. As the ADA concentration in the buffer is increased (lines 4 and 5 in Fig. 3), the deamination is faster at the beginning since the enzyme concentration becomes relatively high compared to adenosine. The reaction also slows down after most of the adenosine has been deaminated.

3.2. Kinetic study of myoglobin degradation

As has been reported before, sample degradation of myoglobin (MO) can occur with an increase in temperature [25,26]. A possible explanation for this is the reduction of Fe^{3+} (ferric) to Fe^{2+} (ferrous) metal ion coordinated to the heme group in myoglobin by either the reducing agent impurity in buffer system or autoreduction, in which an amino acid residue in myoglobin is the reducing agent [26]. Fig. 4 shows the electropherograms of a myoglobin and 3-methylphenol mixture sample obtained from four-point detection. The degradation of initial myoglobin (ferric form) occurs as temperature inside the capillary increases. Again, 3-methylphenol has been used as a reference standard. Fig. 5 demonstrates the temperature effect on the myoglobin degradation. It can be seen that the ratio of integrated absorbance of MO to that of P decreases faster at higher temperature (Fig. 5).

In order to determine the kinetic order of this degradation reaction, different functions of (A_{MO}/A_P) have been plotted against the migration time. The myoglobin degradation can be expressed by the following reaction:

$$\underset{\text{(type III)}}{MO} \rightarrow \underset{\text{(type II}}{MO'}$$

if this reaction obeys first order kinetics, the following equations exist [31]:

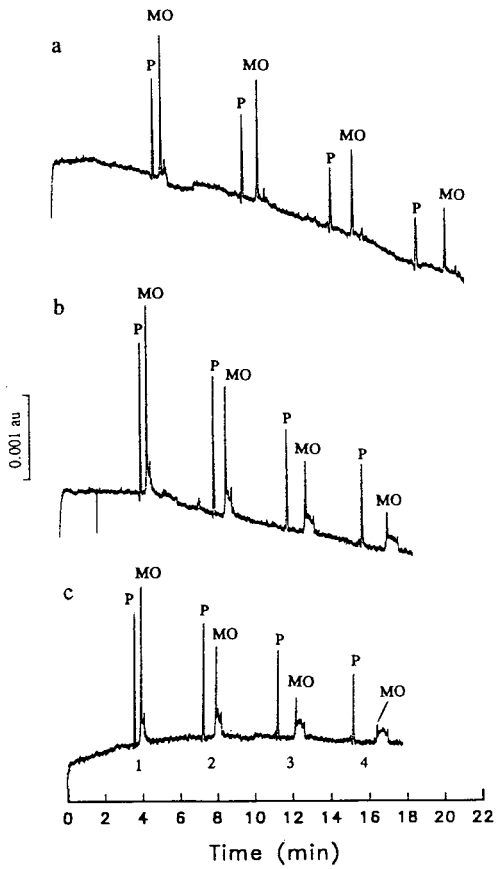

Fig. 4. Electropherograms of myoglobin (MO) and 3-methylphenol (P) obtained from four consecutive detections. Electrophoretic conditions as in Fig. 2, except run buffer was 0.1 *M* Tris, 0.025 *M* boric acid at pH 8.61. (a) 20°C; (b) 26°C; (c) 28°C.

$$-\frac{d[MO]}{dt} = k[MO] \tag{7}$$

$$\log [MO]_0 - \log [MO] = kt \tag{8}$$

where k is the rate constant. From algebraic treatment, we have:

$$\log \frac{[MO]_0}{[P]} - \log \frac{[MO]}{[P]} = kt \tag{9}$$

where P is the 3-methylphenol reference standard which does not participate in the degradation reaction. So, the amount of P remains

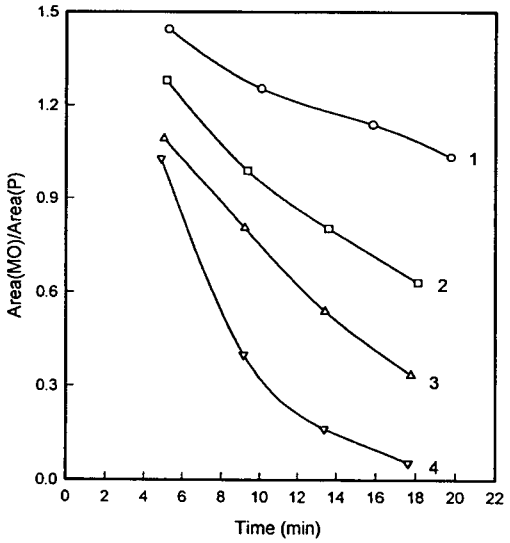

Fig. 5. Plot of the ratio of integrated absorbance area of myoglobin (MO) to that of 3-methylphenol (P) vs. time. Electrophoretic conditions as in Fig. 4. (1) 22°C; (2) 24°C; (3) 26°C (4) 30°C.

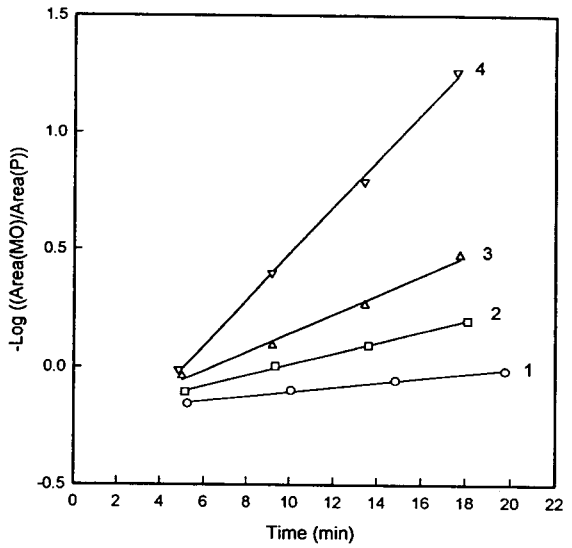

Fig. 6. Relationship of $\log(A_{MO}/A_P)$ with time. Electrophoretic conditions were the same as those of Fig. 4. (1) 22°C; (2) 24°C; (3) 26°C; (4) 30°C.

constant during a HPCE run. According to Beer's law, at one detection point the ratio of concentration of MO to that of P is proportional to the ratio of integrated absorbance area of MO to that of P. The following equation can be derived:

$$\log\frac{(A_{MO})_0}{A_P} - \log\frac{A_{MO}}{A_P} = kt \qquad (10)$$

It follows that $\log(A_{MO}/A_P)$ should have a linear relationship with time (t). The slope of the straight line should be equal to the rate constant, k. From the experimental results, it is found that $\log(A_{MO}/A_P)$ has a linear relationship with run time for all the electrophoretic runs under different conditions (Fig. 6). Therefore, the degradation of myoglobin should follow first order kinetics under certain electrophoretic conditions. Similar results have been reported by Rush *et al.* [26].

The influence of temperature on myoglobin degradation was also studied. The rate constant increases with temperature (Fig. 7). Another result shows that the rate constant does not change obviously in a certain range of electric field strengths (150–200 V/cm) (Fig. 8). This result illustrates the reliability of the method for studying the kinetics of conversion from Fe^{3+} to Fe^{2+} in MO by electric field changes [26].

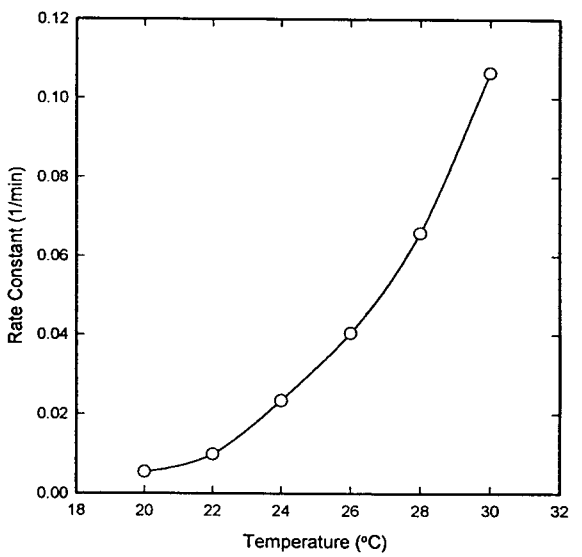

Fig. 7. Effect of temperature on myoglobin degradation rate constant.

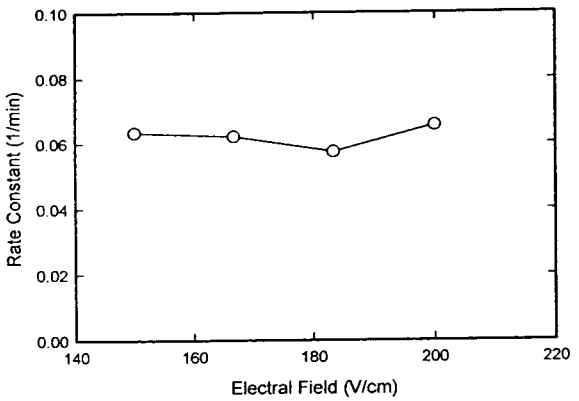

Fig. 8. Rate constant of myoglobin degradation obtained from different electric field strengths.

4. Conclusions

The results show that utilizing multi-point detection in HPCE for on-line kinetic studies is feasible. The major advantage of this method is its simplicity. It can be used to monitor the enzymatic reactions such as on-line enzyme activity studies. Kinetics of degradation of heme protein, myoglobin, has been studied by this method. Another advantage of this method is that very small amounts of agent are needed. It represents a low-cost alternative for some biochemical studies in which expensive agents are needed. It represents a low-cost alternative for some biochemical studies in which expensive agents are needed. This multi-point detection method opens a new application area in HPCE.

Acknowledgements

The support of this work by Thermo Separation Products Analytical Division and Merck Research Laboratories is gratefully acknowledged.

References

[1] J.W. Jorgenson and K.D. Lukacs, *Anal., Chem.*, 53 (1981) 1298–1302.
[2] J.W. Jorgenson and K.D. Lukacs, *Science (Washington, D.C.)*, 222 (1983) 266–272.
[3] B.L. Karger, A.S. Cohen and A. Guttman, *J. Chromatogr.*, 492 (1989) 585–614.
[4] W. Kuhr, *Anal. Chem.*, 62 (1990) 403*R*–414*R*.
[5] W. Kuhr and C. A. Monnig, *Anal. Chem.*, 64 (1992) 398*R*–407*R*.
[6] J.W. Jorgenson and K.D. Lukacs, *J. Chromatogr.*, 218 (1981) 209–216.
[7] W.R. Jones and P. Jandik, *J. Chromatogr.*, 546 (1991) 445–458.
[8] R.M. McCormick, *Anal. Chem.*, 60 (1988) 2322–2328.
[9] P.D. Grossman, K.J. Wilson, G. Petrie and H.H. Lauer, *Anal. Biochem.*, 173 (1988) 265–270.
[10] S. Hoffstetter-Kuhn, A. Paulus, E. Gassmann and H.M. Widmer, *Anal. Chem.*, 63 (1991) 1541–1547.
[11] A.S. Cohen and B.L. Karger, *J. Chromatogr.*, 397 (1987) 409–417.
[12] J.K. Towns and F.E. Regnier, *Anal. Chem.*, 63 (1991) 1126–1132.
[13] A. Guttman, A.S. Cohen, D.N. Heiger and B.L. Karger, *Anal. Chem.*, 62 (1990) 137–141.
[14] H. Drossman, J.A. Luckey, A.J. Kostichka, J.D'Cunha and L.M. Smith, *Anal. Chem.*, 62 (1990) 900–903.
[15] E. Gassmann, J.E. Kuo and R.N. Zare, *Science (Washington, D.C.)*, 230 (1985) 813–814.
[16] S. Fanali, *J. Chromatogr.*, 474 (1989) 441–446.
[17] A. Guttman, A. Paulus, A.S. Cohen, N. Grinberg and B.L. Karger, *J. Chromatogr.*, 448 (1988) 41–53.
[18] K. Otsuka and S. Terabe, *J. Chromatogr.*, 515 (1990) 221–226.
[19] Y.-H. Chu, L.Z. Avila, H.A. Biebuyck and G.M. Whitesides, *J. Med. Chem.*, 359 (1992) 2915–2917.
[20] Y.-H. Chu and G.M. Whitesides, *J. Org. Chem.*, 57 (1992) 3524–3525.
[21] G.E. Barker, P. Russo and R.A. Hartwick, *Anal. Chem.*, 64 (1992) 3024–3028.
[22] W. Nashabeh and Z. El Rassi, *J. Chromatogr.*, 596 (1992) 251–264.
[23] J. Bao and F.E. Regnier, *J. Chromatogr.*, 608 (1992) 217–224.
[24] J.P. Landers, M.D. Schuchard, M. Subramaniam, T.P. Sismelich and T.C. Spelsberg, *J. Chromatogr.*, 603 (1992) 247–257.
[25] R.J. Nelson, A. Paulus, A.S. Cohen, A. Guttman and B.L. Karger, *J. Chromatogr.*, 480 (1989) 111–127,
[26] R.S. Rush, A.S. Cohen and B.L. Karger, *Anal. Chem.*, 63 (1991) 1346–1350.
[27] T. Srichaiyo and S. Hjertén, *J. Chromatogr.*, 604 (1992) 85–89.
[28] P. Sun and R.A. Hartwick, *J. Liq. Chromatogr.*, 17 (1994) 1861–1875.
[29] H. Mollering and H.U. Bergmeyer, in H.U. Bergmeyer (Editor), *Methods of Enzymatic Analysis*, Academic Press, New York, 1965, pp. 491–494.
[30] D. Voet and J.G. Viet, *Biochemistry*, John Wiley & Sons, New York, 1990, pp. 748–760.
[31] W.J. Moore, *Physical Chemistry*, Prentice-Hall, Englewood Cliffs, NJ, 4th ed., 1972, p. 324.

ELSEVIER

Journal of Chromatography A, 695 (1995) 287–296

JOURNAL OF CHROMATOGRAPHY A

Cellulose acetate-coated fused-silica capillaries for the separation of proteins by capillary zone electrophoresis

M.H.A. Busch*, J.C. Kraak, H. Poppe

Laboratory for Analytical Chemistry, Amsterdam Institute for Molecular Studies, University of Amsterdam, Nieuwe Achtergracht 166, 1018 WV Amsterdam, Netherlands

Received 12 October 1994; accepted 30 November 1994

Abstract

Thin-film coatings of cellulose acetate on the surface of fused-silica capillaries were tested for the separation of proteins by capillary zone electrophoresis. The coating procedure is very simple and only involves the filling of the capillary with cellulose acetate solution, followed by flushing the capillary with helium. The coating appears to mask the underlying silanol groups towards basic proteins effectively; column efficiencies up to 10^6 plates per metre were achieved for ribonuclease A. The high efficiency, the batch-to-batch and the run-to-run reproducibility and the long-term stability of the coating are advantageous features of the method. The coating procedure provides a simple, stable and easy to reproduce method of surface deactivation and can be applied with other cellulose derivatives such as cellulose triacetate or cross-linked hydroxypropylcellulose. The films can also be applied to shield the surface of hollow polypropylene fibres. Unfortunately, this skin coating is destroyed above pH 7.5 and therefore cannot be recommended for zone electrophoresis at alkaline pH or for isoelectric focusing.

1. Introduction

There is a great demand for rapid, high-resolution analytical techniques to monitor the isolation and purification of proteins. Capillary zone electrophoresis (CZE) is a method that potentially offers rapid and quantitative protein analyses of high resolution and efficiency. However, satisfactory results are often difficult to obtain in protein separations with CZE. This is mainly due to the inherent tendency of these macromolecules to interact with the silanol groups present on the inside surface of the fused-silica capillary. These undesirable phenomena impede the full adoption of CZE as a routine bioanalytical technique. In order to exploit CZE fully for the analysis of proteins, the interaction between the silanol groups and proteins has to be eliminated.

Four different approaches have been reported and involve, briefly, (i) elimination of the interaction by adjusting the pH of the buffer to such a value that the silanol groups are non-charged [1]; (ii) adjusting the pH of the buffer of such a value that the charges of the silanol groups and protein have the same sign [2,3]; (iii) dynamic modification of the surface by neutral and cationic additives in the buffer [4–9]; and (iv) chemical modification using covalent bonding of the fused-silica surface [10–18].

The first three approaches are simple but are less attractive for the following reasons. To

* Corresponding author.

0021-9673/95/$09.50
SSDI 0021-9673(94)01185-0

diminish the interaction, the pH of the running buffer must be low or high and this increases the risk of hydrolysis [19] or denaturation [20] of the proteins. Also, one wants to retain the pH as an adjustable parameter in the CE of proteins. Dynamic modification by neutral and cationic additives in the background electrolyte has been shown to be an effective way to deactivate the silica surface. However, additives may change the buffer properties and can cause detection problems. Therefore, of the four approaches, chemical modification of the surface looks the most promising, also because of the flexibility to vary the pH to a certain extent. Unfortunately, the reported methods are laborious, except for the method of Malik et al. [21]. Moreover, some of the coatings show poor long-term stability.

Recently Gilges et al. [22] reported on an extremely efficient poly(vinyl alcohol) (PVA) coating by transferring a PVA film into a water-insoluble, permanently adhering layer by thermal treatment. This approach looks very attractive from the point of view of simplicity to prepare coatings.

In this paper, we report on another very simple, rapid and reproducible method to shield surface silanol groups by physically adhering a thin film of cellulose acetate on the capillary wall; we propose the term "skin coating" for this type of shielding. The physically adhered films were tested as a coating for the separation of proteins by CZE.

2. Experimental

2.1. Materials

Fused-silica capillary tubing of 50 μm I.D. (365 μm O.D.) was purchased from Polymicro Technologies (Phoenix, AZ, USA). The 56 μm I.D. (350 μm O.D.) hollow polypropylene (PP) fibre, manufactured by the melt-spinning department of AKZO, was a kind gift from AKZO Research Laboratories (Arnhem, Netherlands). Cellulose acetate (CA), M_r 30 000, and cellulose triacetate (CTA) were obtained from Aldrich Chimie (Steinheim, Germany), Tris–HCl from BDH (Poole, UK), sodium dihydrogenphosphate, sodium hydroxide, hydrochloric acid and paraformaldehyde from Merck (Darmstadt, Germany), acetone and hydroxypropylcellulose (average M_r 100 000) from Janssen Chimica (Geel, Belgium) and methylene chloride from Rathburn Chemicals (Walkerburn, UK). All protein samples were purchased from Sigma (St. Louis, MO, USA): cytochrome *c* (horse heart), lysozyme (chicken egg-white), ribonuclease A (bovine pancreas), trypsinogen (bovine pancreas), α-chymotrypsinogen A (bovine pancreas) and β-lactoglobulin A and B (bovine milk). Table 1 gives the molecular masses (M_r) and p*I* values of these proteins. Deionized water for the preparation of solutions was obtained from a Milli-Q water-purification system (Millipore, Milford, MA, USA).

2.2. Electrophoretic conditions

Electrophoresis was performed at 25°C with a laboratory-built system consisting of a high-voltage power supply (HCN 35-35.000; FUG Electronic, Rosenheim, Germany) and a UV detector, adapted for on-column detection (Model 757; Applied Biosystems, Foster City, CA, USA). The total set-up was placed in a Plexiglas box; opening the door automatically shut off the high voltage. The current in the system was measured over a 1-kΩ resistance in the return circuit of the power supply. The operating voltage was 20 kV unless indicated otherwise. Electromigration sample introduction was used (2 s,

Table 1
Isoelectric points (p*I*) and molecular masses (M_r) of the proteins [23]

Protein	Abbreviation	M_r	p*I*
Cytochrome *c*	Cyt *c*	12 200	10.8
Lysozyme	Lys	14 000	10.0
Ribonuclease A	Ribo A	13 500	8.7
α-Chymotrypsinogen A	α-Chym	21 600	8.7
Trypsinogen	Tryp	24 500	8.7
β-Lactoglobulin A	Lacto A	35 000	5.1
β-Lactoglubulin B	Lacto B	35 000	5.2

20 kV unless indicated otherwise). Before each run we rinsed the column and the collection and source vials with fresh background electrolyte solution. The optical window was prepared by burning off the outer polyimide coating before column preparation. The wavelength used for detection of the proteins was 210 nm, 0.02 AUFS (unless indicated otherwise). Electropherograms were recorded with a BD41 chart recorder (Kipp and Zonen, Delft, Netherlands) at a chart speed of 10 mm/min.

2.3. Column preparation

The flushing and coating solutions used to prepare the columns were delivered via a reservoir which can be pressurized by helium, as shown in Fig. 1. The coating procedure involves the following consecutive steps: a 75-cm long untreated fused-silica capillary is first rinsed with acetone for 15 min at 4 bar, then flushed for 15 min at 4 bar with the selected cellulose acetate solution in acetone. Next, the helium pressure is released and the capillary is pulled out of the coating solution and within 30 s the solution in the capillary is flushed out by restoring the helium pressure quickly to 4 bar, leaving a thin liquid film on the silica surface. The final immobilization is achieved by drying the coating with a gentle stream of helium for 30 min at 4 bar. The capillary is then ready for installation in the CZE system.

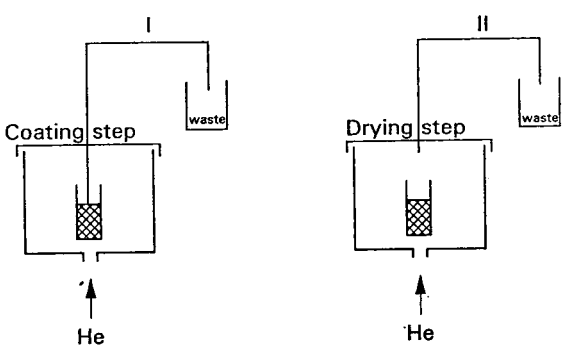

Fig. 1. Schematic representation of the coating and flushing reservoir.

2.4. Cross-linking procedure for hydroxypropylcellulose

The preparation of cross-linked hydroxypropylcellulose (HPC^c) was performed according to Ref. [24] and was as follows: hydroxypropylcellulose (4.5%, w/v) was dissolved in methanol and mixed with a cross-linking agent [3.5% (w/v) paraformaldehyde] and a catalyst [3.5% (w/v) hydrochloric acid] by using a glass rod; this solution should be used directly after its preparation.

3. Results and discussion

Our aim was to develop a simpler method to prepare an efficient coating for the separation of proteins by CZE than the laborious methods used so far. The choice to apply a film of cellulose diacetate, commonly referred to as cellulose acetate (CA), as a coating for the separation of basic proteins was inspired by the application of such films as a permselective layer, e.g., on electrodes to build size-exclusion selectivity into electrochemical detection [25–29] and from application of CA in slab gel electrophoresis [30]. Cellulose acetates are prepared by treating cellulose with a mixture of acetic acid and acetic anhydride in the presence of sulphuric acid as a catalyst. The reaction is generally allowed to proceed to substitute all three hydroxyl groups. The fully substituted triester derivative is then hydrolysed to give the desired level of substitution. Both cellulose acetate (CA) and cellulose triacetate (CTA) are good film-forming agents and have been used in a variety of pharmaceutical applications. The applications of cellulose triacetate include its use in dialysis membranes. Hydroxypropylcellulose (HPC) is a cellulose ether; it is water soluble and therefore has to be chemically cross-linked before it can be applied as a coating in CZE experiments [31].

The developed coating procedure is very simple, but the success rate and quality of the layer turned out to be largely dependent on some important parameters. Therefore, these aspects will be discussed below in more detail.

3.1. Preparation of the cellulose acetate film

Cellulose acetate dissolves in various solvents such as tetrahydrofuran, dimethylsulphoxide and acetone. Acetone had our preference because of its low viscosity, high volatility and non-toxicity. In order to dissolve the cellulose acetate quickly, it was found crucial to add the CA to the acetone with vigorous shaking because it tends to agglomerate on wetting.

The coating method is similar to the dynamic coating technique as used in capillary gas chromatography, and generally consists of filling the column with a solution of the coating phase, followed by forcing this volume through the column with helium pressure, A thin film of this solution is left behind on the capillary wall. Continuous flushing with helium after coating evaporates the remaining solvent and leaves a thin film of the polymer.

Two ways of filling the capillaries with the coating solution were tested, one in which the CA solution is directly introduced in an empty capillary and the other in which the CA solution is introduced into a capillary previously filled with the solvent, acetone in the case of CA. With the former method we obtained less efficient columns. This may be attributed to the poor wettability of the glass surface by the coating solution itself, which can result in droplet formation and subsequent non-uniform films. It has been shown that treatment with pentane, methylene chloride or acetone decreases the critical surface tension of glass by up to 50% [32]. Further, it appears to be important to flush out the CA coating solution from the capillary with helium immediately after the capillary has been disconnected from the coating reservoir. Any delay in that step may cause plugging at the front edge of the capillary.

The film thickness depends on, amongst other parameters, the viscosity of the coating solution and the speed (pressure) with which the solution is flushed out of the capillary. In our experimental set-up, an inlet pressure of 4 ± 0.5 bar produced very efficient coatings. This inlet pressure was established as the experimental result of measuring the efficiency of coatings using the same 1% (w/v) CA coating solution with various inlet pressures (2–5 bar). The adjustment of the pressure in this range is important as larger deviations appeared to result in a considerable loss of efficiency. It is probably possible to find another optimum coating concentration when using another column diameter or pressure drop.

3.2. Column performance

So far, all the coatings developed for the separation of proteins have the purpose of masking the silanol groups on the capillary surface, and as a result the electroosmotic flow is decreased significantly. In that respect the cellulose acetate coating is different as the film is still permeable to small molecules but not for larger molecules such as proteins. It appears that the electroosmotic flow with a mobility of about $9.2 \cdot 10^{-9}$ $m^2/V \cdot s$ differs by only 3% from that of a capillary that was used as delivered. This is surprising as cellulose derivatives are often used as electroosmotic flow suppressors in capillary electrophoresis and isotachophoresis. Apparently, cellulose acetate behaves differently in this respect.

In order to determine the optimum CA concentration with our experimental set-up and conditions, the performances of films fabricated with 0.85–6.0% (w/v) cellulose acetate solutions were investigated with a set of three basic proteins. The effect of the CA concentration on the efficiency is given in Table 2. We expressed the efficiency as plates per metre for a fair comparison with coating procedures already described in literature. Although the highest efficiency was obtained with the 3 and 6% (w/v) CA solutions, the efficiencies differed only slightly.

Etching of the capillary with potassium hydroxide prior to the CA coating treatment appeared to have a negative effect on the separation efficiency, as can be seen in Fig. 2, showing the electropherograms of the test proteins on capillaries prepared with (Fig. 2A) and without (Fig. 2B) prior hydroxide etching.

The performance of the cellulose acetate-coated capillaries was also investigated with the

Table 2
Effect of CA concentration in the coating solution on the separation efficiency

CA (%, w/v)	Efficiency, $N \times 10^5$ (plates/m)		
	Cyt *c*	Ribo A	α-Chym
0.85	9.31	10.13	7.40
1.0	8.06	9.19	9.06
1.2	7.72	9.66	9.48
1.5	7.02	8.15	6.26
3.0	7.86	11.04	10.20
6.0	8.17	10.45	9.71

Tris–HCl (50 m*M*, pH 4.0); applied voltage 20 kV; electromigration injection, 2 s, 20 kV.

same set of basic proteins using phosphate and Tris–HCl as background electrolytes. Fig. 3 shows the electropherograms obtained with the same capillary using 30 m*M* phosphate (pH 4.0) (Fig. 3A) and 50 m*M* Tris–HCl (pH 4.0) (Fig. 3B) as the background electrolyte. As can be seen, efficient separations can be realized with both background electrolytes. Excellent column efficiencies (up to 10^6 plates per metre) were found when using 50 m*M* Tris–HCl in the pH range 3–4.5. A typical separation using 50 m*M* Tris–HCl (pH 4.5) is shown in Fig. 4. The CA coating is stable in the pH range 2–7.5 and shows good reproducibility of the migration

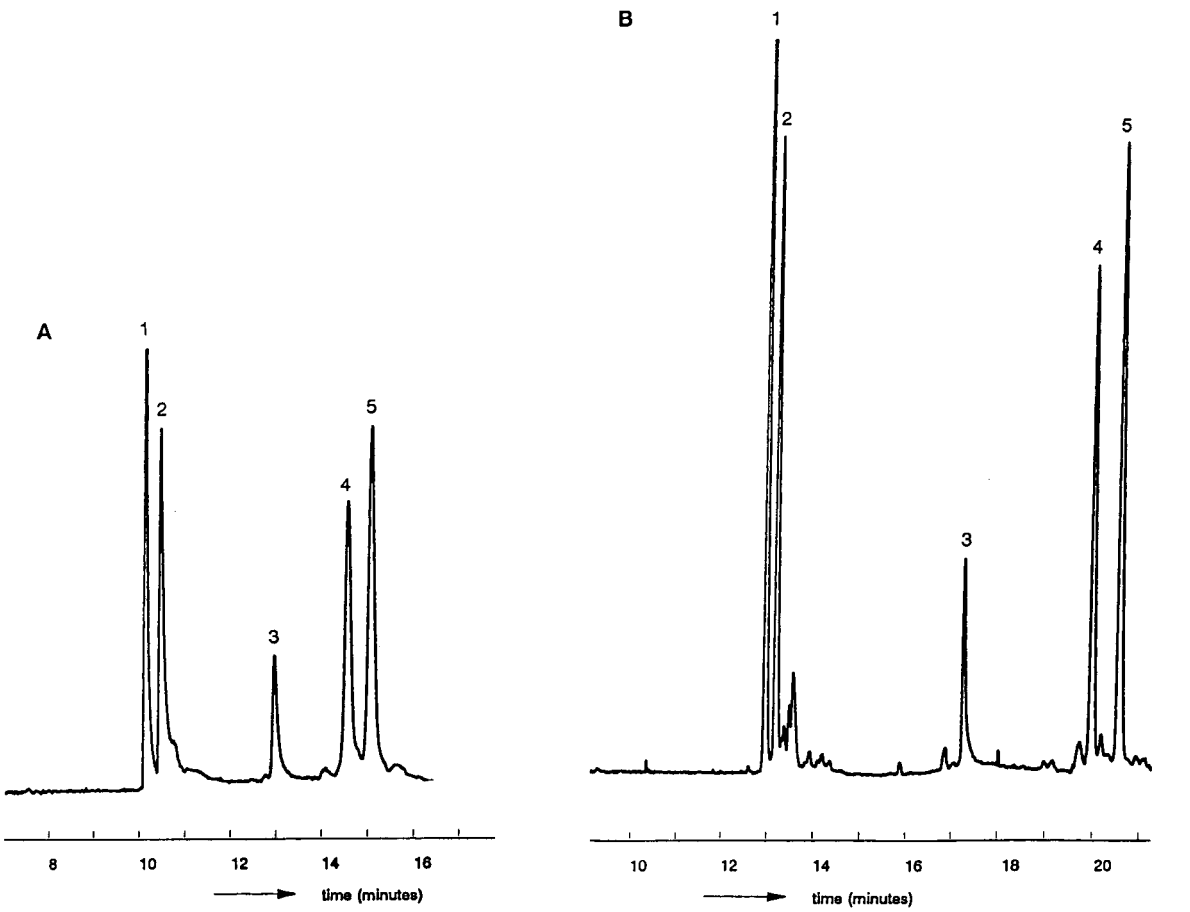

Fig. 2. CZE separation of the protein mixture on a CA-coated column. Total length of capillary, (A) 71.2 and (B) 75.2 cm; 50 μm I.D.; CA coating, 1% (w/v); effective length of capillary, (A) 47.5 and (B) 57.2 cm; electrolyte solution, 50 m*M* Tris–HCl (pH 4.3). Concentration of proteins, 0.2 mg/ml of (1) cytochrome *c*, (2) lysozyme, (3) ribonuclease A, (4) α-chymotrypsinogen A and (5) trypsinogen. (A) Etched fused-silica capillary; (B) unetched fused-silica capillary.

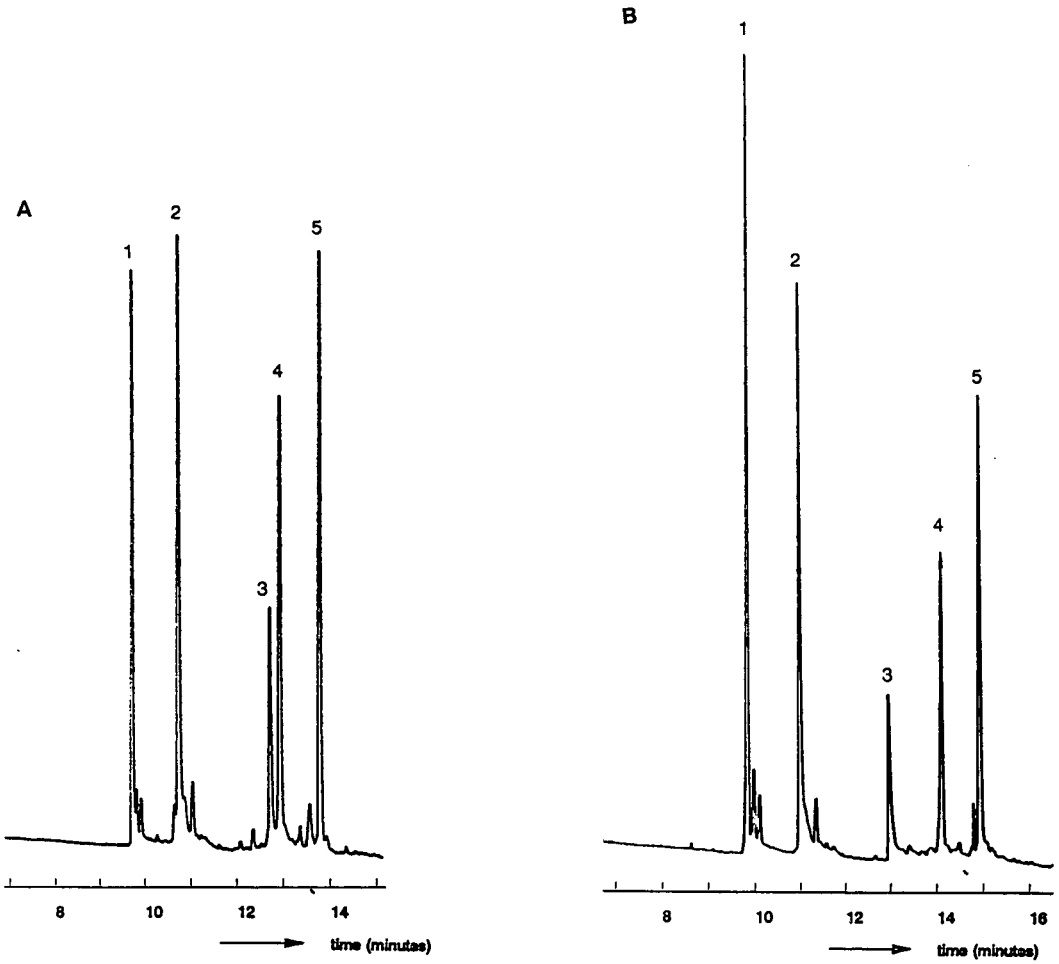

Fig. 3. CZE separation of the protein mixture on a CA-coated column. Total length of capillary, 74.9 cm; 50 μm I.D.; CA coating, 1% (w/v); effective length, 49.8 cm. Concentration of proteins, 0.2 mg/ml of (1) cytochrome *c*, (2) lysozyme, (3) ribonuclease A, (4) α-chymotrypsinogen A and (5) trypsinogen. Electrolyte solution: (A) 30 m*M* phosphate buffer (pH 4.0); (B) 50 m*M* Tris–HCl (pH 4.0).

times as investigated for the basic proteins. The relative standard deviations (R.S.D.s) of migration times are reported in Table 3 and range between 0.2 and 0.4%.

The CA coating is in principle also suitable for acidic proteins, as is illustrated in Fig. 5, showing the separation of the two acidic proteins β-lactoglobulin A and B with theoretical plate numbers of 448 000/m for β-lactoglobulin A and 329 000/m for β-lactoglobulin B at pH 3.0.

3.3. Reproducibility and long-term stability of the CA coating

The reproducibility of the CA coating in terms of efficiency was investigated by measuring the plate number of the proteins on five columns prepared from the same 1.0% (w/v) CA coating solution. The variation in plate number was found to be less than 15%. A similar variation was found with columns produced with 1.0%

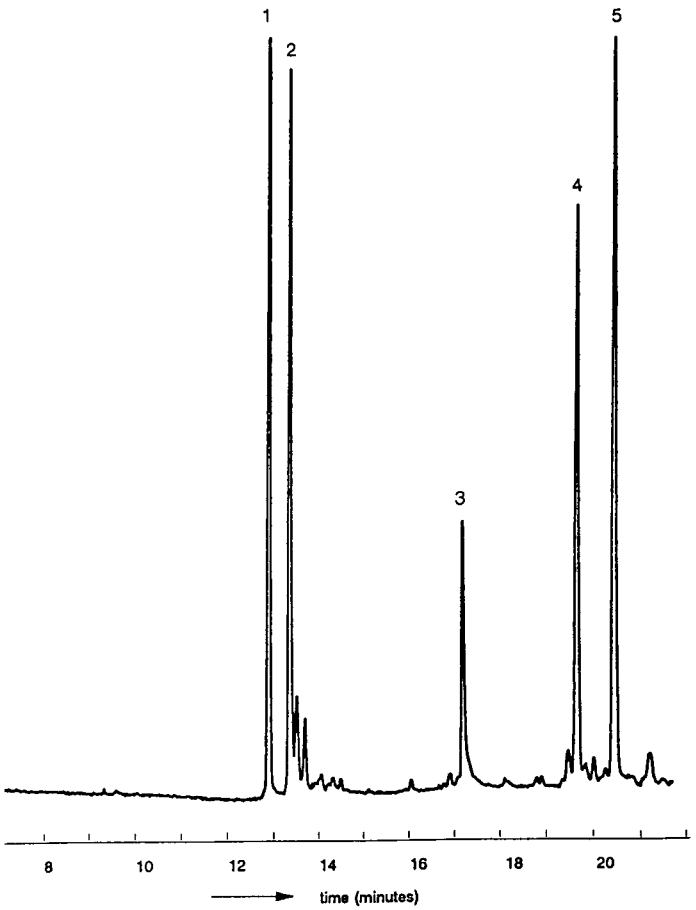

Fig. 4. CZE separation of the protein mixture on a CA-coated column. Total length of capillary, 78.8 cm; 50 μm I.D.; CA coating, 1% (w/v); effective length, 49.4 cm; electrolyte solution, 50 m*M* Tris–HCl (pH 4.5). Concentration of proteins, 0.2 mg/ml of (1) cytochrome *c*, (2) lysozyme, (3) ribonuclease A, (4) α-chymotrypsinogen A and (5) trypsinogen.

Table 3
Relative standard deviations of migration times on a CA-coated capillary

Protein	R.S.D. (%)
Cytochrome *c*	0.3
Lysozyme	0.4
Ribonuclease A	0.3
Trypsinogen	0.2
α-Chymotrypsinogen	0.2

Tris–HCl (50 m*M*, pH 4.0); applied voltage, 20 kV; electromigration injection, 2 s, 20 kV.
[a] R.S.D. calculated from five experiments.

(w/v) CA solutions that were prepared separately. This variation is in our opinion acceptable, but a fair comparison with coating procedures described in the literature is impossible, because information regarding the reproducibility is scarce. In our hands, the success rate in preparing a good CA coating was almost 100%.

An influence of the surface properties of different batches of the fused-silica capillaries from our supplier on the efficiency of deactivation by CA was observed. A similar observation was made by Gilges et al. [22].

The long-term stability of the CA coating was

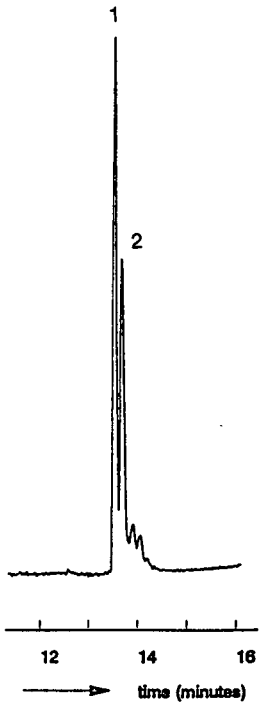

Fig. 5. CZE separation of β-lactoglobulin A and B on a CA-coated column. Total length of capillary, 74.4 cm; 50 μm I.D.; CA coating, 1% (w/v); effective length, 49.3 cm; electrolyte solution, 50 m*M* phosphate buffer (pH 3.0). Concentration of proteins, 0.2 mg/ml of (1) β-lactoglobulin B and (2) β-lactoglobulin A.

investigated by measuring the efficiency with time using Tris–HCl solutions of pH 4.3. No significant change in efficiency was noticed after continuously operating the column for more than 75 injections. Also, storage of columns in the electrolyte solution for 4 months did not alter the efficiency.

In the pH range 2–7.5, the CA coating remained intact. Above pH 7.5 the performance decreased abruptly and could not be regenerated.

3.4. Other cellulosic polymer coatings

The developed coating procedure for CA was also found to be applicable to other cellulosic polymers such as cellulose triacetate and cross-linked hydroxypropylcellulose. Methylene chloride was used to dissolve cellulose triacetate. Table 4 lists the polymers and the electrophoretic characteristics of the prepared capillaries. As can be seen, the prepared capillaries exhibit the same high separation efficiencies as found with the CA coating.

With cross-linked hydroxypropylcellulose (HPC[c]), it was possible to modify the surface of a polypropylene hollow fibre, resulting in excellent efficiency characteristics for basic proteins. A typical separation of the selected test mixture of basic proteins on the HPC[c]-coated hollow fibre is shown in Fig. 6A. Separations of this quality could not be obtained with dynamically coated PP fibres [33] or other coatings described in combination with hollow polymeric fibres [34].

Table 4
Efficiencies of columns prepared with different cellulosic polymer coatings

Polymer	Concentration (%, w/v)	Efficiency, $N \times 10^5$ (plates/m)			
		Cyt *c*	Ribo A	Tryp	α-Chym
Cellulose acetate (fused silica)	1.0	7.38	10.40	8.21	8.09
Cellulose triacetate (fused silica)	1.0	7.17	10.26	–	8.28
HPC[c] (fused silica)	4.5	7.85	9.66	8.98	9.04
HPC[c] (hollow PP fibre)	4.5	7.44	–	8.76	7.00

Tris–HCl (50 m*M*, pH 4.0); applied voltage, 20 kV; electromigration injection, 2 s, 20 kV.

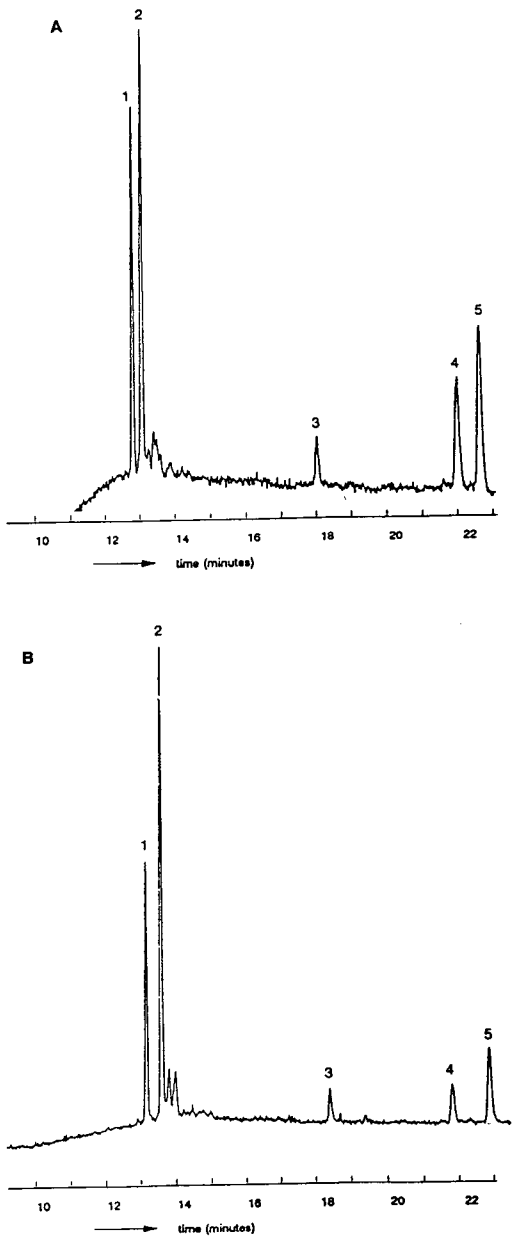

Fig. 6. CZE separation of the protein mixture on an HPC^c-coated hollow PP fibre. Total length of capillary, (A and B) 55.0 cm; HPC^c coating, 4.5% (w/v); effective length, 29.0 cm; electrolyte solution, 50 m*M* Tris–HCl (pH 4.3). Concentration of proteins, 1.5 mg/ml of (1) cytochrome *c*, (2) lysozyme, (3) ribonuclease A, (4) α-chymotrypsinogen A and (5) trypsinogen. Separation voltage, 10 kV; electromigration injection, 2 s, 10 kV; detection wavelength, 280 nm (0.005 AUFS). (A) HPC^c-coated PP fibre; (B) HPC^c-coated fused-silica capillary.

For comparison, the same separation performed in a fused-silica capillary under otherwise identical conditions is shown in Fig. 6B. The R.S.D.s of the migration times and theoretical plate numbers *N* (per metre) on the fused-silica and the polypropylene capillaries coated with HPC^c are given in Table 5. This demonstrates that results of the same quality can be obtained with the PP tubes, which are more convenient and less fragile in practice. The main disadvantage of the polypropylene capillary is the limited UV transparency, which precludes the use of wavelengths below 240 nm, as can be inferred from a published UV absorbance spectrum [33]. Because of this limitation, the proteins were detected at 280 nm. At this wavelength only the aromatic amino acid residues in the proteins are detected, resulting in a decrease in detection sensitivity. The UV absorbance of the fibre material is assumed to be caused by (residues from) additives used in the production process. Further optimization of the production process and a reduction in the O.D.-to-I.D. ratio might improve this drawback in the future. Without coating the polypropylene fibre with cross-linked hydroxypropylcellulose the proteins are adsorbed on the capillary wall. The uncoated hollow polypropylene fibre is strongly hydrophobic and requires pre-wetting before introduction of an aqueous electrophoresis buffer. Methanol was used for this purpose in the

Table 5
Relative standard deviations of migration times and efficiencies with HPC^c surface modification

Protein	R.S.D. (%)[a]		Efficiency, $N \times 10^5$ (plates/m)	
	PP	Silica	PP	Silica
Cytochrome *c*	0.5	0.5	7.44	7.85
Lysozyme	0.6	0.5	6.43	8.03
Ribonuclease A	0.5	0.4	–	9.66
α-Chymotrypsinogen	0.7	0.4	8.76	8.98

Tris–HCl (50 m*M*, pH 4.0); applied voltage, 20 kV; electromigration injection, 2 s at 20 kV.
[a] R.S.D. calculated from ten experiments.

uncoated fibre. The pre-wetting agent can subsequently be simply exchanged with buffer solution.

4. Conclusions

Cellulosic polymer films, dynamically coated and physically adhering to the inside wall of fused-silica capillaries, appear to be an efficient coating for the separation of basic and some acidic proteins by CZE using Tris–HCl as electrolyte. The CA coating remains intact in the pH range 2–7.5.

Apart from the excellent efficiency, the simplicity and speed of fabricating the coating are important advantages compared with the laborious chemical modification methods used so far. Further, it was shown that this method of surface shielding can also be applied to hollow polypropylene fibres.

Acknowledgement

The authors thank Astra Hässle, Sweden, for financial support.

References

[1] R.M. McCormick, *Anal. Chem.*, 60 (1988) 2322.
[2] H.H. Lauer and D. McManigill, *Anal. Chem.*, 58 (1986) 166.
[3] K.J. Lee and G.S. Heo, *J. Chromatogr.*, 559 (1991) 317.
[4] M.M. Bushey and J.W. Jorgenson, *J. Chromatogr.*, 480 (1989) 301.
[5] J.S. Green and J.W. Jorgenson, *J. Chromatogr.*, 478 (1978) 63.
[6] J.K. Towns and F.E. Regnier, *Anal. Chem.*, 63 (1991) 1126.
[7] A. Emmer, M. Jansson and J. Roeraade, *J. Chromatogr.*, 547 (1991) 544.
[8] M. Gilges, H. Husmann, M.-H. Kleemiss, S.R. Motsch and G. Schomburg, *J. High Resolut. Chrometry.*, 15 (1992) 452.
[9] J.A. Bullock and L.-C. Yuan, *J. Microcol. Sep.*, 3 (1991) 241.
[10] S. Hjertén, *J. Chromatogr.*, 347 (1985) 191.
[11] G.J.M. Bruin, R. Huisden, J.C. Kraak and H. Poppe, *J. Chromatogr.*, 480 (1989) 339.
[12] M. Huang and M.L. Lee, *J. Microcol. Sep.*, 4 (1992) 491.
[13] J.W. Jorgenson and K.D. Lukacs, *Anal. Chem.*, 53 (1981) 1298.
[14] J.A. Lux, H. Yin and G. Schomburg, *J. High Resolut. Chromatogr.*, 13 (1990) 145.
[15] J.K. Towns and F.E. Regnier, *J. Chromatogr.*, 471 (1989) 429.
[16] B.J. Herren, S.G. Shafer, J. Alstine, J.M. Harris and R.S. Snyder, *J. Colloid Interface Sci.*, 115 (1987) 46.
[17] S.A. Swedberg, *Anal. Biochem.*, 185 (1990) 51.
[18] Y.-F. Maa, S.A. Swedberg and K.J. Hyver, *J. High Resolut. Chromatogr.*, 14 (1991) 63.
[19] B.L. Karger, A.S. Cohen and A.J. Guttman, *J. Chromatogr.*, 492 (1989) 585.
[20] S.A. Swedberg, *Anal. Biochem.*, 185 (1990) 51.
[21] A. Malik, Z. Zhao and M.L. Lee, *J. Microcol. Sep.*, 5 (1993) 119.
[22] M. Gilges, M.H. Kleemiss and G. Schomburg, *Anal. Chem.*, 66 (1994) 2038.
[23] P.G. Righetti and T. Caravaggio, *J. Chromatogr.*, 127 (1976) 1.
[24] S. Suto, H. Tashiro and M. Karasawa, *J. Appl. Polym. Sci.*, 45 (1992) 1569.
[25] L.S. Kuhn, S.G. Weber and K.Z. Ismail, *Anal. Chem.*, 61 (1989) 303.
[26] G. Sittampalam and G.S. Wilson, *Anal. Chem.*, 57 (1983) 1608.
[27] J. Wang and L.D. Hutchins, *Anal. Chem.*, 57 (1985) 1536.
[28] L.D. Hutchins, J. Wang and P. Tuzhi, *Anal. Chem.*, 58 (1986) 1019.
[29] C.-W. Wang and I.-C. Chen, *Anal. Chem.*, 64 (1992) 2461.
[30] J. Ambler, B. Janik and G. Walker, *Clin. Chem.*, 29 (1983) 340.
[31] V. Kumar and G.S. Banker, *Drug Dev. Ind. Pharm.*, 19 (1993) 1.
[32] M.L. Lee and B.W. Wright, *J. Chromatogr.*, 184 (1980) 235.
[33] M.W.F. Nielen, *J. High Resolut. Chromatogr.*, 16 (1993) 62.
[34] P.Z. Liu, A. Malik, M.C.V. Kuchar, W.P. Vorkink and M.L. Lee, *J. Microcol. Sep.*, 5 (1993) 245.

ELSEVIER

Journal of Chromatography A, 695 (1995) 297–308

JOURNAL OF CHROMATOGRAPHY A

The separation of dihydrofolate reductase inhibitors and the determination of $pK_{a,1}$ values by capillary zone electrophoresis

Jing Cao, Reginald F. Cross*

School of Chemical Sciences Swinburne University of Technology John Street, Hawthorn, Vic. 3122, Australia

First received 23 September 1994; revised manuscript received 23 November 1994

Abstract

CZE was used as a method to separate eight dihydrofolate reductase inhibitors (DHFRI). Separation of the eight DHFRI was difficult to achieve and occurs only under very specific conditions. Baseline resolution occurred in 250 m*M* phosphate buffer of pH 2.1 at 13 kV. In an attempt to understand the mechanism of separation, $pK_{a,1}$ values have been determined and the effective hydrodynamic radii estimated by modeling the molecules. The consequential plot of Z/r versus the measured electrophoretic mobility gave a good linear correlation, thus demonstrating the fundamental nature of the separation mechanism.

1. Introduction

In the veterinary field, dihydrofolate reductase inhibitors (DHFRI) have acted as potentiators in combination with sulfonamides (SFA) for the prevention of bacterial and protozoal diseases of animals [1]. Although to a lesser degree, the same combinations are used in human medicine both in prophylactic and curative roles. There are three common DHFRI (trimethoprim, diaveridine and pyrimethamine) that have been used extensively and assays for these and the accompanying sulphonamide in urine, serum and animal tissues are scattered throughout the literature and continue to appear [2,3]. However, there are several other DHFRI that have either been used commercially with animals (ormetoprim) [1] or have been the subject of therapeutic studies in humans (brodimoprim) [4,5] and deposition and clearance studies in animals (ormetoprim) [6]. In addition, further DHFRI have been produced [1].

In total there appear [1] to have been eight DHFRI produced. They are pyrimethamine (PYR), diaveridine (DI), ormetoprim (OR), trimethoprim (TRI), aditoprim (ADI), metioprim (MET), tetroxoprim (TET) and brodimoprim (BRO).

If the eight are ever released for usage in the same market, the need for screening could arise. In this study we examine the suitability of capillary zone electrophoresis for that task. The general structures of the compounds is shown in Scheme 1 and the specific structural formula [1] and molecular masses are given in Table 1.

TRI has a pK_a of 6.6 and PYR has a pK_a of 7.0 [7]. The CZE behavior of these and DI in the vicinity of pH 8 clearly indicated [7] deprotona-

* Corresponding author.

0021-9673/95/$09.50
SSDI 0021-9673(94)01163-X

Table 1
Structural formulas and molecular masses for the eight dihydrofolate reductase inhibitors

DHFRI	n	R_1	R_2	R_3	R_4	M_r
Aditoprim	1	OCH_3	$N(CH_3)_2$	OCH_3	H	303.4
Pyrimethamine	0	H	Cl	H	CH_2CH_3	248.7
Diaveridine	1	OCH_3	OCH_3	H	H	260.3
Ormetoprim	1	CH_3	OCH_3	OCH_3	H	274.3
Brodimoprim	1	OCH_3	Br	OCH_3	H	339.2
Trimethoprim	1	OCH_3	OCH_3	OCH_3	H	290.3
Metioprim	1	OCH_3	SCH_3	OCH_3	H	306.4
Tetroxoprim	1	OCH_3	$OCH_2CH_2OCH_3$	OCH_3	H	334.4

tion to the electrically neutral form. It was observed that the easy separation of those three DHFRI may have been the fortuitous consequence of one of them being PYR. PYR is the only one of these three that is differently substituted in the pyrimidine ring where protonation can occur. Therefore it is the only DHFRI that could possibly carry a significantly different charge on the heterocycle. Of the other five, ADI is the only other drug that will be separable on the basis of total charge. The additional site for protonation on the basic dimethylamine substituent on the phenyl ring will ensure that ADI carries an additional charge at low enough pH. The other six will depend upon differences in size for variation in mobility and thus separation.

Consequently, it was not expected that CZE would easily separate these drugs. On the other hand, the plate counts achievable in CZE could enable the small size differences to be exploited.

2. Experimental

2.1. Instrumental

A Model 270 A CZE System by Applied Biosystems Inc. (Foster City, CA, USA) was used for all CZE experiments. The analytes were detected by UV–VIS absorbance at 225 nm. The detector time constant was set at 0.3 s in all experiments.

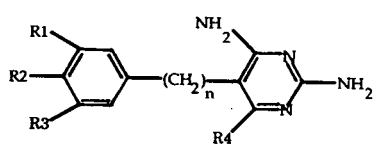

Scheme 1.

The determinations were performed on a 71.2 cm × 50 μm I.D. (220 μm O.D.) fused-silica capillary (Applied Biosystems) with the detection window located 52 cm from the injection end. The samples were injected at the anode (+) by vacuum injection for all analytes. All experiments were performed at 30° C. Electropherograms were recorded on a DeskJet Plus recorder and data were collected and integrated with a Model 270 capillary electrophoresis system interfaced to an Apple Macintosh computer. The 20 μm I.D. (350 μm O.D.) fused-silica capillary was supplied by J&W Scientific (Folsom, CA, USA). Its critical lengths were as for the 50 μm I.D. capillary.

2.2. Chemicals and materials

PYR, DI and TRI were obtained from Sigma (St. Louis, MO, USA), BRO was supplied by Helsinn (Biasca, Switzerland), and, ADI, MET, ORM and TET were provided by Hoffmann-La Roche (Basel, Switzerland). Standard stock solutions of each compound were prepared by precisely dissolving 0.1 g in 100 ml of HPLC grade methanol (BDH). Each compound was diluted with milli-q water to give a final concentration of 2.5 ng/μl. Sample solutions were filtered (0.45 μm) before injection. The neutral marker solution was prepared by weighing 0.1 g phenol and dissolving it in 1 l of HPLC grade methanol.

Phosphate buffers at 50–250 m*M* were prepared using Na_2HPO_4 and adjusted to the desired pH with 20% H_3PO_4 or 0.1 *M* NaOH. All chemicals were of AR grade and milli-q water was used to prepare all solutions.

2.3. Methods

Capillary preparation at the start of each day of experimentation involved initial purging with 0.1 *M* NaOH for 2 min, followed by milli-q water purging for 2 min and then with the running buffer for 2 min. Between the runs, the capillary was purged with 0.1 *M* NaOH for 2 min followed by running buffer for 2 min. Vacuum injections for 10 s were chosen to ensure signal-to-noise greater than 20:1. At the nominal 4 nl per second [8], 40 nl would have been injected. However, this nominal rate refers to water uptake. Hence the more viscous buffers used would lead to greatly reduced injection volumes. Furthermore, as the sample was dissolved in water, sample stacking compensates for this larger than usual volume.

3. Results and discussion

Given the apparent ease of separation of TRI, DI and PYR around pH 7 in 50 m*M* phosphate [7], these were the initial conditions chosen. However, in the vicinity of pH 6–7 with phosphate buffers, the doubly charged ADI is well resolved, but the remainder of the DHFRI comprised one broad band. Next we decreased the pH. The aim of these experiments was to decrease the electroosmotic flow and thereby permit differences in electrophoretic mobility to operate over an extended period. Fig. 1 shows the apparent mobilities. 50 m*M* phosphate buffer was used with 20 kV applied. It can be seen that the decrease in the apparent mobilities of the DHFRI follow that of the neutral marker but increased discrimination occurred. Fig. 2(a) shows the electropherogram at pH 2.1 where the resolution appeared to be marginally better than at surrounding pH values. With 20 kV applied, 50 m*M* NaCl–HCl solutions yielded similar resolution at pH 2, 3 and 4. At pH 1 no analyte peaks were observed. For $NaNO_3$–HNO_3 mobile phases, slightly inferior resolution was obtained and baseline noise was excessive.

At pH 2.1, with 50 m*M* phosphate buffers the effect of applied voltage was then examined. The results are shown in Fig. 3. There were not any significant changes in resolution over the voltage range examined. The only advantage observed was of reduced analysis times at higher applied voltages.

Fig. 4 shows the effect of phosphate buffer concentration on the apparent mobilities at pH 2.1 with 13 kV applied. With the higher buffer concentration, larger applied voltages led to the loss of all peaks. This was presumed to be due to Joule heating. As the maximum applied voltage for which peaks could be observed in 250 m*M* phosphate buffer was 13 kV, this voltage was chosen across the range of ionic strengths. It can be seen that the last pair of analytes (ORM, BRO) are finally separated in 250 m*M* phosphate buffer. Fig. 2 (b) shows the separation. In this high salt concentration (250 m*M*) the observed noise is many times larger than in the more normal range of buffer concentrations around 50 m*M* [see Fig. 2 (a)].

3.1. Buffer selection

In an attempt to effect separation at lower salt concentrations, we then tried some organic buffers. The commonly used buffers in the low pH range chosen were HCOOH–CH_3COOH pH 1.9 (24.4 ml, 90% and 87 ml, 99.8% respectively into 1 litre) and H_2NCH_2COOH–HCOOH pH 3.1 (0.1 *M* glycine, pH adjusted with HCOOH). The first of these is approximately 6 m*M* with respect to formate and 2 m*M* with respect to acetate whereas the glycine buffer is about 100 m*M*. At 13 kV, unfortunately only ADI was baseline resolved and the other seven DHFRI were combined in one broad, complex band in each case.

It may be that the brief search for a more dilute and less conducting buffer with appropriate selectivity was a futile exercise. It is notable in the work of Atamna et al. that it was

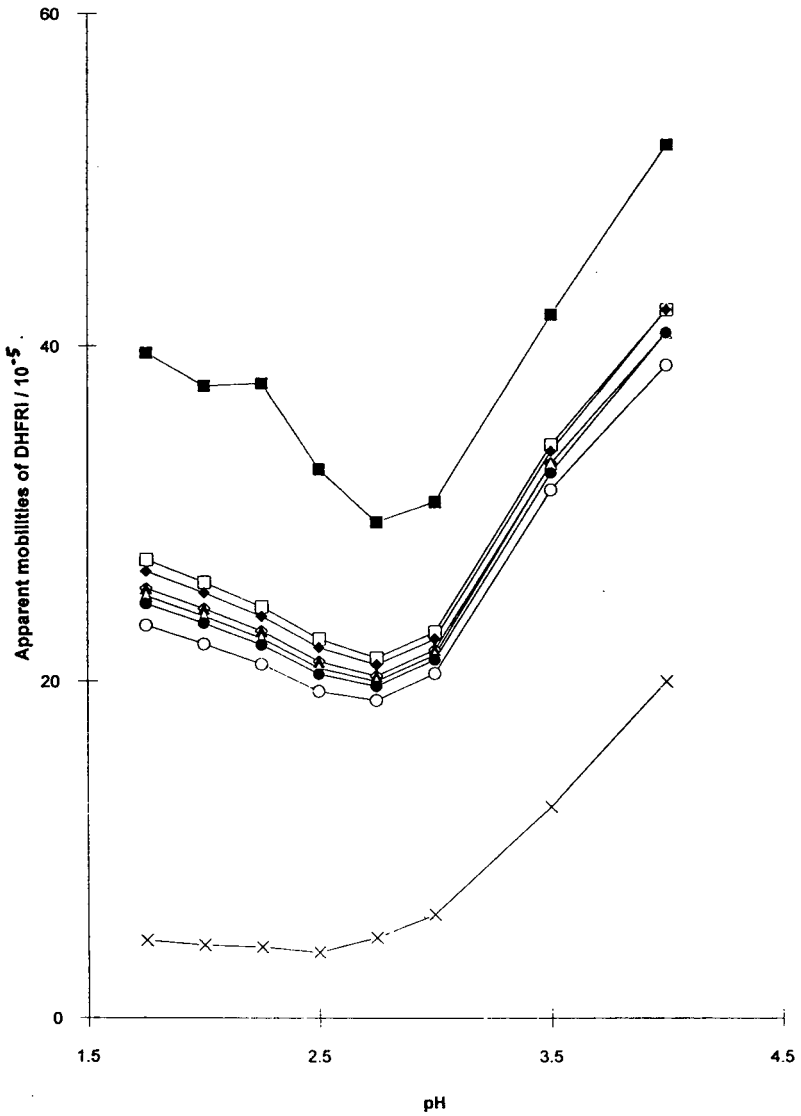

Fig. 1. Apparent mobilities ($cm^2\ s^{-1}\ V^{-1}$) as a function of pH for the eight DHFRI (50 m*M* phosphate buffer at 20 kV). Legend: (■) ADI, (□) PYR, (◆) DIA, (◇) ORM, (▲) BRO, (△) TRI, (●) MET, (○) TET, (×) neutral marker.

the most highly conducting buffer that provided the best separations. When the role of the cation was examined, it was only in the most highly conducting cesium buffer where close to baseline resolution was observed. The lighter the alkali metal in the buffer, the further the separation deteriorated [9]. Similarly, when the role of the anion was isolated, the best resolution occurred in the most highly conducting citrate buffer, the worst resolution was observed in the least conducting bicarbonate buffer and the second least conducting acetate buffer had the second worst selectivity [10]. It has also been demonstrated that over a wide range of applied voltages resolution increases with increasing phosphate buffer concentration, up to 75 m*M* [11]. In the

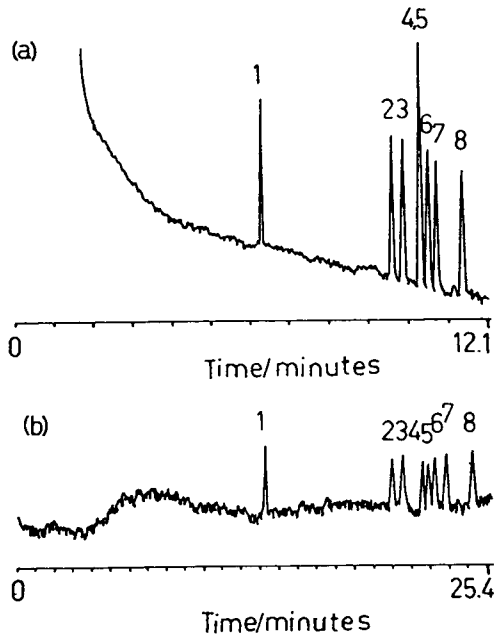

Fig. 2. Electropherograms of the eight DHFRI at pH 2.1. (a). In 50 m*M* phosphate buffer with 20 kV applied. (b). In 250 m*M* phosphate buffer with 13 kV applied.

current study, it is only in high concentration of the highly conducting phosphate buffer that all peaks are resolved. It therefore appears that at least for some classes of analytes there is a correlation between highly conducting buffers and increased selectivity. The consequence of this of course is that whilst a lowly conducting buffer such as lithium acetate may provide a good probe for Joule heating, it is likely to the worst choice for separation.

3.2. Peak loss

During the investigation there had been several sets of conditions under which all of the peaks had disappeared. Firstly, this occurred at 50 m*M* phosphate concentration with applied voltages greater than 25 kV. Secondly, for higher phosphate concentrations the peaks disappeared at progressively lower voltages. In the third instance, peaks were not observed for pH less than 1.75. In all of these cases the combination of high salt concentrations and/or high voltages indicated that excessive currents must have given rise to thermal mixing and dispersion. Unfortunately, currents were not automatically or systematically recorded. However, this seemed the most logical explanation. For the low pH solutions (1.75) the high concentration of protons in solution were probably the cause. This is consistent with observations by other workers restricting the practical pH range for CZE to 2–12 [12].

The other evidence for Joule heating lies in Fig. 3. Mobilities are known to increase by 2.7% per°C [13] due to the decreased viscosity and density of the supporting buffer [14]. For this reason, plots of mobility (both electroosmotic and electrophoretic) versus voltage are upward curving. The effects are more exaggerated at higher buffer concentrations and have been demonstrated very clearly [11]. Whilst the work of Issaq et al. [11] indicated the onset of this curvature above 50 m*M* buffer (for acetate at pH 5 and phosphate at pH 7), the effect is likely to be exacerbated for DHFRI in phosphate buffers at pH 2.1. As phosphoric acid has its $pK_{a,1}$ at 2.15 and the DHFRI have a $pK_{a,1}$ about 1 pH unit away (see next section) all mobilities will be heightened by increased dissociation as a result of Joule heating [11].

Thermal mixing

In view of the apparent heating problem leading to peak loss, it was decided to investigate the effect of decreasing the internal diameter of the capillary. Accordingly, the 20 μm I.D. capillary was obtained. It was hoped that better heat dissipation per cross-sectional area and would enable higher voltages to be applied, enabling quicker analyses to be achieved whilst maintaining baseline resolution of all analytes. Under the same conditions used for resolution of the sample previously (250 m*M* phosphate buffer, pH 2.1, 13 kV), no peaks were observed. This was totally unexpected and is contrary to the literature which indicates that Joule heating should not be a problem.

In the first instance, Knox [15] has calculated "Boundary conditions under which plate height contributions from thermal effects is less that 0.1

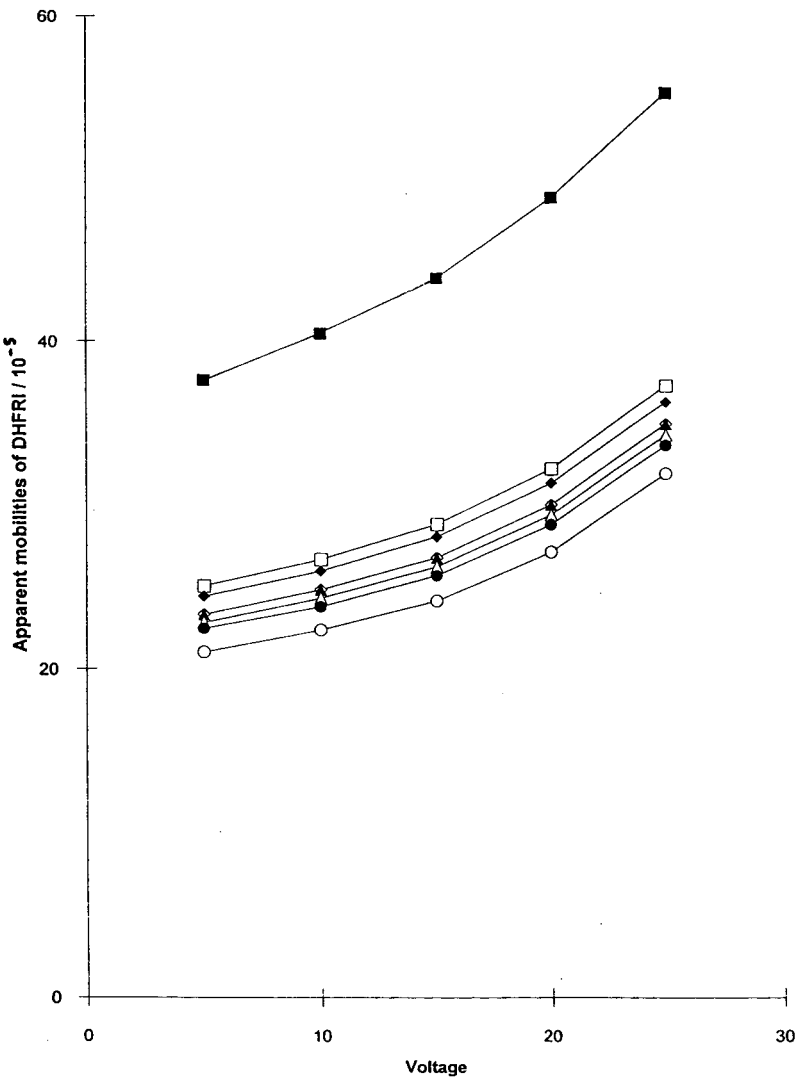

Fig. 3. Apparent mobilities ($cm^2\ s^{-1}\ V^{-1}$) as a function of voltage for the eight DHFRI (50 m*M* phosphate buffer at pH 2.1). Symbols as in Fig. 1.

times the plate height contribution from axial diffusion." A tabulation of limiting capillary diameters (d_c) for 10, 20, 50 and 100 kV m^{-1} across 10^{-3}, 10^{-2} and 10^{-1} mol dm^{-3} buffer solutions is given. Log–log plots of d_c versus buffer concentration are good linear plots for 10, 20 and 50 kV m^{-1} and were extrapolated to 0.25 mol dm^{-3}. The corresponding values of d_c, when plotted versus the applied voltage (V) on log–normal paper yielded a gently concave relationship. Interpolated to our applied voltage of 13 kV/0.712 m, the limiting diameter is 133 μm. Even allowing for the increased conductivity due to low pH, by a liberal extrapolation of the d_c versus V lines to 1 mol dm^{-2} buffer, the diameter for 10% increase in plate height is still 83 μm. (Our capillary was 50 μm diameter).

Similarly, Gruska et al. [16] have estimated that for small molecules in 0.1 *M* buffers there will be negligible loss in HETP for capillaries

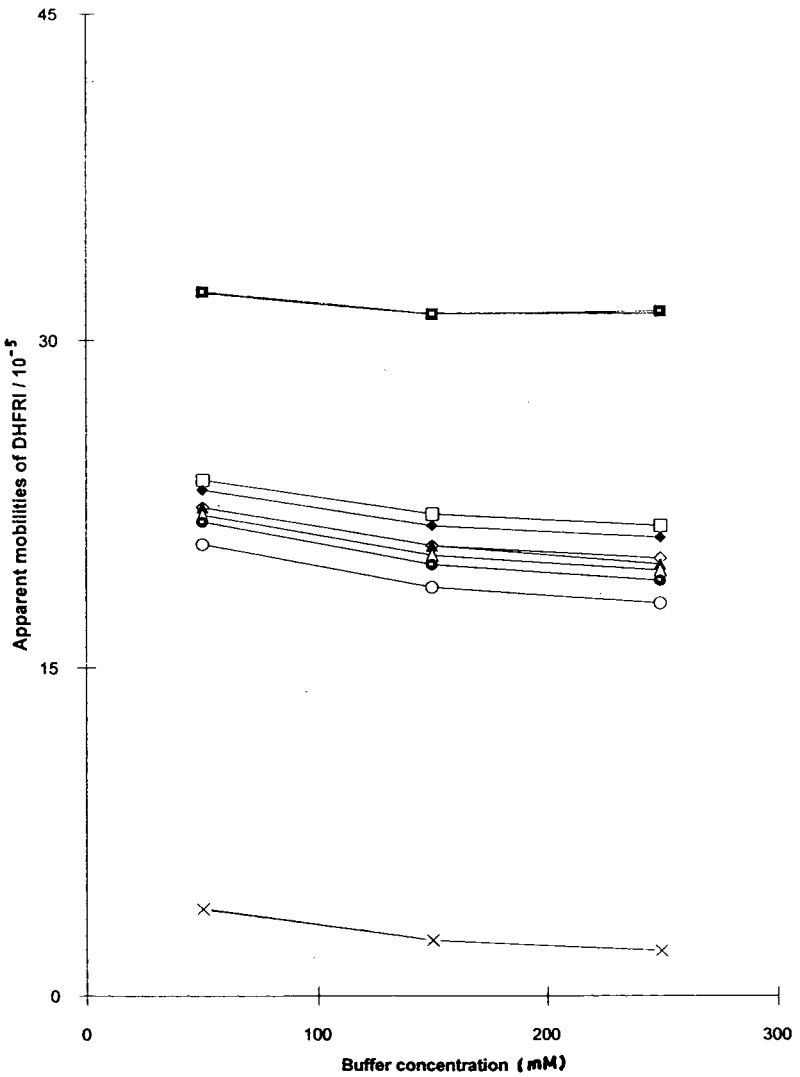

Fig. 4. Apparent mobilities ($cm^2\ s^{-1}\ V^{-1}$) as a function of concentration of buffer for the eight DHFRI (with 13 kV at pH 2.1). Symbols as in Fig. 1.

between 50 and 100 μm internal diameter with 30 kV m^{-1} applied and analyte velocities in the range of 1–10 cm min^{-1}. Plate losses are greatest at the highest velocities, but are still negligible. For 50 μm I.D. capillaries at approximately 4 cm min^{-1} (typical for our analyses), the HETP is clearly coincidental with the theoretical curve of maximum efficiency.

Thus the available evidence in the literature appears to deny significant loss of efficiency due to Joule heating under our experimental conditions. The only possible additional factor that requires some examination is the effect of the greater overall diameter and wall thickness in the case of the 20 μm I.D. capillary. (See Instrumental section.) The 20 μm I.D. capillary has a semi-insulating coating of 165 μm of fused silica compared to 85 μm around the 50 μm I.D. capillary. However, with the thermal conductivity of the capillary wall being far greater than that

of buffer solutions [16], conventional wisdom is that this will not cause excessive Joule heating to occur [17].

Adsorption

The alternate explanation for peak losses is adsorption. Loss of proteins on the walls of fused-silica capillaries has been recognized as a problem in CZE from very early on [19]. The technique proposed to avoid this was to coat the wall and thereby prevent interaction with the ionized negatively charged silanols. Alternate approaches involve adjustment of the pH to values above the p*I* for the proteins to ensure net negative charge and repulsion from the capillary walls or to use swamping concentrations of strong electrolytes to saturate adsorption sites in the electrical double layer [20].

In the case of small (non zwitterionic) molecules, another alternative is to adjust the pH to yield electrically neutral species and use micellar electrokinetic capillary chromatography (MECC). However, CZE is simpler and will therefore be preferred if adsorption is avoided.

The acid–base properties of silica have been well understood for a long time [21]. The pK_a for the silanols is between 6 and 7 and the potential of zero charge is at about pH 2. Consequently, electrostatic adsorption of cationic species on the silica walls would be expected to increase in proportion to surface charge with increasing pH, if permissible under the given conditions. In fact a water soluble, non surfactant, polymeric cation (trimethylammonium glycol chitosan iodide) has been shown to adsorb on silica in a fashion that exactly mirrors the increase in charge density on silica gel between pH 3.5 and 10 [22]. In this case, negligible adsorption was indicated in the lower pH range. On the other hand, in 10 m*M* NaBr C_{14}TAB exhibits decreasing adsorption from pH 6 down but appears to flatten out well above zero in the vicinity of pH 2 [23]. Also, in the case of polyvinylimidazole (a cationic polyelectrolyte with p$K_a \sim 5$), similar behavior versus pH is observed up to the region of the pK_a, but at low pH the extent of adsorption is strongly dependent upon ionic strength [24]. Contrary to expectations [25], the extent of adsorption increases with NaCl concentration. More importantly, the trend in the data with pH allows for finite adsorption in the vicinity of pH 2. As imidazoles are 1,3-dinitrogen heteroaromatics, this data is particularly relevant. With similar chemistry and charge distribution, similar behavior may be expected of the DHFRI.

There are several other factors to be considered in conjunction with the possibility of the adsorption of the DHFRI on silica at low pH. Firstly, at the potential of zero charge (pH $\sim$ 2), it is the net charge that is zero. There will be negative (and positive) charges on the surface. Secondly, the extent of ionization of the surface silanols is increased by adsorption. In solution-depletion experiments involving large surface areas of silica and small volumes of C_{14}TAB in 10 m*M* NaBr, the bulk solution is observed to proportionately decrease in pH [23]. Clearly, the process must be viewed as ion exchange rather than simple adsorption. Thirdly, with a pK_a in the vicinity of 1, the DHFRI will be more strongly preferred counter ions for exchange as the pH approaches 1. Fourthly, it is known that maximal adsorption of carboxylic acids and amines occurs for pHs around the pK_a [21]. This is presumed to be due to the favorable energetics of the proton exchange mechanism. This leads to the last salient point which is that non electrostatic adsorption due to strong hydrogen bonding on the surface is also possible. Increasing adsorption due to this mechanism might be expected as the pH approaches the potential of zero charge for the silica (around 2).

For the 20 μm I.D. capillary, the increased internal surface area-to-volume ratio in the smaller I.D. capillary, the smaller radial distances of diffusion to the walls and the reduced sample size (at fixed injection interval) would all facilitate adsorption.

In the absence of more definitive evidence the above indicates that DHFRI adsorption is a distinct possibility from electrolyte solutions at low pH. However, the significance of these equilibrium studies to flowing solutions in CZE will also depend upon adsorption kinetics.

The simplest way to test for adsorption would be to substitute a coated capillary in place of the

untreated silica under otherwise identical conditions. The appearance of peaks would then strongly indicate adsorption, whilst their continued absence would tend to deny it.

3.3. Migration order

To understand the order of migration of the eight analytes we have looked to the basics of the migration process. The electrophoretic mobility, μ_{ep} is given [14] by Eq. 1:

$$\mu_{ep} = Z/(6\pi\eta r) \quad (1)$$

where Z is the effective charge on the ion, η is the viscosity and r is the hydrodynamic radius. For any prescribed condition of separation, η will be fixed and therefore the order of separation will depend only upon Z and r. We therefore set out to determine these values for the analytes.

Determination of Z

As the successful separation of the eight analytes occurred at pH 2.1, it is there that the calculations have been done.

For all of the DHFRI we can write the ionic equilibria as shown in Scheme 2.

Analysis of the hydrogen bonding and molecular packing of DHFRI and related compounds by Cody et al. [26], and by others, using computational methods and crystal structure determinations leave little doubt that the preferred site for protonation is on the N1 (ring nitrogen). These give rise to the $pK_{a,2}$ values between 6 and 7 and full protonation at pH 2.1. As with many nitrogen heterocycles, $pK_{a,1}$ values are expected around 1 or 2 [27] and in the case of the DHFRI it is expected that protonation will occur at the N3 position [26]. Overall then we expect that the DHFRI will have a net charge of 1.x in general around pH 2.1.

For ADI there is also the additional protonation on the dimethylammonium group on the phenyl ring (see Scheme 3).

We do not have a value for this pK_a, but reference to the available data allows an estimate to be made [28]. Aniline has a pK_b of 9.38 whereas o-methoxy aniline has a pK_b of 9.51. Hence we assume that the pK_b of aniline derivatives will have their pK_b values increased by 2×0.13 due to disubstitution by methoxy groups in the ortho positions. Similarly, N,N-dimethyl substitution of aniline leads for an increase in pK_b of $+0.22$. Given that the pK_b for *p*-methylaniline is 9.00, the pK_b for 2,6-dimethoxy-4-methyl-(N,N-dimethylaniline) will be approximately $9.00 + 0.22 + 0.26 \sim 9.48$ and $pK_{a,3}$ (ADI) ~ 4.52. While this estimate is clearly qualitative, it does indicate that the remaining pK_a for ADI is probably significantly above 2.1 and that we may assume full protonation at pH 2.1.

To determine the fraction of protonation due to the $pK_{a,1}$ we have used the method of Beckers et al. [18]. The two solutions used to determine $pK_{a,1}$ were 250 m*M* phosphate buffer at pH 2.1 with 13 kV applied and 50 m*M* phosphate buffer at pH 3.5 with 15 kV applied. Due to the lower limitation on the useful range of pH for CZE, it was not feasible to go to lower pH [12]. Table 2 shows the raw data from which the calculation were done.

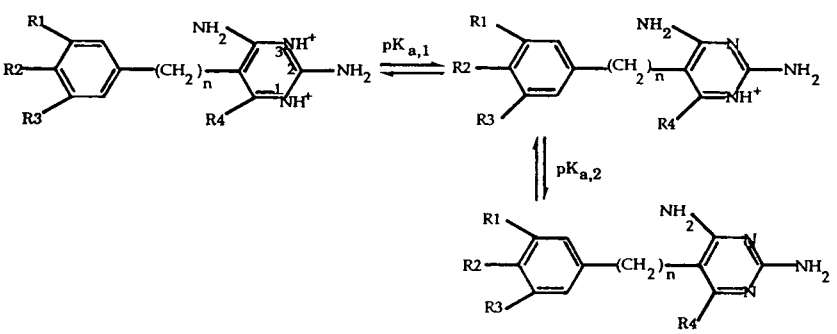

Scheme 2.

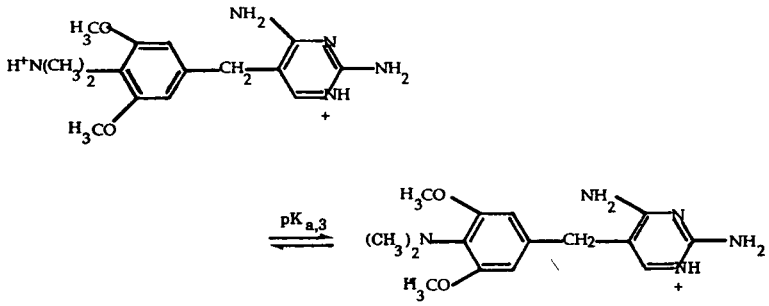

Scheme 3.

Table 2
Apparent migration times for the DHFRI and the neutral marker (minutes) and calculated pK_a values

DHFRI	Migration time		pK_a
	pH 2.1	pH 3.5	
Aditoprim	15.755	10.31	1.065
Pyrimethamine	22.44	14.38	1.2334
Diaveridine	22.99	14.645	1.2441
Ormetoprim	24.065	15.125	1.2758
Brodimoprim	24.375	15.125	1.3401
Trimethoprim	24.7	15.325	1.3234
Metioprim	25.295	15.59	1.3361
Tetroxoprim	26.64	16.245	1.3418
Neutral marker	169.52	49.205	–

The Debye–Hückel expression for activity coefficients was used as in Beckers et al. [18]. The effective hydrodynamic radii used were those calculated in the next section and shown in Table 3. The calculated pK_a values are given in the final column of Table 2.

Determination of r

Prior to determining values of r, the molecular masses of the DHFRI were used as a first approximation to the relative molecular volumes. This proportionality has previously led to a good correlation between electrophoretic mobility and "charge to mass" ratio [7]. However, in that case the analytes under consideration were sulphonamides and the majority of heteroatom variations from carbon were nitrogens and oxygens with approximately the same atomic density. For the DHFRI, BRO is clearly an outlier in any such calculation due to the exceptionally high density of the bromine atom.

Initial attempts to determine r were based upon physical model building with spheres. However, imprecision in size scaling of the

Table 3
Values used in the calculation of Z/r and its correlation with μ_{ep}

DHFRI	Z	r	Z/r	μ_{ep}
Aditoprim · $2H_2O$	2.083	3.107	0.67	27.33
Pyrimethamine · H_2O	1.12	2.738	0.409	18.35
Diaveridine · H_2O	1.122	2.85	0.394	17.85
Ormetoprim · H_2O	1.13	2.856	0.396	16.92
Brodimoprim · H_2O	1.148	2.962	0.388	16.67
Trimethoprim · H_2O	1.143	2.921	0.391	16.42
Metioprim · H_2O	1.147	2.96	0.388	15.97
Tetroxoprim · H_2O	1.149	3.153	0.364	15.02

atoms and the bond lengths led us to look for a more precise method of estimation.

The Sybyl 6.01 molecular modeling software was used to obtain minimum energy configurations of the eight DHFRI with a water of hydration added to each of the fully protonated sites; that is, one water of hydration at the N1 site for all DHFRI and a second water of hydration on the dimethylammonium site for ADI.

As there was no mechanism in the software for calculating an averaged radius, we initially used the cross-sectional area of the molecule when the charge (or charges in the case of ADI) were to the forefront dragging the molecule through the solution. These areas were estimated from printouts of the appropriately averaged electron cloud diagram with a superimposed angstrom grid. Values so determined led to correlations which appear to deny the validity of an electrostatically enforced preferred ionic orientation in the electric field during migration.

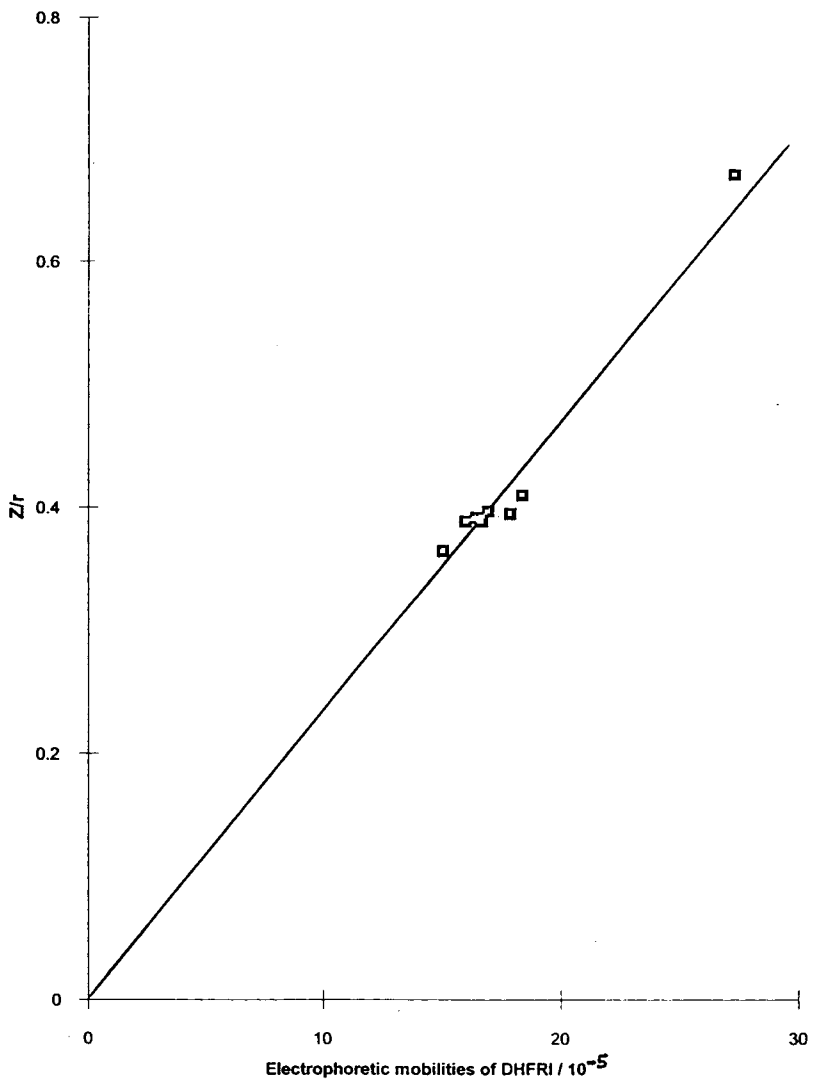

Fig. 5. Z/r values as a function of electrophoretic mobilities ($cm^2\ s^{-1}\ V^{-1}$). Symbols as in Fig. 1.

Since there was not any measurement of volume available we opted for the "contact" surface area from which the radius of an equivalent sphere was calculated. The data are given in Table 3.

Correlation

Table 3 shows the data used to calculate Z/r and the values of electrophoretic mobilities of the ions. Fig. 5 shows the plot of Z/r versus electrophoretic mobilities. From a least squares regression the correlation coefficient is 0.980. In general, the compliance of the data with Eq. 1 is quite good and the order of migration appears to be determined primarily by the fundamental molecular properties of charge and size.

The spread of the data about the line of best fit is likely to arise from both possible sources of errors; the values of pK_a and of r. In the case of pK_a, the inability to do experiments at a sufficiently low pH will contribute to less precise values of pK_a. Also, estimates of the activity coefficients in the method of pK_a calculation will be approximate due to the use of the Debye–Hückel expression up to ionic strengths of 0.25. For r, the modeling package is likely to yield an extremely accurate approximation to the molecule, but our usage of the contact surface to calculate the radii of equivalent spheres may not be as a good an approximation to the effective hydrodynamic radius in all cases.

Acknowledgements

We thank Hoffmann-La Roche for the donation of four of the DHFRI, and Helsinn for the donation of brodimoprim. We also thank Ashley Mansell for his experimental support, Dr. Margaret Wong for her help with the molecular modeling and Dr. Ian Harding of the centre for Applied Colloid Science, Swinburne for useful discussions regarding adsorption.

References

[1] W.F. Rehm, K. Teelmann and E. Weidekamm, in A.G. Rico (Editor), *Drug Residues in Animals*, Academic, Orlando, FL, 1986, Ch. 4.
[2] M.M. Lemnge, A. Ronn, H. Flachs and I.C. Bygbjerg, *J. Chromatogr.*, 613 (1993) 340–346.
[3] P. Nachilobe, J.O. Boison, R.M. Cassidy and A.C.E. Fesser, *J. Chromatogr.*, 616 (1993) 243–252.
[4] H.J. Laurencot, A. Schlosser and J.L. Hempstead, *Poult. Sci.*, 51 (1972) 1181–1187.
[5] E. Weidekamm, E. Eschenhof, B. Weber and A. Darragh, in K.H. Spitzy and K. Karrer (Editors), *Proceedings of the 13th International Congress on Chemotherapy, Vienna,* 1983, Egerman, Vienna, p. 59/1.
[6] E. Werner, A. Braunsteiner, F. Finsinger and Z. Maric, in K.H. Spitzy and K. Karrer (Editors), *Proceedings of the 13th International Congress on Chemotherapy, Vienna,* 1983, Egerman, Vienna, p. 59/16.
[7] M.C. Ricci and R.F. Cross, *J. Microcol Sep.*, 5 (1993) 207–215.
[8] *Model 270A User's Manual*, Applied Biosystems, Santa Clara, CA, 1989.
[9] I.A. Atamna, C.J. Metral, G.M. Muschik and H.J. Issaq, *J. Liq. Chromatogr.*, 13 (1990) 2517–2527.
[10] I.A. Atamna, C.J. Metral, G.M. Muschik and H.J. Issaq, *J. Liq. Chromatogr.*, 13 (1990) 3201–3210.
[11] H.J. Issaq, I.Z. Atamna, G.M. Muschik and G.M. Janini, *Chromatographia*, 32 (1991) 155–161.
[12] J.A. Cleveland, Jr., M.H. Benko, S.J. Gluck and Y.M. Walbroehl, *J. Chromatogr A.*, 652 (1993) 301–308.
[13] S. Hjerten, *Electrophoresis*, 11 (1990), 665–690.
[14] R.J. Wieme, in E. Heftmann (Editor), *Chromatography: A Laboratory Handbook of Chromatographic and Electrophoretic Methods*, Van Nostand Reinhold, New York, 3rd ed., 1975, p. 267.
[15] J.H. Knox, *Chromatographia*, 26 (1968) 329–337.
[16] E. Gruska, R.M. McCormick and J.J. Kirkland, *Anal. Chem.*, 61 (1989) 241–246.
[17] M. Verhoef, personal communication.
[18] J.L. Beckers, F.M. Everaerts and M.T. Ackermans, *J. Chromatogr.*, 537 (1991) 407–428.
[19] J.W. Jorgenson and K.D. Lukacs, *Science*, 222 (1983) 266–272.
[20] S.F.Y. Li, *Capillary Electrophoresis*, Elsevier, Amsterdam, 1992.
[21] T.W. Healy, *J. Macromol. Sci. - Chem.*, A8 (1974) 603–619.
[22] E. Kokufuta, S. Fujii, Y. Hirai and I. Nakamura, *Polymer*, 23 (1982) 452–456.
[23] P. Wangnerud and G. Olofsson, *J. Colloid Interface Sci.*, 153 (1992) 392–398.
[24] B. Popping, A. Deratani, B. Sebille, N. Desbois, J.M. Lamarche and A. Foissy, *Colloids Surfaces*, 64 (1992) 125–135.
[25] I.H. Harding, personal communication.
[26] C.H. Schwalbe and V. Cody, in J.A. Blair (Editor), Proceedings of the *7th International Symposium on Structural Studies of Antifolate Drugs, Birmingham, 1982*, de Gruyter, Berlin, 1983, pp. 511–515.
[27] D.D. Perrin, *Dissociation Constants of Organic Bases in Aqueous Solution*, IUPAC, Butterworths, London, 1965 and 1972.
[28] P. Sykes, *A Guidebook to Mechanism in Organic Chemistry*, Longmans, London, 1961.

ELSEVIER

Journal of Chromatography A, 695 (1995) 309–317

JOURNAL OF CHROMATOGRAPHY A

Non-aqueous capillary electrophoretic separation of polyethers and evaluation of weak complex formation

Tetsuo Okada

Faculty of Liberal Arts, Shizuoka University, Shizuoka 422, Japan

First received 18 October 1994; revised manuscript received 29 November 1994; accepted 29 November 1994

Abstract

The use of pure methanol as a separation medium for capillary electrophoresis (CE) has made possible the separation of non-ionic polyethers and the determination of their complexation constants with an electrolyte cation. The developed technique has proved to be efficient for the evaluation and detection of weak interactions (e.g., the interaction of benzo-12-crown-4 with various cations can be detected). This is a good example showing that the use of non-aqueous solvents in CE has allowed the utilization of interactions that hardly take place in water.

1. Introduction

Capillary electrophoresis (CE) has proved to be effective for the separation of compounds with various chemical properties [1,2]. This method basically differentiates ionic compounds migrating towards the oppositely charged electrode according to their mobilities in a medium. However, the separation of non-ionic compounds is also feasible if appropriate modifications are made to the electrolyte system, e.g., the use of ionic micelles has permitted the separation of a variety of electrically neutral compounds [3,4]. CE and related techniques are mostly recognized as useful for practical purposes because of their excellent separation ability, and a number of papers describing various applications have been published. However, the author believes that CE is also useful for fundamental purposes and can be used for the detection and evaluation of some physico-chemical properties in solution.

Separation methods have an essential advantage over other spectrometric or electrochemical methods in studying solution chemistry, e.g., as the evaluation method itself involves separation and purification processes, impurities contained in samples have little influences on the results obtained. From such a viewpoint, the author reported the chromatographic evaluation of the solution behaviour of ions [5,6] and polyethers [7–10]. The complexation of monodisperse polyoxyethylene (POE) with a variety of chain lengths was, for example, quantitatively evaluated by the method developed [7], and the thermodynamic origin of the selectivity in the complexation of POE with alkali metal ions was elucidated as a result [9]. However, chromatography involves several drawbacks: (1) the retention equilibria must not be affected by solution equilibria; and (2) the mobile phase conditions are restricted, and must not cause damage to the stationary phase. The fact that CE basically involves no stationary phase promises

0021-9673/95/$09.50
SSDI 0021-9673(94)01182-6

its preference and versatility as an approach to solution chemistry.

Addition of organic solvents to an aqueous solution in CE has been extensively attempted [1,11–15]. However, in most studies, it was intended to enhance the selectivity or to modify the electroosmotic flow (EOF) by addition of organic solvents. In contrast, the use of an entirely non-aqueuos solvent has rarely been attempted in CE. This might be because the high separation ability of CE did not require the use of a non-aqueous medium in a practical sense. Kenndler and Gassner [16], for example, reported non-aqueous CE (in their study 99.5% methanol), in which methanol was used to vary the selectivity of the separation of anions. Recently, Sahota and Khaledi [17] reported that CE in formamide promises higher efficiency and shorter analysis times because of the high viscosity and the high dielectric constant of the solvent.

The primary aim of this paper is to show that the use of non-aqueous solvents permits the utilization of reactions and interactions, that do not take place in water but do so in non-aqueous media in CE separations. Subsequently, information on the solution chemistry can in some instances be extracted from the retention data in the usual manner.

2. Experimental

The capillary electrophoretic system was composed of a Matsusada high-voltage power supply (HCZE-30P No. 25; the maximum voltage was 30 kV and the maximum current 250 μA), a JASCO UV–visible detector (870-CE) and a fused-silica capillary (50 μm I.D., 375 μm O.D., 44.6 cm long, 29.6 cm effective length, with a detection window located 15 cm from the negative end). Unless stated otherwise, currents typically ranged from 35 to 45 μA under a 20-kV applied voltage. Samples were introduced into the capillary by siphoning at the positive end. Conductivity measurements were carried out at 25°C with a TOA CM20S conductimeter.

Reagents were of analytical-reagent grade. If necessary, salts were dried at an appropriate temperature under vacuum. Methanol was distilled twice. Tetraethylammonium chloride was added to adjust the ionic strength of the solution.

Crown ethers were synthesized according to the literature [18] and recrystallized from heptane. The crown ethers synthesized were benzo-12-crown-4 (B12C4), benzo-15-crown-5 (B15C5), benzo-18-crown-6 (B18C6), dibenzo-18-crown-6 (DB18C6), dibenzo-21-crown-7 (DB21C7), dibenzo-24-crown-8 (DB24C8) and dibenzo-30-crown-10 (DB30C10). Dinitrobenzoyl-POE (DNB-POE) was prepared by the reaction of POE with 3,5-dinitrobenzoyl chloride with magnesium as a catalyst in dry benzene.

3. Results and discussion

3.1. Migration of non-ionic polyethers by on-capillary complexation

Polyether complexation takes place unfavourably in solvents having a strong solvation ability for hard cations or having too low dielectric constants; in the former instance (e.g., water), polyether cannot replace solvent molecules existing in the solvation shell, and in the latter (e.g., dioxane), ion-pair formation interferes with the complexation. In this study, methanol was selected as a solvent from such a viewpoint, i.e., methanol has a moderate dielectric constant ($\varepsilon = 32.6$) and is a weaker solvent than water. In addition, as this solvent has been extensively used as a solvent for the study on polyether complexation, comparison of results is also easy [19,20].

The apparent electrophoretic mobility of an electroneutral polyether is determined by both the complexation ability with an electrolyte cation and the mobility of the resulting complex. The overall mobility of a polyether (μ_{app}) can be described by

$$\mu_{app} = \mu_{eo} + \mu_{ep} \quad (1)$$

where μ_{eo} and μ_{ep} denote the electroosmotic and the electrophoretic mobility, respectively. If only

1:1 complexation takes place in the capillary, Eqn. 1 can be written as

$$\mu_{app} = \mu_{eo} + \beta\mu_{max}$$
$$= \mu_{eo} + K_1[M]\mu_{max}/(1 + K_1[M]) \quad (2)$$

where β represents the degree of the complexation, μ_{max} is the intrinsic electrophoretic mobility of the complex, K_1 is the 1:1 complex formation constant and [M] refers to the equilibrium concentration of the uncomplexed cation in the analyte segment. As [M] can be calculated from the analytical concentration of the metal ion (C_M), non-linear regression gives both K_1 and μ_{max}. However, when evaluating weak interactions, we can regard [M] as C_M. The difference between C_M and [M] is at most 2% over the usual concentration ranges ($C_M \geq 0.01$ *M*, the concentration of the polyether being assumed to be 0.5 m*M*), when K_1 is smaller than 68. In such a case, we can determine K_1 from the linear relationship between $1/(\mu_{app} - \mu_{eo})$ and $1/C_M$.

3.2. Separation of polyethers

Fig. 1 shows electropherograms of DNB-POE(*n*)D (D denotes dodecyl ether and *n* refers to the number of repeating oxyethylene units), where NH_4^+ is used as an electrolyte cation. In order to keep the EOF almost constant (or to keep the pH constant), triethylamine (Et_3N) was added to the solution; as triethylammonium ion (Et_3NH^+) did not form complexes with POE, the addition of Et_3N had no significant effects on the electrophoretic mobility of POE. Peaks were identified by the addition of standard monodisperse DNB-POE($n = 8$)D to a sample. The peaks of POE($n > 4$)D are resolved from the peak migrating together with the EOF. As shown in Fig. 1B, POE($n = 3$)D also migrates faster than the EOF when K^+ is incorporated with NH_4^+. Similar results were obtained for Na^+, Rb^+ and Cs^+. These results imply that POE($n = 3$) forms a complex with K^+ and POE($n = 4$) does so with NH_4^+. It was found on the same basis that 5–6 oxyethylene units are required to form the complexes with monoalkylammonium ions.

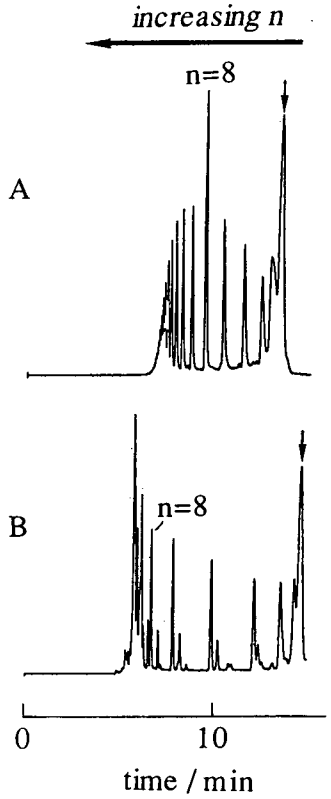

Fig. 1. Electropherograms of DNB-POE(*n*)D. Solution: (A) 50 m*M* NH_4Cl + 50 m*M* Et_3N; (B) 5 m*M* KCl + 45 m*M* NH_4Cl + 45 m*M* Et_3N. Detection at 250 nm. Applied voltage, 20 kV. The peak of the EOF marker, which is a DNB derivative not having complexation ability, is indicated with an arrow.

In previous studies, we speculated that at least 5–6 oxyethylene units would be required to form stable complexes with heavy alkali metal ions using chromatography [7]. NMR [21] and conductimetry [22] also indicated that the minimum numbers required for K^+ complexation are six and four, respectively. However, these methods are incapable of detecting very weak complexation, e.g., a chromatographic method is suitable for the determination of complexation constants of 10^3 although it is varied by the ion-exchange capacity of the resin used as the stationary phase [23], and similarly for conductimetry [24]. These methods therefore cannot detect weak complexation such as when $K_1 < 10$.

NH_4^+ is not favourably complexed by polyethers, whereas K^+ in general forms much more stable complexes [7,19,20]. Therefore, it is predictable that the incorporation of K^+ with NH_4^+ will bring about drastic changes in separation. Fig. 1B shows an electropherogram obtained with a solution containing 5 m*M* K^+. The addition of K^+ enlarges the separation window for relatively short POE chains, while the resolution becomes worse as *n* increases. This point will be discussed quantitatively later. In Fig. 1B, there are some small peaks other than the main series of DNB-POE(*n*)D. It was verified by comparison of electrophoretic mobilities that these are peaks of DNB-POEs bearing a tetradecyl, a hexadecyl or an octadecyl group.

The selectivity of POE separation was not altered by varying the electrolyte cations, i.e., the longer the POE chain length the faster is the mobility. This clearly indicates that the longer POE molecule always forms the more stable complex with any cation. In contrast, the migration of crown ethers is influenced considerably by an electrolyte cation in solution. Fig. 2 shows the variation of the separation of crown ethers with cations. The migration orders are B18C6 > DB18C6 ≥ DB21C7 > DB30C10 > DB24C8 > B15C5 > B12C4 for NH_4^+, B18C6 > DB18C6 > DB21C7 > B15C5 > DB24C8 > DB30C10 > B12C4 for monoalkylammonium ion and B18C6 > DB18C6 > DB24C8 > DB21C7 > B15C5 > DB30C10 > B12C4 for dimethylammonium ion. DB30C10, for example, forms a cage-like three-dimensional complex with K^+ [25]. If the same structure is maintained in the complexes with ammonium ions, the above changes in the migration of DB30C10 are understandable; alkyl groups interfere with the formation of the cage-like structure of this ligand, and retard the elution of DB30C10 as a result.

It should be noted that the interactions of B12C4 with all the cations listed above are detected by the present method. Although the complexation of B12C4 with Li^+ has been reported ($K_1 = 22$ in methanol [20]), its complexation with other cations has not.

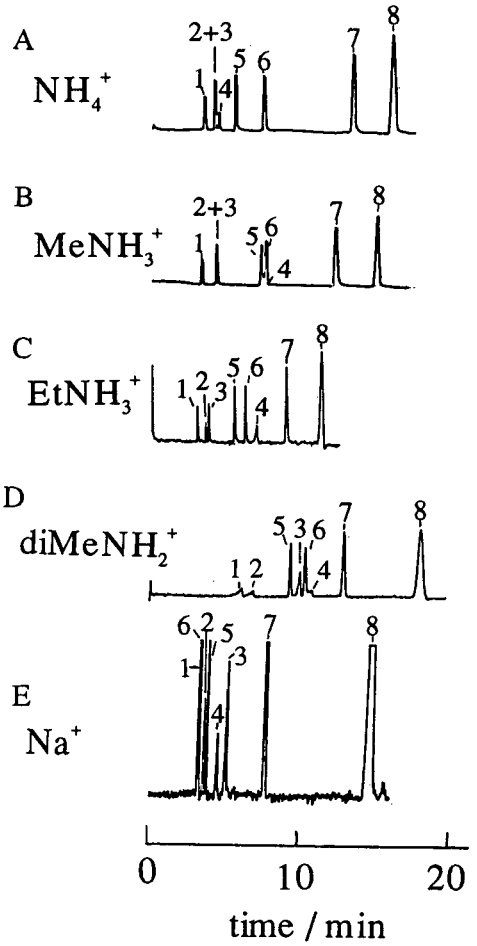

Fig. 2. Separation of crown ethers. Solution: (A) 25 m*M* NH_4Cl + 25 m*M* Et_3N + 25 m*M* Et_4NCl, (B) 15 m*M* $MeNH_3Cl$ + 15 m*M* Et_3N + 35 m*M* Et_4NCl, (C) 40 m*M* $EtNH_3Cl$ + 40 m*M* Et_3N + 10 m*M* Et_4NCl, (D) 40 m*M* $diMeNH_2Cl$ + 40 m*M* Et_3N + 10 m*M* Et_4NCl, (E) 25 m*M* NaCl + 25 m*M* Et_3NHCl + 25 m*M* Et_3N. Peaks: 1 = B18C6; 2 = DB18C6; 3 = DB21C7; 4 = DB30C10; 5 = DB24C8; 6 = B5C5; 7 = B12C4; 8 = acetone. Detection at 280 nm. Applied voltage, 20 kV.

3.3. Determination of complexation constants

Fig. 3 shows examples of plots based on Eq. 2 obtained for NH_4^+ and DNB-POE(*n*)D. As predicted, linear relationships are obtained, which allow us to detemine both the K_1 and μ_{max} values.

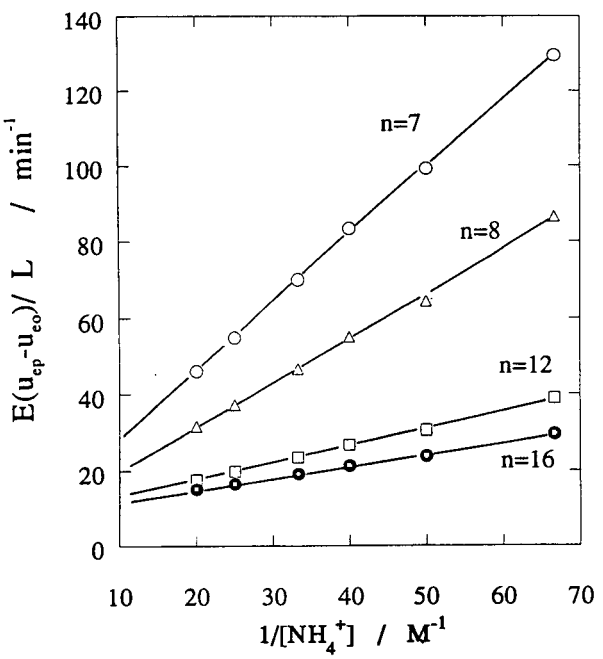

Fig. 3. Example plots based on Eq. 2 for DNB-POE(n)D and NH_4^+.

Table 1 summarizes K_1 and μ_{max} for 1:1 complexes of several cations with DNB-POE(n)D and B12C4. The dissociation of cations except for Na^+ was calculated from conductimetric measurements according to the following equation:

$$\alpha = (\Lambda - \Lambda_2)/(\Lambda_1 - \Lambda_2)$$

where Λ_1, Λ_2 and Λ are molar conductances, measured at the identical concentration, of the chloride salt of a given ammonium ion, Et_3NHCl, that is, the chloride salt of the conjugate acid of Et_3N added to the solution for pH adjustment, and an equimolar mixture of these, respectively. For a 0.05 M solution, the α values were 0.49, 0.73, 0.62 and 0.69 for NH_4^+, $MeNH_3^+$, $diMeNH_3^+$ and $EtNH_3^+$, respectively. It was difficult to determine α of $PrNH_3^+$ according to the above equation because of a small difference between the Λ_1 and Λ_2 values. $PrNH_2$ was therefore used instead of Et_3N; in this case, $\alpha = 1$.

Taking POE($n = 10$) as an example, the K_1 values decrease in the order NH_4^+ (26.7) > $MeNH_3^+$ (15.8) > $EtNH_3^+$ (13.2) > $PrNH_3^+$ (7.8); this order correlates with the order of the size of the alkyl group. The complexation of POE with $diMeNH_3^+$ was also detected, but was so weak that we could not evaluate it quantitatively. This also implies a correlation between the complexation strength and the number of methyl groups. POE traps a cation in a helix structure [26], and usually forms a spherical coordination shell around the cation. An ammonium ion–POE complex will have a similar structure, although the details have not been elucidated. Such a spherical coordination shell is unfavourably formed around an ammonium ion having a large alkyl group or more alkyl groups. Hence the above results are simply explained by steric hindrance.

The mobilities listed in Table 1 are smaller than expected from the conductivity measurements. Taking NH_4^+ as an example, the molar conductance of NH_4Cl was 67.68 S cm^2 mol^{-1} in 0.05 M methanolic solution. Although we did not measure the transference number, it will be reasonable to assume identical ionic conductances for NH_4^+ and Cl^-. The ionic conductance of NH_4^+, 34 S cm^2 mol^{-1}, corresponds to $\mu_{max} = 3.5 \cdot 10^{-8}$ m^2 s^{-1} V^{-1}, which is nearly three times larger than the values for the complexes listed in Table 1. Although it is usual for complexation to lower the mobility, this difference is too large. The reason has not been elucidated.

Fig. 4 shows the variations of K_1 and μ_{max} for NH_4^+–DNB-POE(n)D complexes with n. As is known for POE complexation with other cations [7], K_1 increases linearly with increase in n. On the other hand, μ_{max} increases for $n < 10$ and decreases after the maximum at $n = 10$. The linear increase in K_1 with increase in n is explained by a statistical effect: the number of oxygen atoms capable of coordination to an ammonium ion increases as the POE chain length increases. The explanation of the change in μ_{max} is more complicated, however. Correlating the size of a ligand with that of the resulting complex is straightforward; a decrease in μ_{max} is

Table 1
Complexation constants and mobilities of POE and B12C4 complexes with various cations

	Na^+		NH_4^+		$MeNH_3^+$		$diMeNH_2^+$		$EtNH_3^+$		$PrNH_3^+$	
	K_1	μ_{max}	K_1	μ_{max}	K_1	μ_{max}	K_1	μ_{max}	K_1	μ_{max}	K_1	μ_{max}
POE(6)	4.3	2.89										
POE(7)	8.6	1.58	12.2	1.02	10.5	0.66			8.1	0.46	5.6	0.48
POE(8)	12.4	1.55	17.8	1.13	10.1	0.97			9.4	0.54	5.7	0.65
POE(9)	17.4	1.46	21.4	1.29	12.9	1.02			11.3	0.59	6.9	0.69
POE(10)	22.0	1.41	26.7	1.31	15.8	1.04			13.2	0.61	7.8	0.74
POE(11)	26.2	1.37	32.4	1.31	18.6	1.04			14.1	0.66	9.1	0.74
POE(12)	26.6	1.49	38.8	1.29	20.5	1.08			15.8	0.68	9.9	0.76
POE(13)	30.9	1.42	44.5	1.27	22.6	1.09					10.7	0.78
POE(14)	34.8	1.37	49.6	1.25	25.2	1.08						
POE(15)	37.7	1.37	54.5	1.24	26.7	1.09						
POE(16)	38.9	1.38	59.4	1.23	28.1	1.11						
POE(17)			63.3	1.23	28.9	1.13						
B12C4	15.9	2.10	50.2	0.38	20.7	0.87	31.8	0.54	28.1	0.50	19.0	0.55

The u_{max} values are in 10^{-8} m^2 s^{-1} V^{-1}. Ionic strength, 0.05 *M*.

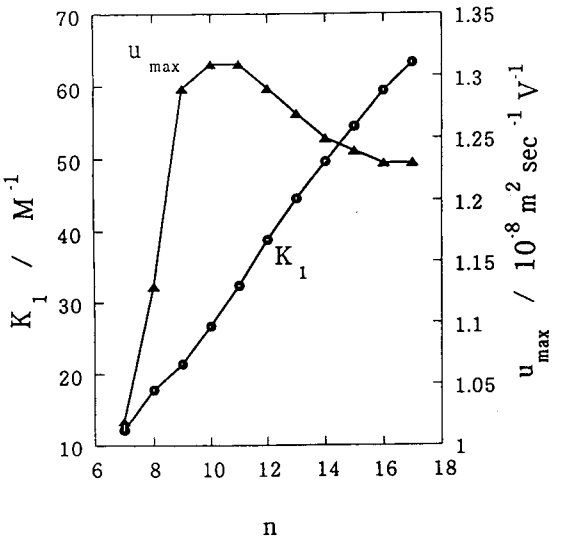

Fig. 4. Variations of K_1 and μ_{max} with n for NH_4^+ complex.

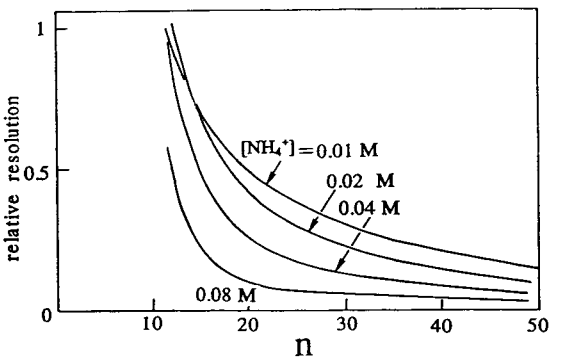

Fig. 5. Simulated decreases in relative resolution for DNB-POE(n)d separation with NH_4Cl as a carrier cation. K_1 and μ_{max} were extrapolated on the basis of the relationships depicted in Fig. 4. Identical diffusion coefficients were assumed for all oligomers for simplicity.

also explained by the increasing size of the ligand. This consideration holds if a POE molecule is large enough to remove solvent molecules completely from the solvation shell of an ammonium ion. However, other factors should be taken into account in some instances. When a few solvent molecules still exist in the solvation shell of NH_4^+, the size of the solvated complex is larger than expected from the size of the ligand, and the mobility is lowered. Such complex formation will take place when a POE chain is not large enough to replace solvent molecules completely. These phenomena are superimposed in Fig. 4.

3.4. Simulation of separation

As mentioned already, the present method is suitable for the separation of relatively short POEs. We can simulate the separation of POEs with NH_4^+ as an electrolyte cation using the values listed Table 1. K_1 and μ_{max} values for larger POE were calculated by extrapolation of the data depicted in Fig. 4; a linear and an exponential relationship were assumed between K_1 and n and between μ_{max} and n ($\geq$10), respectively. The resolution (R) between adjacent peaks was calculated by [1]

$$R = 0.25\,[\mu_{ep}(1) - \mu_{ep}(2)]V^{1/2}[2LD(\mu_{ep} + \mu_{eo})]^{-1/2}$$

where $\mu_{ep}(1)$, $\mu_{ep}(2)$ and μ_{ep} are electrophoretic mobilities for two solutes of interest and the average electrophoretic mobility, respectively, and V, L and D are the voltage applied, the length of the capillary and the diffusion coefficient of the solute. If identical D values can be assumed for all complexes, we can calculate the relative resolution for POE chains of $n \geq 10$. Fig. 5 shows the results. The relative resolution becomes worse as n increases, regardless of the concentration of NH_4^+. Also, a lower C_M generally provides a better separation.

Fig. 6 shows the simulated and experimental electropherograms. Although a constant EOF was assumed for the simulation, it was difficult to keep it constant experimentally; this makes direct comparison difficult. However, the above consideration in general describes the actual separation well.

4. Conclusions

It has been shown that electrophoresis in methanol is effective for the evaluation of poly-

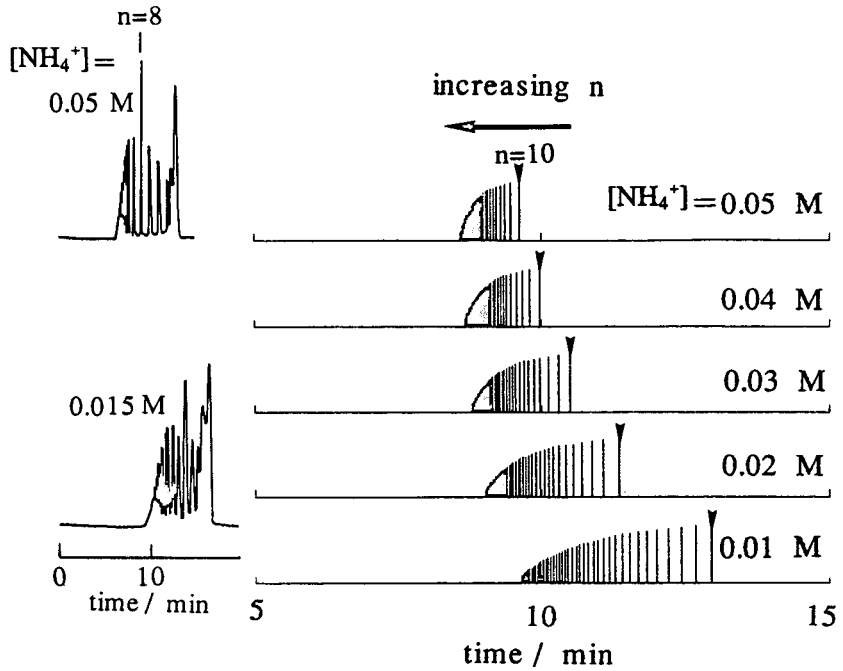

Fig. 6. Simulated and actual electropherograms for the separation of DNB-POE(*n*)D. Simulation was done with basically the same method as in Fig. 5. Experimental conditions: upper electropherogram, 50 m*M* NH_4Cl + 50 m*M* Et_3N; lower electropherogram, 15 m*M* NH_4Cl + 15 m*M* Et_3N + 35 m*M* Et_4NCl. Detection at 250 nm.

ether complexation and the separation of polyethers. It will also be possible to use a weak interaction, which is not detected by other methods, for the separation and to evaluate it.

Interactions and equilibria taking place in non-aqueous solvents have usually been studied by, e.g., spectrometry or electrochemical methods. However, the present method is also effective for many reasons mentioned already. Although the separation in methanol was taken as an example here to show the efficiency, the present method is applicable to other non-aqueous solvents. The author believes that non-aqueous electrophoresis can be a better and more reliable approach to solution chemistry and that, in a particular case, this method can possibly elucidate interactions that have not even been detected by other methods. Novel applications of this technique will make this point clearer in the near future.

Acknowledgement

This work was supported in part by a Grant-in-Aid for Scientific Research from the Ministry of Education, Science and Culture, Japan.

References

[1] S.F.Y. Li, *Capillary Electrophoresis —Principles, Practice and Applications*, Elsevier, Amsterdam, 1992.
[2] M. Albin, P.D. Grossman and S.E. Moring, *Anal. Chem.*, 65 (1993) 489A.
[3] S. Terabe, *Micellar Electrokinetic Chromatography*, Beckman, Fullerton, CA, 1992; and references cited therein.
[4] J. Vindevogel and P. Sandra, *Introduction to Micellar Electrokinetic Chromatography*, Hüthig: Heidelberg, 1992; and references cited therein.
[5] T. Okada, *J. Chromatogr.*, 538 (1991) 341.
[6] T. Okada, *Anal. Chem.*, 64 (1992) 589.
[7] T. Okada, *Macromolecules*, 23 (1990) 4216.

[8] T. Okada, *J. Chem. Soc., Faraday Trans.*, 87 (1991) 3027.
[9] T. Okada, *J. Chem. Soc., Chem. Commun.*, 1991, 1209.
[10] T. Okada, *Anal. Chim. Acta.*, 281 (1993) 85.
[11] J. Liu, K.A. Cobb and M. Novotny, *J. Chromatogr.*, 468 (1988) 55.
[12] W. Buchberger and P.R. Haddad, *J. Chromatogr.*, 608 (1992) 59.
[13] S.A.C. Wren and R.C. Rowe, *J. Chromatogr.*, 609 (1992) 363.
[14] G.M. Janini, K.C. Chan, J.A. Barnes, G.M. Muschik and H.J. Issaq, *Chromatographia*, 35 (1993) 497.
[15] M. Idei, I. Mezo, Z. Vadasz, A. Horvath, I. Teplan and G. Keri, *J. Liq. Chromatogr.*, 15 (1992) 3181.
[16] E. Kenndler and B. Gassner, *Anal. Chem.*, 62 (1990) 431.
[17] R.S. Sahota and M.G. Khaledi, *Anal. Chem.*, 66 (1994) 1141.
[18] C.J. Pedersen, *J. Am. Chem. Soc.*, 89 (1967) 7017.
[19] R.M. Izatt, J.S. Bradshaw, S.A. Nielsen, J.D. Lamb and J.J. Christensen, *Chem. Rev.*, 85 (1985) 271.
[20] Y. Inoue, T. Hakushi and Y. Lui, in Y. Inoue and G.W. Gokel (Editors), *Cation Binding by Macrocycles*, Marcel Dekker, New York, 1990, Ch. 1.
[21] K. Liu, *Macromolecules*, 1 (1968) 308.
[22] K. Ono, H. Konami and K. Murakami, *J. Phys. Chem.*, 83 (1979) 2665.
[23] T. Okada and T. Usui, *Anal. Chem.*, 66 (1994) 1654.
[24] D.Ph. Zollinger, E. Bulten, A. Christenhusz, M. Bos and W.E. van der Linden, *Anal. Chim. Acta*, 198 (1987) 207.
[25] D.E. Fenton, in G. Wilkinson, R.D. Gillard and J.A. McCleverty (Editors), *Comprehensive Coordination Chemistry*, Vol. 30, Pergamon Press, Oxford, 1987, Ch. 23.
[26] T. Okada, *Analyst*, 118 (1993) 959; and references cited therein.

ELSEVIER

Journal of Chromatography A, 695 (1995) 319–323

JOURNAL OF CHROMATOGRAPHY A

Short communication

Determination of fumonisins B_1, B_2, B_3 and B_4 by high-performance liquid chromatography with evaporative light-scattering detection

Jon G. Wilkes[a,*], John B. Sutherland[b], Mona I. Churchwell[a], Anna J. Williams[b]

[a]*Division of Chemistry, National Center for Toxicological Research, United States Food and Drug Administration, Jefferson, AR 72079, USA*

[b]*Division of Microbiology, National Center for Toxicological Research, United States Food and Drug Administration, Jefferson, AR 72079, USA*

First received 15 August 1994; revised manuscript received 11 January 1995; accepted 13 January 1995

Abstract

Fumonisins B_1, B_2, B_3 and B_4 (FB_1–FB_4), a group of mycotoxins produced by the fungus *Fusarium moniliforme*, were separated by HPLC using an analytical-scale, base-deactivated C_8 column and a gradient of trifluoroacetic acid buffer (pH 2.7) and acetonitrile. An evaporative light-scattering detector was used to detect the fumonisin peaks. A semi-preparative-scale, base-deactivated C_8 column with a 1:14 mobile phase split facilitated the purification of analytical standards of FB_1.

1. Introduction

The fumonisins are a group of aliphatic mycotoxins, produced by *Fusarium moniliforme* and a few other fungi [1–3], which have been found in many food products made from corn [4]. Seven different fumonisins have been described: FA_1, FA_2, FB_1, FB_2, FB_3, FB_4 and FC_1 [5–7]. The most abundant of these are the four B-type fumonisins (Fig. 1). Corn containing these toxins induces leukoencephalomalacia in horses, pulmonary edema in hogs, and hepatic carcinomas in rats [2,3,8]. FB_1 has also been associated with high incidences of esophageal cancer in humans in South Africa [9] and China [10].

Analysis of fumonisins by high-performance liquid chromatography (HPLC) normally requires derivatization with various reagents to

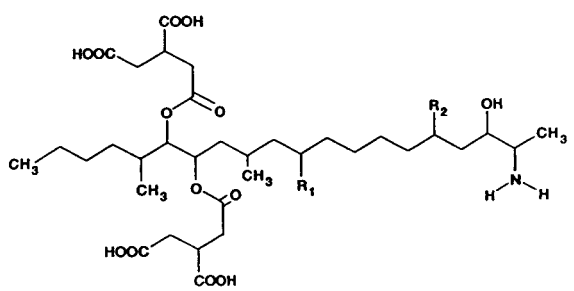

Fig. 1. Structures of fumonisins B_1–B_4. FB_1: $R_1 = R_2 = OH$; FB_2: $R_1 = H$, $R_2 = OH$; FB_3: $R_1 = OH$, $R_2 = H$; FB_4: $R_1 = R_2 = H$.

* Corresponding author.

0021-9673/95/$09.50
SSDI 0021-9673(95)00064-X

allow detection. Maleic anhydride derivatization and a UV detector were used in the first method [11]. Other reagents requiring fluorescence detection have been used: *o*-phthaldialdehyde [4,12], fluorescamine [13–15], 4-fluoro-7-nitrobenz-2-oxa-1,3-diazole [16]; naphthalene 2,3-dicarboxaldehyde [17–19] and 9-fluorenylmethyl chloroformate [20]. LC–mass spectrometry (MS) has also been used for analysis of FB_1 [21,22].

In this study we describe the use of HPLC for the determination of underivatized fumonisins with evaporative light-scattering detection (ELSD). This detection method facilitates both the purification of fumonisins for analytical standards and the collection of impurities for further, off-line analysis.

2. Experimental

FB_1 and FB_2 were obtained from the Council for Scientific and Industrial Research, Pretoria, South Africa. FB_3 and FB_4 were obtained from Dr. R.D. Plattner of the Agricultural Research Service, United States Department of Agriculture, Peoria, IL, USA.

For the analytical-scale experiments, a Shimadzu (Kyoto, Japan) liquid chromatograph was used with a 250 × 4.6 mm, 5 μm YMCbasic base-deactivated C_8 column (YMC, Wilmington, NC, USA). The column was maintained at 40°C. The mobile phase consisted of a binary, three-step, variable concentration gradient with a constant flow rate of 1.0 ml/min. Solution A was acetonitrile–water–trifluoroacetic acid (TFA) (5:95:0.025, v/v). The resulting solution had a pH of 2.7. Solution B was acetonitrile–water–TFA (90:10:0.025, v/v). The gradient comprised a linear program of 20 to 60% B in 30 min, followed by 60 to 80% B in 10 min, and then 80 to 100% B in 2 min.

Aqueous samples (20 μl) of FB_1, FB_2, FB_3 and FB_4 (nominal concentrations of 100, 100, 103 and 132 μg/ml, respectively) and of solvent blanks were injected. A Varex MK III evaporative light-scattering detector (Alltech, Deerfield, IL, USA) was used to detect fumonisins and other components. A 1:1 mobile phase split was achieved by directing the 1.0 ml/min flow into a ZT1 zero-dead-volume tee (Valco, Houston, TX, USA) with two identical outlet arms, each a 350 mm length of stainless-steel capillary tubing. This apparatus allowed simultaneous detection and collection of all low-volatility analytes. Detector response was registered by a Shimadzu Model C-R3A Chromatopac integrator.

For the semi-preparative-scale experiments, a 250 × 10 mm, 5 μm YMCbasic C_8 column and the same HPLC hardware were used. However, to achieve optimal separation of minor impurities from FB_1, the chromatographic conditions were modified: column temperature 50°C, HPLC flow-rate 5.0 ml/min, and solvents A and B (as defined above) with a mixture composition of 30% B for the first 20 min and 100% B thereafter. The detector plumbing configuration was modified to produce a 14:1 split, which was appropriate for the much larger mobile phase flow allowed by the larger column. The 14:1 split modification was achieved using two fused-silica capillaries as outlet legs from the ZT1 tee. The minor flow outlet (125 mm × 50 μm I.D.) was connected to the detector inlet, while the major flow outlet (250 mm × 100 μm I.D.) led the majority of the mobile phase to waste or, whenever a peak was detected, to collection. Linear flow-rate calculations for each leg confirmed that the asymmetric design led to a difference in exit time from the outlets of less than 0.5 s and that the detected portion of the sample exited before the collectable portion. Detector output for the Varex MK III ELSD is indicated in real time from a digital meter located, with other parameter readouts, on the front panel. The Shimadzu integrator response, when used in normal acquisition mode rather than plotting mode, typically lagged the real time signal by about 5 s. These details are significant because the purpose of the second instrumental configuration and associated chromatographic conditions was to enable collection of trace components in amounts sufficient for off-line identification by MS. By watching the detector output, rather than the integrator trace, accurate collection of separated components was possible.

The sample for the second set of experiments

consisted of partially purified FB_1 produced by growing *F. moniliforme* NRRL-13616 on corn for 28 days. After extraction and cleanup [15], it was dissolved in 100% water at a concentration of 25 mg/ml. Sample injection volumes were varied from 1 to 10 μl and the mobile phase composition was also varied. The objective was to find the maximum sample load consistent with quality separation of minor components. Good separation with reasonable sensitivity was obtained using a 4-μl injection at 30% B. In that case, 100 μg was the total sample load on the column.

3. Results and discussion

The analytical base-deactivated C_8 column, with the water–acetonitrile gradient, successfully separated the four fumonisins tested. The retention times of FB_1, FB_2, FB_3 and FB_4 in this gradient were 16.3, 21.4, 19.1 and 24.5 min, respectively (Fig. 2). No peaks were found after the injection of pure water.

Each of the fumonisin samples and solvent controls showed a peak, which has not yet been identified, at $t_R \approx 3.3$ min (Fig. 2). Most of this peak disappeared if the sample solutions were stored in plastic rather than Pyrex vials.

Fig. 2 demonstrates good separation, reasonable chromatographic peak shape and, with one exception, good detector sensitivity with low background noise. The greatly reduced signal for FB_4 (Fig. 2D, peak at $t_R = 24.5$ min) arises from uncertainty in the concentration of the standard available, rather than from a reduced ELSD sensitivity for this fumonisin.

Fig. 3 shows a separation, using the semi-preparative C_8 column, of FB_1 and several minor impurities extracted from cultures of *F. moniliforme* on corn. The approximate mass of the impurity at $t_R = 10.6$ min was less than 1 μg, but due to the flow split, only ca. 60 ng of this peak entered the detector. The experimental arrangement allowed collection of ca. 800 ng of this impurity and up to 90 μg of the FB_1 from a single injection of the crude extract. The recovery of each purified component in the semi-preparative-scale experiment was determined by the split ratio used. That is with a 14:1 split, 1/15 of each component went to the detector and was lost. The remaining 14/15 = 93% of each sample was recovered.

ELSD appeared to be sufficiently sensitive to detect ca. 60 ng of FB_1 per injection. Depending on the split used, the limits of detection for components in solution varied from 6 μg/ml for the analytical-scale system to 220 μg/ml for the semi-preparative-scale system. This amounted to ca. 120 ng of analyte injected for the analytical-scale column and ca. 900 ng for the semi-preparative column.

Because the analytical base-deactivated C_8 column separates all four of the B-type fumonisins by HPLC without precolumn derivatization, aliquots can be collected individually as they elute from the column. Larger-scale purification of each, if desired, is possible with the semi-preparative column. As mentioned above, other methods for the separation and purification of fumonisins require either sample derivatization [12,13,15–17,20] or the use of MS [21,22] for detection.

For preparation of analytical standards of FB_1, detection methods using derivatization require blind sampling of the chromatographic eluate. The fumonisin itself does not produce a fluorescence detector response and the fumonisin derivatives, which can be detected, are not the product desired. The derivatized fumonisin cannot be used as an internal chromatographic standard in reversed-phase chromatography to aid collection of the fumonisin itself because it elutes *after* free fumonisin (data not shown).

A similar practical difficulty is found with on-line MS detection methods, such as that of Young and Lafontaine [22], who assayed FB_1, FB_2 and FB_3 by LC–particle beam MS using tetramethyl ester derivatives. The methyl esters have sufficient volatility for efficient vaporization and ionization to occur in the particle beam MS source. Since this is not true for fumonisin as a free acid, without the methylation step, blind sampling would again be required. Since the fumonisin methyl ester derivative elutes later than the free fumonisin, it could only be used as

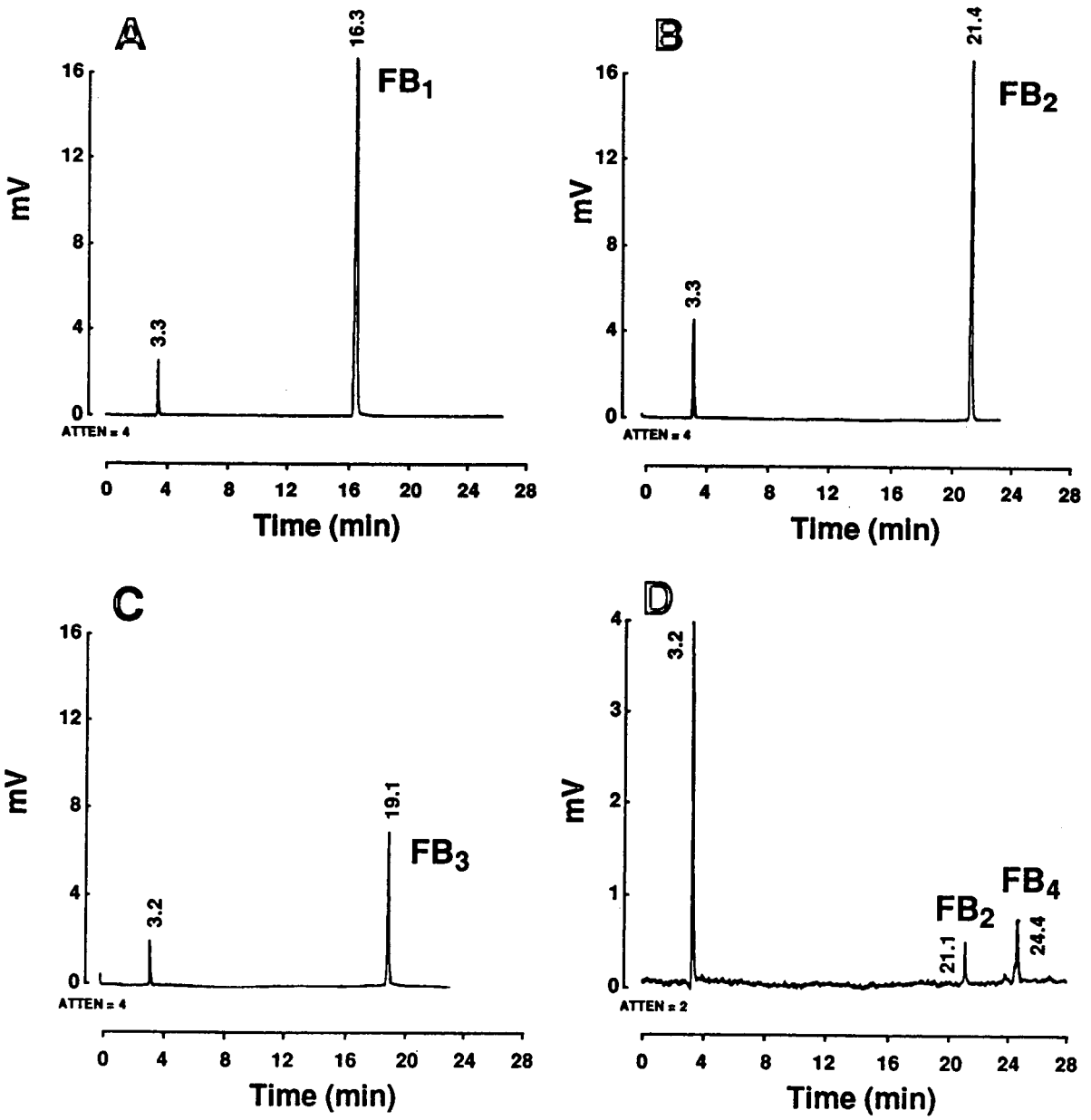

Fig. 2. HPLC elution profiles of FB_1–FB_4, produced with the analytical system. (A) FB_1, (B) FB_2, (C) FB_3, (D) FB_2 and FB_4. The experimental samples were nominally 2 μg each as injected on the column and 1 μg each as presented to the detector.

an external chromatographic standard. Such problems are resolved by the use of ELSD.

For safety, since analytes with low volatility are detected as an aerosol by ELSD, this aerosol must be contained and vented to a chemical fume hood. The integrity of plumbing connections must also be verified before working with toxic substances.

This work has demonstrated that reversed-phase HPLC–ELSD is feasible for the determi-

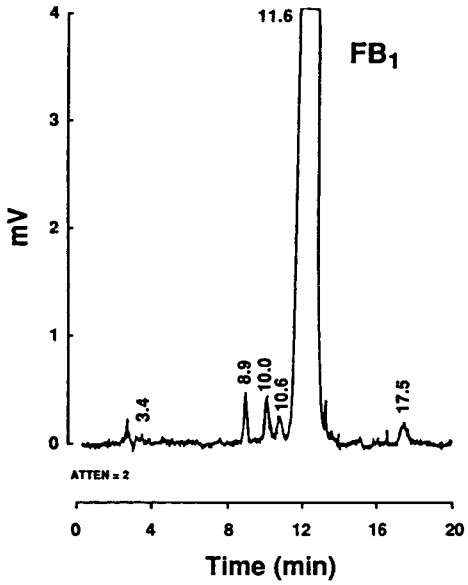

Fig. 3. Low-attenuation HPLC chromatogram of FB_1, showing trace impurities, produced with the semi-preparative system. From an experimental sample of 100 μg, about 7 μg reached the detector and the remainder was available for collection. This separation yielded almost 90 μg of pure FB_1 from an impure sample of 100 μg.

nation, without derivatization, of FB_1, FB_2, FB_3 and FB_4 as well as for the purification of FB_1.

Acknowledgements

We thank R.D. Plattner for kindly providing some of the fumonisin samples. We also thank Manuel Holcomb for helpful discussions related to his experience with the fluorescamine and 9-fluorenylmethoxycarbonyl derivatization techniques for fumonisin analysis. Finally, we thank J.P. Freeman for his help during manuscript preparation.

References

[1] P.E. Nelson, A.E. Desjardins and R.D. Plattner, *Annu. Rev. Phytopathol.*, 31 (1993) 233.
[2] W.P. Norred, *J. Toxicol. Environ. Health*, 38 (1993) 309.
[3] P.M. Scott, *Int. J. Food Microbiol.*, 18 (1993) 257.
[4] M.E. Stack and R.M. Eppley, *J. Assoc. Off. Anal. Chem. Int.*, 75 (1992) 834.
[5] S.C. Bezuidenhout, W.C.A. Gelderblom, C.P. Gorst-Allman, R.M. Horak, W.F.O. Marasas, G. Spiteller and R. Vleggaar, *J. Chem. Soc., Chem. Commun.*, (1988) 743.
[6] M.E. Cawood, W.C.A. Gelderblom, R. Vleggaar, Y. Behrend, P.G. Thiel and W.F.O. Marasas, *J. Agric. Food Chem.*, 39 (1991) 1958.
[7] B.E. Branham and R.D. Plattner, *J. Nat. Prod.*, 56 (1993) 1630.
[8] N.P.J. Kriek, T.S. Kellerman and W.F.O. Marasas, *Onderstepoort J. Vet. Res.*, 48 (1981) 129.
[9] J.P. Rheeder, W.F.O. Marasas, P.G. Thiel, E.W. Sydenham, G.S. Shephard and D.J. van Schalkwyk, *Phytopathology*, 82 (1992) 353.
[10] F.S. Chu and G.Y. Li, *Appl. Environ. Microbiol.*, 60 (1994) 847.
[11] W.C.A. Gelderblom, K. Jaskiewicz, W.F.O. Marasas, P.G. Thiel, R.M. Horak, R. Vleggaar and N.P.J. Kriek, *Appl. Environ. Microbiol.*, 54 (1988) 1806.
[12] G.S. Shephard, E.W. Sydenham, P.G. Thiel and W.C.A. Gelderblom, *J. Liq. Chromatogr.*, 13 (1990) 2077.
[13] E.W. Sydenham, W.C.A. Gelderblom, P.G. Thiel and W.F.O. Marasas, *J. Agric. Food Chem.*, 38 (1990) 285.
[14] T.M. Wilson, P.F. Ross, L.G. Rice, G.D. Osweiler, H.A. Nelson, D.L. Owens, R.D. Plattner, C. Reggiardo, T.H. Noon and J.W. Pickrell, *J. Vet. Diagn. Invest.*, 2 (1990) 213.
[15] M. Holcomb, J.B. Sutherland, M.P. Chiarelli, W.A. Korfmacher, H.C. Thompson, J.O. Lay, L.J. Hankins and C.E. Cerniglia, *J. Agric. Food Chem.*, 41 (1993) 357.
[16] P.M. Scott and G.A. Lawrence. *J. Assoc. Off. Anal. Chem. Int.*, 75 (1992) 829.
[17] R.J. Bothast, G.A. Bennett, J.E. Vancauwenberge and J.L. Richard, *Appl. Environ. Microbiol.*, 58 (1992) 233.
[18] G.M. Ware, O. Francis, S.S. Kuan, P. Umrigar, A. Carman, L. Carter and G.A. Bennett, *Anal. Lett.*, 26 (1993) 1751.
[19] G.A. Bennett and J.L. Richard, *J. Assoc. Off. Anal. Chem. Int.*, 77 (1994) 501.
[20] M. Holcomb, H.C. Thompson and L.J. Hankins, *J. Agric. Food Chem.*, 41 (1993) 764.
[21] J. Chen, C.J. Mirocha, W. Xie, L. Hogge and D. Olson, *Appl. Environ. Microbiol.*, 58 (1992) 3928.
[22] J.C. Young and P. Lafontaine, *Rapid Commun. Mass Spectrom.*, 7 (1993) 352.

ELSEVIER

Journal of Chromatography A, 695 (1995) 324–328

JOURNAL OF CHROMATOGRAPHY A

Short communication

Carbon monoxide generation from hydrocarbons at ambient and physiological temperature: a sensitive indicator of oxidant damage?

Michael D. Levitt[a,*], Carol Ellis[a], John Springfield[a], Rolf R. Engel[b]

[a]*Department of Veterans Affairs Medical Center (151), 1 Veterans Drive, Minneapolis, MN 55417, USA*

[b]*Hennepin County Medical Center, Minneapolis, MN, USA*

First received 31 October 1994; revised manuscript received 13 December 1994; accepted 14 December 1994

Abstract

This paper shows that a variety of carbon-containing materials (wool, cotton, wood, paper, latex, Tygon) release CO during incubation at ambient temperature. This CO production was enhanced by aerobic versus anaerobic incubation, increasing temperature, and exposure to fluorescent light. CO production from glucose solutions was enhanced by alkaline pH or prior boiling or autoclaving and reduced by the presence of superoxide dismutase or catalase. We conclude that a variety of materials are constantly undergoing oxidation at ambient or physiological temperature as evidenced by the release of CO. Measurements of this CO production could provide a simple, rapid and sensitive means of assessing oxidative damage.

1. Introduction

An enzymatically catalyzed breakdown of heme to biliverdin [1,2] is thought to be the sole source of carbon monoxide (CO) production in living organisms. In the course of measuring CO excretion to assess heme turnover in rats, the chow and bedding were found to liberate quantities of CO far in excess of the rat's endogenous production. This observation led us to investigate the possibility that other compounds similarly might be undergoing spontaneous oxidation as evidenced by the production of CO. In this paper we demonstrate that a wide variety of compounds are constantly liberating CO at ambient temperature and suggest that measurement of this CO formation could serve as a novel indicator of oxidant damage.

2. Materials and methods

Studies of CO release from test substances were carried out in 50-ml glass syringes lubricated with mineral oil and sealed with plastic stopcocks. The test material was placed in a 10-ml glass vial that rested on the plunger in a vertically maintained syringe. The syringe was purged with gas rendered CO-free via passage through a combuster (Cat-1 catalytic combustion filter; Trace Analytical, Menlo Park, CA, USA) and then filled with 44 ml of the gas. Incubations were carried out at 4°C, laboratory temperature (approximately 21°C) or 38°C, both in the dark

* Corresponding author.

0021-9673/95/$09.50
SSDI 0021-9673(94)01232-6

or light (20–30 cm distant from a lamp containing two standard 15 W fluorescent bulbs).

Materials tested included pine wood, paper (white, bond), white cotton, wool, latex rubber, Tygon (tubing), polyolefin and glucose. Glucose was studied in the crystalline state or as a 5 g/dl solution in water or 0.2 *M* $NaPO_4$. In some studies, 420 units of catalase (Sigma, St. Louis, MO, USA) or 330 U of superoxide dismutase (SOD) (Sigma) were added to the reaction mixture. A unit of catalase decomposes 1 μmol of H_2O_2/min at pH 7 and 25°C. One unit of superoxide dismutase produces a 50% inhibition of the reduction rate of cytochrome *c* in a coupled system with xanthine and xanthine oxidase at pH 7.8 and 25°C.

Carbon monoxide was measured by gas chromatography (GC) using a 3 ft. × 1/8 in. (1 ft. = 30.48 cm, 1 in. = 2.54 cm) column packed with molecular sieve (type 5A, 40–60 mesh) and a reduction detector (Trace Analytical). The carrier gas was argon (40 ml/min), and the oven temperature 100°C. The lowest detectable concentration of CO (relative standard deviation ± 10%) was about 0.1 ppm. Comparison of selected CO measurements obtained with a Digilab Model FTS-40 Fourier transform infrared spectrometer agreed to within ± 10% of GC results.

3. Results

We initially attempted to measure CO production from various substrates in 60-ml plastic syringes (Beckton Dickenson, Franklin Lakes, NJ, USA). However, the syringe itself produced appreciable CO. For example, after 24-, 48- and 72-h incubations in the dark at 37°C, CO concentrations in the syringe were 0.9, 1.8 and 2.9 ppm, respectively. Comparable values for incubations under fluorescent light were 11, 28 and 39 ppm. Studies of the components of the plastic syringes placed in glass syringes demonstrated that CO primarily was derived from the polypropylene body of the syringe (0.036 μmol/24 h) rather than the rubber seal (0.0028 μmol/24 h).

Studies of oiled glass syringes showed CO concentrations of less than 0.15 ppm (0.00036 μmol) after 24 h of incubation. In all reported studies, CO production by a test substance was determined from the CO accumulating in the gas space of a glass syringe.

Fig. 1 shows the CO accumulation observed when a variety of common carbon containing compounds were incubated at ambient temperature and ambient partial oxygen pressure (P_{O_2}) either in the dark or under a fluorescent light. Each compound released some CO, although the rate of release per g varied widely between compounds. Exposure to light markedly enhanced the release of CO by most of these materials.

Fig. 2 shows that the rate of production of CO by these compounds during exposure to light increased as the incubation temperature was raised from 4°C to 21°C or 37°C. The substitution of an argon atmosphere for air markedly reduced but did not totally inhibit CO production (Fig. 3).

Table 1 summarizes the results of studies of glucose incubated with air at 37°C in the dark. The crystalline sugar yielded negligible CO as did a distilled water solution of glucose. Glucose dissolved in 0.2 *M* phosphate buffer demonstrated increasing CO release with increasing pH. Experiments at pH 7 showed that when the glucose solution was boiled for 4 min or autoclaved for 15 min, CO production was enhanced

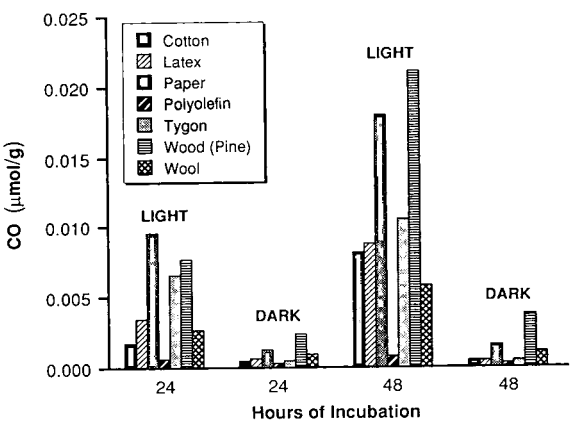

Fig. 1. Production of CO by various materials incubated at ambient temperature and P_{O_2}, either in the dark or under fluorescent lighting.

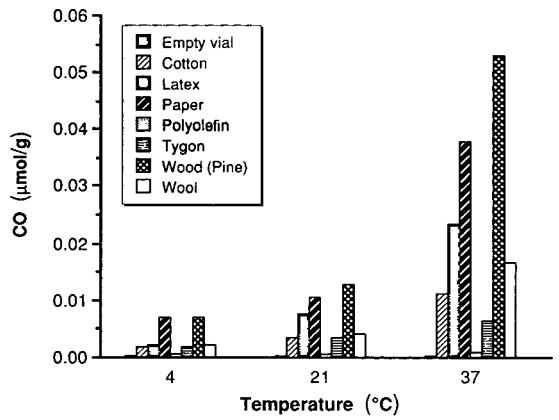

Fig. 2. Influence of temperature on production of CO by various materials during exposure to ambient P_{O2} and fluorescent lighting.

by about 50-fold and 150-fold, respectively. The addition of superoxide dismutase (330 units) or catalase (420 units) to the boiled or autoclaved glucose solutions reduced, but did not eliminate, CO production. When boiled glucose was incubated anaerobically, CO production was undetectable. Production of CO was roughly doubled when glucose was incubated in the light as opposed to the dark (data not shown).

Studies with a commercial source of sterile glucose for oral use (5% Glucose Water, Ross Labs.) demonstrated sizable CO production (0.14 μm g^{-1} 24 h^{-1}) when a 1:1 dilution in pH 7.4 phosphate buffer was incubated in the light.

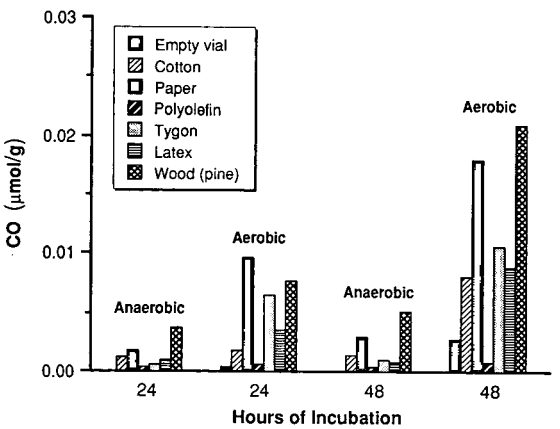

Fig. 3. Production of CO by various materials at ambient temperature under fluorescent lighting when incubated aerobically (ambient P_{O2}) or anerobically.

4. Discussion

Accurate measurement of CO production from substrates required an incubation system that produced minimal quantities of this gas. Plastic syringes released appreciable CO, particularly when exposed to light, a phenomenon previously attributed to dissolution of atmospheric CO from the plastic [3]. However, this CO seemingly must reflect production by the syringe since the CO concentration in our syringes reached values (39 ppm) which were far in excess of atmospheric CO concentration (<2 ppm). Glass syringes lubricated with mineral oil and sealed with stopcocks leaked at a negligible rate and produced minimal CO, and the CO production from various substrates was therefore assessed via the release of CO into the gas space of glass syringes.

A wide variety of common non-biological substances (cotton, wood, paper, Tygon, latex) were found to liberate CO when incubated at ambient temperature and P_{O2} (see Fig. 1). The rate of this CO release was diminished during anaerobic incubation, enhanced with increasing temperature (4°C to 37°C), and increased by exposure to fluorescent light. Each of these findings supports the concept that the CO release reflected an oxidative process, rather than desorption of CO dissolved in the test materials. The influence of light indicates that photo-oxidation, presumably via singlet oxygen, was an important mechanism in the CO production.

Additional studies were carried out with glucose (see table), a well-defined, biologically important compound. During incubation at ambient P_{O2} and at 37°C in the dark, little or no CO production was observed with glucose in the crystalline state or in distilled water. With dissolution in PO_4 buffer, CO production was very dependent upon pH, increasing linearly as pH was increased from 5 to 9. Boiling a glucose solution markedly enhanced the subsequent CO

Table 1
Production of CO from glucose (5 g/dl) incubated at ambient P_{O_2} in the dark at 37°C

Form	pH	Heat treatment	Antioxidant	CO (μmol g^{-1} 24 h^{-1})
Crystalline		No	None	Not detectable[a]
In distilled water		No	None	Not detectable
In PO_4 buffer	5.0	No	None	Not detectable
In PO_4 buffer	6.0	No	None	0.0063
In PO_4 buffer	7.0	No	None	0.022
In PO_4 buffer	8.0	No	None	0.046
In PO_4 buffer	9.0	No	None	0.23
In PO_4 buffer	7.0	Boiled	None	1.38
In PO_4 buffer	7.0	Boiled	SOD	0.38
In PO_4 buffer	7.0	Boiled	Catalase	0.30
In PO_4 buffer	7.0	Autoclaved	None	4.1
In PO_4 buffer	7.0	Autoclaved	SOD	2.1
In PO_4 buffer	7.0	Autoclaved	Catalase	1.5

[a] Not detectable indicates CO production of <0.2 nmol above that observed in control syringe.

production, and even greater CO release was observed with autoclaving. Autoclaving has been demonstrated to alter the structure of glucose [4], and the increased CO from the heated compound presumably indicates that the altered molecule was more susceptible to oxidant damage. The appreciable CO production observed with a commercial glucose solution used in patient care similarly suggests that this glucose had been altered by the sterilization process.

Production of CO by boiled glucose was totally eliminated when an argon atmosphere was used in place of air. The low, but measurable, CO production observed during anaerobic incubation of the non-biological compounds (Fig. 1) may reflect the inability to adequately deoxygenate these compounds because of their solid state or the involvement of different types of oxidative reactions. The addition of either superoxide dismutase or catalase to the glucose solution reduced the release of CO, suggesting that superoxide and hydrogen peroxide played roles in the CO release.

We conclude from the CO generation in the above studies that a wide array of compounds undergo spontaneous oxidation at ambient or physiological temperature. The biomedical literature contains only a few references to such CO release. Vreman et al. [5] reported that light exposure induced CO production from a variety of compounds (including glucose) in the presence of the photosensitizer, tin protoporphyrin. Wolff and Bidlack [6] reported that CO was released during lipid peroxidation. In addition, CO production at ambient temperature has been reported during the auto-oxidation of phenols [7] such as L-3,4-dihydroxyphenylalanine [8]. Lastly, we observed that mouse feces and urine produced CO via a non-enzymatic reaction [9].

In the biomedical literature, most references to CO production concern the release of this gas during the heme oxygenase catalyzed breakdown of heme to biliverdin. The finding that CO production rather accurately reflects heme breakdown [1,2] suggests that the non-specific CO production observed in the present study is inhibited by body antioxidants. The present study demonstrates that accurate assessment of the CO production resulting from heme turnover requires extreme care in order to exclude artifacts resulting from non-specific CO production by the materials employed in the collection of the gas samples.

We propose that CO production might serve as a novel indicator of oxidant damage. In our assay system, the production of 0.2 nmol of CO could be differentiated from background CO. In the case of glucose, this amount of CO reflected

the oxidation of about $1/10^7$ of the carbon molecules. With minor modifications of the assay system, the sensitivity of the technique could be enhanced by several orders of magnitude. In addition, the method is technically very simple. The low solubility of CO in heme-free liquids results in the quantitative accumulation of CO in the gas space over the solution. The untreated gas space is directly injected onto the GC column, and CO elutes in about 2 min with no interference from other gases. Thus, measurement of CO release could provide a simple, rapid and sensitive means of quantitatively assessing oxidative damage to a wide variety of compounds.

Acknowledgements

This study was supported in part by the Department of Veterans Affairs and NIDDKD RO1 DK13309-25.

References

[1] R.F. Coburn, W.J. Williams and S.B. Kahn, *J. Clin. Invest.*, 45 (1966) 460.
[2] S.A. Landaw, E.W. Callahan, Jr. and R.J. Schmid, *J. Clin. Invest.*, 49 (1970) 914.
[3] F.L. Rodkey, H.A. Collison and R.R. Engel, *J. Appl. Physiol.*, 27 (1969) 554.
[4] R.B. Taylor, B.M. Jappy and J.M.J. Neil, *Pharm. Pharmacol.*, 23 (1971) 121.
[5] H.J. Vreman, M.J. Gillman, K.R. Downum and D.K. Stevenson, *Dev. Pharmacol. Ther.*, 15 (1990) 112.
[6] D.G. Wolff and W.R. Bidlack, *Biochem. Biophys. Res. Commun.*, 673 (1976) 850.
[7] S. Miyahara and H.J. Takahashi, *J. Biochem.*, 69 (1971) 231.
[8] M.J. Cooper and R.R. Engel, *Clin. Chim. Acta*, 202 (1991) 105.
[9] M.D. Levitt, C.J. Ellis and R.R. Engel, *J. Lab. Clin. Med.*, 113 (1989) 241.

Author Index

Quality Assurance for Environmental Analysis

Method Evaluation within the Measurements and Testing Programme (BCR)

Edited by **Ph. Quevauviller**, **E.A. Maier** and **B. Griepink**

Techniques and Instrumentation in Analytical Chemistry, Volume 17

Quality assurance (QA) for environmental analysis is a growing feature of the nineties as is illustrated by the number of QA guidelines and systems which are being implemented nowadays. This book focuses on the technical aspects of quality assurance. The techniques used in different analytical fields are critically reviewed and existing tools for evaluating their performance are described. Particular reference is made to the activities of the Measurements and Testing Programme (BCR) of the European Commission towards the improvement of quality control of environmental analysis.

Contents: 1. Quality assurance for environmental analysis (Ph. Quevauviller *et al.*). 2. Development of ICPMS and ID-ICPMS with the determination of Pb and Hg in environmental matrices as an example (M. Campbell). 3. Detection of sources of error in the determination of Cr in environmental matrices by FAAS and ETAAS (G. Rauret *et al.*). 4. Analysis of environmental and biological samples by atomic spectroscopic methods (M. Hoenig, M.F. Gunn). 5. Validation of neutron activation analysis techniques (K. Heydorn). 6. Flow-through (bio)chemical sensors in environmental analysis (M.D. Luque de Castro, M. Válcarcel). 7. Fiber optical sensors applied to field measurements (C. Cámara *et al.*). 8. Chromium speciation in environmental and biological samples (K. Vercoutere, R. Cornelis). 9. Determination of aluminium species in natural waters (B. Fairman, A. Sanz-Medel). 10. Selenium speciation analyses in water and sediment matrices (C. Cámara *et al.*). 11. Antimony speciation in water (M.B. de la Calle- Guntiñas *et al.*). 12. Arsenic speciation in environmental matrices (A. Amran *et al.*). 13. Mercury speciation in biological matrices (I. Drabæk, Å Iverfeldt). 14. Speciation analysis of organolead compounds. Status and future prospects (R. Lobinski *et al.*). 15. Speciation analysis of organotin by GC-AAS and GC-AES after extraction and derivatization (W.M.R. Dirkx *et al.*). 16. High performance liquid chromatography - isotope dilution - inductively coupled plasma - mass spectrometry for lead and tin speciation in environmental samples (S.J. Hill *et al.*). 17. Speciation of organotin compounds in environmental samples by GC-MS (R. Morabito *et al.*). 18. Development of supercritical fluid extraction procedures for the determination of organotin compounds in sediment (J.M. Bayona). 19. Hydride generation for speciation analyses using GC/AAS (R. Ritsema *et al.*). 20. Single and sequential extraction schemes for trace metal speciation in soil and sediment (A.M. Ure *et al.*). 21. Methods for the determination of chlorinated biphenyls in air (M. Morosini, K. Balschmitter). 22. Sample handling and determination of carbamate pesticides and their transformation products in various matrices (M. Honing *et al.*). 23. Method development for the determination of polycyclic aromatic hydrocarbons (PAHs) in environmental matrices (J. Jacob). 24. Method validation for the determination of dioxins (T. Rymen). Subject index.

©1995 670 pages Hardbound
Price: Dfl. 475.00 (US$279.50)
ISBN 0-444-89955-3

ELSEVIER
An imprint of Elsevier Science

ORDER INFORMATION

ELSEVIER SCIENCE B.V.
P.O. Box 330
1000 AH Amsterdam
The Netherlands
Fax: +31 (20) 485 2845

For USA and Canada:
P.O. Box 945, New York
NY 10159-0945
Fax: +1 (212) 633 3680

US$ prices are valid only for the USA & Canada and are subject to exchange rate fluctuations; in all other countries the Dutch guilder price (Dfl.) is definitive. Customers in the European Union should add the appropriate VAT rate applicable in their country to the price(s). Books are sent postfree if prepaid.

Trace Element Analysis in Biological Specimens

Edited by **R.F.M. Herber** and **M. Stoeppler**

Techniques and Instrumentation in Analytical Chemistry Volume 15

The major theme of this book is analytical approaches to trace metal and speciation analysis in biological specimens. The emphasis is on the reliable determination of a number of toxicologically and environmentally important metals. It is essentially a handbook based on the practical experience of each individual author. The scope ranges from sampling and sample preparation to the application of various modern and well-documented methods, including quality assessment and control and statistical treatment of data. Practical advice on avoiding sample contamination is included.

In the first part, the reader is offered an introduction into the basic principles and methods, starting with sampling, sample storage and sample treatment, with the emphasis on sample decomposition. This is followed by a description of the potential of atomic absorption spectrometry, atomic emission spectrometry, voltammetry, neutron activation analysis, isotope dilution analysis, and the possibilities for metal speciation in biological specimens. Quality control and all approaches to achieve reliable data are treated in chapters about interlaboratory and intralaboratory surveys and reference methods, reference materials and statistics and data evaluation.

The chapters of the second part provide detailed information on the analysis of thirteen trace metals in the most important biological specimens. The following metals are treated in great detail: Aluminium, arsenic, cadmium, chromium, copper, lead, selenium, manganese, nickel, mercury, thallium, vanadium and zinc.

The book will serve as a valuable aid for practical analysis in biomedical laboratories and for researchers involved with trace metal and species analysis in clinical, biochemical and environmental research.

Contents: Part 1. Basic Principles and Methods.

©1994 590 pages Hardbound
Price: Dfl. 475.00 (US$ 279.50)
ISBN 0-444-89867-0

ELSEVIER
An imprint of Elsevier Science

ORDER INFORMATION

ELSEVIER SCIENCE B.V.
P.O. Box 330
1000 AH Amsterdam
The Netherlands
Fax: +31 (20) 485 2845

For USA and Canada:
P.O. Box 945
New York, NY 10159-0945
Fax: +1 (212) 633 3680

US$ prices are valid only for the USA & Canada and are subject to exchange rate fluctuations; in all other countries the Dutch guilder price (Dfl.) is definitive. Customers in the European Union should add the appropriate VAT rate applicable in their country to the price(s). Books are sent postfree if prepaid.

PUBLICATION SCHEDULE FOR THE 1995 SUBSCRIPTION

Journal of Chromatography A and *Journal of Chromatography B: Biomedical Applications*

MONTH	1994	J	F	M	A	M	
Journal of Chromatography A	Vols. 683–688	689/1 689/2 690/1 690/2	691/1 + 2 692/1 + 2 693/1 693/2	694/1 694/2 695/1 695/2	696/1 696/2 697/1 + 2 698/1 + 2	699/1 699/2 700/1 + 2 702/1 + 2	The publication schedule for further issues will be published later.
Bibliography Section				713/1			
Journal of Chromatography B: Biomedical Applications		663/1 663/2	664/1 664/2	665/1 665/2	666/1 666/2	667/1 667/2	

INFORMATION FOR AUTHORS

(Detailed *Instructions to Authors* were published in *J. Chromatogr. A*, Vol. 657, pp. 463–469. A free reprint can be obtained by application to the publisher, Elsevier Science B.V., P.O. Box 330, 1000 AH Amsterdam, Netherlands.)

Types of Contributions. The following types of papers are published: Regular research papers (full-length papers), Review articles, Short Communications and Discussions. Short Communications are usually descriptions of short investigations, or they can report minor technical improvements of previously published procedures; they reflect the same quality of research as full-length papers, but should preferably not exceed five printed pages. Discussions (one or two pages) should explain, amplify, correct or otherwise comment substantively upon an article recently published in the journal. For Review articles, see inside front cover under Submission of Papers.

Submission. Every paper must be accompanied by a letter from the senior author, stating that he/she is submitting the paper for publication in the *Journal of Chromatography A* or *B*.

Manuscripts. Manuscripts should be typed in **double spacing** on consecutively numbered pages of uniform size. The manuscript should be preceded by a sheet of manuscript paper carrying the title of the paper and the name and full postal address of the person to whom the proofs are to be sent. As a rule, papers should be divided into sections, headed by a caption (*e.g.*, Abstract, Introduction, Experimental, Results, Discussion, etc.). All illustrations, photographs, tables, etc., should be on separate sheets.

Abstract. All articles should have an abstract of 50–100 words which clearly and briefly indicates what is new, different and significant. No references should be given.

Introduction. Every paper must have a concise introduction mentioning what has been done before on the topic described, and stating clearly what is new in the paper now submitted.

Experimental conditions should preferably be given on a *separate* sheet, headed "Conditions". These conditions will, if appropriate, be printed in a block, directly following the heading "Experimental".

Illustrations. The figures should be submitted in a form suitable for reproduction, drawn in Indian ink on drawing or tracing paper. Each illustration should have a caption, all the *captions* being typed (with double spacing) together on a *separate sheet*. If structures are given in the text, the original drawings should be provided. Coloured illustrations are reproduced at the author's expense, the cost being determined by the number of pages and by the number of colours needed. The written permission of the author and publisher must be obtained for the use of any figure already published. Its source must be indicated in the legend.

References. References should be numbered in the order in which they are cited in the text, and listed in numerical sequence on a separate sheet at the end of the article. Please check a recent issue for the layout of the reference list. Abbreviations for the titles of journals should follow the system used by *Chemical Abstracts*. Articles not yet published should be given as "in press" (journal should be specified), "submitted for publication" (journal should be specified), "in preparation" or "personal communication".

Vols. 1–651 of the *Journal of Chromatography*; *Journal of Chromatography, Biomedical Applications* and *Journal of Chromatography, Symposium Volumes* should be cited as *J. Chromatogr.* From Vol. 652 on, *Journal of Chromatography A* (incl. Symposium Volumes) should be cited as *J. Chromatogr. A* and *Journal of Chromatography B: Biomedical Applications* as *J. Chromatogr. B.*

Dispatch. Before sending the manuscript to the Editor please check that the envelope contains four copies of the paper complete with references, captions and figures. One of the sets of figures must be the originals suitable for direct reproduction. Please also ensure that permission to publish has been obtained from your institute.

Proofs. One set of proofs will be sent to the author to be carefully checked for printer's errors. Corrections must be restricted to instances in which the proof is at variance with the manuscript.

Reprints. Fifty reprints will be supplied free of charge. Additional reprints can be ordered by the authors. An order form containing price quotations will be sent to the authors together with the proofs of their article.

The Data Analysis Handbook

By **I.E. Frank** and **R. Todeschini**

Data Handling in Science and Technology Volume 14

Analyzing observed or measured data is an important step in applied sciences. The recent increase in computer capacity has resulted in a revolution both in data collection and data analysis. An increasing number of scientists, researchers and students are venturing into statistical data analysis; hence the need for more guidance in this field, which was previously dominated mainly by statisticians.

This handbook fills the gap in the range of textbooks on data analysis. Written in a dictionary format, it will serve as a comprehensive reference book in a rapidly growing field. However, this book is more structured than an ordinary dictionary, where each entry is a separate, self-contained entity. The authors provide not only definitions and short descriptions, but also offer an overview of the different topics. Therefore, the handbook can also be used as a companion to textbooks for undergraduate or graduate courses.

Approximately 1700 entries are given in alphabetical order grouped into 20 topics and each topic is organized in a hierarchical fashion. Additional specific entries on a topic can be easily found by following the cross-references in a top-down manner. Several figures and tables are provided to enhance the comprehension of the topics and a list of acronyms helps to locate the full terminologies. The bibliography offers suggestions for further reading.

©1994 386 pages
Hardbound
Price: Dfl. 325.00
US$ 185.50
ISBN 0-444-81659-3

ELSEVIER
An imprint of Elsevier Science

ORDER INFORMATION

ELSEVIER SCIENCE B.V.
P.O. Box 330, 1000 AH
Amsterdam, The Netherlands
Fax: +31 (20) 485 2845

For USA and Canada:
P.O. Box 945, New York, NY
10159-0945
Fax: +1 (212) 633 3680

US$ prices are valid only for the USA & Canada and are subject to exchange rate fluctuations; in all other countries the Dutch guilder price (Dfl.) is definitive. Customers in the European Union should add the appropriate VAT rate applicable in their country to the price(s). Books are sent postfree if prepaid.

0021-9673(19950331)695:2;1-G